الجمهورية الجزائرية الديمقراطية الشعبية
République Algérienne Démocratique et Populaire
وزارة التعليم العالي والبحث العلمي
Ministère de l'Enseignement Supérieur et de la Recherche Scientifique

Université Mohamed Khider - Biskra
Faculté des Sciences et Technologie
Département: Génie civil et Hydraulique
Réf: ……

جـــامعة محمد خيـضر بـــسكرة
كـلية العـلـــوم و التكـــنولوجـيا
قسم: الهنـدسـة المـدنيـة و الـري
المرجع: .....

Mémoire présenté en vue de l'obtention

du diplôme de

Doctorat LMD en Génie Civil

Option : Modélisation numérique en génie civil

Analyse des pressions de terre passive et active sur les structures de soutènement par approche numérique

Présenté par:

Houssem Eddine LANABI

Soutenu publiquement

Devant le jury composé de :

Pr. Lamine Belounar	Professeur	Président	Université de Biskra
Pr. Sadok Benmebarek	Professeur	Rapporteur	Université de Biskra
Pr. Naima Benmebarek	Professeur	Rapporteuse	Université de Biskra
Pr. Mohamed Saddek Remadna	Professeur	Examinateur	Université de Biskra
Pr. Rafik Demagh	Professeur	Examinateur	Université de Biskra

الجمهورية الجزائرية الديمقراطية الشعبية
People's Democratic Republic of Algeria
وزارة التعليم العالي والبحث العلمي
Ministry of Higher Education and Scientific Research

Mohamed Khider University - Biskra
Faculty of Science and Technology
Department: Civil and Hydraulic Engineering
Ref: ……

جـــامعة محمد خيضر بـــسكرة
كـلية العـلـــوم و التكـــنولوجـيا
قسم: الهندسـة المـدنيـة و الـري
المرجع:.....

Thesis presented with a view to obtaining

LMD Doctorate in Civil Engineering

Option: Numerical modeling in civil engineering

Analysis of passive and active earth pressures on retaining structures with numerical approach

Presented by:

Houssem Eddine LANABI

Publicly supported on:

before the jury composed of:

Pr. Lamine Belounar	Professor	Chair	University of Biskra
Pr. Sadok Benmebarek	Professor	Supervisor	University of Biskra
Pr. Naima Benmebarek	Professor	Co-Supervisor	University of Biskra
Pr. Mohamed Saddek Remadna	Professor	Examiner	University of Biskra
Pr. Rafik Demagh	Professor	Examiner	University of Batna

ACKNOWLEDGMENTS

I would like to express my sincere gratitude to all those who have contributed to this thesis with their invaluable support, guidance, and expertise. I would like to take this opportunity to express my heartfelt gratitude to the individuals who have been instrumental in the completion of this thesis.

I want to express my Profound thanks to Professor Sadok Benmebarek, who served as my supervisor and thesis advisor, as well as Professor Naima Benmebarek, for offering invaluable scientific guidance throughout this research. I must acknowledge that he demonstrated exceptional insight, consistently steering me in the right direction during moments of uncertainty. His accessibility, extensive expertise, and meticulous attention to detail were instrumental in the success of this thesis. It was truly an honor and a pleasure to have the opportunity to work under his guidance.

I also extend my gratitude to the members of my thesis committee, Professor Lamine Belounar for bestowing upon me the great honor of chairing the thesis committee, as well as Professor Mohamed Saddek Remadna and Professor Rafik Demagh for their invaluable insights and constructive critiques. Your collective expertise enriched the depth and rigor of this work.

I would like to acknowledge the NMISSI Laboratory team for the support they provided during my research, without which this thesis would not have been possible. Your investment in my education is deeply appreciated.

I extend my thanks to the staff and resources at Mohamd Khider Biskra University, whose facilities, library resources, and administrative support greatly facilitated the research process.

Furthermore, I am grateful to my friends and family for their unwavering encouragement, understanding, and patience. Your belief in me and your emotional support sustained me through the challenging moments.

Lastly, I would like to acknowledge all the participants and interviewees who generously shared their time and knowledge, contributing to the empirical foundation of this thesis.

To all those whose names may not be mentioned here but have, in one way or another, contributed to this endeavor – thank you. Your collective efforts have made this thesis a reality.

ABSTRACT

The current design methodologies for retaining walls predominantly hinge on assumptions related to translational movement. However, in practical scenarios, retaining structures often experience rotational movements, particularly in cases involving integral bridge abutments, strutted walls, embedded walls, and sheet piles. This critical distinction has prompted a surge of interest and research in understanding lateral earth pressure behavior behind rotating retaining walls in recent years.

This thesis conducts comprehensive numerical investigations into the influence of various types of wall movements: translation, rotation about the top and rotation about the bottom, on both two-dimensional and three-dimensional lateral earth pressure. The investigation is performed using the explicit difference software FLAC and FLAC3D for accurate and detailed analysis. The examination of multi-dimensional behaviors allows for a comprehensive assessment of the active and passive earth pressures under various conditions of wall movements. The results of the present numerical analysis demonstrate that in the case of translational movement of the retaining wall, the obtained active and passive earth pressure distributions exhibit a linear pattern; similar to the one provided by commonly used theories from literature. However, when rotational movement is introduced, the distribution tends to obtain a non-linear pattern, with active earth pressure coefficients higher than those from translation mode and lower passive ones. In the case of rotation about top, the generated passive earth pressure is almost null at the upper part of the wall, while an important increment of passive load can be noticed with depth. Hence, the resulting earth pressure centroid is situated below the one-third of the wall height. The active earth pressure in that case is also distributed with a non-linear shape having a centroid situated at a higher position than that used in literature. Conversely, in rotation about bottom, the rotational motion of the wall induces a full mobilization of passive earth pressure in the upper half of the wall. This is followed by a partial mobilization that rapidly decreases, ultimately converging towards the earth pressure at rest near the base of the wall. This movement pattern results in an earth pressure distribution centroid surpassing one-third of the wall's height. However, the active earth pressure shows a centroid situated at a lower position. These variations in active and passive earth pressure distributions and magnitudes under different modes of wall movements underscore the intricate nature of soil-structure interactions. Understanding these responses holds practical implications for the design and stability of retaining structures.

ملخص

تتمحور المنهجيات الحالية لتصميم جدران الدعم بشكل رئيسي حول الافتراضات المتعلقة بالحركة الاسحابية المستقيمة. لكن ميدانيا، غالباً ما تتعرض الهياكل لحركات دورانية، خاصة في حالات تشمل الجسورالمتكاملة، والجدران المدفونة المدعمة والغير مدعمة. لقد أدت هذه الفارقة الحرجة إلى زيادة الاهتمام والبحث في فهم سلوك الضغط الجانبي للتربة خلف جدران الدعم المعرضة لحركة دورانية في السنوات الأخيرة.

تقوم هذه الرسالة بإجراء تحقيقات عددية شاملة حول تأثير مختلف أنواع حركات الجدران: الجركة المستقيمة، والدوران حول الجزء العلوي أو حول الجزء السفلي، على الضغط الأرضي ثنائي وثلاثي الأبعاد. يتم إجراء هذا التحقيق باستخدام البرمجيات FLAC و FLAC3D لتحليل دقيق ومفصل. يسمح فحص السلوكات متعددة الأبعاد بتقييم شامل للضغط الأرضي في ظروف متنوعة من حركات الجدار. تظهر نتائج التحليل العددي الحالي أنه في حالة الحركة المستقيمة للجدار، يظهر توزيع الضغط الأرضي السلبي المحصل نمطًا خطيًا، مشابهاً للنمط الذي يتم توقعه من قبل النظريات المعتمدة عموماً. لكن عندما يتم إدخال الحركة الدورانية، يميل التوزيع إلى الحصول على نمط غير خطي، مع قيم معامل الضغط الأرضي السلبي أقل من تلك في الوضع المستقيم. في حالة الدوران حول الجزء العلوي، يكاد يكون الضغط الأرضي السلبي المولد معدومًا تقريبًا في الجزء العلوي من الجدار، في حين يمكن ملاحظة زيادة مهمة في الضغط السلبي مع العمق. وبالتالي، يتم وضع مركز الضغط الأرضي الناتج أسفل ثلث ارتفاع الجدار. وعلى العكس من ذلك، في حالة الدوران حول الجزء السفلي، تثير الحركة الدورانية للجدار تحريكًا كاملاً للضغط الأرضي السلبي في النصف العلوي من الجدار. يتبع ذلك تحريكًا جزئيًا ينخفض بسرعة، ليكون في النهاية مشابها للضغط الأرضي عند الراحة بالقرب من قاعدة الجدار. يؤدي هذا النمط من الحركة إلى توزيع في الضغط الأرضي يتجاوز مركزه ثلث ارتفاع الجدار. تؤكد هذه الاختلافات في توزيعات ومقدار الضغط الأرضي السلبي تحت وسائط مختلفة من حركات الجدار على الطبيعة المعقدة لتفاعلات التربة والهيكل. وفهم هذه الاستجابات يحمل تأثيرات عملية على تصميم واستقرار الهياكل الحائزة.

TABLE OF CONTENTS

INTRODUCTION OF THE THESIS 1

CHAPTER I: LITERATURE REVIEW ON RETAINING WALLS

1.1. Introduction 5

1.2. Reminder on the types of retaining structures 5

1.2.1. Rigid Gravity Walls 5

1.2.2. Inverted-T Semi-Gravity Walls 6

1.2.3. Non-Gravity Embedded Retaining Structures 6

1.2.4. Mechanically Stabilized Earth Walls 9

1.2.5. Soil Nail Wall 9

1.3. Retaining Structures subjected to rotational movements 11

1.3.1. Integral bridge abutments 11

1.3.2. Embedded walls 14

1.3.3. Anchored and Strutted walls 14

1.4. Literature review on Rotational Movements 18

1.4.1. James and Bransby (1970) 18

1.4.2. Fang et al. (1994) 19

1.4.3. Dave & Dasaka (2012) 24

1.4.4. Peng et al. (2012) 29

1.4.5. Tang et al. (2018) 31

1.5. Conclusion 34

CHAPTER II: EARTH PRESSURE CONCEPTS

2.1. Introduction 36

2.2. At-rest earth pressure 39

2.3. Active and passive earth pressures 39

2.4. Earth pressure theories 41

2.4.1. Rankine's (1857) Earth Pressure Theory 42

2.4.2. Coulomb's Earth Pressure Theory (1776) 44
2.4.3. The Log-Spiral Method 47
2.4.4. Trial Wedge Method 48
2.5. Surcharge loads 48
2.5.1. Uniform Surcharge Loads 50
2.5.2. Concentrated Load (Point Load) 51
2.5.3. Line Load (q/m) 51
2.5.4. Strip Load 52
2.6. Three-dimensional earth pressure 53
2.6.1. Brinch Hansen (1966) 53
2.6.2. Ovesen and Stromann (1972) 54
2.6.3. Soubra and Regenass (2000) 54
2.6.4. Benmebarek et al. (2008) 58
2.7. Conclusion 61

CHAPTER III: NUMERICAL MODELING

3.1. Introduction 63
3.2. Overview on numerical modeling 63
3.3. Introduction to FLAC & FLAC3D programs 65
3.4. Available numerical methods (continuum models) 65
3.4.1. Finite element method 66
3.4.2. Finite difference method 68
3.4.3. Discrete element method 70
3.4.4. Boundary element method 71
3.5. Constitutive models 72
3.5.1. Mohr-Coulomb Model (linear elastic perfectly plastic model) 73
3.5.2. Plastic-Hardening model (hyperbolic model) 77
3.6. Modeling procedure 79
3.7. Conclusion 83

CHAPTER IV: LATERAL EARTH PRESSURE DUE TO SOIL UNIT WEIGHT UNDER VARIOUS MODES OF WALL MOVEMENT

4.1. Introduction **84**

4.2. Validation of numerical modeling in translating mode **86**

4.2.1. Active and passive earth pressure coefficients *86*

4.2.2. Active and passive earth pressure distributions *86*

4.3. Active and Passive Earth Pressures in Various Modes of Movement **89**

4.3.1. Maximum Shear strain rate Distribution *89*

4.3.2. Evolution of Kp with wall movement *90*

4.3.3. Passive earth pressure distribution in RT mode *92*

4.3.4. Passive earth pressure distribution in RB mode *94*

4.3.5. Active and passive earth pressures with various magnitudes of wall movement *95*

4.3.6. Discussion of results for RB and RT modes *103*

4.4. Conclusions **106**

CHAPTER V: LATERAL EARTH PRESSURE DUE TO SURCHARGE LOADING UNDER VARIOUS MODES OF WALL MOVEMENT

5.1. Introduction **108**

5.2. Validation of the numerical model **109**

5.3. Evolution of lateral earth pressure with wall movement **111**

5.4. ActiVe and Passive earth pressure distribution **112**

5.5. Failure mechanism **115**

5.6. Three dimensional passive earth pressure **120**

5.6.1. Calculation process *120*

5.6.2. Passive earth pressure coefficient *121*

5.6.3. Comparison with results from literature *122*

5.1.1. Shape factors *122*

5.2. Conclusions **125**

General conclusion **128**

LIST OF FIGURES

CHAPTER I: LITERATURE REVIEW ON RETAINING WALLS

Figure 1. 1. Gravity retaining wall construction. a) Excavation b) wall construction c) finalized gravity wall 6
Figure 1. 2. Inverted-T Retaining Walls 7
Figure 1. 3. a) Embedded retaining wall b) anchored retaining wall 7
Figure 1. 4. Continuous sheet piles 8
Figure 1. 5. Soldier Pile Retaining Wall 9
Figure 1. 6: MSE Wall with Precast Concrete Face Panels 10
Figure 1. 7: Soil Nail Wall 10
Figure 1. 8. Integral Bridge Abutment 11
Figure 1. 9. Integral bridge abutment movement during winter and summer 12
Figure 1. 10. Full scale monitoring bridge - "Route 2 high-speed connector underpass" New Brunswick – Canada 12
Figure 1. 11 Instrumentation locations on a) east abutment b) west abutment 13
Figure 1. 12 Linear effective earth pressure distribution for embedded walls a) assumed earth pressure b) idealized earth pressure 15
Figure 1. 13 Experimental set-up by Bica & Clayton (1998) 15
Figure 1. 14 Experimental distribution of earth pressure on embedded walls (Lyndon & Pearson, 1984) 16
Figure 1. 15. Anchored retaining wall 16
Figure 1. 16. Strutted retaining walls 18
Figure 1. 17 Laboratory test by James and Bransby (1970) a) large glass-side tank b) front view of wall showing load cells 19
Figure 1. 18. Shear strain contour increment for different wall rotations by James and Bransby (1970) a) dense sand b) loose sand 20
Figure 1. 19 Fang et al. (1994) laboratory set-up 21
Figure 1. 20 Types of wall movement by Fang et al. (1994) 21
Figure 1. 21 Evolution of passive earth pressure coefficient with wall movement for RTT mode 22
Figure 1. 22 Evolution of passive earth pressure coefficient with wall movement for RBT mode 22

Figure 1. 23 Distribution of passive earth pressure for RTT mode (Fang et al., 1994) a) n=0.00 b) n= 0.50 c) n=1.81 d) n=7.43 23
Figure 1. 24 Distribution of passive earth pressure for RBT mode (Fang et al., 1994) a) n=0.00 b) n= 0.50 c) n=1.81 d) n=7.43 24
Figure 1. 25. Experimental set up from Dave & Dasaka (2012) 25
Figure 1. 26. At-rest earth pressure distribution, when the edge of surcharge load is located at the face of the wall (Dave & Daska, 2012) 26
Figure 1. 27. At-rest earth pressure distribution, when the edge of surcharge load is distanced h/4 from the the wall (Dave & Daska, 2012) 26
Figure 1. 28. Active earth pressure distribution under surcharge loading from Dave & Dasaka (2012) 28
Figure 1. 29. Passive earth pressure distribution under surcharge loading from Dave & Dasaka (2012) 28
Figure 1. 30 Passive displacement modes from Peng et al. (2012) a)$m \geq 0, Smax = Stop$ b) $m \leq 0, Smax = Sbottom$ 29
Figure 1. 31 Distribution of passive earth pressure with various wall movements (Peng et al., 2012) a) RB mode b) T mode c) RT mode 31
Figure 1. 32 Different states of earth pressure: a) stress states with dfferent wall movements b) Mohr circles for different stresss states 32
Figure 1. 33 Distribution of passive earth pressure from tang et al.(2018) for RBT mode a) n=0 b) n=0.21 c) n=0.50 d) n=13.78 33
Figure 1. 34 Distribution of passive earth pressure from tang et al.(2018) for RTT mode a) n=0 b) n=0.21 c) n=1.81 d) n=7.43 34

CHAPTER II: EARTH PRESSURE CONCEPTS

Figure 2. 1. Active and passive earth pressures 37
Figure 2. 2. active and passive earth pressure with wall movement a) Mohr Circle b) stress-strain curve 37
Figure 2. 3. Lateral Earth Pressure Variation with Depth 38
Figure 2. 4 : Active - Passive – At rest earth pressure resulted from the wall movement 40
Figure 2. 5 : Mohr Circle Representation of the Stress State for a Cohesionless Backfill 40
Figure 2. 6 : Rankine's Active Wedge 43
Figure 2. 7: Rankine' s Passive Wedge 44
Figure 2. 8: Coulomb's Active Wedge 45

Figure 2. 9: Coulomb's Passive Wedge 46
Figure 2. 10 Illustration of the Logarithmic Spiral Failure Surface 47
Figure 2. 11. Active Trial Wedge 49
Figure 2. 12. Different types of surcharge loads behind a retaining wall a) uniform surcharge load b) concentrated load c) line load d) strip load 49
Figure 2. 13 Lateral Pressure Due to Uniform Surcharge 50
Figure 2. 14. Concentrated load behind retaining walls a) lateral earth pressure doubled due to mirror image effect b) distribution of earth pressure with wall depth c) distribution of earth pressure with wall length 52
Figure 2. 15. Strip load behind retaining walls 52
Figure 2. 16. Parameters used in Brinch Hansen (1966) formula 53
Figure 2. 17. Force components for the analysis of 3D passive earth pressure (Ovesen and Stromann, 1972) 55
Figure 2. 18. Variation of Kp $Kpcos\delta$ with $Kpsin\delta$ (Ovesen and Stromann, 1972) 55
Figure 2. 19. Notations for anchors (Ovesen and Stromann, 1972) a)strip anchors b) row anchors 56
Figure 2. 20. Variation of $(Be - L)(H + B)$ with $(S' - L)(H + B)$ (Ovesen and Stromann, 1972) ... 56
Figure 2. 21. Failure mechanisms by Soubra and Regenass (2000) a) one-block b) multi-block c) truncated multi-block 57
Figure 2. 22. Benmebarek et al. (2006) numerical model 58

CHAPTER III: NUMERICAL MODELING

Figure 3. 1. Representation of a retaining wall a) Physical problem b) continuum model 66
Figure 3. 2Finite element (Clayton, 1993) 67
Figure 3. 3 Examples of two-dimensional finite elements 67
Figure 3. 4. Components of FLAC interface element 70
Figure 3. 5. Zone dimensions used in stiffness calculation (Itasca, 2013) 70
Figure 3. 6. Representation of the Mohr-Coulomb criterion in the Mohr plane 73
Figure 3. 7. Mohr Coulomb yield criterion in the principal stress space 74
Figure 3. 8. Figure Stress-strain relationship for the Mohr-Coulomb model 74
Figure 3. 9. Mohr-Coulomb failure 75
Figure 3. 10. a) Inclination of failure plan in soil with major principal plane b) Mohr's circle and failure envelope 76
Figure 3. 11. Modeling of dilation angle from the triaxial test (Vermeer and de Borst, 1984) 78

Figure 3. 12. Hyperbolic stress-strain relation in primary loading for a standard drained triaxial test . 79
Figure 3. 13. FLAC Numerical model for the analysis of the three types of movement..... 80
Figure 3. 14. Three types of wall movements: T, RT and RB..... 81
Figure 3. 15. Active (P_a) and passive (P_p) earth pressures acting on the retaining wall..... 82
Figure 3. 16. FLAC3D numerical model..... 82

CHAPTER IV: LATERAL EARTH PRESSURE DUE TO SOIL UNIT WEIGHT UNDER VARIOUS MODES OF WALL MOVEMENT

Figure 4. 1. Distribution of active earth pressure in T mode..... 88
Figure 4. 2. Distribution of passive earth pressure in T mode..... 88
Figure 4. 3. FLAC distribution of maximum shear strain rates and shear zone radiographs (Widulinski et al. 2011) in active case a) Translation mode b) Rotation around top c) Rotation around base. 90
Figure 4. 4. FLAC distribution of maximum shear strain rates and shear zone radiographs (Widulinski et al. 2011) in passive case a) Translation mode b) Rotation around top c) Rotation around base. 91
Figure 4. 5. Variation of K_p with different wall movement with $\varphi = 30.9°, \delta = 19.2°$ a) T mode b) RB mode c) RT mode. 92
Figure 4. 6. Comparison of passive earth pressure distribution in RT mode corresponding to $S_{max}/H = 0.05$ (5%H) and $S_{max}/H = 0.20$ (20%H) with experimental data and analytical solutions. 93
Figure 4. 7. Comparison of passive earth pressure distribution in RB mode ($S_{max}/H = 0.20$) with experimental data and analytical solutions 94
Figure 4. 8. Comparison of stress-strain behavior between Mohr-Coulomb and Plastic-Hardening model 96
Figure 4. 9. Distribution of active earth pressure in RB mode for various distances – Mohr-Coulomb model..... 97
Figure 4. 10. Distribution of active earth pressure in RB mode for various distances – Plastic-Hardening model..... 98
Figure 4. 11. Distribution of active earth pressure in RT mode for various distances – Mohr-Coulomb model..... 99
Figure 4. 12. Distribution of active earth pressure in RT mode for various distances – Plastic-Hardening model..... 100

Figure 4. 13. Distribution of passive earth pressure in RB mode for various distances – Mohr-Coulomb model 100
Figure 4. 14. Distribution of passive earth pressure in RB mode for various distances – Plastic-Hardening model 101
Figure 4. 15. Distribution of passive earth pressure in RT mode for various distances – Mohr-Coulomb model 102
Figure 4. 16. Distribution of passive earth pressure in RT mode for various distances – Plastic-Hardening model 103

CHAPTER V: LATERAL EARTH PRESSURE DUE TO SURCHARGE LOADING UNDER VARIOUS MODES OF WALL MOVEMENT

Figure 5. 1 Active earth pressure with 50kPa surcharge load 111
Figure 5. 2. Passive earth pressure with 50kPa surcharge load 111
Figure 5. 3. Passive earth pressure distribution with various wall rotations in RT mode. A) Mohr-Couomb b) Plastic-Hardening 113
Figure 5. 4. Passive earth pressure distribution with various wall rotations in RB mode. A) Mohr-Couomb b) Plastic-Hardening 114
Figure 5. 5. Active earth pressure distribution with $\varphi = 30°$, (a) $\delta\varphi = 0$ and (b) $\delta\varphi = 23$ 116
Figure 5. 6. Passive earth pressure distribution with $\varphi = 30°$, (a) $\delta\varphi = 0$ and (b) $\delta\varphi = 23$ 117
Figure 5. 7. Active earth pressure distribution in RT and RB modes with various φ and δ values 118
Figure 5. 8. Passive earth pressure distribution in RT and RB modes with various φ and δ values 119
Figure 5. 9. Maximum shear strain increment under various modes of wall movements 120
Figure 5. 10. Comparison of passive earth pressure coefficients for $\varphi = 30°$, $\delta\varphi = 23$ and different values of the ration bh 124
Figure 5. 11. Comparison of passive earth pressure coefficients between analytical and numerical results 126

LIST OF TABLES

Table 1. 1. Summary of east and west abutment seasonal movements 13

Table 1. 2. Anderson et al (1984) test program 17

Table 1. 3 Relationship between m and wall displacement modes 30

Table 1. 4 Formulas for the determination of passive earth pressure "p" and location of passive earth thrust $z0$ (Peng et al., 2012) 30

Table 2. 1. Comparison of $Kp\gamma(3D)$ from Benmebarek et al. (2006) and Soubra and Regenass (2000) 59

Table 2. 2. Comparison of $Kpq(3D)$ from Benmebarek et al. (2006) and Soubra and Regenass (2000) 60

Table 2. 3. Comparison of $Kp\gamma(3D)$ from Benmebarek et al. (2006) and theorem of corresponding states solutions (Equation 2.41) 61

Table 4. 1. Active and passive earth pressure coefficients with various internal friction angles and soil-wall friction angles in translation mode 87

Table 4. 2. Mohr-Coulomb soil parameters representing the Ottawa air-dry sand used in the experiment. 87

Table 4. 3. Soil parameters used in the prediction of the distribution of maximum shear strain rates and the comparison with Cambridge experimental results 90

Table 4. 4. Mohr-Coulomb soil parameters used to study the impact of S_{max}/H 95

Table 4. 5. Plastic-Hardening soil parameters used to study the impact of S_{max}/H 96

Table 4. 6. Variation of K_a and point of application with S_{max}/H for RB mode 98

Table 4. 7. Variation of K_a and point of application with S_{max}/H for RT mode 99

Table 4. 8. Variation of K_p and point of application with S_{max}/H for RB mode 102

Table 4. 9. Variation of K_p and point of application with S_{max}/H for RT mode 103

Table 4. 10. Active earth pressure coefficient (Ka) and point of application of the resultant force with various wall movement 105

Table 4. 11. Passive earth pressure coefficient (Kp) and point of application of the resultant force with various wall movement 105

Table 5. 1. Plastic-Hardening soil parameters representing Dave and Dasaka (2012) experiment 110

Table 5. 2. Mohr-Coulomb soil parameters representing Dave and Dasaka (2012) experiment 111

Table 5. 3. Three dimensional Passive earth pressure coefficients due to surcharge loading 122

INTRODUCTION OF THE THESIS

Retaining walls are essential structural elements designed to serve a dual purpose: to support and stabilize soil, while also adding aesthetic appeal to landscapes. These versatile structures have been employed for centuries in various engineering and landscaping projects, and their importance in preventing erosion, managing sloped terrains, and enhancing outdoor spaces cannot be overstated. The right estimation of active and passive earth pressure is the key for save design of retaining structures. The existing approaches are based on the translation movement of the retaining walls. Nevertheless, the real behavior that many existing retaining structures exert is rotation until failure. The first chapter (I) presents a summary on the available different types of retaining structures. They can be sorted into gravity, semi-gravity and non-gravity retaining walls. Next, among these types, a particular attention will be provided to those that are subjected mostly to rotational movements, which can be described in what follow:

- Integral bridge abutments refer to cases where the abutment wall is connected directly to the deck without any joints. This design aims to reduce joint corrosion and minimize maintenance costs. However, it's important to note that this configuration exposes the bridge to expansions and compressions during summer and winter time respectively. The change in deck dimensions will exert an extra push on the abutment wall from the top of it, causing it to rotate about the bottom. This chapter references numerous field experiments. An especially noteworthy example is the full-scale monitoring of the 'Route 2 High-Speed Connector Underpass' in New Brunswick, Canada (Huntley and Valsangkar, 2013). The test not only confirmed and provided detailed information regarding the rotational movement of these types of bridges, but also demonstrated the non-linear distribution of passive earth pressure on the adjacent backfill.

- Embedded walls, also known as cantilever walls, are another type of retaining structure primarily subjected to rotational movements. These walls are designed to be partially buried into the ground, using their depth to attain stability through the passive force generated in front of the wall, countering the active thrust behind it. Failure in cantilever retaining walls arises from a rotational movement pivoting near the wall's base. Previous laboratory tests, referenced in this chapter (Krey, 1932; Lyndon & Pearson, 1984; Bica & Clayton, 1998), demonstrated that during these rotational movements, the measured passive earth pressure crucial for the structure's stability design does not follow a linear

distribution as conventionally assumed by theories. Instead, it exhibits a significantly lower magnitude, which could potentially lead to design insecurity in such structures.

- Embedded walls can also be reinforced with anchors and struts, fortifying the structure to support higher backfills. This creates another type of retaining wall that is susceptible to rotational movements. Anderson et al. (1984) conducted a series of laboratory tests on anchored walls, deducing that the rotational failure occurs either at a point beneath the wall's toe or at the top of the wall, depending on the pre-stress loads.

The second chapter (II) provides an overview of three types of lateral earth pressures: At-rest, active, and passive earth pressure. At-rest earth pressure develops when the wall experiences no lateral movement. Active earth pressure generates when the earth retaining system is free to move away from the backfill. Passive earth pressure develops when the earth retaining system moves towards the soil mass. The estimation of at-rest earth pressure can be achieved through simple concepts depending on the soil consolidation (Terzaghi, 1923; Jaky, 1944; Meyerhof, 1976; Mayne & Kulhawy, 1982). However, there are numerous methods available for evaluating active and passive earth pressures, primarily based on three analytical concepts: the limit equilibrium method, slip line method, and the limit analysis method. Coulomb's (1776) and Rankine's (1857) theorems are the most commonly used for estimating lateral earth pressure even to this day.

The chapter then offers a concise explanation of the impact of surcharge loads behind retaining structures, which can manifest as uniform surcharge load, concentrated load, line load, or strip load. Following this, the chapter delves into the discussion of lateral earth pressure behind limited width retaining walls, accompanied by a review of the existing literature on three-dimensional earth pressure theories.

The focus of this thesis is to evaluate how the type of wall movement influences active and passive earth pressures through numerical analysis. This study was conducted using both two-dimensional and three-dimensional commercially available software FLAC and FLAC3D codes. This dual approach allows for a more nuanced understanding of how different types of wall movement influence lateral earth pressure under various conditions. Chapter III provides a concise overview of these two software applications. The chapter also introduces the primary numerical techniques employed in geotechnical investigations, which are the finite element method and the finite difference method. It is important to note that FLAC software employs the finite difference method. Additionally, a third one known as the boundary element method is explained in the chapter. This last finds greater utility in rock mechanics applications compared to soil mechanics, owing to its effectiveness in addressing non-homogeneous materials.

One of the most critical parameters in numerical simulations is the judicious selection of the constitutive model, as it plays a pivotal role in accurately describing the simulated soil's behavior. Various constitutive models are available within the FLAC software, each tailored to provide the best representation of specific soil conditions. In the current analysis, two distinct constitutive models were employed. The first, and perhaps most widely utilized in numerical studies, is the Mohr-Coulomb model. This foundational constitutive model holds paramount importance in geotechnical engineering and soil mechanics. It effectively characterizes the response of soils and rocks under a diverse range of stress conditions, making it an indispensable tool in the field. The second model employed is the Plastic-Hardening model, which intricately describes the hyperbolic stress-strain behavior exhibited by materials. This model is particularly adept at capturing the nonlinear response of soils and rocks to applied stresses. In the case of rotational movement of the wall, a partial mobilization of the adjacent soil occurs. This leads to the attainment of limit earth pressure on one side before the other. A comprehensive comparison of the results obtained from both constitutive models is presented in Chapters IV and V, specifically tailored to address this type of movement.

Chapter IV presents numerical computations using FLAC code to evaluate the active and passive earth pressure magnitudes and distribution against a retaining wall subjected to different wall movement modes. In agreement with classical solutions, the results proved that, in translation mode, lateral earth pressure distribution was substantially hydrostatic with depth for all the wall displacement stages. However, when the rotational mode was considered, either about top or bottom, a clear non-linear distribution that was strongly affected by the wall displacement magnitude was noted. For the rotation about top mode, due to the arching effect, the increase in earth pressure behind the lower half of the wall was more pronounced in passive case, with the wall displacement hardly affecting the centroid of the passive load distribution located below the commonly used one-third of the wall height. Active earth pressure, in the case of a wall rotating about its base, is also distributed nonlinearly with depth, having a centroid situated at the middle of wall. In rotation about bottom mode, as wall rotation progressed, the passive earth pressure mobilized in upper part of the wall increases and its distribution gradually changed from non-linear to linear. Furthermore, Compared to previous experimental results available in the literature, it was found that mobilized passive earth pressure under rotational movements requires more movement to reach the limit value than the translation mode. Moreover, the chapter proves well that the active earth pressure is less influenced by the rotation about bottom movement.

Chapter V investigates numerically the active and passive earth pressure behind a rigid retaining wall under uniform surcharge loading subjected to rotational wall movement using the FLAC code. The numerical results show that the obtained passive earth pressure coefficients are much lesser than the ones from translating mode used in literature, with values ranging from 63% to 98%.

Moreover, the rectangular distribution of active and passive earth pressures due to surcharge loading with depth is not perfectly valid in the case of a retaining wall subjected to rotational movement. The study proves well the influence of the type of wall movement on the magnitude and distribution of earth pressure due to surcharge loading which cannot be neglected.

Chapter I

LITERATURE REVIEW ON RETAINING WALLS

1.1. INTRODUCTION

The Earth retaining structures must be designed to endure lateral pressures from backfills and water flows, as well as the impacts of additional loads, such as surcharge and the weight of the wall itself, along with seismic forces. These specifications pertain to safety. Furthermore, the design of earth retaining systems should ensure they possess sufficient structural strength allowing for permissible displacements, as well as ample foundation capacity with acceptable settling. It's also imperative to maintain the overall stability of slopes near the walls. These criteria are associated with serviceability. The acceptable levels of lateral and vertical deformations are determined by the specific type and placement of the wall structure, as well as the surrounding infrastructure.

One more important parameters for the stability of retaining structures is the well estimation of forces acting on the retaining structures imposed by the soil medium, pore water pressure, any live load surcharges and seismic forces before the safety factors are considered. There exist many approaches for the estimation of lateral earth pressure exerted on the retaining wall, will be summarized in §2.4. However, most of these approaches are based on the translation movement of the retaining structure. In this chapter, a reminder about the different existing types of retaining structures, and revealing those subjected to rotational movements. In addition to the different existing studies about retaining structures under different types of movement from literature.

1.2. REMINDER ON THE TYPES OF RETAINING STRUCTURES

Modern retaining walls can come in many shapes and sizes; gravity retaining walls, which derive their stability thought the dead weight of the wall to resist lateral loads, semi-gravity retaining walls represented as inverted-T mainly constructed of reinforced concrete, non-gravity embedded, anchored or strutted retaining structures and reinforced-soil retaining walls.

1.2.1. Rigid Gravity Walls

A gravity wall primarily relies on its own mass along with the inherent strength of the ground to achieve stability. The horizontal movement of the wall is primarily thwarted by the friction between

its base and the underlying soil. Gravity walls have a long history of use, owing to their straightforward construction, often composed of materials like masonry or mass concrete as illustrated in Figure 1. 1 However, due to their substantial weight, they necessitate a solid foundation soil and are typically not the most efficient choice for retaining significant amounts of backfill at elevated heights.

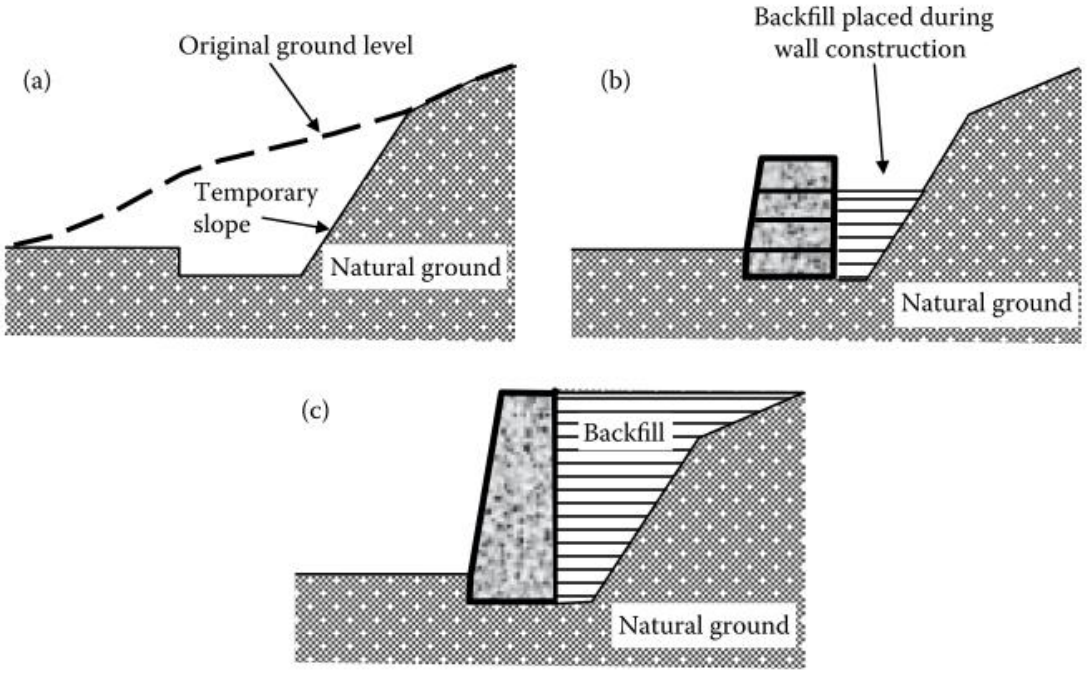

Figure 1. 1. Gravity retaining wall construction. a) Excavation b) wall construction c) finalized gravity wall

1.2.2. Inverted-T Semi-Gravity Walls

Semi-gravity cantilever and counterfort walls, designed in an Inverted-T configuration, are fabricated using reinforced concrete. They find application in both excavated and filled areas, featuring comparatively slim base widths. These walls can be sustained by foundations, whether shallow or deep, and their stem-to-footing positioning can be adjusted to meet right-of-way limitations. Additionally, they can be fortified with counterforts and keys, or constructed atop piles as depicted in Figure 1. 2. These walls are capable of providing support for sound walls, signage structures, and other elements along highways, offering optimal cost-effectiveness for walls of modest to intermediate heights.

1.2.3. Non-Gravity Embedded Retaining Structures

Embedded walls partly or wholly prevent lateral movement by embedding the base of the wall in the ground to significant depths below the excavation level. It may be constructed with precast concrete, treated timber, driven steel piles or sheets piles placed in drilled holes then backfilled with

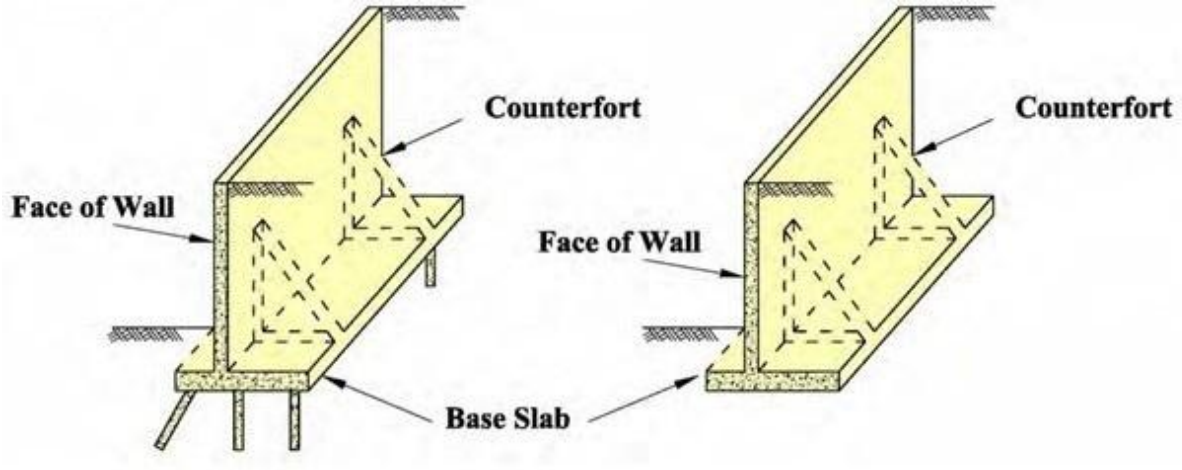

Figure 1. 2. Inverted-T Retaining Walls

concrete or reinforced concrete cast-in-place. They either can be self-stabilized by the passive force as embedded retaining walls (Figure 1. 3**Erreur ! Source du renvoi introuvable.**a) or provided with additional support to the upper part of the wall by anchors into the natural ground behind the retained side of the wall (Figure 1. 3b).

Anchored walls typically employ the same elements mentioned earlier for embedded walls. However, they gain extra lateral support from anchors positioned at one or more levels of the retaining structure. These anchors can be ground anchors, often referred to as tiebacks, which involve drilled holes with pre-stressed steel tendons grouted in place. These tendons extend from the wall face to an anchor zone located behind potential failure planes within the retained soil or rock mass. Anchored walls are commonly utilized in cut scenarios where construction progresses from the top to the bottom of the wall. They are primarily employed to stabilize unstable sites.

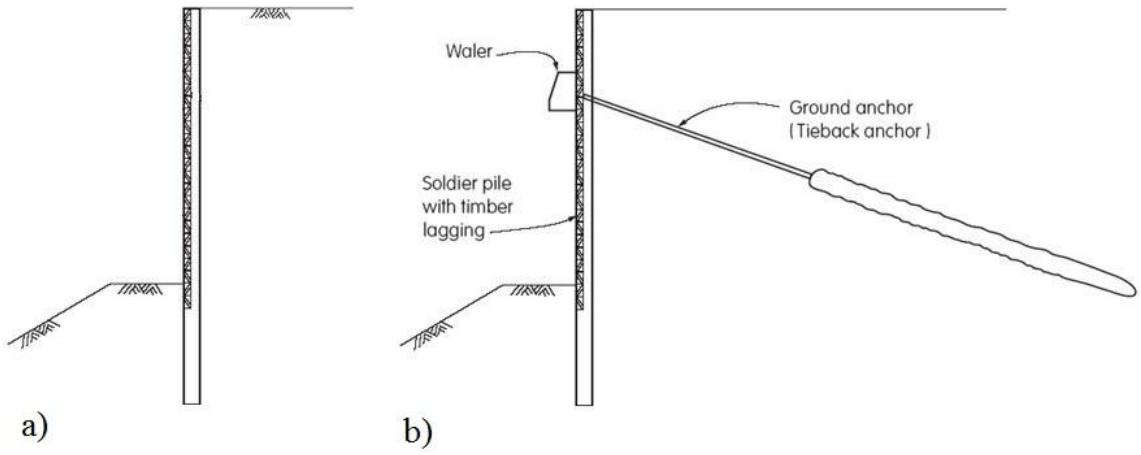

Figure 1. 3. a) Embedded retaining wall b) anchored retaining wall

Non-gravity retaining walls can take the form of continuous sheet piles, as shown in Figure 1. 4, constructed from materials such as precast concrete, pre-stressed concrete, or steel sheet piles. They can also manifest as soldier piles, as depicted in Figure 1.5, which are adorned with facings of treated timber, reinforced shotcrete, reinforced cast-in-place concrete, precast concrete, or metal elements. This type of wall relies on both the passive resistance of the foundation material and the moment-resisting capacity of the vertical structural members for stability. Consequently, the maximum load-bearing capacity of these retaining structures is determined by the foundation material and the moment-resisting capacity of the vertical retaining elements.

Embedded walls are typically employed in two distinct forms. The first type comprises pre-formed walls, exemplified by sheet piles, which are crafted by driving slender steel, timber, or concrete 'sheets' into the ground. This construction method does not entail any excavation during the initial phase. However, there may be minor ground displacement while installing sheets. The ground will be excavated then once the sheeting and any required anchors have been established.

The second type is defined by in situ walls, which involve the creation of diaphragm or bored-pile walls. This process entails the excavation of deep trenches or the drilling of auger holes, followed by the placement of reinforcement and the subsequent filling with concrete. Diaphragm and bored pile walls stand out as widely favored approaches for basement construction.

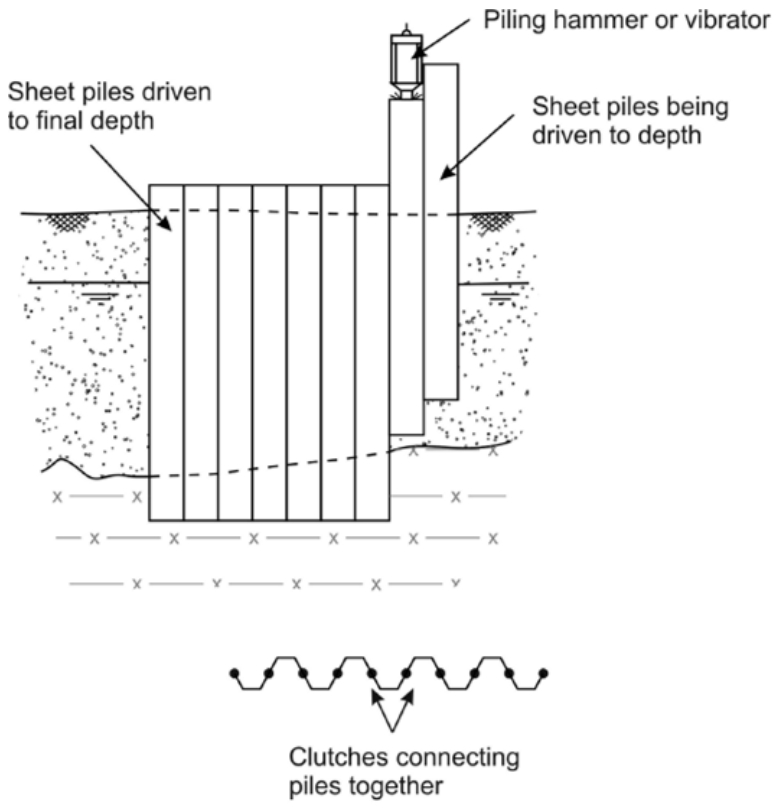

Figure 1. 4. Continuous sheet piles

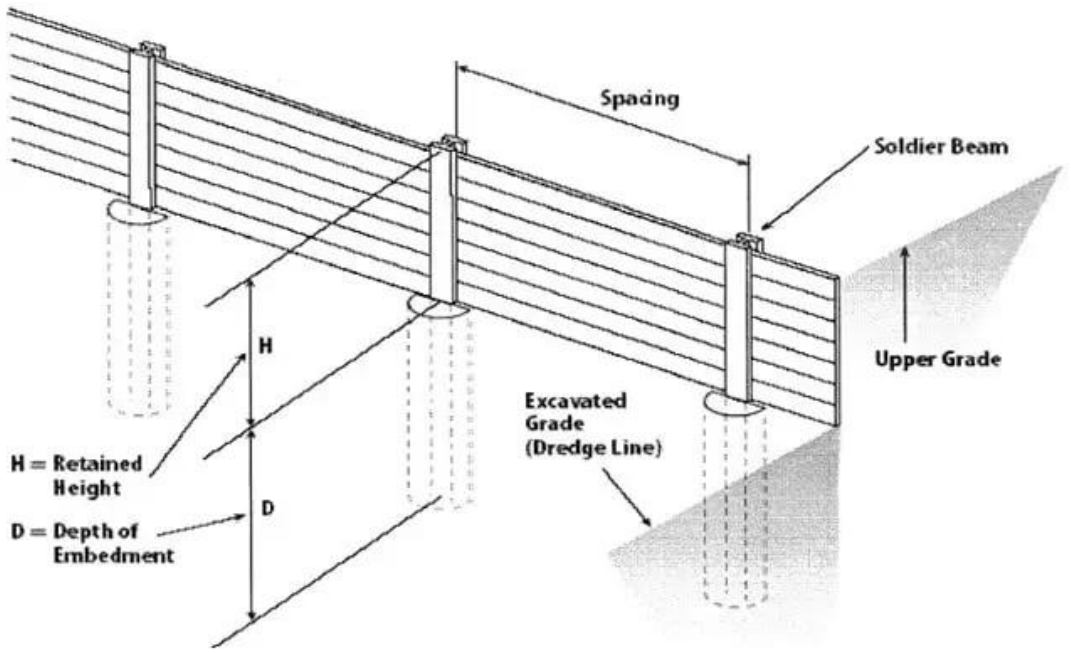

Figure 1. 5. Soldier Pile Retaining Wall

1.2.4. Mechanically Stabilized Earth Walls

Mechanically Stabilized Earth (MSE) walls utilize either metallic (non-extendable) or geosynthetic (extendable) soil reinforcement integrated within the soil mass. These reinforcements work in conjunction with vertical or near-vertical facing elements, as illustrated in Figure 1. 6. Similar to gravity walls, these structures derive their lateral resistance from the combined weight of the reinforced soil mass and the facing structure. MSE walls are typically employed in situations where traditional reinforced concrete retaining walls would be considered. They are particularly effective in areas where substantial total and differential settlements are anticipated. The permissible differential settlement is determined by the flexibility of the wall-facing elements within the plane of the wall. The practical height of an MSE wall is limited by the stability of the specific foundation material at the site.

1.2.5. Soil Nail Wall

A soil nail wall is constructed by grouting steel bars into drilled holes, which are inclined and directed back into the retained mass of soil, as illustrated in Figure 1. 7. Typically, soil nails are spaced at intervals of approximately 4 to 6 feet both horizontally and vertically. Their lengths generally range from 0.7 to 1.2 times the height of the wall. For permanent soil nail walls, the soil nail bars incorporate an additional layer of corrosion protection, usually an epoxy coating. Following the installation of soil nails, prefabricated drainage panels are affixed against the excavated slope. Subsequently, the slope is covered with reinforced concrete that is linked to the nail "heads." The concrete can be finished with a

textured "nozzle finish" or a smoother "cut finish." In cases where the wall is visible, the concrete can be sculpted and tinted to mimic the surrounding soil or rock, or polished to achieve a sleek surface.

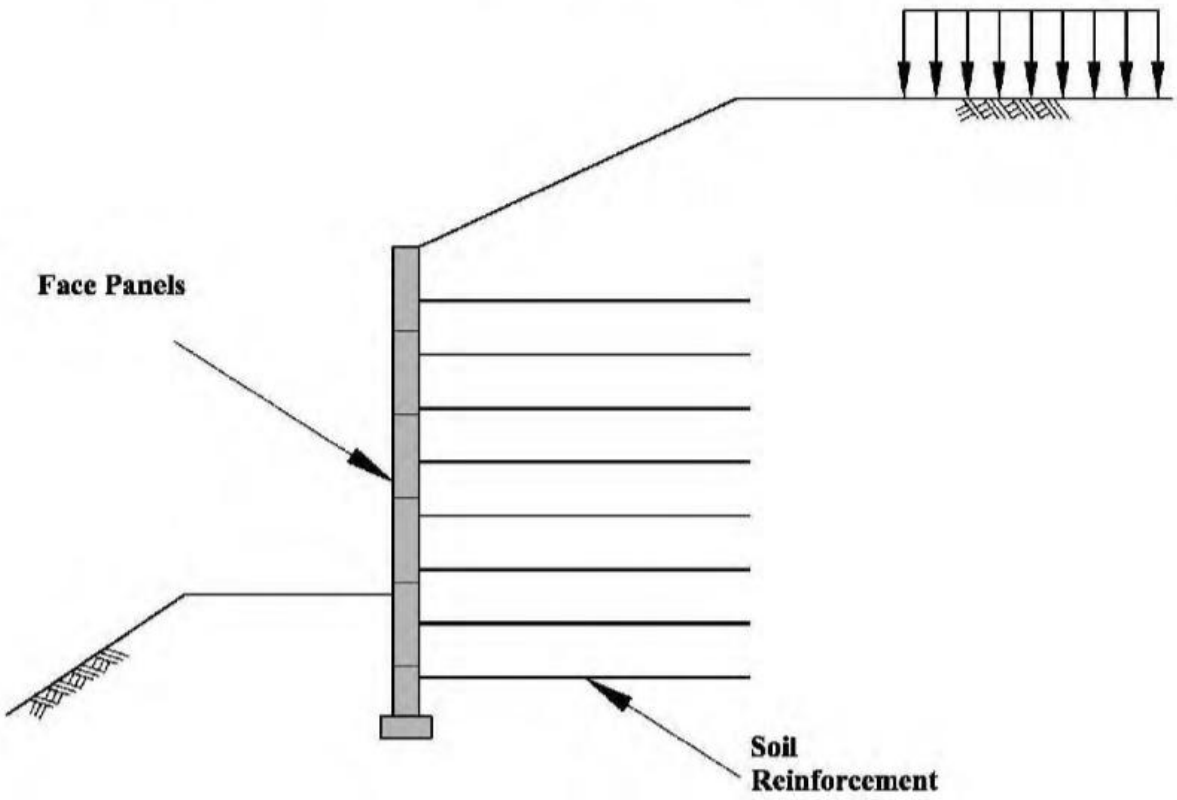

Figure 1. 6: MSE Wall with Precast Concrete Face Panels

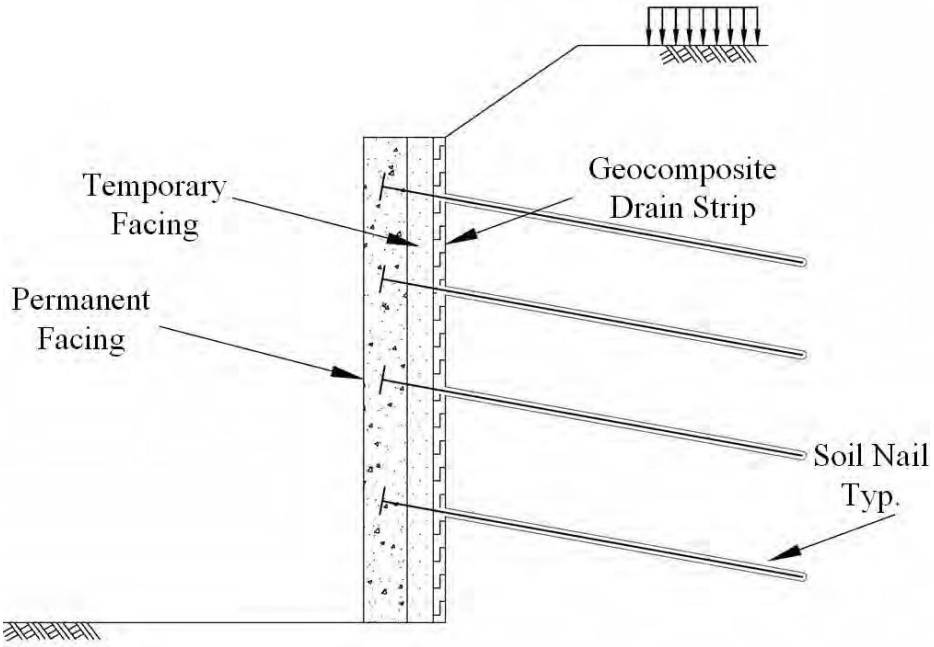

Figure 1. 7: Soil Nail Wall

1.3. RETAINING STRUCTURES SUBJECTED TO ROTATIONAL MOVEMENTS

1.3.1. Integral bridge abutments

The integral bridge is built in a unified framework, ensuring that the superstructure (deck) is directly linked to the foundation at the diaphragm-abutment interface. This type of bridge is often referred to as a "jointless" bridge due to the absence of the thermal expansion joint commonly found in older bridge designs (see Figure 1. 8). With a traditional expansion joint, bridges are susceptible to higher rates of corrosion as saltwater may seep into the joint. The elimination of the expansion joints has resulted in reduced maintenance costs (Steinberg et al., 2004). Furthermore, the integral design proves more efficient in terms of construction expenses, construction time, durability, and overall life cycle costs.

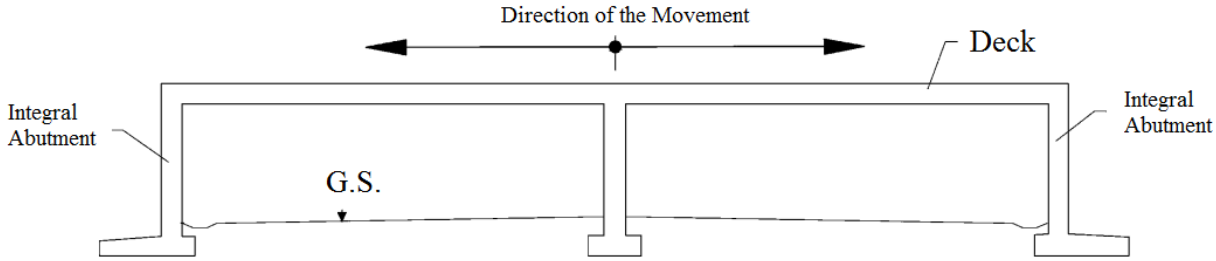

Figure 1. 8. Integral Bridge Abutment

Integral bridges are designed with foundations that offer higher flexibility. This ensures that the foundation can respond to the expansion of the superstructure during the change of temperature. In such situations, significant pressure can build up behind the abutment wall. While the foundation's flexibility permits movement, some bridges, particularly those of considerable length or with substantial skew angles, may require more movement than the foundation can accommodate. As a result, the abutment may experience rotational movement about its base, as depicted in Figure 1. 9.

This kind of jointless bridges have the advantages of lower initial construction costs, fewer maintenance costs, and greater earthquake resistance (Clayton et al. 2006). Many previous researches investigated the lateral earth pressure exerted by the backfill behind those kinds of bridges (Springman et al. 1996; Wood and Nash 2000; Cosgrove and Lehane 2003; Clayton et al. 2006), the type of movement of their abutment wall (Arsoy 2004) and the changes on lateral earth pressure over time (England and Tsang, 2005). Huntley and Valsangkar (2013) conducted a full-scale field test on “Route 2 high-speed connector underpass” that have been constructed in New Brunswick – Canada (Figure 1. 10). The bridge abutment was 76m long. The examination has taken over during three years of

monitoring, using pressure cells and deformation meters implemented on the bridge abutment in both sides as presented in Figure 1. 11.

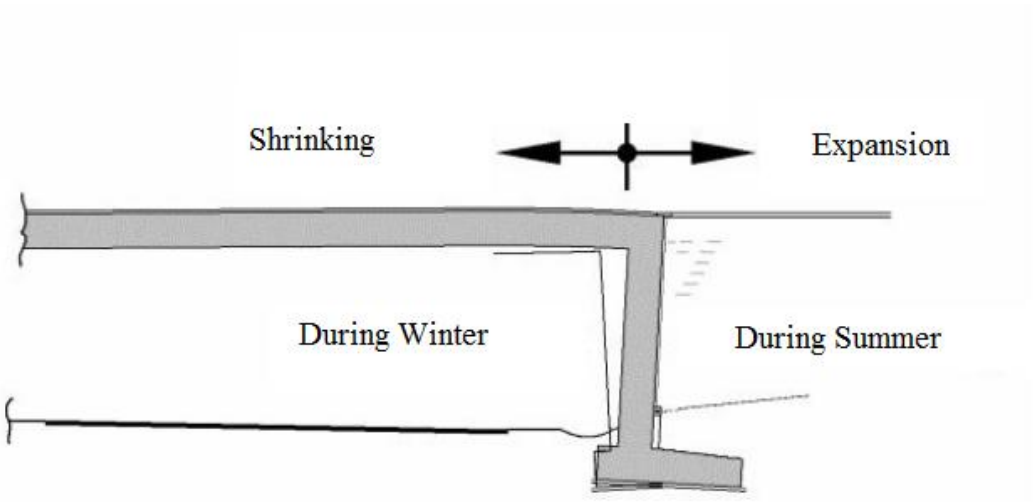

Figure 1. 9. Integral bridge abutment movement during winter and summer

Figure 1. 10. Full scale monitoring bridge - "Route 2 high-speed connector underpass" New Brunswick – Canada

Results of the experiment show that both east and west abutments were subjected to rotational movement in addition to translation movement with the changes of temperature. Movements are summarized in Table 1. 1. Summary of east and west abutment seasonal movements. The stress ratio obtained from pressure cells situated at the top of the abutment seem to present higher pressure than those in middle and the bottom of the wall, which explain than triangular distribution of passive earth pressure is no longer valid in rotational movement of retaining walls. Authors explained that using theatrical passive earth pressure coefficient methods for translation movement is not suitable for the entire height of the abutment.

Table 1. 1. Summary of east and west abutment seasonal movements

	East abutment				West abutment			
	Translation (mm)		Rotation (°)		Translation (mm)		Rotation (°)	
Year	Upper sensor	Lower sensor	Upper sensor	Lower sensor	Upper sensor	Lower sensor	Upper sensor	Lower sensor
1	12.1	10.3	0.06	0.05	14.6	12.0	0.06	0.09
2	10.3	8.8	0.06	0.06	14.8	8.8	0.31	0.05
3	11.4	9.9	0.09	0.06	13.2	12.1	0.09	0.09

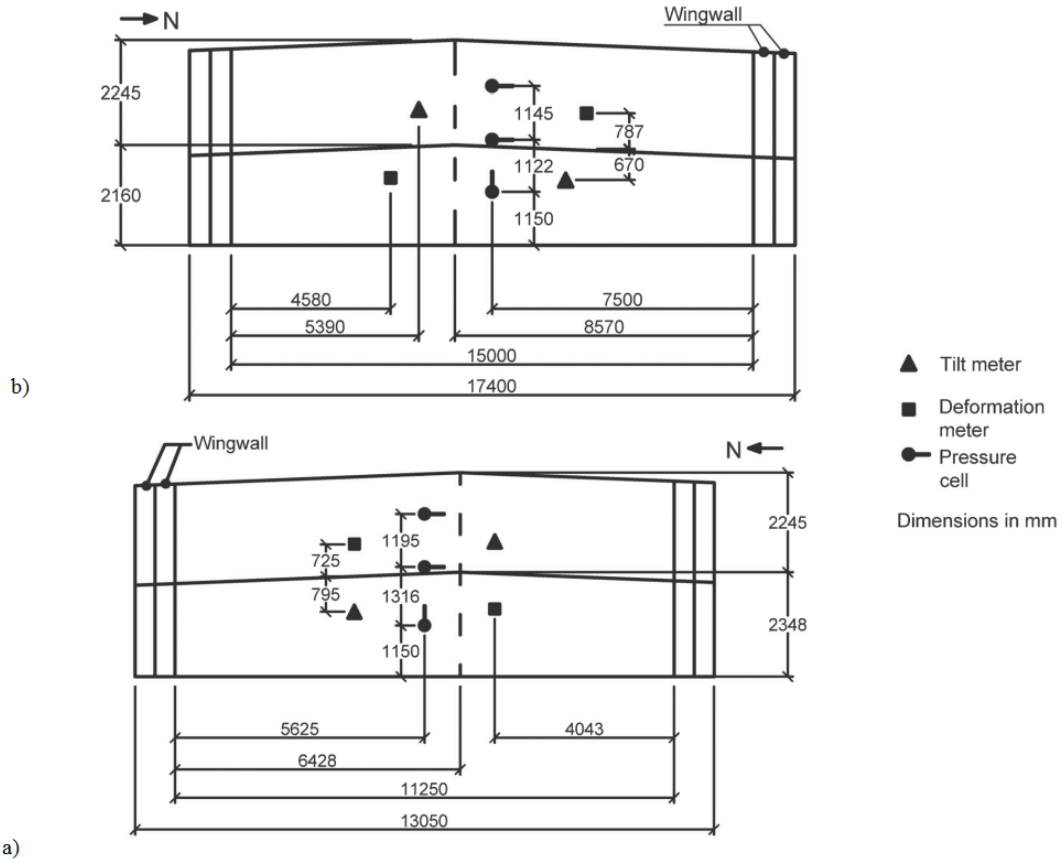

Figure 1. 11 Instrumentation locations on a) east abutment b) west abutment

1.3.2. Embedded walls

Unpropped embedded walls depend entirely on a sufficient depth of embedment for their stability. They do not receive support from any other source, and their failure is likely to occur through rotation about a pivot point near the base. Active earth pressure is assumed behind the retaining wall while passive earth pressure is assumed in front of it. Moment equilibrium requires an existence of a center of rotation located just above the wall bottom. The orientation of the stresses is inverted below this center as presented in Figure 1. 12a.

An idealized stress distribution at failure, based on limiting active or passive stresses in zones of soil where the wall is moving away from or into the soil, as shown in Figure 1. 12b (Blum, 1930). Design methodologies for embedded walls, founded on the conceptual stress distribution at the point of collapse, were developed by previous researchers like Blum (1930) and outlined by Terzaghi (1943). During that era, these primarily pertained to sheet pile walls. In Blum's approach, it was posited that earth pressures escalate linearly with depth, as depicted in Figure 1. 12a. This was then adjusted by a factor of safety, acting as a reduction to the linear passive pressure.

Many researchers investigated experimentally the stability of such retaining walls, Krey (1932), Lyndon & Pearson (1984) and Bica & Clayton (1998) used a small-scale model of a retaining wall embedded in sand. The experimental set up carried out by Bica and Clayton (1998), as presented in Figure 1. 13, involved the measurement of both shear and normal stresses at the interface between the soil and the wall. Additionally, wall displacements were tracked as the load on the wall was incrementally raised until failure occurred. The findings indicate that notably elevated earth pressures, linked to substantial effective angles of wall friction, are activated just beneath the soil surface in front of the wall. Earth pressures on the retained side, below the center of rotation of the wall, decreases to create a non-linear distribution of earth pressure. Confirming the view from Krey's and Lyndon & Pearson (1984) on the downwards direction of wall friction at this location, as presented in Figure 1. 14.

1.3.3. Anchored and Strutted walls

Anchored retaining walls, also known as anchored bulkheads (see Figure 1. 15), fulfill the same function as traditional retaining walls. However, unlike retaining walls where the weight is a significant portion of the sliding wedge's weight, bulkheads are composed of a single row of relatively lightweight sheet piles. These sheet piles have their lower ends driven into the earth while their upper ends are secured by tie or anchor rods. These rods, in turn, are stabilized by anchors embedded in the backfill at a substantial distance from the bulkhead.

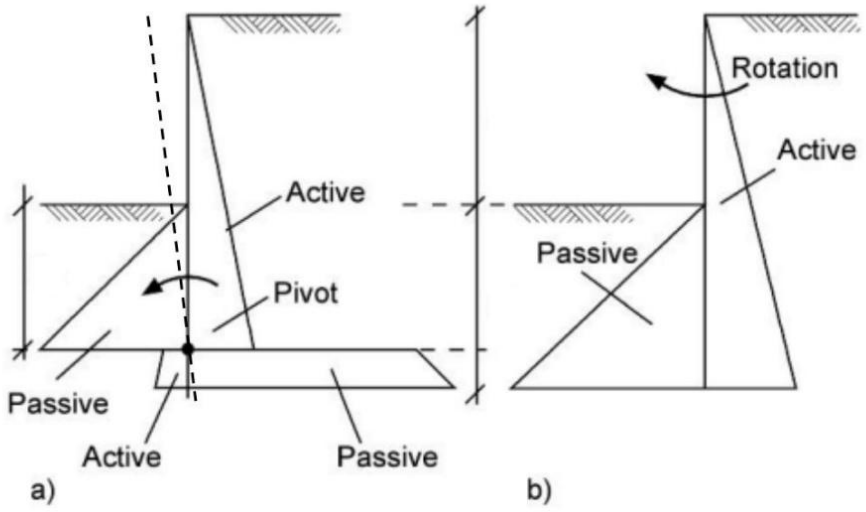

Figure 1. 12 Linear effective earth pressure distribution for embedded walls a) assumed earth pressure b) idealized earth pressure

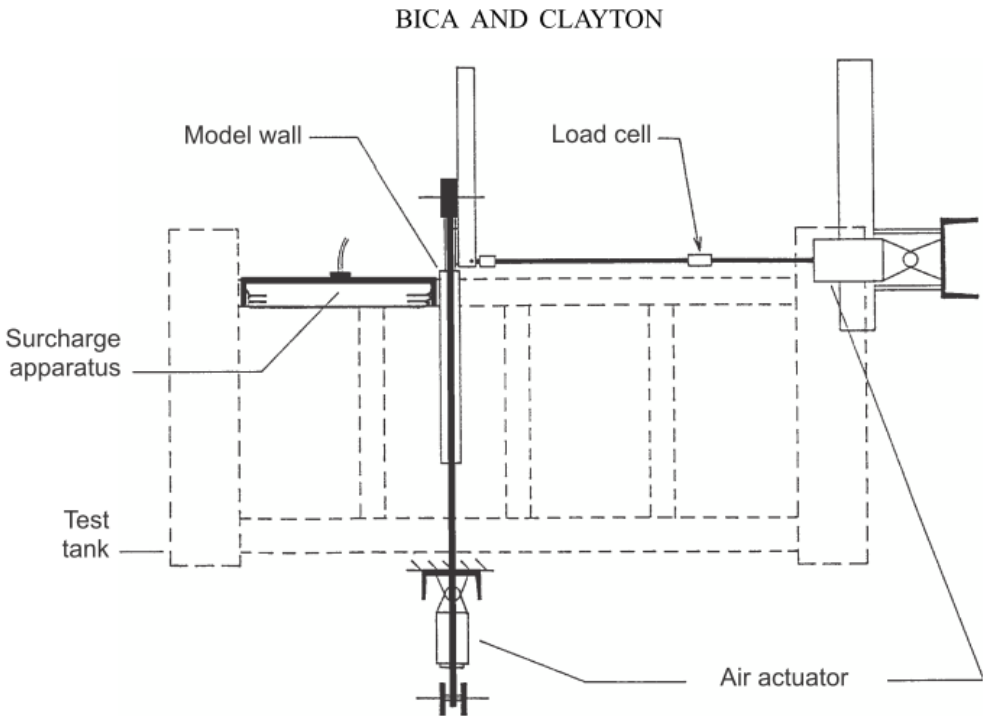

Figure 1. 13 Experimental set-up by Bica & Clayton (1998)

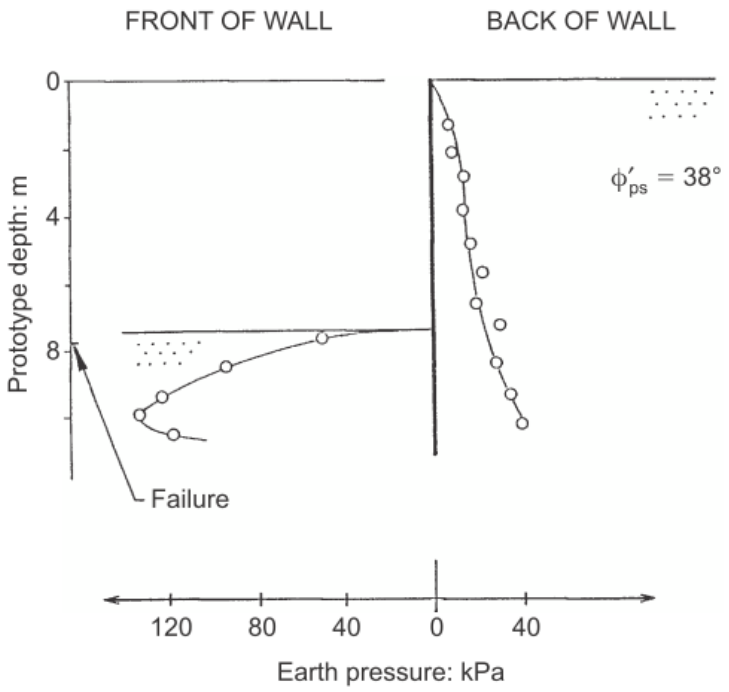

Figure 1. 14 Experimental distribution of earth pressure on embedded walls (Lyndon & Pearson, 1984)

Anchored retaining walls are widely used for dock and harbor structures. This construction provides a vertical wall so that ships may tie up alongside, or to serve as a pier structure, which may jet out into the water. In these cases, sheeting may be required to laterally support a fill on which railway lines, roads or warehouses may be constructed so that ship cargoes may be transferred to other areas. Failure of such walls occurs around the anchors (Figure 1. 15), which makes them subjected to rotation about top that must be properly estimated for the well stability of the retaining structure.

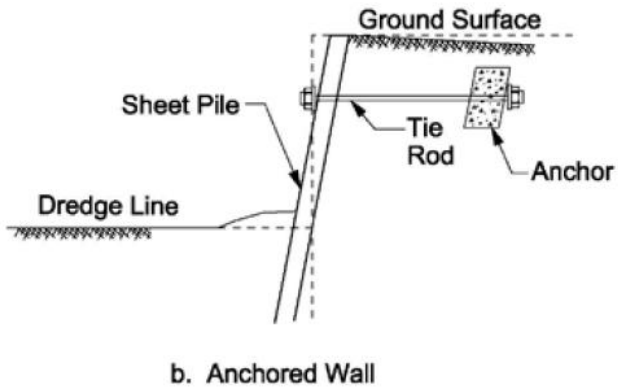

Figure 1. 15. Anchored retaining wall

Anderson et al (1984) conducted series of laboratory scale tests in which field construction of anchored rigid retaining walls were simulated, based on four different support system, where in the three first (A, B, C), the anchor forces were calculated assuming a rectangular earth pressure distribution, with the earth pressure coefficient suggested by Hanna & Matellana (1970), equal to $\frac{(K_0+K_a)}{2}$. Overall stability was then checked in series A by the original Kranz (1953) method, in series B by the Ostermayer (1977) method, and in series C by the method detailed in the French Code of Practice (1972). In test series D, anchor forces were determined using the James and Jack (1974) method for the determination of earth pressure which incorporates the effects of temporary support produced by the passive pressure at intermediate excavation stages. The stability was checked using a log spiral as suggested by Littlejohn (1972). The full test program is summarized in Table 1. 2. Results showed that the wall movement observed during the different construction stages indicate that two basic patterns of movements can be expected with an anchored retaining wall system. Whichever pattern occurs depends mainly on the anchor pre-stress loads. If the anchors are pre-stressed according to a triangular earth pressure distribution from James and Jack (1974), rotation about a point under the toe is to be expected. However, if the pre-stress loads are calculated as in the three other methods, the wall will rotate about a point near its top.

Table 1. 2. Anderson et al (1984) test program

Series	Test number	Support system	Method of calculating anchor forces	Method of checking overall stability
A	A2	2 rows, horizontal	Rectangular pressure distribution after Henna and Metallana (1970)	Kranz wedge (1953)
	A3	3 rows, horizontal		
	A4	4 rows, horizontal		
	AI	3 rows, 30° inclined		
B	B2	2 rows, horizontal	Rectangular pressuredistribution after Henna and Metellana (1970)	Ostermayer wedge (1977)
	B3	3 rows, horizontal		
	B4	4 rows, horizontal		
	BI	3 rows, 30° inclined		
C	C2	2 rows, horizontal	Rectangular pressure distribution after Henna and Metallana (1970)	French Code of Practice wedge (1972)
	C3	3 rows, horizontal		
	C4	4 rows, horizontal		
	CI	3 rows, 30° inclined		
D	D2	2 rows, horizontal	James and Jack (1974)	Littlejohn log spiral (1972)
	D3	3 rows, horizontal		
	D4	4 rows, horizontal		
	DI	3 rows, 30° inclined		

Another type of retaining walls which is subjected rotational movement is strutted retaining walls. This kind of retaining walls is needed to support shallow excavations. In cases where there is sufficient space to establish slopes allowing the material to stand on its own, excavations can be made without the need for additional support. However, on many building sites that extend to the property lines, the sides of the excavation must be made vertical and typically require support through bracing. Figure 1. 16 illustrates common methods for bracing the sides when the depth of excavation does not

exceed approximately 3 meters. The typical practice involves driving vertical timber planks, known as sheeting, along the sides of the excavation. These sheetings are held in place by horizontal beams called wales, which are commonly supported by horizontal struts extending across the excavation. For widths not exceeding about 2 meters, these struts are usually made of timber. In cases of greater widths, metal pipes known as trench braces are commonly employed. Strutted retaining walls are also subjected to rotational movement about the base due to the push of one another, which has been investigated by various researchers from literature (Georgiadis and Anagnostopoulos, 1999; Nakai et al., 1999; Takemura et al., 1999; Tefera et al., 2006; Chowdhury et al., 2014).

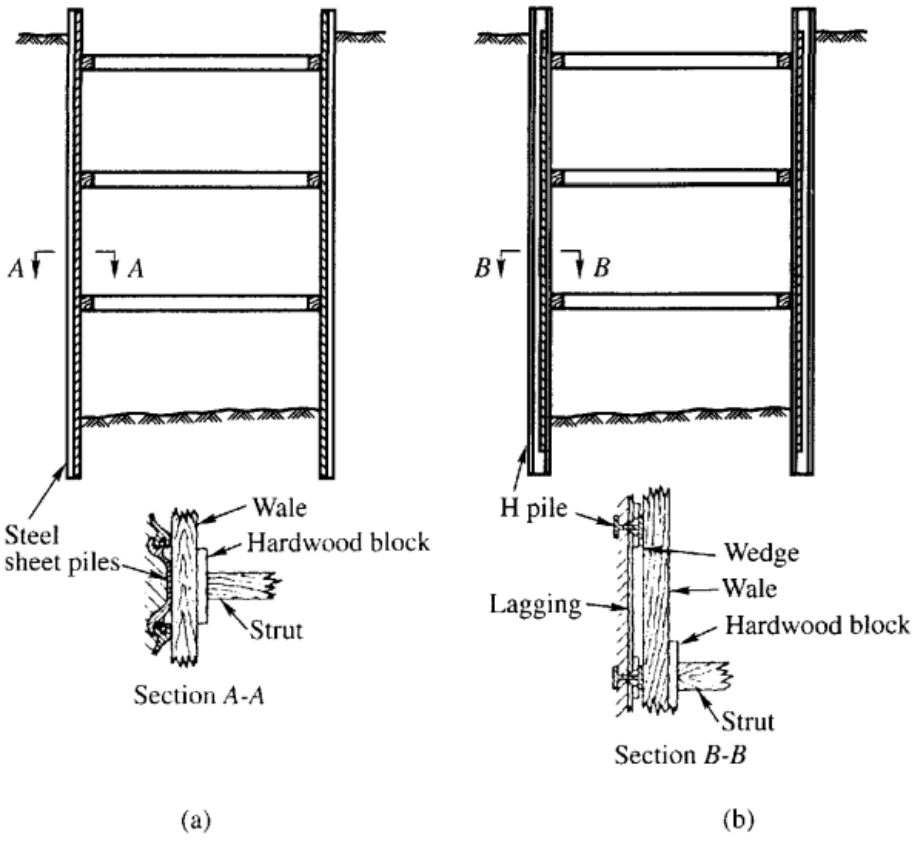

Figure 1. 16. Strutted retaining walls

1.4. LITERATURE REVIEW ON ROTATIONAL MOVEMENTS

1.4.1. James and Bransby (1970)

James and Bransby (1970) investigated passive earth pressure using large glass-sided tank associated with 330×200 mm wall rotating aboutj its base into a dry backfill sand with horizontal backfill surface. Load cells were implemented in the model wall in order to measure normal and shear stresses, as presented in Figure 1. 17. The strains in the soil mass were determined by X-ray of the

position of buried lead shots. The strain data were used to investigate the mobilized φ constant assumption from Sokolovski (1960) which enables a staticallty admissible stress state to be developed from the known boundary conditions of the problem. The assumption was satisfied over a large region of deforming mass of dense sand, but not in loose sand. The magnitude of the passive stress obtained from tests on dense sand are much greater than the ones obtained from tests on loose sand, which create a major difference in the form of the load-displacement relationships. Furthermore, the shapes of the lateral stress distribution on the retaining wall in tests on loose and dense sand are different, as presented in Figure 1. 18. The shape of the distribution changes slowly with wall rotation during a test on loose sand, while the distribution changes considerably during a test on dense sand. The curved distribution of lateral earth pressure is observed in all the cases at any stage of the test.

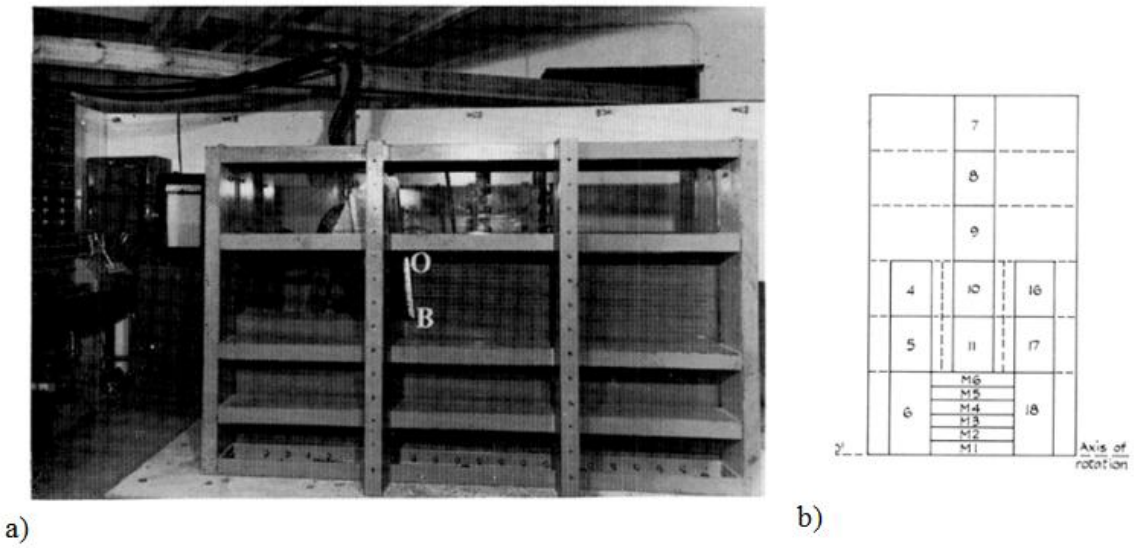

Figure 1. 17 Laboratory test by James and Bransby (1970) a) large glass-side tank b) front view of wall showing load cells

1.4.2. Fang et al. (1994)

Fang et al. (1994) studied earth pressure acting against a vertical rigid wall moving into a mass of dry loose sand with a horizontal ground surface under various modes of wall movement. The movable model retaining wall, as well as the sand box and the driving system are illustrated in Figure 1. 19. The model wall is solid plate made of steel with a 1,000-mm-wide, 550-mm-high, and 120-mm-thick. The effective wall height H (or height of backfill above wall base) is only 500 mm. Wall movements were rotation about a point above the top (RTT) and rotation about a point below the wall base (RBT) as seen in Figure 1. 20. In RTT mode, parameter "n" in the figure is the ratio of the distance from center of rotation to the wall top, and the wall height. In RBT mode, "n" is the ratio of the distance from center of rotation to wall bottom, to wall height. S_{max} signifies the maximal distance of wall displacement in the three cases of wall movement. Figure 1. 21 and Figure 1. 22 show the

evolution of the passive earth pressure coefficients in the cases RTT and RBT modes, respectively. The translation mode case is also plotted in both figures. It can be noticed that the more "n" increases the evolution of earth pressure magnitude increases with wall movement in both cases RTT and RBT, until reaching the evolution from translation mode case which reveal the highest evolution.

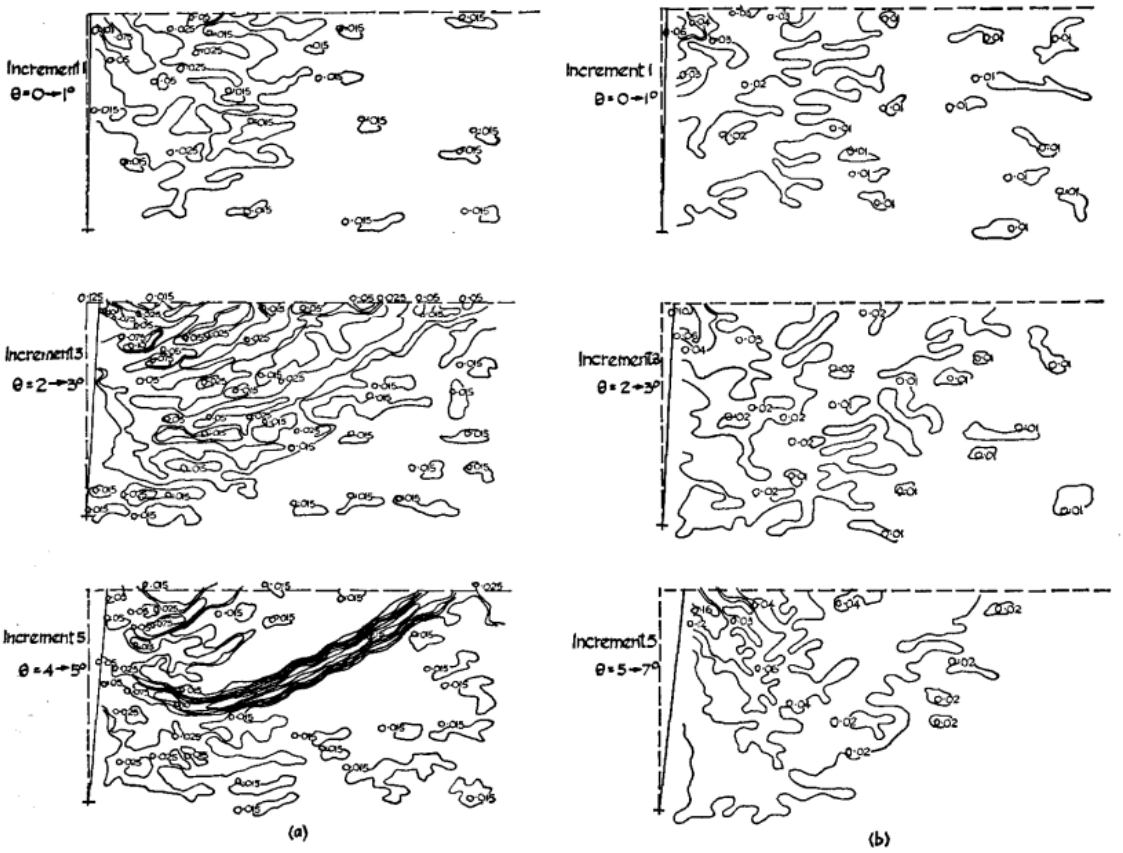

Figure 1. 18. Shear strain contour increment for different wall rotations by James and Bransby (1970) a) dense sand b) loose sand

Figure 1. 23 presents the stress distribution with wall movement for difference values of the location of rotation center equal to n=0.00, n=0.50, n=1.81 and n=7.43 in the case of RTT, where maximum lateral displacement occurred at the wall base, while no lateral movement was allowed at the top. Consequently, the earth pressure recorded near the base of the wall experiences a swift escalation with the passive movement of the wall, while the pressure near the top remains relatively stable. When the wall reaches a movement of S_{max}/H = 0.20, the pressure distribution observed deviates significantly from linearity. These changes are well revealed in the case of n=0.00 (Figure 1. 23a). The shape of the distribution tends to change from non linear to linear with the increase of "n" to converge to the one obtained in translation mode case with high values of "n" (Figure 1. 23d).

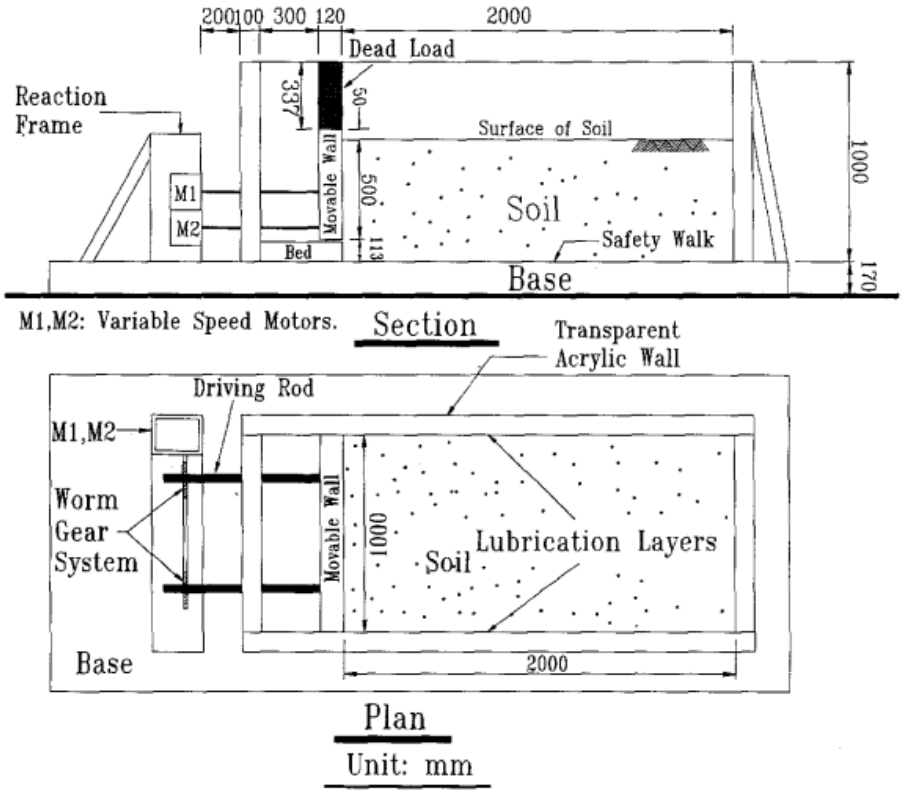

Figure 1. 19 Fang et al. (1994) laboratory set-up

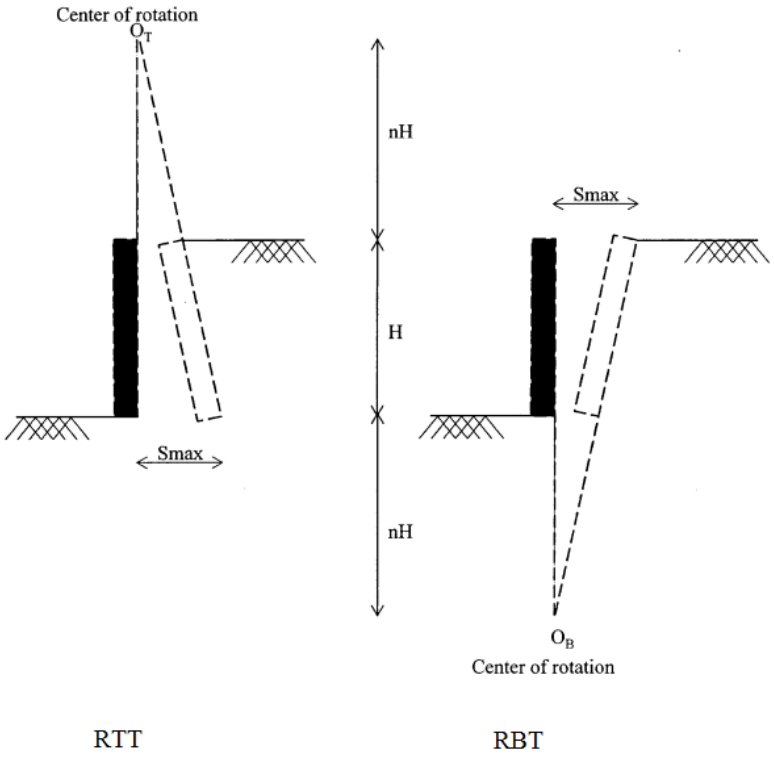

Figure 1. 20 Types of wall movement by Fang et al. (1994)

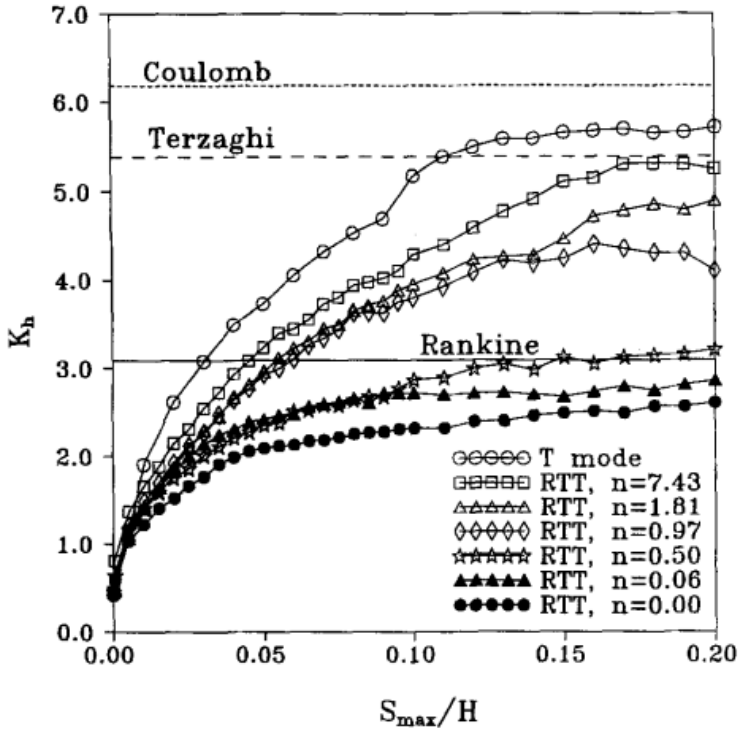

Figure 1. 21 Evolution of passive earth pressure coefficient with wall movement for RTT mode

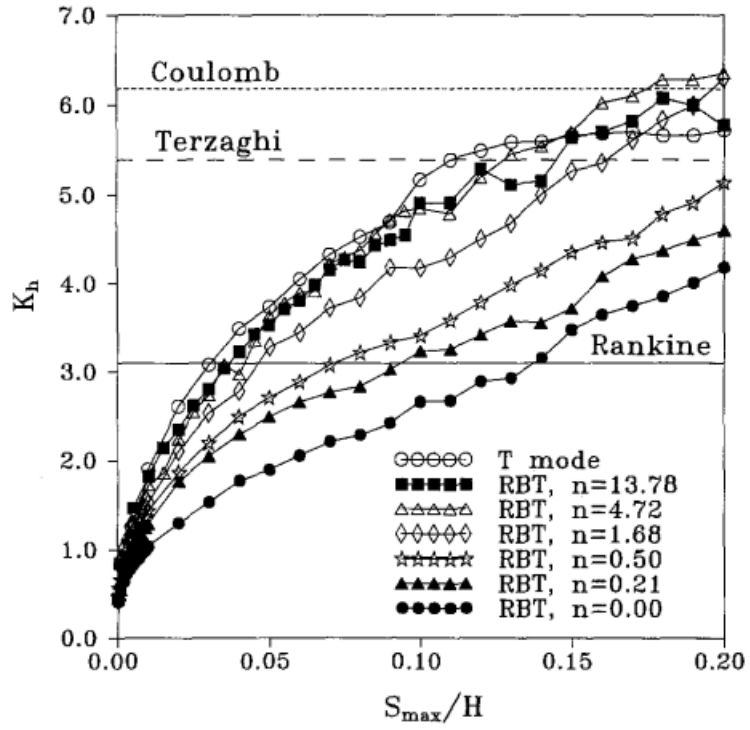

Figure 1. 22 Evolution of passive earth pressure coefficient with wall movement for RBT mode

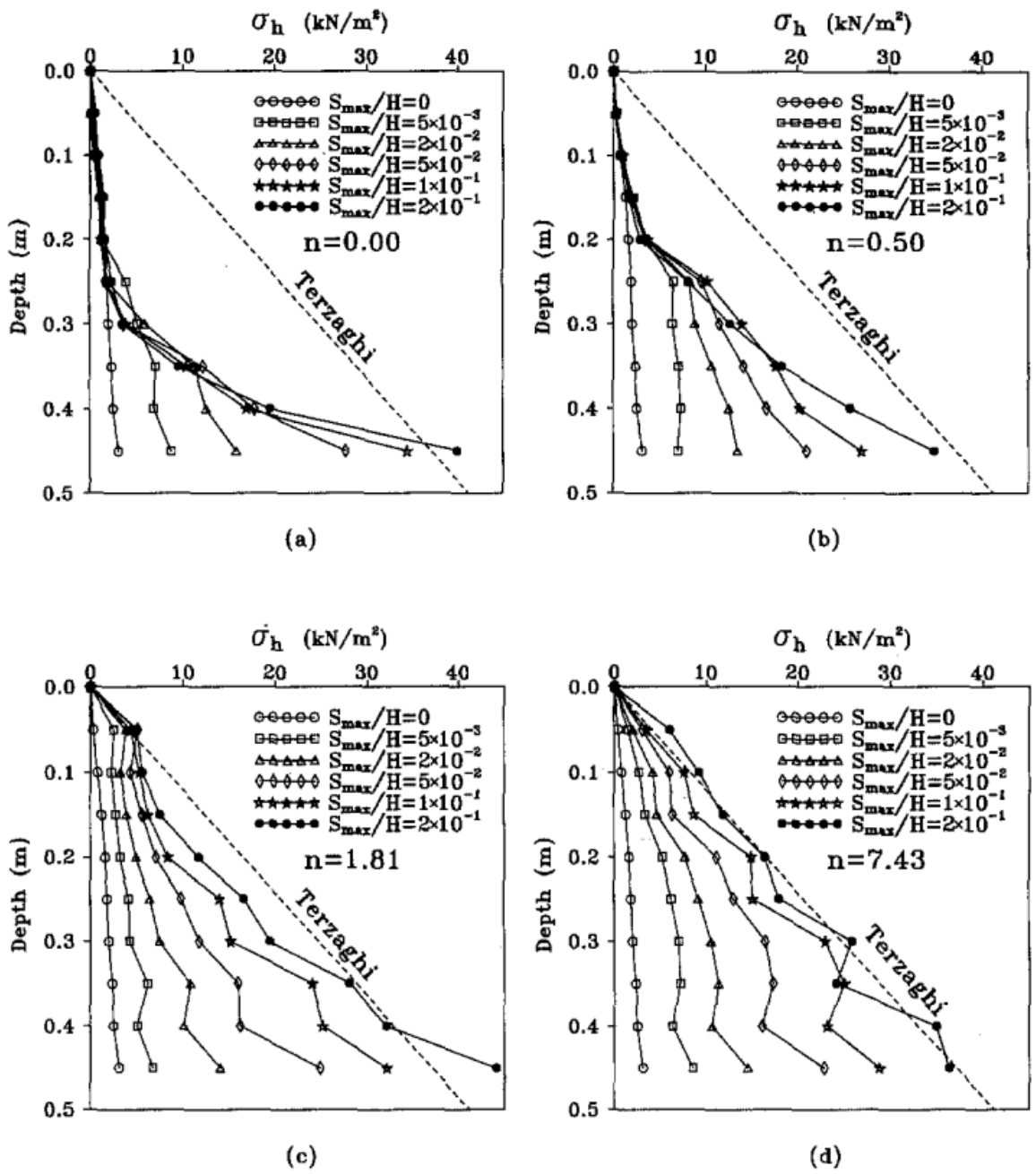

Figure 1. 23 Distribution of passive earth pressure for RTT mode (Fang et al., 1994) a) n=0.00 b) n= 0.50 c) n=1.81 d) n=7.43

The lateral earth pressure distribution in the case of RBT for different stages of wall movements is presented in Figure 1. 24. It is clear from the test data that the soil pressure measured near the top increases with increasing wall movement, while the change of stress near the wall base seems to be smaller. The stresses near midheight of the wall rose continually with increasing wall movement. Similar to RTT mode, the distribution of lateral earth pressure tends to change from non linear to linear to approach the translation mode results with the increment of rotation center "n".

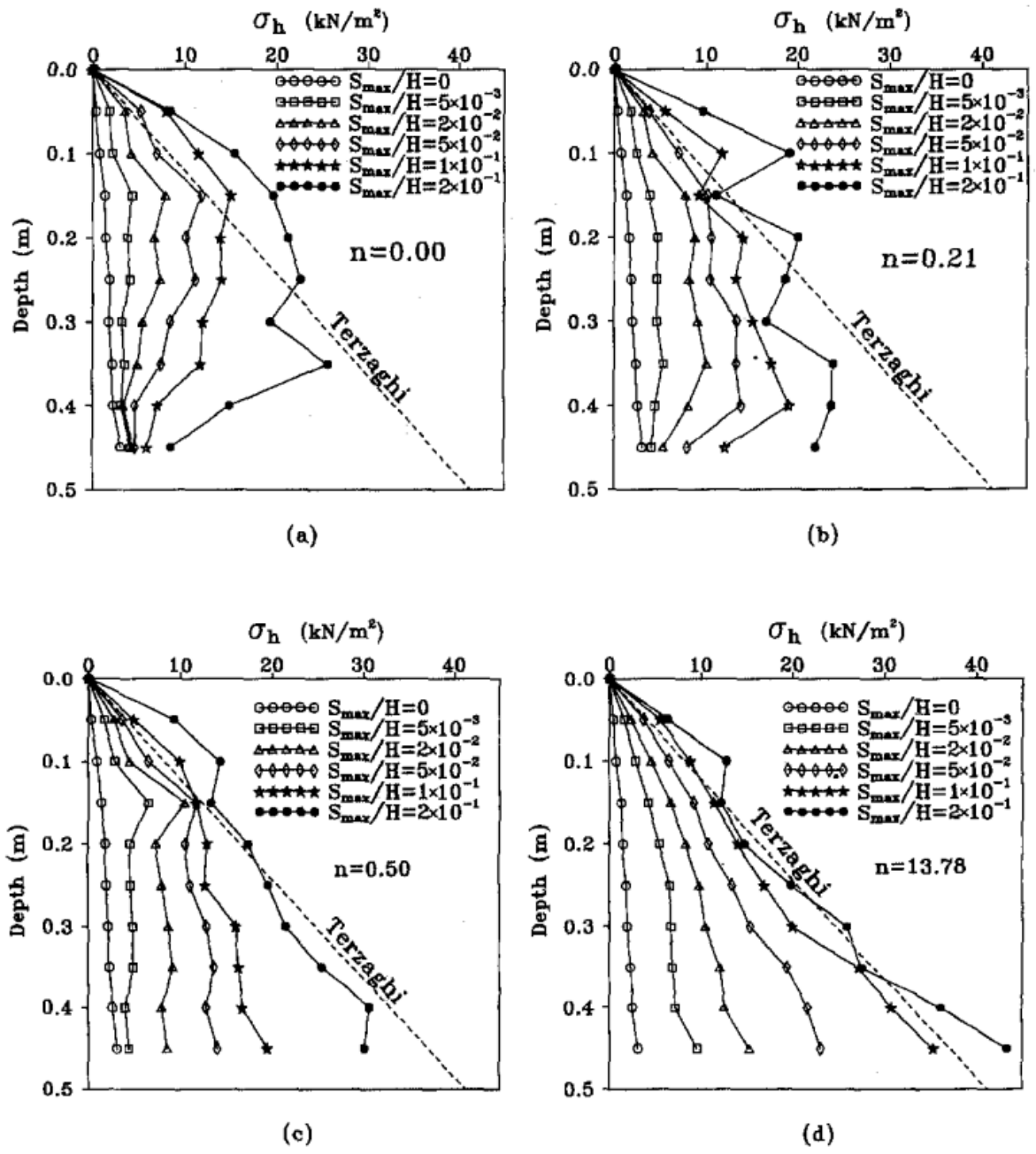

Figure 1. 24 Distribution of passive earth pressure for RBT mode (Fang et al., 1994) a) n=0.00 b) n= 0.50 c) n=1.81 d) n=7.43

1.4.3. Dave & Dasaka (2012)

In the study conducted by Dave and Dasaka (2012), experimental investigations were carried out on small-scale retaining walls supporting a cohesionless backfill material and subjected to surcharge loading. The laboratory setup involved modeling wall movement by allowing rotation about its base to simulate the behavior of rigid cantilever retaining walls. The experimental configurations are illustrated in Figure 1. 25.

The authors referenced numerous prior studies that underscored the discrepancy between the theoretical concepts of hydrostatic earth pressures resulting from backfill and uniform earth pressure due to surcharge loads, highlighting that these estimations often significantly overstate the actual earth pressures. Thus, the laboratory test conducted by Dave and Dasaka (2012) was designed with the primary objectives of determining the magnitude and distribution of earth pressure on the retaining wall under different wall movements, all while subjected to surcharge loading, through small-scale model experiments. The study encompassed various cases will be detailed in what follows.

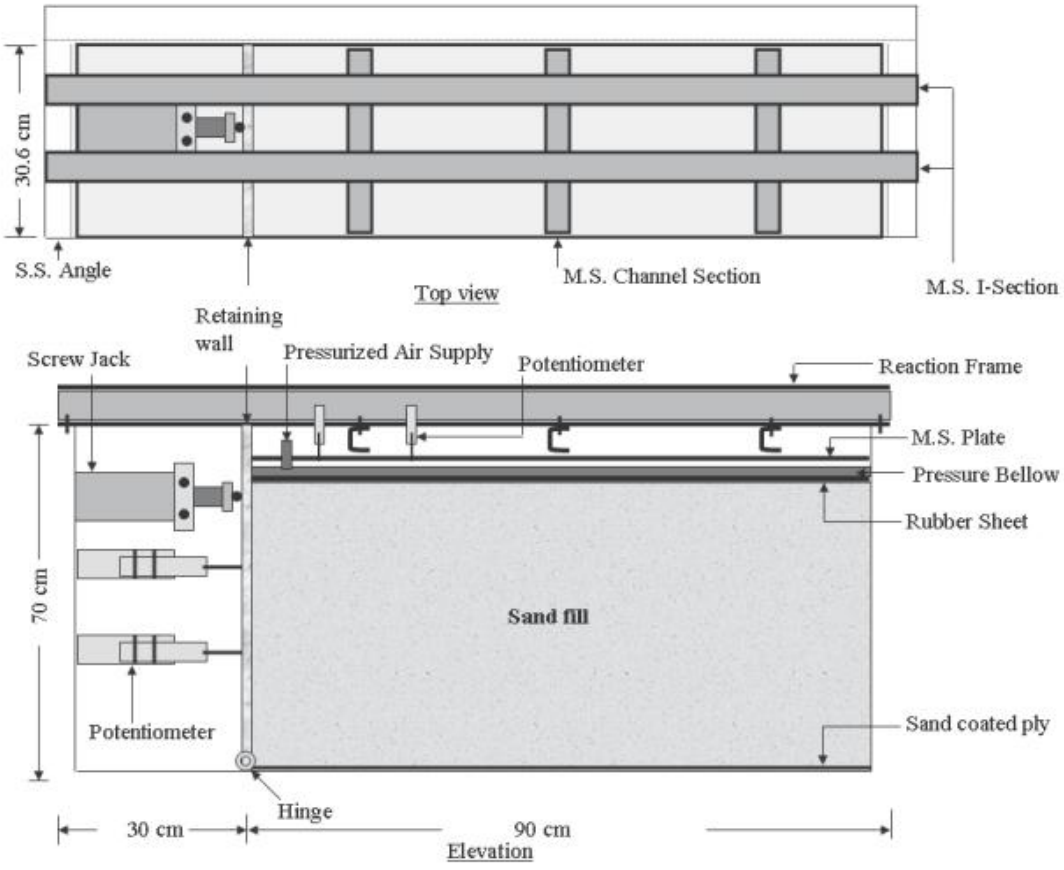

Figure 1. 25. Experimental set up from Dave & Dasaka (2012)

The first case of the study investigated the magnitude and variation of at-rest earth pressures at different locations along the height of the wall. This was done under two conditions: when a surcharge was placed directly adjacent to the wall and when it was positioned at a distance of h/4 (0.15 m) away, as depicted in Figure 1. 26 and Figure 1. 27, respectively. Additionally, earth pressures were calculated using Jaky's well-established equation for backfill with and without a surcharge load of 50 kPa, and the results were presented in both figures.

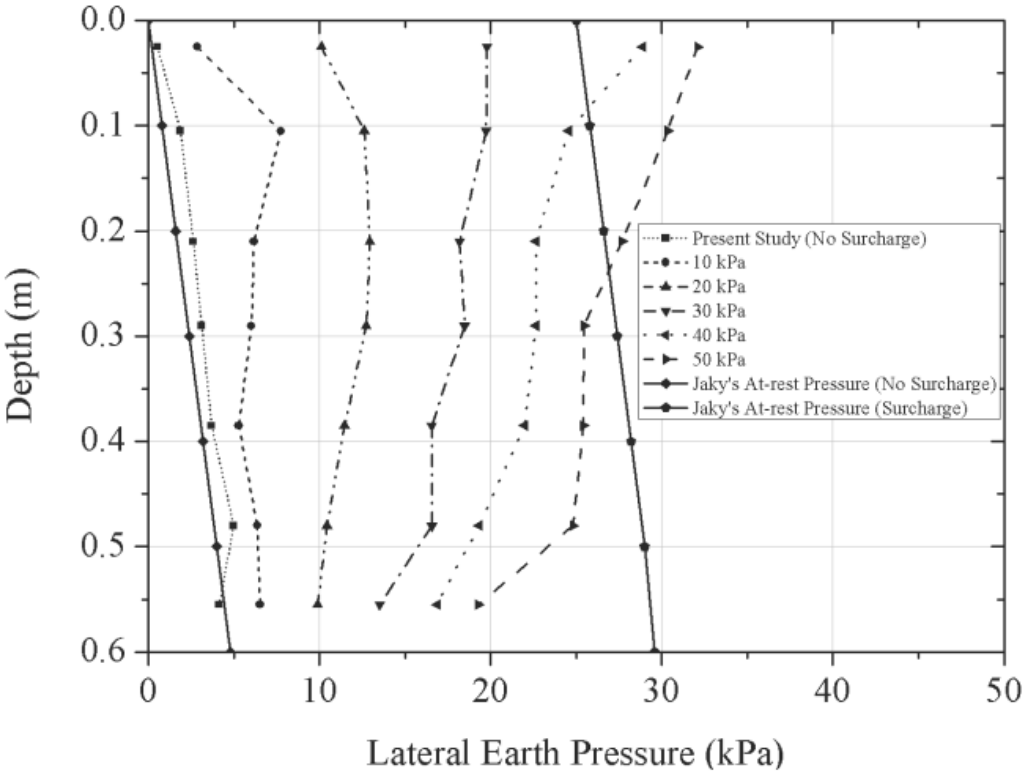

Figure 1. 26. At-rest earth pressure distribution, when the edge of surcharge load is located at the face of the wall (Dave & Daska, 2012)

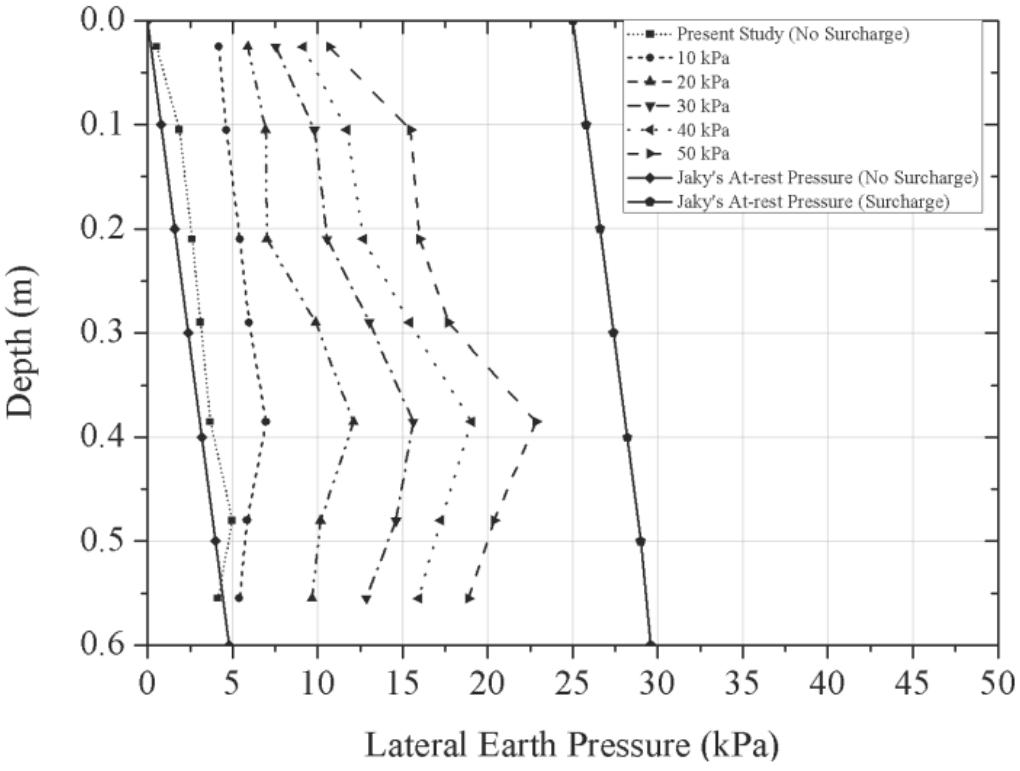

Figure 1. 27. At-rest earth pressure distribution, when the edge of surcharge load is distanced h/4 from the the wall (Dave & Daska, 2012)

Comparing the measured earth pressure without surcharge loading to Jaky's equation, it was noted that the measured values were slightly higher. The earth pressure was found to increase with depth in both cases. Figure 1. 26 illustrated that with an increase in surcharge loading, the measured earth pressures also increased at all depth locations. Furthermore, the influence of surcharge on earth pressure diminished with depth, with the highest earth pressure near the top of the wall and the lowest near the bottom. At the mid-height of the wall, Jaky's equation tended to underestimate the earth pressure in one half and overestimate it in the other. However, the maximum earth pressure closely aligned with Jaky's estimated value.

Figure 1. 27 provided insight into the magnitude and distribution of earth pressure when a surcharge was situated at h/4 distance from the wall top. Notably, as the distance between the surcharge and wall increased, its impact on earth pressure decreased. While earth pressure increased with depth, it remained notably lower than what Jaky's equation predicted.

The second case of the study involved measuring earth pressure after applying each displacement. Active movement included maintaining a surcharge pressure of 50 kPa. The results, shown in Figure 1. 28, depicted the magnitude and distribution of earth pressure when the wall moved in an active direction.

In the third case, which simulates passive movement, the wall was gently pushed towards the backfill using a screw jack while maintaining a surcharge of 50 kPa. Earth pressures were measured after each displacement, and the results can be seen in Figure 1. 29. Comparisons were drawn between the measured earth pressures and those calculated using Rankine's theory as well as the widely utilized 45˚ distribution method. It was observed that Rankine's method tended to overestimate the active earth pressure. Nevertheless, the observed pressures closely matched those derived from the 45˚ distribution method in the upper half of the wall. Some reduction in observed pressure was noted in the lower half, with a minimum near the base. Furthermore, as the wall moved away from the backfill, the influence of surcharge on earth pressure in the upper half diminished. It is worth noting that during the movement towards the backfill under surcharge loading, the wall could not be sufficiently moved to form a passive wedge due to constraints from the top surcharge plate and practical limitations in jack movement. This prevented the upward movement of the soil mass.

It is important to mention that Authors explained that the results presented in their study were based on limited experimental findings, and further research in this area is warranted for a deeper understanding of the behavior of retaining walls subjected to surcharge loads.

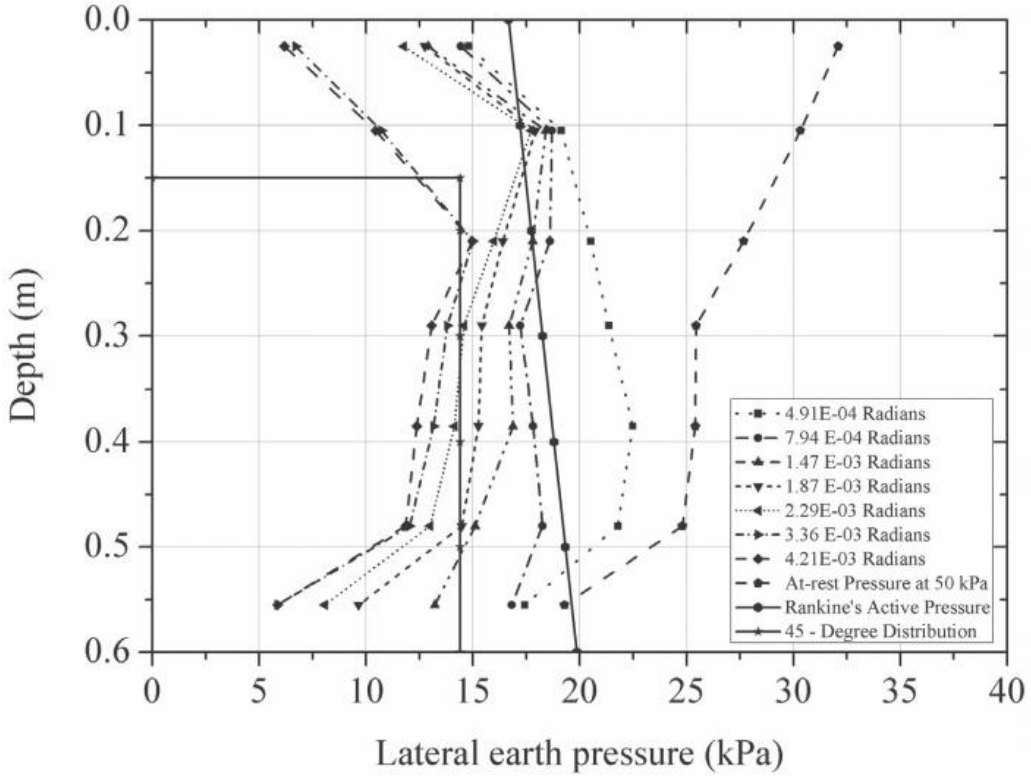

Figure 1. 28. Active earth pressure distribution under surcharge loading from Dave & Dasaka (2012)

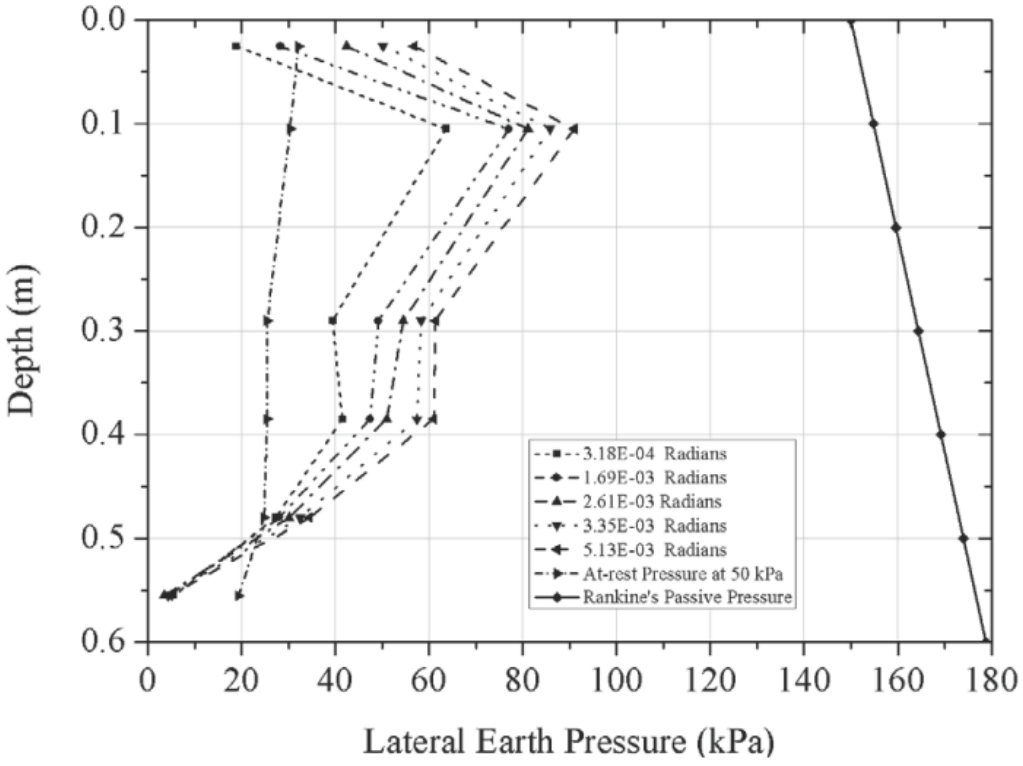

Figure 1. 29. Passive earth pressure distribution under surcharge loading from Dave & Dasaka (2012)

1.4.4. Peng et al. (2012)

Peng et al. (2012) studies was about creating a general analytical method to calculate the passive earth pressure behind rigid retaining walls which can fit all displacement modes. In this method, a parameter that defines passive displacement mode "m" was introduced, which represent the ratio between horizontal and vertical movement such as $m = x/h$. The initial movement of the wall top toward the soil is denoted S_{top}, the bottom wall movement is called S_{bottom}, as illustrated in Figure 1. 30. The ratio of S_{top}/S_{bottom} can be expressed by Eq. (1.4).

$$\frac{S_{top}}{S_{bottom}} = \frac{m}{m-1} \qquad (1.4)$$

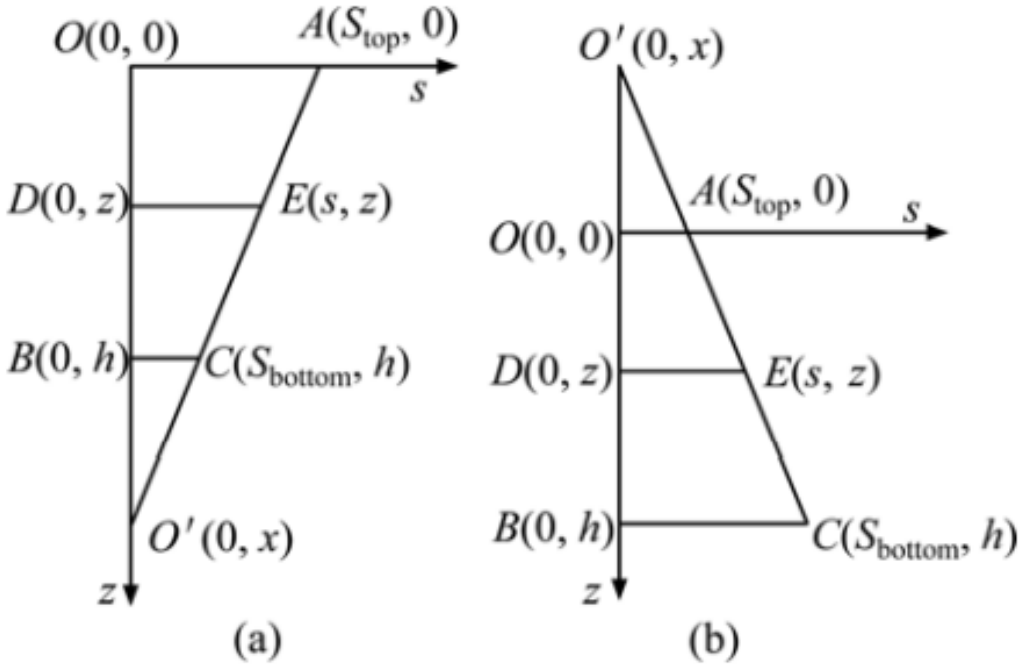

Figure 1. 30 Passive displacement modes from Peng et al. (2012) a)$m \geq 0, S_{max} = S_{top}$ b) $m \leq 0, S_{max} = S_{bottom}$

The point O in figure can be situated in either the top or the bottom of the retaining wall, depending on the type of passive movement. When O is at the wall toe, $m \geq 1$, and the maximum movement of the wall is $S_{max} = S_{top}$. When O is located at the wall top, $m \leq 1$, and $S_{max} = S_{bottom}$. The relationship between the factor "m" and the displacement modes can be summarized in Table 1. 3. The passive earth pressure denoted "p" proposed by Peng et al. (2012) in function of the depth z can be expressed with the following form in equation (1.5):

$$p = (K_p - K_0)\rho g \left(\frac{3}{2-3m}\frac{z^2}{h} - \frac{3m}{2-3m}z\right) + K_0 \rho g z \qquad (1.5)$$

Table 1. 3 Relationship between m and wall displacement modes

m	Displacement mode
∞	T
$1-\infty$	RBT
1	RB
0	RT
$0--\infty$	RTT
$-\infty$	T

The location of the passive earth pressure thrust z_0 is defined by:

$$z_0 = \frac{1-2m}{2(2-3m)} - \frac{K_0}{K_p}\frac{1}{6(2-3m)} \qquad (1.6)$$

Simplified formulates for the determination of passive earth pressure and the location of the resultant passive earth pressure force in the three types of wall movement T, RT and RB are summarized in Table 1. 4.

Table 1. 4 Formulas for the determination of passive earth pressure "p" and location of passive earth thrust z_0 (Peng et al., 2012)

m	Displacement mode	p	z_0
0	RT	$(K_p - K_0)\rho g\frac{3z^2}{2h} + K_0\rho gz$	$\frac{1}{4}h - \frac{K_0}{K_p}\frac{h}{12}$
$\pm\infty$	T	$K_p\rho gz$	$\frac{1}{3}h$
1	RB	$3(K_p - K_0)\cdot \rho g\left(z - z^2/h\right) + K_0\rho gz$	$\frac{1}{2}h + \frac{K_0}{K_p}\frac{h}{6}$

Figure 1. 31 presents a comparison among the distribution of passive load from the general analytical method presented by Peng et al. (2012), earth pressure distribution from Coulomb's equation, as well as the laboratory test from Fang et al. (1994) are also plotted. It can be seen that the results from Peng et al. equation meet well with those from experimental test conducted by Fang in the

case of RB mode with a curved distribution shape, while Coulomb theory present a linear distribution Figure 1. 31a. In the other hand, an agreement can be seen under T mode between the three plotted methods. Under RT mode, Peng et al. (2012) method present a slightly curved distribution situated between Fang et al. (1994) test and the linear distribution from Coulomb.

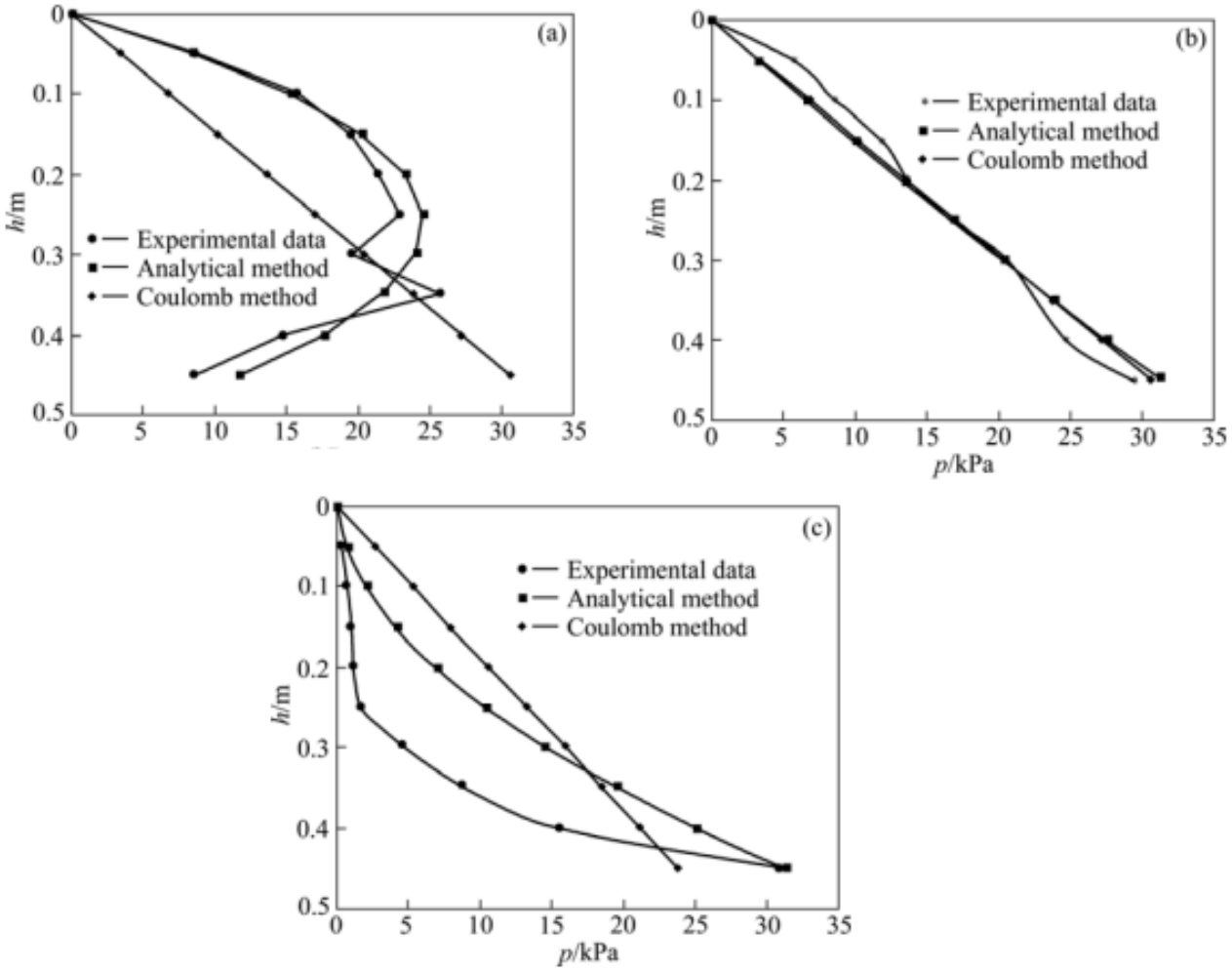

Figure 1. 31 Distribution of passive earth pressure with various wall movements (Peng et al., 2012) a) RB mode b) T mode c) RT mode

1.4.5. Tang et al. (2018)

Tang et al. (2018) proposed a theoretical model for calculating earth pressure, taking into account various modes and magnitudes of wall displacements. This model was constructed based on the hyperbolic stress-strain relationship, with incorporation of the classical earth pressure theory for the limit state to predict earth pressure under significant wall movement. As the retaining wall moves away from the soil mass, the lateral earth pressure diminishes, while the corresponding Mohr circle expands, as illustrated in Figure 1. 32b

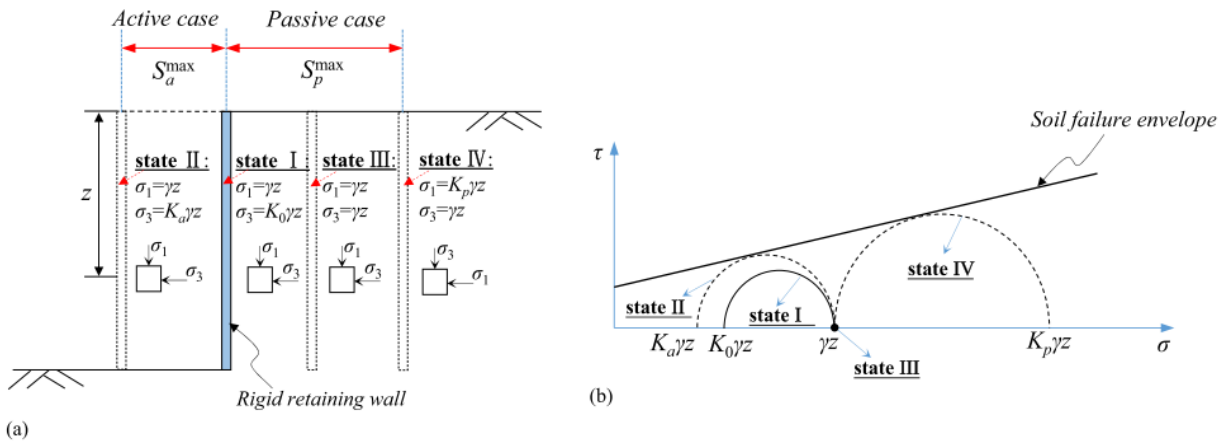

Figure 1. 32 Different states of earth pressure: a) stress states with dfferent wall movements b) Mohr circles for different stresss states

When this Mohr circle reaches the soil failure envelope, the earth pressure corresponds to the limit active earth pressure at State II, characterized by a coefficient K_a , signifying that the lateral earth pressure at depth z is $K_a\gamma z$. The necessary wall displacement to achieve this limit active state is denoted S_a^{max}, as shown in Figure 1. 32b. On the other hand, if the wall moves towards the soil mass, the lateral earth pressure intensifies and may reach the limit passive earth pressure (State IV), at which point the lateral earth pressure at depth z is $K_p\gamma z$, with K_p representing the passive earth pressure coefficient. The wall displacement corresponding to the limit passive state is S_p^{max}. According to the research by Mei et al. (2017), there exists a pivotal point in the variation of earth pressure as the wall moves towards the soil mass, known as State III in Figure 1. 32a. At this juncture, the lateral earth pressure is equal to the vertical stress. Put differently, this turning point aligns with the isotropic stress state, leading to the reduction of the corresponding Mohr circle to a singular point, as exemplified in Figure 1. 32b.

The deviatoric stress exhibits a hyperbolic relationship with the lateral strain, as described in Duncan and Chang's (1970) nonlinear soil stress-strain relationship. In the passive case, the major principal stress $\sigma_1 = p$, while $\sigma_3 = \gamma z$; the lateral strain ε_p for this passive case is under compression. Therefore, the deviatoric stress can be determined using the hyperbolic model from equation (1.1):

$$\sigma_1 - \sigma_3 = p - \gamma z = \frac{\varepsilon_p}{a + b\varepsilon_p} \qquad (1.1)$$

where the coefficient a is ascertainable through the initial tangential modulus of the soil and is contingent upon the confining stress (Janbu, 1963). On the other hand, coefficient b can be established based on the stress difference's asymptotic value.

The coefficient of passive earth pressure proposed by Tang et al. can be extracted from equation (1,2) as:

$$K_h = 1 + \frac{(1-R_f)(1-K_0)(1-K_a)(1-K_p)(1-\eta_p)+\eta_p(K_p-1)^2(R_f+K_a-R_fK_0-1)}{(\eta_pR_f-R_f+1)(K_p-1)(R_f+K_a-R_fK_0-1)+R_f(1-R_f)(1-K_0)(1-K_a)(1-\eta_p)} \qquad (1.2)$$

where

$$\eta_p = \frac{\varepsilon_p}{\varepsilon_{pf}} = \frac{S_p}{S_p^{max}} \qquad (1.3)$$

and R_f is the failure ratio introduced by Duncan and chang (1970), has to be between 0.75 and 1.00. Figure 1. 33 Figure 1. 34 present results of the analytical equation proposed by Tang et al. (2018) from equation (1.2) compared with the experimental test conducted by Fang et al. (1994) for different values of center of rotation "n".

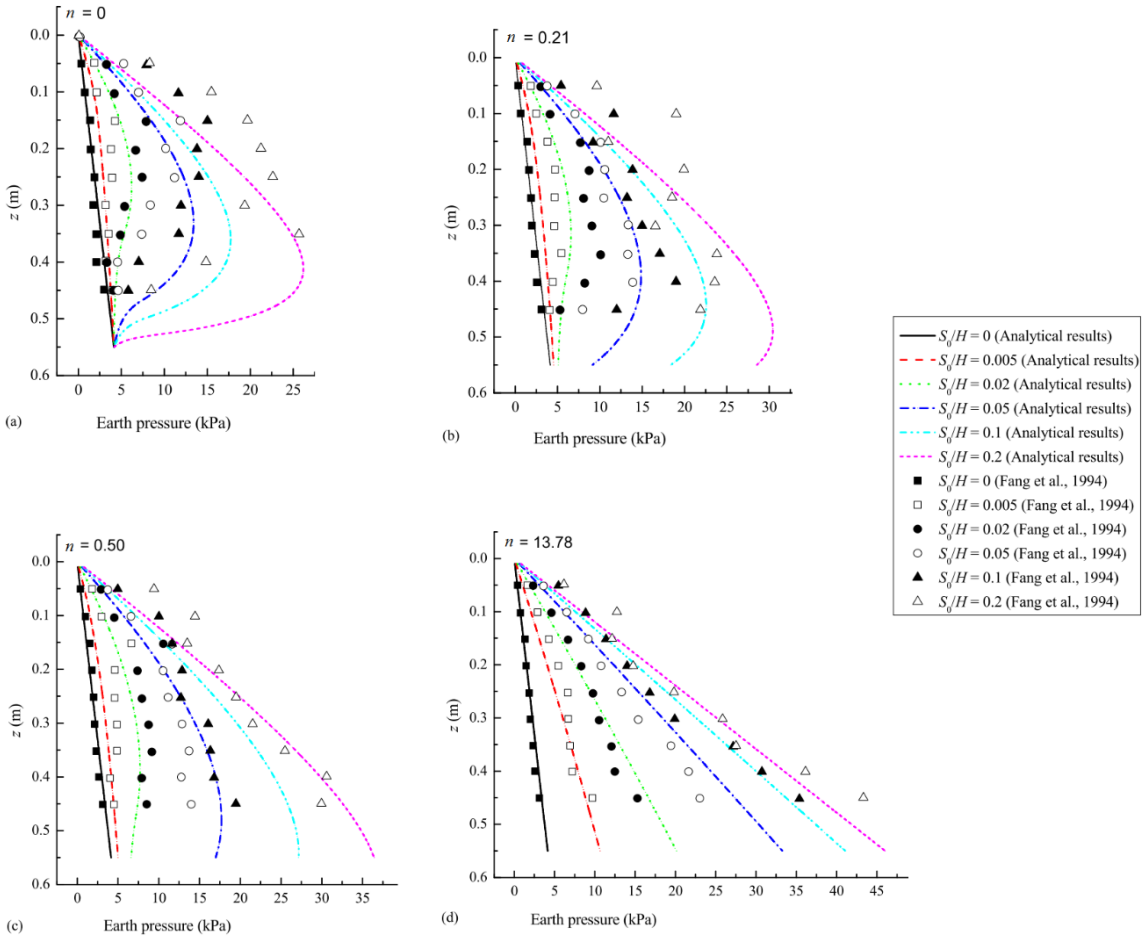

Figure 1. 33 Distribution of passive earth pressure from tang et al.(2018) for RBT mode a) n=0 b) n=0.21 c) n=0.50 d) n=13.78

RBT mode case present a curved distribution of passive earth pressure identical with rotation about the wall top (n=0) as presented in Figure 1. 33a. This distribution changes from non linear to linear with increasing of n to reach a linear distribution of passive earth pressure. RTT mode resolve a null earth pressure at the wall top. Afterward, an important increment on the earth pressure can be noticed in the lower part of the wall in the case of a center of rotation located near the wall base. The increase of "n" results a change in the distribution of lateral earth pressure to become linear with high

values of "n". A large agreement can be observed between the analytical results of Tang et al. (2018) and experimental tests conducted by Fang et al. (1994).

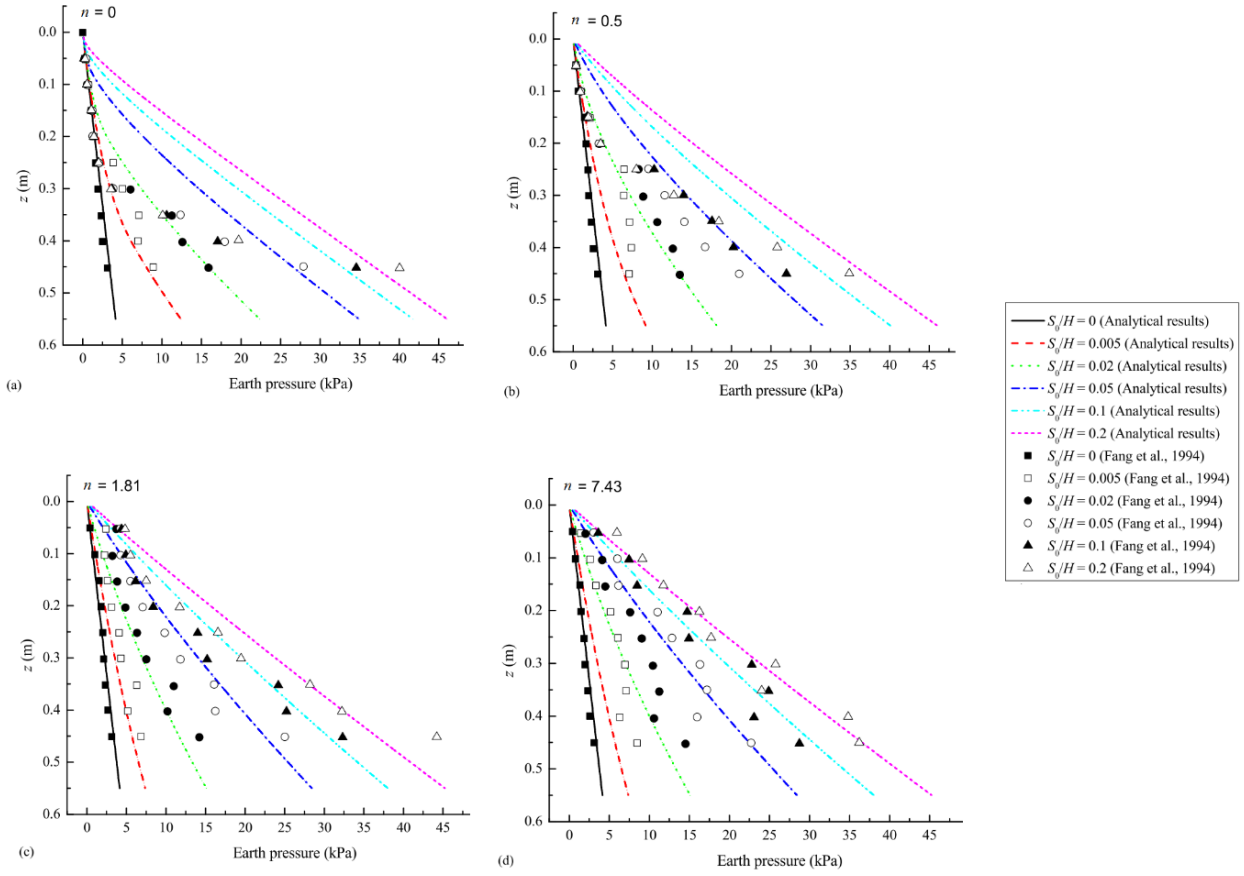

Figure 1. 34 Distribution of passive earth pressure from tang et al.(2018) for RTT mode a) n=0 b) n=0.21 c) n=1.81 d) n=7.43

1.5. CONCLUSION

This chapter reviewed the different types of retaining structures generally, and indicated those that are subjected to rotational movement on failure, which can be summarized in: integral bridge abutments, embedded cantilever, anchored and strutted retaining structures. Integral bridges are mainly subjected to seasonal expansions due to the movement of temperature during winter and summer. The abutment of these jointless bridges then will be subjected to deck push, which will create a rotational movement. The full-scale monitoring test conducted by Huntley and Valsangkar (2013) on Route 2 connector underpass shows well than the abutment wall is subjected to rotational movement in addition to the translation submitted by the change the temperature during the three monitoring years. Authors also proved that the passive earth pressure measured on the top of the wall is much higher than those predicted with existing methods from literature.

Embedded wall are also a type of retaining wall that are subjected to rotational movement. The self-stability of embedded walls is based on the passive force created in front of the wall. Bica and Clayton (1998) with his small-scale test on a cantilever retaining wall, confirmed Krey (1984) assumption saying that the passive earth pressure is nonlinear distributed behind those kind of retaining walls, which lead the insecure on the design of such walls.

This chapter presented also the different studies that investigated the rotational movement of the retaining walls. James & Bransby (1970) was from the first that experimentally investigated this case, and proved that the distribution of passive earth pressure behind retaining walls had a curved shape. Fang et al. (1994) confirmed this non-linearity with another laboratory test, which investigated the three different types of movement; translation, rotation about top and rotation about bottom, in addition to rotational movement when the center of rotation is situated in various locations. Fang et al. (1994) extracted curves describing the distribution of passive earth pressure under various stages of wall movement which have been used later as a reference in many analytical studies such as Peng et al. (2012) Tang et al. (2018).

Chapter II

EARTH PRESSURE CONCEPTS

2.1. INTRODUCTION

The well determination of the active and passive load diagram from an appropriate theory is a major issue in the design of safe retaining structures. The magnitude of lateral earth pressure is influenced by several factors, including:

The physical characteristics of the soil backfill.

- The geometric configuration of the backfill.
- The nature of the soil-structure interface.
- Surcharge loading acting on the system.
- Seepage forces within the soil.
- The centroid of the resultant load.
- Potential modes of movement and deformation and the structural stiffness of the earth retaining system.

In terms of modes of displacement, lateral earth pressure can be classified into three types:

- At-Rest Earth Pressure
- Active Earth Pressure
- Passive Earth Pressure

At-rest earth pressure occurs when the wall undergoes no lateral movement, and therefore does not mobilize the shear strength of the soil backfill. Active earth pressure, on the other hand, occurs when the earth retaining structure moves away from the backfill, as illustrated in Figure 2. 1. Earth retaining walls that are permitted to move away from the backfill must be designed to withstand the full force of active earth pressure. Passive earth pressure, depicted in Figure 2. 2, develops when the earth retaining system moves towards the soil mass.

The variation of lateral load between the active and the passive earth pressure values can be generated only by lateral movements within the soil backfill. Considering a segment of the granular soil below the surface, as presented in Figure 2. 1, it is assumed that the vertical stress (σ_v) remains consistent at a specific point. When the wall moves away from the backfill, the lateral stress (σ_h)

gradually decreases until it reaches the critical value known as active earth pressure (σ_a). Conversely, if the wall moves towards the soil, the lateral stress (σ_h) gradually increases until it reaches the critical value known as passive earth pressure (σ_p), as illustrated in Figure 2. 2.

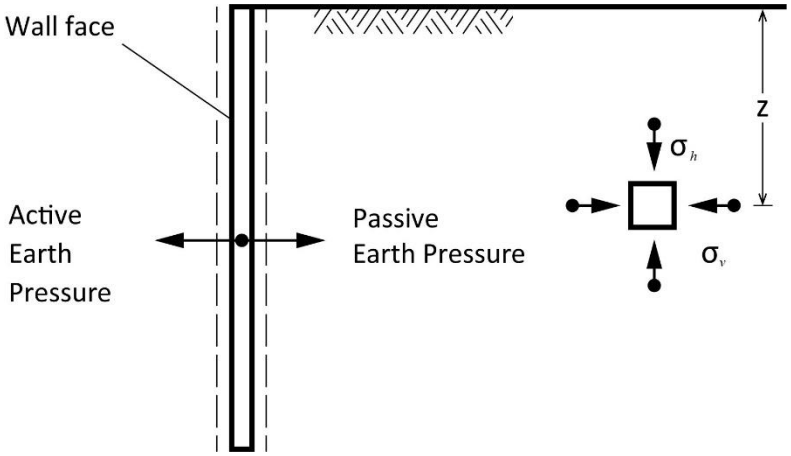

Figure 2. 1. Active and passive earth pressures

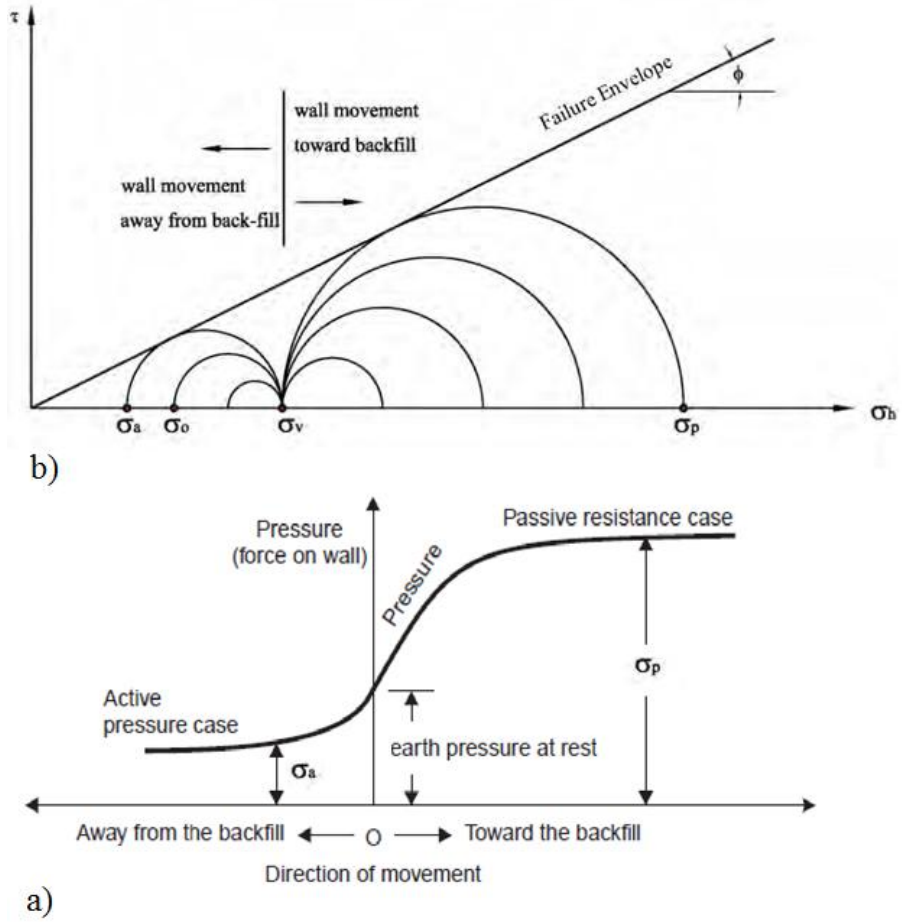

Figure 2. 2. active and passive earth pressure with wall movement a) Mohr Circle b) stress-strain curve

The selection of methods to assess lateral earth pressures is a pivotal stage in the design of earth retaining systems. The subsequent section outlines common analytical approaches for calculating static lateral loads. Initially, we assume that the backfill possesses characteristics of being horizontal, homogeneous, and isotropic. Additionally, the distribution of vertical stress (σ_v) with respect to depth follows a hydrostatic pattern, as depicted in Figure 2. 3. The horizontal stress (σ_h) varies linearly with depth and is a multiple of the vertical stress (σ_v), as described in Equation (2.1):

$$\sigma_h = \sigma_v K = \gamma h \qquad (2.1)$$

The value of coefficient *K* corresponds to different conditions of wall movement; the active coefficient (K_a), the passive coefficient (K_p), and the at-rest coefficient (K_0) for earth pressure. Here, *h* denotes the distance between the pressure surface and the ground at the base of the wall. The lateral force exerted by the earth (represented by *P*) is equivalent to the area enclosed by the load diagram defined in equation (2.2):

$$P = \frac{1}{2}\sigma_h h \qquad (2.2)$$

The force *P* is considered to act at a point positioned *h*/3 above the wall toe. This resulting force *P* is responsible for inducing bending, sliding, and potential overturning effects in the wall.

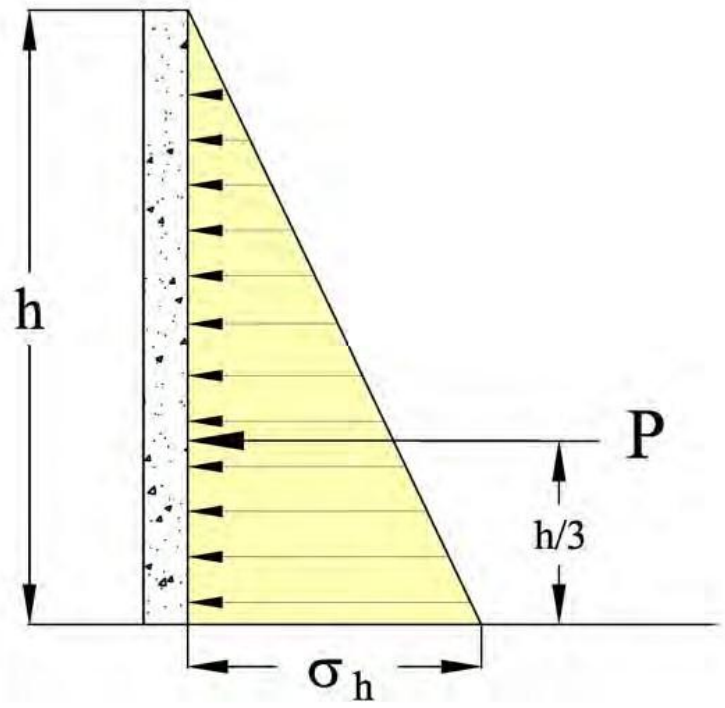

Figure 2. 3. Lateral Earth Pressure Variation with Depth

2.2. AT-REST EARTH PRESSURE

Under conditions of zero shear strain, the relationship between horizontal and vertical stresses is determined by Poisson's ratio (ν), as articulated by Terzaghi in 1923:

$$K_0 = \frac{\nu}{1-\nu} \quad (2.3)$$

In the case of normally consolidated soils and vertical walls, the at-rest lateral earth pressure coefficient can be expressed in terms of the internal soil friction angle (φ), as follows (Jaky in 1944):

$$K_0 = 1 - \sin\varphi \quad (2.4)$$

In the case of over-consolidated soils with a level backfill behind a vertical wall, the coefficient of at-rest lateral earth pressure can be considered to be dependent on factors like the over-consolidation ratio (OCR) or stress history. This coefficient can be determined using either equation (2.5) from Meyerhof (1976) or equation (2.6) from Mayne and Kulhawy (1982), as indicated below:

$$K_0 = (1 - \sin\varphi)\sqrt{(OCR)} \quad (2.5)$$

$$K_0 = (1 - \sin\varphi)OCR^{\sin\varphi} \quad (2.6)$$

2.3. ACTIVE AND PASSIVE EARTH PRESSURES

The status of the active or passive earth pressure relies on the transition of the backfill material from its elastic state to a state of plastic equilibrium, which can occur through either expansion or compression. Active earth pressures are developed when the soil mass behind the wall system moves outward as a result of the retaining wall displacement. Movement of the wall in the opposite direction (i.e., toward the soil) in turn mobilizes the shear strength of the soil and is referred to as passive earth pressure, as presented in Figure 2. 4. Due to the deflection of the wall, active and passive wedges are formed behind and in front of the retaining structure. The soil in these areas experiences two primary stresses: a vertical stress (σ_v) and a horizontal stress (σ_h). In the active case, σ_h is the smaller principal stress while σ_v is the larger principal stress. Conversely, in the passive case, σ_h becomes the larger principal stress while σ_v is the smaller principal stress. Figure 2. 5 illustrates the Mohr Circle Representation of the Stress State for a Cohesionless Backfill, which can be employed to establish the relationship for active and passive earth pressures as follows:

$$\sigma_a = OC = OA - AC \quad (2.7)$$

As:

$$AC = AB = OA\sin\varphi \quad (2.8)$$

$$\sigma_a = OA(1 - \sin\varphi) \quad (2.9)$$

Also:

$$\sigma_v = OA + AB = OA(1 + sin\,\varphi) \qquad (2.10)$$

From the equation (2.9) and (2.10):

$$K_a = \frac{\sigma_a}{\sigma_v} = \frac{(1-sin\,\varphi)}{(1+sin\,\varphi)} = tan^2\left(45° - \frac{\varphi}{2}\right) \qquad (2.11)$$

Through same steps, passive earth pressure can be deduced as follow:

$$K_p = \frac{\sigma_p}{\sigma_v} = \frac{(1+sin\,\varphi)}{(1-sin\,\varphi)} = tan^2\left(45 + \frac{\varphi}{2}\right) \qquad (2.12)$$

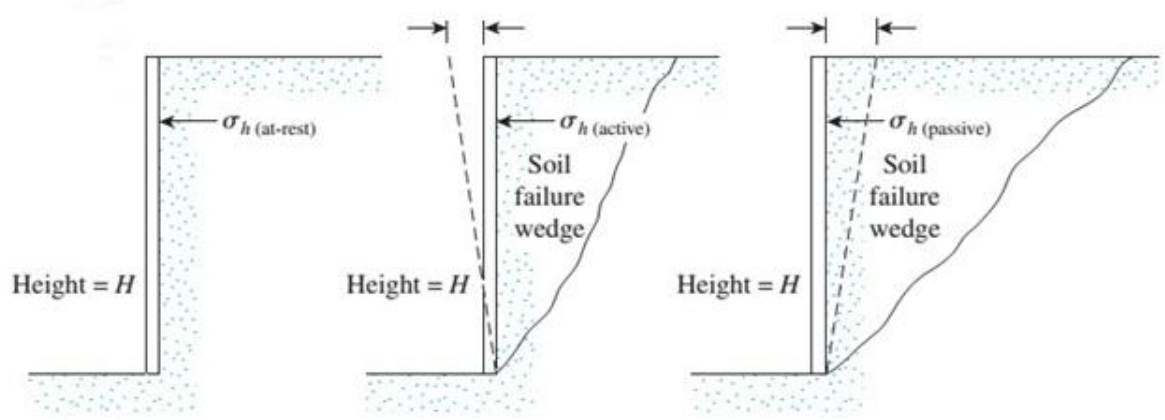

Figure 2. 4 : Active - Passive – At rest earth pressure resulted from the wall movement

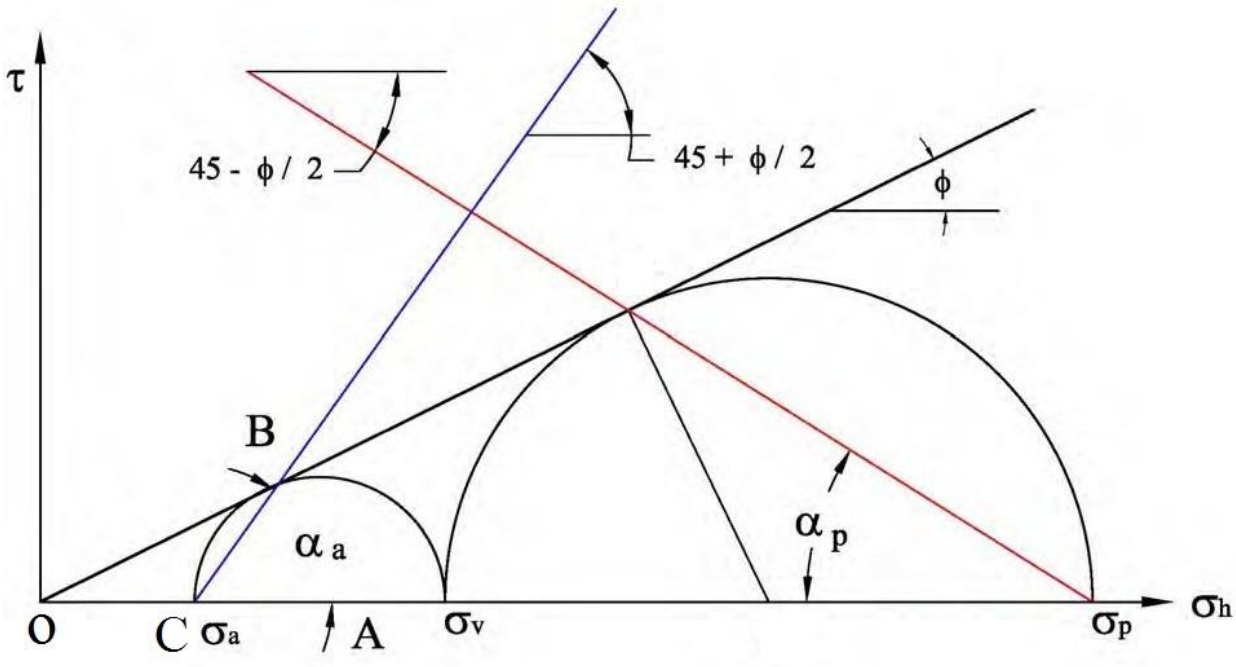

Figure 2. 5 : Mohr Circle Representation of the Stress State for a Cohesionless Backfill

2.4. EARTH PRESSURE THEORIES

When Coulomb (1773) and Rankine (1857) formulated their foundational two-dimensional earth pressure theories (discussed in §2.4.2 and §2.4.1, respectively), they introduced two straightforward analytical approaches: limit equilibrium and slip line methods. While both methods rely on plasticity principles, they vary in their approach to obtaining solutions. The limit equilibrium method is the more widely employed technique for analyzing retaining structures. The method attempts first to identify a mode of failure where limit state conditions are assumed, which makes it possible to solve various problems by simple tactics. This limit equilibrium approach requires making adequate assumptions about the stress distribution along the failure surface. This makes it possible to formulate a comprehensive equilibrium equation, expressed in terms of stress resultants, for a specific problem. The solutions obtained using this method have been compiled and presented in graphical or tabular formats in the study by Terzaghi (1943) and Taylor (1948). These solutions have since gained widespread acceptance and application in practical engineering practice.

The slip line method initially attempts to derive fundamental differential equations that enable the solution of various problems through the determination of the slip-line network. These slip-line equations were formulated first by Kötter (1903), for plan deformation cases. Following this, Prandtl (1920) was the first to provide an analytical closed-form solution for a footing on a weightless soil. In his analysis, he introduced a singular point with a set of straight slip-lines passing through it. Afterwards, Reissner (1924) and Novotortsev (1938) applied these results to specific problems related to the bearing capacity of footings on a weightless soil. This was done in cases where at least one family of slip-lines was straight, allowing for closed-form solutions. However, the introduction of soil weight significantly complicates the mathematical solution, leading to the development of numerous approximate methods. Sokolovskii (1965) adopted a numerical analysis based on finite difference approach of the slip-line equations. This led to the resolution of various complex problems related to the bearing capacity of footings, slopes, and lateral earth pressure behind retaining walls; cases where closed-form solutions proved unattainable. De Jong (1957), on the other hand, pursued a different path, devising a graphical method for solutions. Additional approximate solutions involved the application of perturbation methods (Spencer, 1962) and series expansion techniques (Dembicki et al., 1964).

Another third method known as Limit Analysis has been developed to address problems related to active and passive earth pressure. This method simplifies the stress-strain relationship of soil through an idealized representation, referred to as normality or the flow rule. These idealizations form the foundation for the limit theorems upon which limit analysis relies. Under these assumptions, the approach is rigorous and the methods can be as effective as those of limit equilibrium, and in some

cases, even simpler. The plastic limit theorems proposed by Drucker et al. in 1952 can be conveniently applied to establish both upper and lower bounds for collapse loads in stability issues, such as determining critical heights of unsupported vertical cuts or assessing the bearing capacity of nonhomogeneous soils.

Beside these analytical methods, there exist many numerical methods for the evaluation of active and passive earth pressure, which will be cited in chapter III in §3.4. Many studies have been developed based on the analysis methods cited above. In what follows, an overview on a number of key earth pressure models.

2.4.1. Rankine's (1857) Earth Pressure Theory

In contrast to Rankine's theory, Coulomb's (1776) earth pressure theory assumes that the wall is not totally smooth having a friction angle. The configurations of Coulomb's wedges are presented in Figure 2. 6 and Figure 2. 7. The inclusion of wall-backfill interface friction essentially means that shear stresses come into play between the retaining wall and the backfill soil, altering the orientation of the principal planes. Coulomb's theory operates on the following implicit assumptions:

- The wall possesses a rough surface.
- The existence of friction or adhesion between the wall and the soil.
- The failure wedge forms a planar surface, contingent on the soil friction (φ), wall friction (δ), backfill slope (β), and wall slope (ω).
- Lateral earth pressure varies in a linear fashion with wall depth.
- The direction of the lateral earth pressure deviates by an angle δ from the surface of the retaining wall.
- The earth pressure centroid acts at a distance equal to one-third of the wall height from the base.
- The backfill slope has to be smaller than the backfill friction angle.

The values for the coefficient of active lateral earth pressure using the Rankine's theory are given by

$$K_a = \cos\beta \frac{\cos\beta - \sqrt{\cos^2\beta - \cos^2\varphi}}{\cos\beta + \sqrt{\cos^2\beta - \cos^2\varphi}} \qquad (2.13)$$

In the case of $= 0$:

$$K_a = \frac{1-\sin\varphi}{1+\sin\varphi} \qquad (2.14)$$

The magnitude of active earth pressure can be determined using

$$P_a = \frac{1}{2}\gamma h^2 K_a \qquad (2.15)$$

The failure plane angle α_a is given by

$$\alpha_a = \left(45 + \frac{\varphi}{2}\right) - \frac{1}{2}\left(sin^{-1}\left(\frac{\sin\beta}{\sin\varphi}\right) - \beta\right) \qquad (2.16)$$

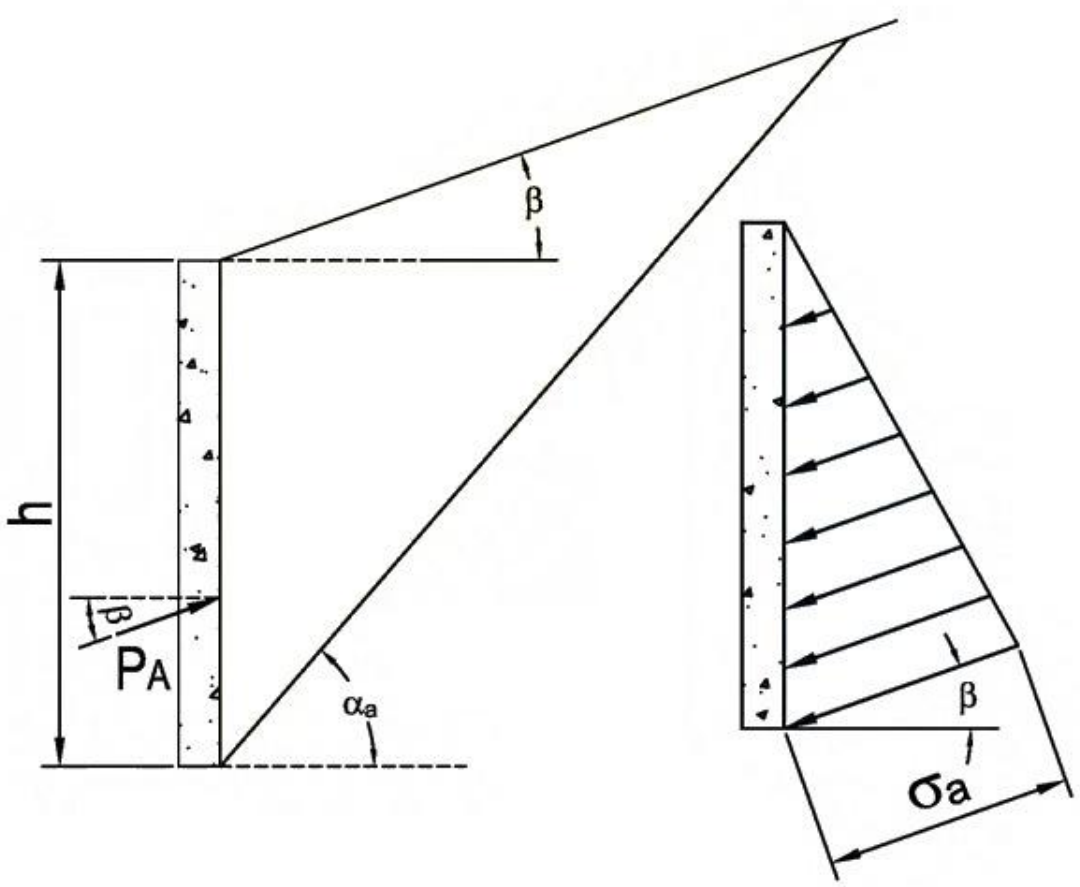

Figure 2. 6 : Rankine's Active Wedge

Rankine employed comparable assumptions in his calculation of passive earth pressure. The coefficients for active lateral earth pressure, as per Rankine's theory, are provided as follows:

$$K_p = \cos\beta \frac{\cos\beta + \sqrt{\cos^2\beta - \cos^2\varphi}}{\cos\beta - \sqrt{\cos^2\beta - \cos^2\varphi}} \qquad (2.16)$$

In the case of $= 0$:

$$K_p = \frac{1+\sin\varphi}{1-\sin\varphi} \qquad (2.17)$$

The calculation of passive earth pressure magnitude can be established by:

$$P_p = \frac{1}{2}\gamma h^2 K_p \qquad (2.18)$$

The failure angle in passive case α_p is determined from:

$$\alpha_p = \left(45 - \frac{\varphi}{2}\right) - \frac{1}{2}\left(sin^{-1}\left(\frac{sin\,\beta}{sin\,\varphi}\right) + \beta\right) \quad (2.19)$$

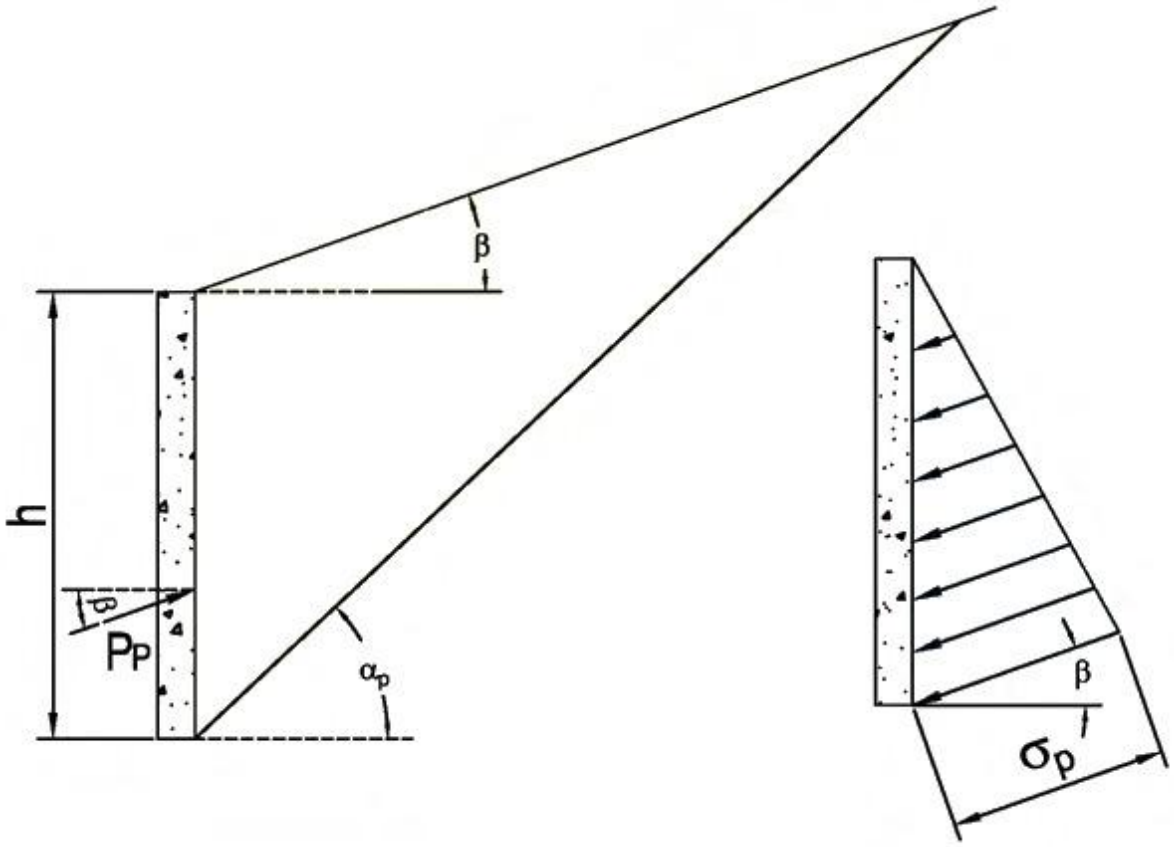

Figure 2. 7: Rankine' s Passive Wedge

Although Rankine's equation for passive earth pressure is presented above, it is not advisable to apply it when the backfill angle is greater than zero (β > 0). This is because the K_p values remain the same for both positive (β > 0) and negative (β < 0) backfill slopes. Consequently, it is recommended to refrain from using the Rankine equation to determine the passive earth pressure coefficient for sloping terrain.

2.4.2. Coulomb's Earth Pressure Theory (1776)

In contrast to Rankine's earth pressure theory, Coulomb's (1776) theory takes into account that the wall is not frictionless. The configurations of Coulomb's wedges are illustrated in Figure 2. 8 and Figure 2. 9. The inclusion of friction at the wall-backfill interface introduces shear stresses between the back of the wall and the backfill, altering the orientation of the principal planes. Coulomb's theory operates under the following assumptions:

- The wall has a rough surface.
- There exists friction or adhesion between the wall and the soil.

- The failure wedge forms a planar surface, determined by soil friction (φ), wall friction (δ), backfill slope (β), and wall slope (ω).
- Lateral earth pressure changes linearly with depth.
- The direction of lateral earth pressure forms an angle δ with the normal surface of the wall.
- The resultant earth force acts at a distance equivalent to one-third of the wall height from the base.
- The backfill slope must be less than the backfill friction angle.

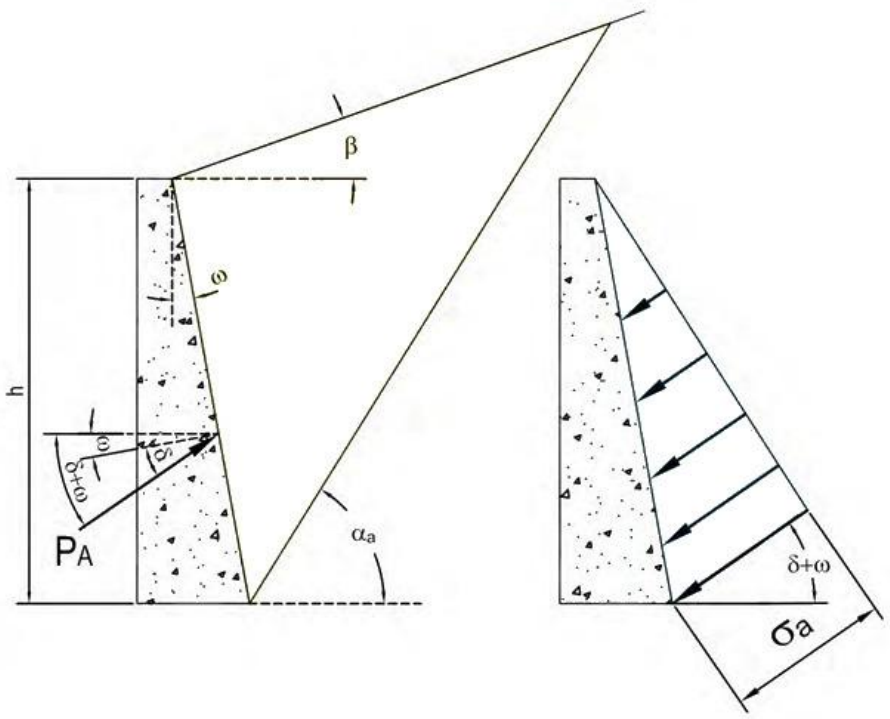

Figure 2. 8: Coulomb's Active Wedge

The active earth pressure coefficient might be expressed as:

$$K_a = \frac{cos^2(\varphi-\omega)}{cos^2\,\omega\,cos(\delta+\omega)\left(1+\sqrt{\frac{sin(\varphi+\delta)\,sin(\varphi-\beta)}{cos(\omega+\delta)\,cos(\omega-\beta)}}\right)^2} \qquad (2.19)$$

and the magnitude of active earth force can be given by equation (2.15) similar to Rankine's method:

$$P_a = \frac{1}{2}\gamma h^2 K_a \quad (2.15)$$

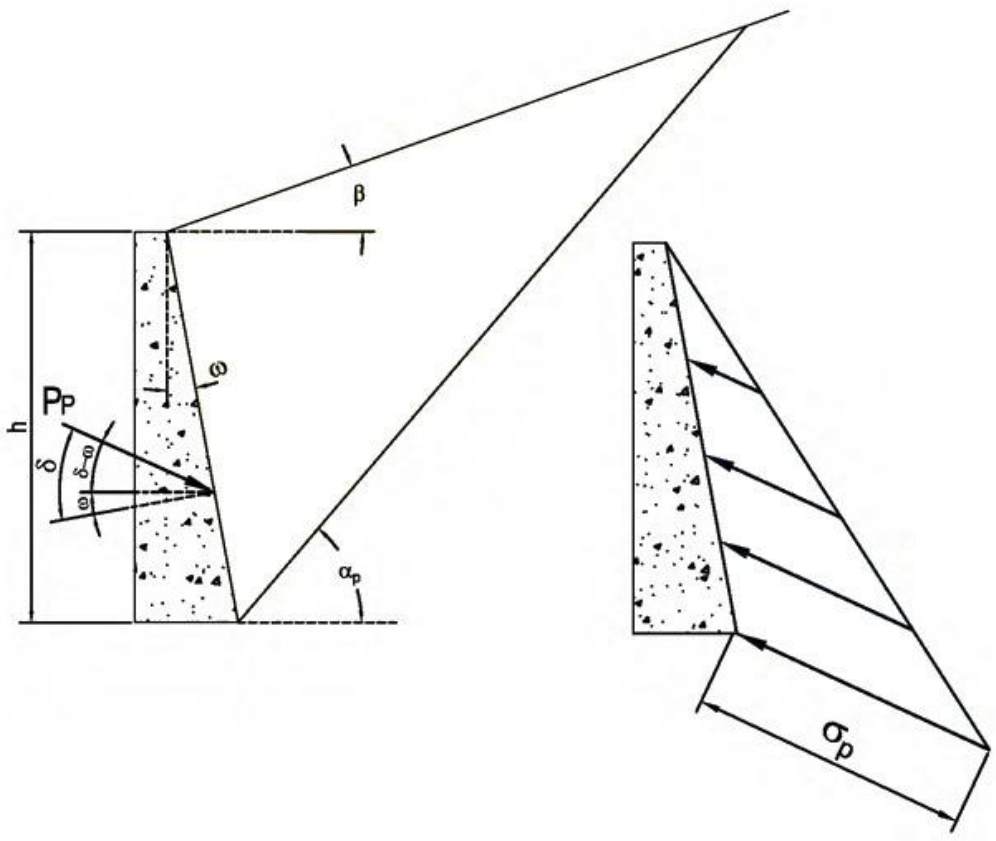

Figure 2. 9: Coulomb's Passive Wedge

The angle of the active failure plane is provided by

$$\alpha_A = \varphi + tan^{-1}\left(\frac{-tan(\varphi-\beta)+C_{1A}}{C_{2A}}\right) \quad (2.20)$$

where

$$C_{1A} = \sqrt{tan(\varphi-\beta)(tan(\varphi-\beta)+cot(\varphi-\omega))(1+tan(\delta+\omega)cot(\varphi-\omega))} \quad (2.21)$$

$$C_{2A} = 1 + tan(\delta+\omega)(tan(\varphi-\beta)+cot(\varphi-\omega)) \quad (2.22)$$

Coulomb's equations for passive earth pressure are derived in a similar manner to the equations for active earth pressure. However, there is a distinction in the direction of the force, as illustrated in Figure 2. 9. The coefficients for passive lateral earth pressure can be determined from:

$$K_p = \frac{cos^2(\varphi+\omega)}{cos^2\,\omega\, cos(\delta-\omega)\left(1+\sqrt{\frac{sin(\varphi+\delta)\,sin(\varphi+\beta)}{cos(\omega-\delta)\,cos(\omega-\beta)}}\right)^2} \quad (2.22)$$

The passive earth pressure can be provided by equation (2.18):

$$P_p = \frac{1}{2}\gamma h^2 K_p \quad (2.18)$$

The passive failure angle is:

$$\alpha_p = -\varphi + tan^{-1}\left(\frac{tan(\varphi+\beta)+C_{1p}}{C_{2p}}\right) \quad (2.23)$$

Where

$$C_{1p} = \sqrt{tan(\varphi+\beta)(tan(\varphi+\beta)+cot(\varphi+\omega))(1+tan(\delta-\omega)cot(\varphi+\omega))} \quad (2.24)$$

$$C_{2p} = 1 + tan(\delta-\omega)(tan(\varphi+\beta)+cot(\varphi+\omega)) \quad (2.25)$$

2.4.3. The Log-Spiral Method

The assumption of a planar failure surface can be problematic, particularly when the wall surface is not perfectly smooth. According to Terzaghi (1943) and Terzaghi et al. (1996), if the interface friction angle (called δ) between the retaining wall and the backfill soil is greater than zero, the failure surface does not take on a triangular plane. Terzaghi et al. (1996) asserted that when the angle δ surpasses $\delta/3$, the curvature of the failure surface occurred becomes significant. Therefore, it becomes imperative to take on consideration for this curvature in calculating the passive earth pressure. Terzaghi (1943) proposed that satisfactory results can be achieved by employing a logarithmic spiral arc to represent the lower segment of the rupture surface (see Figure 2. 10). The remainder of the surface takes the form of a tangential line to the logarithmic spiral curve, showing at an angle equal to $(45 - \frac{\varphi}{2})$ with respect to the horizontal.

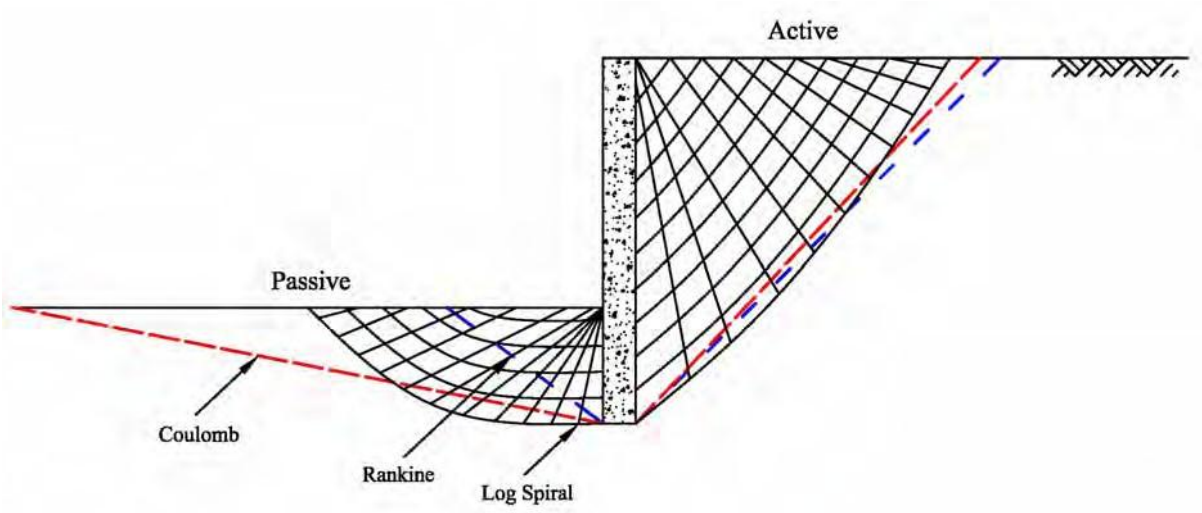

Figure 2. 10 Illustration of the Logarithmic Spiral Failure Surface

In the case of active conditions, both Rankine's and Coulomb's methods yield failure surfaces that closely approximate the log-spiral failure surface. However, under the case of passive conditions, notable discrepancies can be noticed. Specifically, when the angle of wall-interface friction (δ) exceeds one-third of the backfill friction angle (φ), the planar failure surfaces predicted by the two methods (Rankine and Coulomb) diverge significantly from the one determined by the log-spiral approach.

Both active and passive earth pressures are intrinsically linked to the soil mass residing within the failure surface. Within the Coulomb and Rankine active zones, the mobilized soil is approximately equivalent to the one within a log-spiral active zone. In contrast, within the Coulomb passive zone, the mobilized soil mass is considerably greater than that within the log-spiral passive zone, while the Rankine method shows significantly smaller passive zone than the log-spiral counterpart.

In light of these observations, it can be concluded that Coulomb's theory tends to overestimate the magnitude of the passive earth pressure. However, Rankine's theory tends to underestimate it. Consequently, Rankine's earth pressure theory is conservative, while Coulomb's theory is non-conservative, and the log-spiral result provides the most realistic estimate for the passive earth pressure.

Further developments has been added to the non-linear failure plane theory by Caquot and Kérisel (1948), which produced charts/tables for Ka and Kp values based on the log-spiral and linear failure surface. Using the logarithmic spiral to represent the rupture surface in both active and passive derivations considering the soil-wall interface friction angle.

2.4.4. Trial Wedge Method

The Trial Wedge method use a general limit equilibrium approach to estimate the forces exerted on earth retaining walls. This method is versatile and can be applied regardless of the irregularity of the backfill, as well as the adhesion and interface friction angle of the wall. The sliding wedge is defined by the ground surface at the top, the rupture surface on one side, and the back of the wall on the other side, as illustrated in Figure 2. 11.

In the active case, the critical wedge is the one that necessitates the maximum earth force acting at the wall-soil interface to obtain the equilibrium of the mobilized soil wedge at failure. Conversely, in the passive case, it is the wedge requiring the minimum force.The trial wedge method has been incorporated into various design guidelines (AASHTO, 2012; Caltrans, 2011) for evaluating active earth forces. However, in the case of the passive earth pressure, this method is rarely used. This is primarily due to the fact that its application under cohesionless backfill conditions results an unsafe design.

2.5. SURCHARGE LOADS

One of the important problems that comes across while designing retaining walls is the effect of loads behind the retaining wall, which can appear in various forms as shown in Figure 2. 12 ; uniform surcharge load (embankment), concentrated load (trucks or machines), line load (railway line)

and strip load (footing). In what follow, the standard solutions recommended for the above cited cases of surcharge loading.

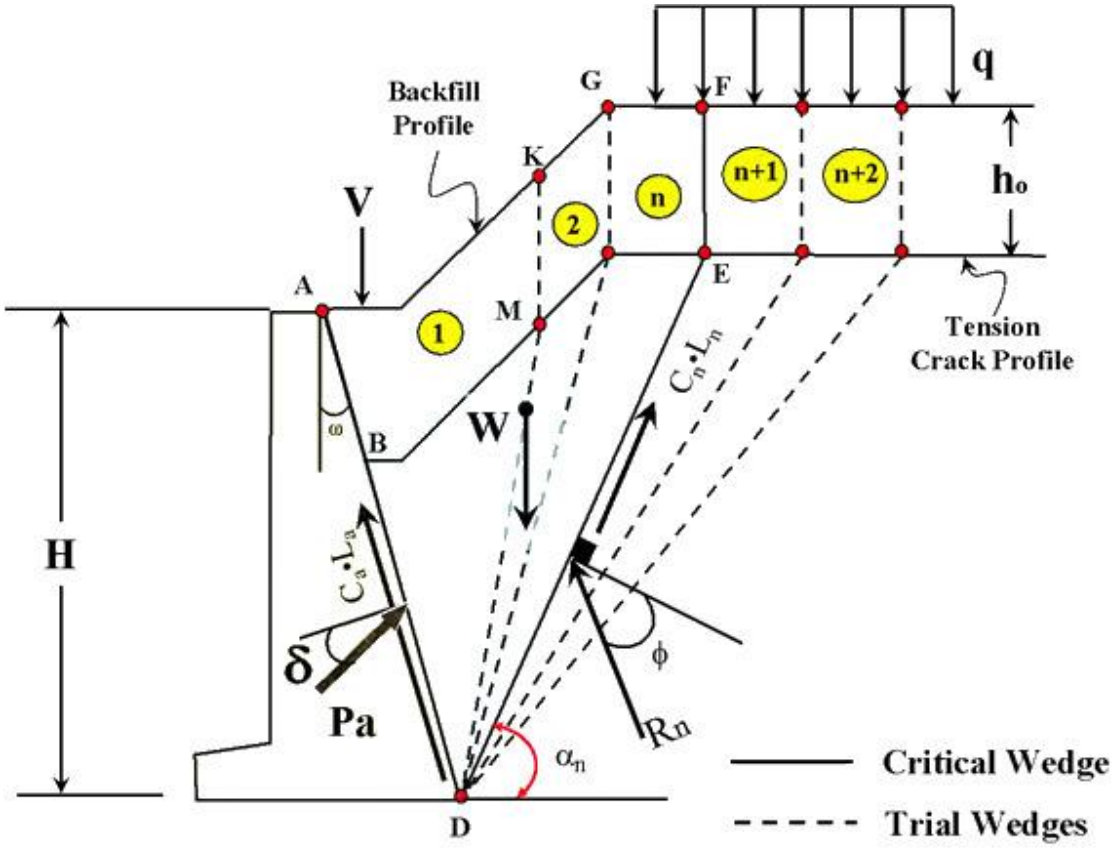

Figure 2. 11. Active Trial Wedge

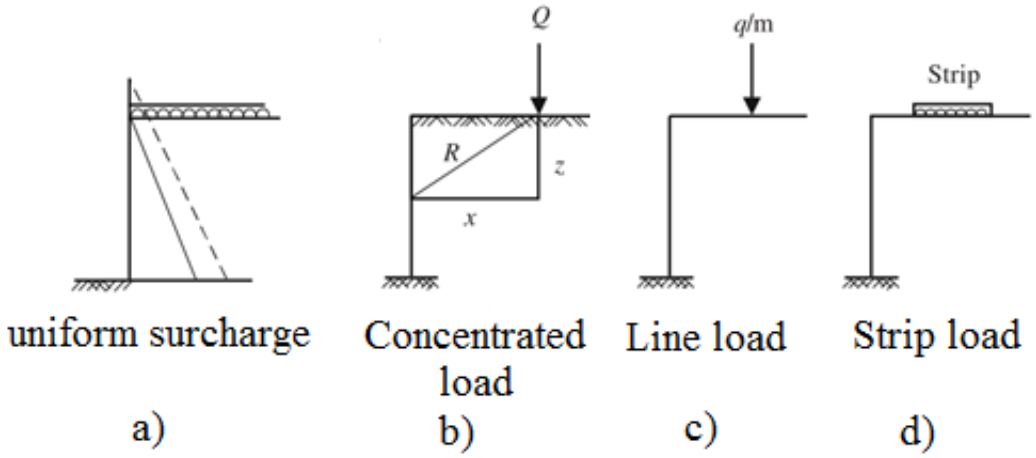

Figure 2. 12. Different types of surcharge loads behind a retaining wall a) uniform surcharge load b) concentrated load c) line load d) strip load

2.5.1. Uniform Surcharge Loads

In cases where a uniform surcharge is applied, as illustrated in Figure 2.13, a consistent horizontal earth pressure needs to be included alongside the fundamental lateral earth pressure. This steady earth pressure can be defined as:

$$\sigma_h = KQ \qquad (2.25)$$

where K is the earth pressure coefficient that can be used in the three cases; K_0 at rest, K_a active, and K_p passive earth pressure. In reality, the lateral earth pressure resulting from surcharge loads tends to decrease with depth. The simplified stress distribution depicted in Figure 2. 13 does not align with this practical observation. Consequently, the constant earth pressure proposed by equation (2.25) should not be assumed to persist indefinitely below the ground surface. In engineering design, it is customary to apply the constant earth pressure only within the span between the ground line and the excavation line. In the case of passive earth pressure due to uniform surcharge loading, the most common method used rather than Coulomb's and Rankine's is the one reported by Kerisel and Absi (1990). This last was based on logspiral mechanism to report passive earth pressure coefficients due to surcharge load (K_{pq}) for various combinations of soil properties (internal friction angle, soil-wall interface friction angle, geometrical properties, wall and backfill inclination).

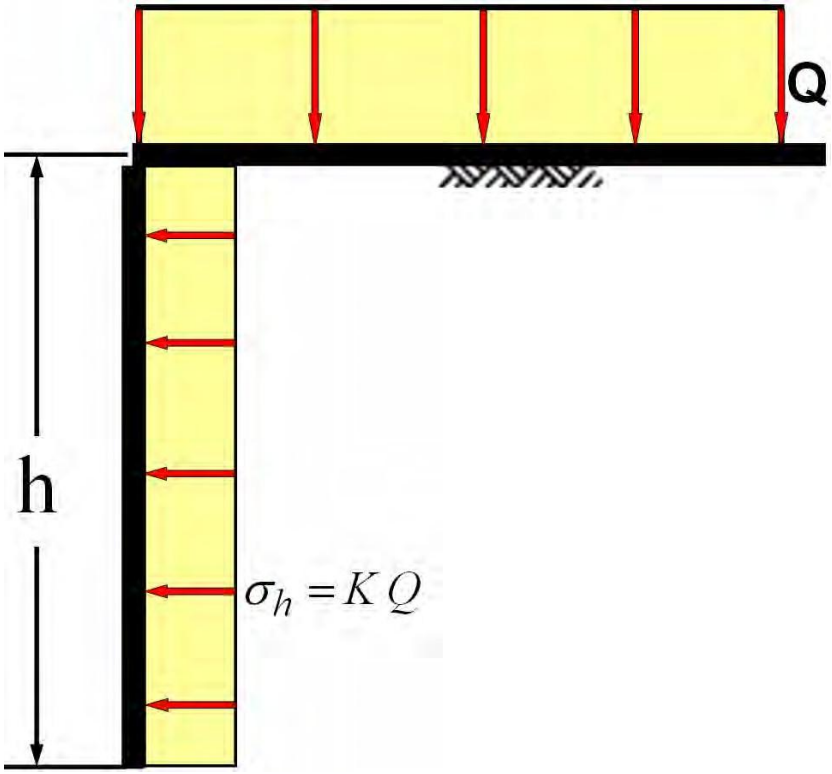

Figure 2. 13 Lateral Pressure Due to Uniform Surcharge

2.5.2. Concentrated Load (Point Load)

Spangler (1936) conducted extensive laboratory tests focused on concentrated loads acting on sand backfills, and demonstrated that Boussinesq's equation (1885) could reliably predict the effects of concentrated loads behind retaining walls. Furthermore, Spangler's (1936) observations indicated that the pressure on rigid walls could be nearly twice the value calculated by the elastic theory, which can be explained by recognizing that the elastic theory assumes the possibility of strains and deformations. However, rigid walls block such deformations, resulting in the application of a mirrored load that effectively doubles the lateral pressure on the wall in the case of rigid and unyielding structures.

Boussinesq's equation for horizontal stress σ_x gives the maximum value when $\mu = 0.5$ (which represents material deforming at constant volume) and is as follows (see Fig. Figure 2. 14a):

$$\sigma_x = \frac{Q}{2\pi}\left(\frac{3x^2z}{R^5} - \frac{1-2\mu}{R(R+z)}\right) = \frac{3Q}{2\pi}\left(\frac{x^2z}{R^5}\right) \; when\; \mu = 0.5 \quad (2.26)$$

Here, Q is the total load. As stated above its value should be doubled for rigid walls (Terzaghi, 1954; Wilun and Starzewski, 1975). Referring to Figure 2. 14b, where m and n are defined, Terzaghi formulated the following equations based on elasticity theory (with μ =0.5) for the maximum pressure distribution on the plane of the concentrated load. These empirical formulas do not necessitate doubling. The maximum horizontal pressure is located along the vertical line closest to the load and is given by the following formula:

$$p_h = \frac{1.77Q}{H^2}\,\frac{m^2n^2}{(m^2+n^2)^3}\;(m > 0.4) \quad (2.27)$$

If m is less than 0.4, the value of m can be set to 0.4 to determine the pressure as follows:

$$p_h = \frac{0.28Q}{H^2}\,\frac{n^2}{(0.16+n^2)^3}\;(m \leq 0.4) \quad (2.28)$$

The horizontal variation of pressure along the length of the wall is described by the following equations (see Figure 2. 14c):

$$p_0 = p_1\, cos(1.1\alpha) \quad (2.29)$$

2.5.3. Line Load (q/m)

Terzaghi (1954) proposed the empirical equations below for a line load (q/meter) with μ =0.5. This formula provides the horizontal pressure distribution at a depth of nH for a load positioned mH away from the wall (as presented in figure Figure 2. 14b). The total pressure can be determined by integrating p_h:

$$p_h = \frac{1.27qm^2n}{H(m^2+n^2)^2}\; when\; m > 0.4 \quad (2.30)$$

$$p_h = \frac{0.203qn}{H(0.16+n^2)^2} \; when\; m \leq 0.4 \qquad (2.31)$$

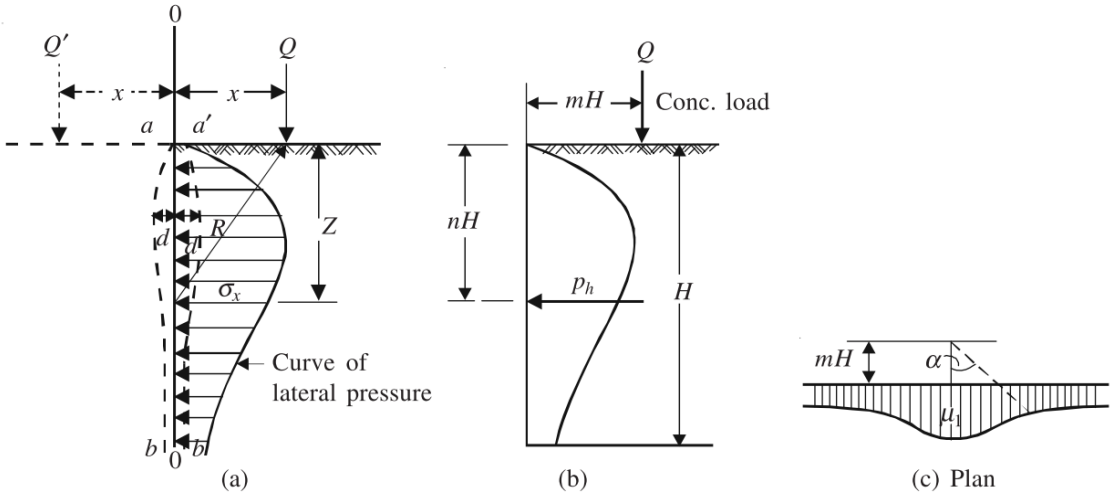

Figure 2. 14. Concentrated load behind retaining walls a) lateral earth pressure doubled due to mirror image effect b) distribution of earth pressure with wall depth c) distribution of earth pressure with wall length

2.5.4. Strip Load

The following empirical formula (Terzaghi and Peck, 1948; Teng, 1995) is recommended for finding the effect of a strip load of finite width running parallel to the rigid wall, as shown in Figure 2. 15.

$$p_h = \frac{2q}{\pi}(\beta + sin\,\beta)\,sin^2\,\alpha + \frac{2q}{\pi}(\beta - sin\,\beta)\,cos^2\,\alpha \qquad (2.32)$$

It is also expressed as:

$$p_h = \frac{2q}{\pi}(\beta - sin\,\beta\,cos\,2\alpha) \qquad (2.33)$$

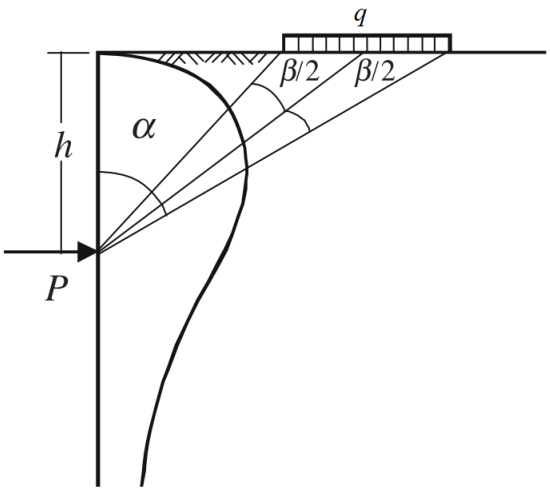

Figure 2. 15. Strip load behind retaining walls

2.6. THREE-DIMENSIONAL EARTH PRESSURE

The existing theories for the calculation of active and passive earth resistance mobilized by a backfill are two-dimensional. These theories does not account for the frictional resistance provided by shear surfaces at the edges of the structure in limiting width retaining walls. Many approaches have been taken to account for the three-dimensional effects by increasing the plane strain resistance to represent the development of a three dimensional failure surface. In this section, several approaches for the estimation of 3D passive earth pressure presented by Brinch Hansen (1966), Ovesen and Stromann (1972), and Soubra and Regenass (2000) are summarized.

2.6.1. Brinch Hansen (1966)

Through a series of small-scale lateral earth pressure tests on granular soils, Ovesen (1964) distinguished between the boundary conditions at the central and end sections of an anchor slab. Based on the experimental findings of Ovesen (1964), Brinch Hansen (1966) put forward an empirical expression (Equation 2.34) for computing the three-dimensional passive resistance, P_u, of rectangular anchor slabs:

$$P_u = M.(K_p - K_a).p_0'.b.h \quad (2.34)$$

M: correction factor to account for 3D effects on passive resistance (Ovesen, 1964)

$$M = 1 + (K_p + K_a)^{0.67}\left(1.1E^4 + \frac{1.6B_b}{1+5(B/h)} + \frac{0.4(K_p+K_a)E^3B^2}{1+0.05(B/h)}\right) \quad (2.35)$$

K_p: passive earth pressure coefficient

K_a: active earth pressure coefficient

$B = 1 - (b/s)^2$

$E = 1 - h/(z+h)$

p_0': effective earth pressure at midheight of anchor block

z, h, b and s parameters are presented in Figure 2. 16.

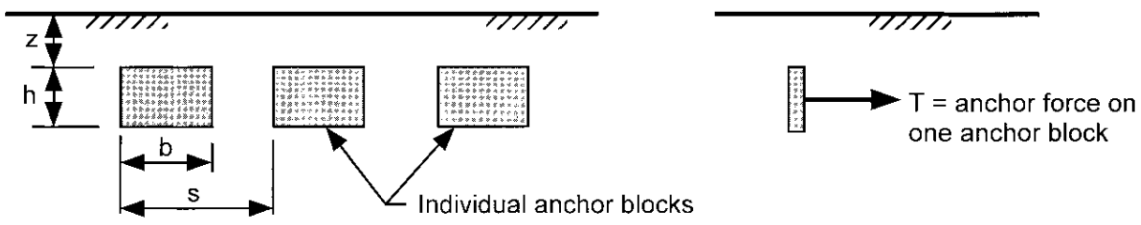

Figure 2. 16. Parameters used in Brinch Hansen (1966) formula

2.6.2. Ovesen and Stromann (1972)

based on the laboratory tests conducted by Ovesen (1964) and Hueckel (1957), as well as the field tests carried out by the U.S. Naval Civil Engineering Laboratory (1966), Ovesen and Stromann (1972) introduced a semi-empirical approach to estimate the ultimate resistance of anchors in sandy soils. The ultimate pullout resistance of a continuous anchor (Figure 2. 17), per unit length of anchor, P_u can be calculated from equation (2.36)

$$P_u = \frac{1}{2}H^2(K_p \cos\delta - K_a \cos\varphi) \qquad (2.36)$$

The term $K_p \cos\delta$ can be obtained from Figure 2. 18 using the angle of internal friction φ and $K_p \sin\delta$ from equation (2.37):

$$K_p \sin\delta = \frac{W+0.5H^2K_a \sin\varphi}{0.5H^2} \qquad (2.37)$$

W represents the effective weight per unit length of the anchor slab, while the coefficients for active and passive earth pressures, K_a and ,K_p respectively, are derived under the assumption that δ equals φ. In the case of a continuous strip anchor (see Figure 2. 19a) with a height denoted as B (which is smaller than the depth of embedment, H), the corrected ultimate resistance per unit length is given by:

$$P_{us} = \left(\frac{C_{ov}+1}{C_{ov}+\frac{H}{B}}\right)P_u \qquad (2.38)$$

Where P_{us} represents the ultimate resistance in the strip case. For dense sand, C_{ov} is equal to 19, while for loose sand, it is equal to 14. In practical applications, anchors are arranged in a row with a center-to-center spacing denoted as S' (refer to Figure 2.19b). The ultimate resistance for each anchor with a length of L is given by:

$$P_u = P_{us}B_e \qquad (2.39)$$

Where B_e the equivalent length and can be obtained from Figure 2. 20.

2.6.3. Soubra and Regenass (2000)

Soubra and Regenass (2000) used the upper-bound method from limit analysis theory (defined in §2.4) to investigate the three-dimensional progression of passive earth pressure within backfills. In order to capture the failure modes of different soil types, they considered three overarching mechanisms denoted as *M1*, *Mn*, and *Mnt* in their analysis. The initial failure mechanism, *M1*, is known as the one-block mechanism, where a solitary rectangular rigid block is employed to represent the horizontal movement of the backfill soil mass. This block is an extension of the 2D Coulomb failure mechanism into three dimensions and is assumed to undergo rigid translation in the direction of

loading. For a more precise depiction of the passive failure mechanism, the second mechanism, *Mn*, is characterized by a radial shear zone consisting of "n" rigid blocks. Similar to the one-block mechanism, these "n" blocks are postulated to translate as rigid bodies with wall deflection. In the third mechanism, *Mnt*, the multi-block approach is further refined by truncating the lateral and lower boundaries of the mechanism using two sections of right circular cones. Figure 2. 21 provides visual representations in both 3D and profile views for the three failure mechanisms, *M1*, *Mn*, and *Mnt*.

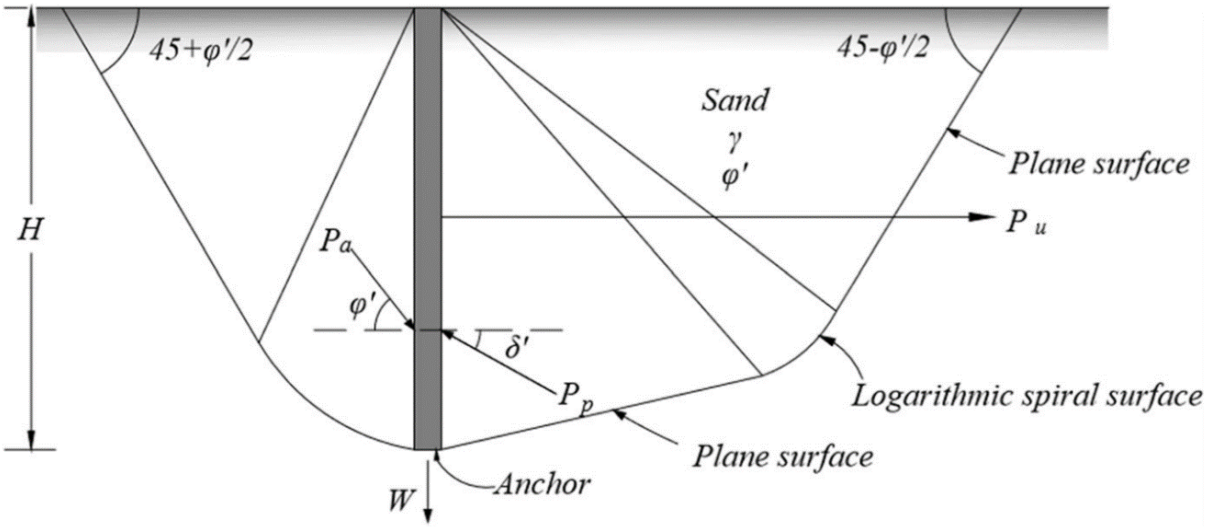

Figure 2. 17. Force components for the analysis of 3D passive earth pressure (Ovesen and Stromann, 1972)

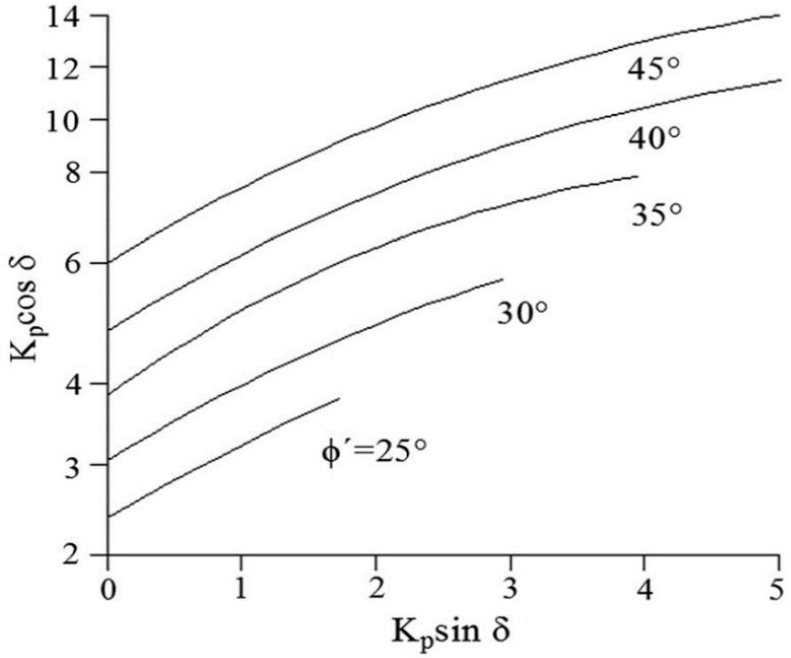

Figure 2. 18. Variation of Kp K_p cos δ with K_p sin δ (Ovesen and Stromann, 1972)

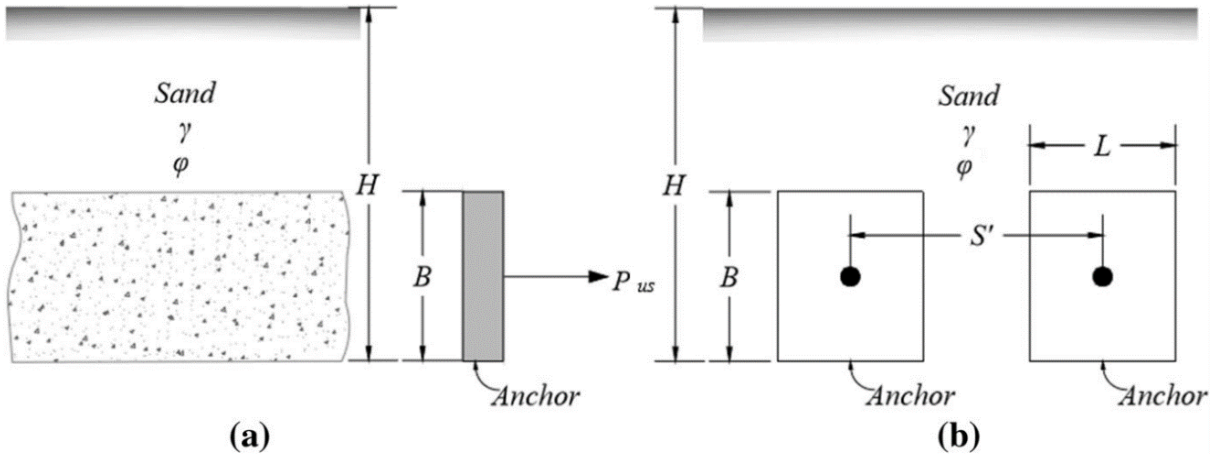

Figure 2. 19. Notations for anchors (Ovesen and Stromann, 1972) a)strip anchors b) row anchors

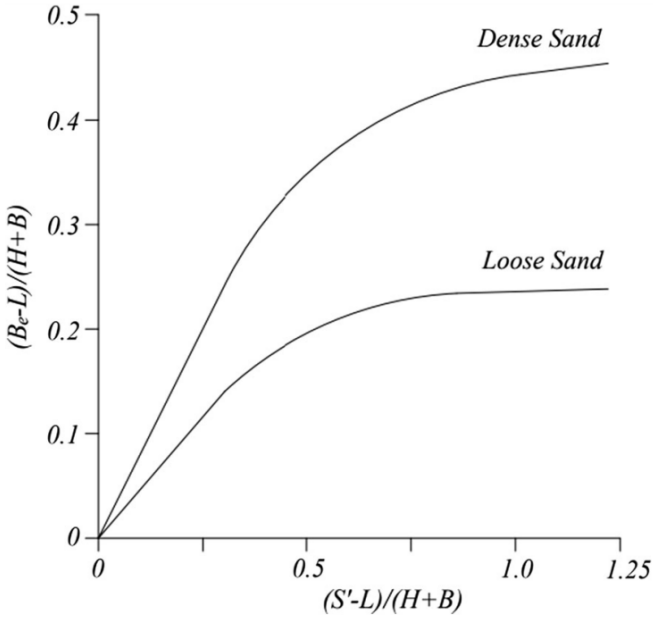

Figure 2. 20. Variation of $(B_e - L)/(H + B)$ *with* $(S' - L)/(H + B)$ *(Ovesen and Stromann, 1972)*

By assuming that energy dissipates at interfaces between the rigid blocks, the soil-wall interface, and the failure surface interface in a truncated multi-block mechanism, a work equation can then be formulated. This equation balances the rate of external work with the rate of internal energy dissipation. Employing this approach leads to the derivation of equation 2.40, which calculates the three-dimensional passive force in a specified backfill. This equation considers the influence of soil weight, cohesion, and surcharge loading through the utilization of dimensionless coefficients, denoted as $K_{p\gamma}$, K_{pc} , and K_{pq} respectively.

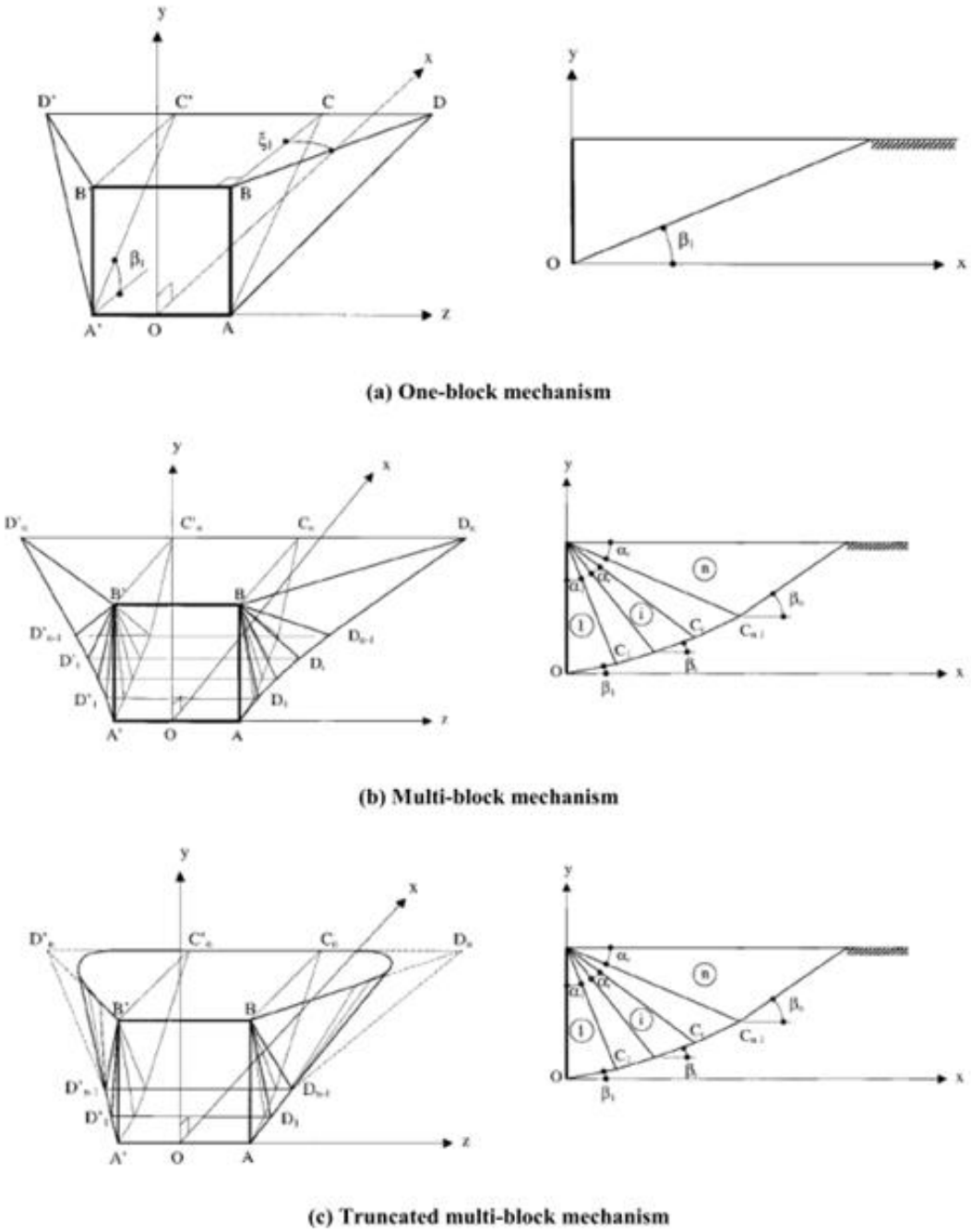

Figure 2. 21. Failure mechanisms by Soubra and Regenass (2000) a) one-block b) multi-block c) truncated multi-block

$$P_u = \left(\frac{1}{2}K_{p\gamma}\gamma H^2 + K_{pc}cH + K_{pq}qH\right)B \qquad (2.40)$$

where γ represents the unit weight of the backfill soil, while c denotes its cohesion. q stands for the surcharge applied on the ground surface. H corresponds to the height of the wall, and B represents the width of the wall. Additionally, $K_{p\gamma}, K_{pc}$ and K_{pq} refer to the coefficients associated with passive earth pressure due to soil weight, cohesion, and surcharge load, respectively. $K_{p\gamma}$ and K_{pq} are extracted from Caquot and Kérisel (1948) tables. The passive earth coefficient associated with cohesion, K_{pc} can be found from the following equation:

$$K_{pc} = \frac{K_{pq} - \left(1/\cos\delta\right)}{\tan\varphi} \qquad (2.41)$$

Where δ and φ are wall and soil friction angles, respectively.

2.6.4. Benmebarek et al. (2008)

Bembebarek et al. (2006) investigated the 3D effect of passive earth pressure through a finite difference numerical analysis, aimed to develop a numerical procedure for the analysis of a rigid retaining wall with horizontal backfill. The analysis covered the evolution of passive earth pressure under the effect of soil weight, cohesion, and uniform surcharge loading. As a result, the passive earth pressure ratio K_{3D}/K_{2D} increases with the increase of b/h ratio where b is the wall with ad h is its height as presented in Figure 2. 22. The ratio value exceeds 2 for small widths retaining wall ($b/h \leq 1$). Benmebarek et al. (2006) also showed, while investigating failure mechanisms, that *Mnt* mechanism proposed by Soubra and Regenass (2000) greatly overestimates the failure surface behind the retaining wall in the case of high soil friction angles (above 30°). The distance of failure surface from the *Mnt* mechanism proposed by Soubra and Regenass (2000) is 6 times the wall penetration for a soil friction angle of 40° and a smooth wall (null soil-wall interface friction angle).

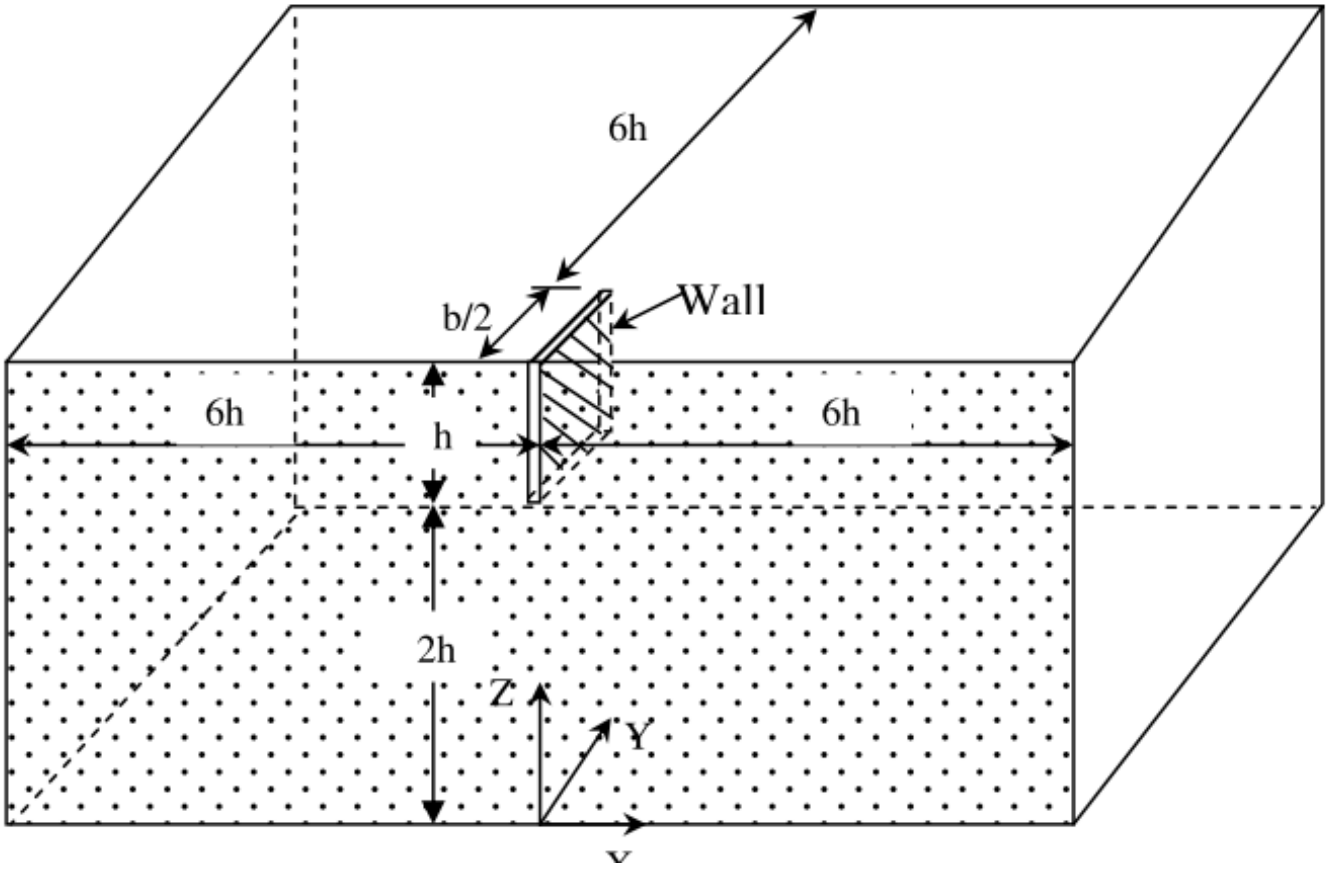

Figure 2. 22. Benmebarek et al. (2006) numerical model

Table 2. 1. Comparison of $K_{p\gamma(3D)}$ from Benmebarek et al. (2006) and Soubra and Regenass (2000)

b/h	φ(°)	Soil-wall interface friction angle (δ/φ)							
		0		1/3		2/3		1	
		Soubra	FLAC3D	Soubra	FLAC3D	Soubra	FLAC3D	Soubra	FLAC3D
0.1	20	–	6.513	–	7.199	–	7.959	–	8.763
	25	–	10.268	–	11.96	–	13.913	–	15.804
	30	–	16.288	–	20.146	–	24.647	–	29.483
	35	–	25.318	–	33.875	–	44.215	–	56.015
	40	–	40.747	–	60.25	–	87.768	–	113.548
0.25	20	5.399	4.547	6.624	5.181	8.301	5.751	10.595	6.350
	25	7.983	6.606	10.528	7.939	14.582	9.304	20.583	10.680
	30	11.886	9.565	17.012	12.335	27.017	15.520	42.510	19.279
	35	20.044	14.018	29.026	19.633	54.775	26.871	95.509	35.078
	40	50.43	20.883	70.281	32.384	140.561	49.834	240.815	65.895
0.5	20	3.726	3.391	4.538	3.896	5.629	4.378	6.994	4.814
	25	5.229	4.666	6.849	5.680	9.379	6.756	12.776	7.913
	30	7.443	6.502	10.604	8.372	16.634	10.626	25.085	13.108
	35	11.984	9.080	17.354	12.798	32.487	17.642	54.064	23.645
	40	28.594	13.101	40.954	20.281	79.700	31.961	131.753	45.457
1	20	2.887	2.770	3.487	3.180	4.279	3.583	5.139	4.010
	25	3.850	3.639	5.001	4.356	6.760	5.192	8.798	6.159
	30	5.221	4.875	7.391	6.275	11.418	7.910	16.273	9.796
	35	7.954	6.584	11.518	9.140	21.308	12.561	33.202	16.647
	40	17.676	9.199	25.317	14.208	49.269	22.057	77.015	32.698
2	20	2.466	2.459	2.956	2.805	3.593	3.164	4.171	3.515
	25	3.159	3.096	4.069	3.735	5.435	4.493	6.746	5.212
	30	4.111	3.952	5.777	5.073	8.787	6.543	11.764	8.082
	35	5.939	5.109	8.600	7.606	15.683	10.109	22.607	13.464
	40	12.218	7.015	17.499	10.957	32.329	17.006	49.371	24.903
5	20	2.211	2.262	2.633	2.568	3.133	2.876	3.561	3.194
	25	2.743	2.797	3.505	3.314	4.542	3.957	5.456	4.536
	30	3.444	3.489	4.801	4.470	6.965	5.731	8.948	6.812
	35	4.730	4.459	6.849	6.13	11.519	8.350	16.035	10.885
	40	8.942	5.80	12.808	8.80	21.145	13.28	32.361	19.602
10	20	2.125	2.103	2.524	2.480	2.954	2.793	3.348	3.102
	25	2.604	2.512	3.315	3.181	4.178	3.821	5.004	4.412
	30	3.222	3.218	4.473	4.275	6.209	5.610	7.958	6.751
	35	4.327	4.030	6.266	5.773	9.87	7.913	13.730	10.675
	40	7.851	5.095	11.244	8.105	17.226	12.331	26.424	18.108

However, the numerical analysis by Benmebarek et al. (2006) proves well that the surface failure in plan view from the front of the wall does not exceed 2.5 times of the wall penetration, which matches well with previous experimental results (Weissenbach, 1961; Belabdelouhab, 1988; Meksaouine, 1993; Duncan and Mokwa, 2001).

Benmebarek et al. (2006) suggested tables for the computed values of three-dimensional passive earth pressure coefficients due to soil weight, surcharge loads and cohesion ($K_{p\gamma}, K_{pc}$ and K_{pq}) which include a comparison between the previous 3D results; $K_{p\gamma}$ and K_{pq} from Soubra and Regenass (2000) and K_{pc} from the theorem of corresponding state by Caquot and Kérisel (1948). Comparison results are presented in Table 2. 1, Table 2. 2 and Table 2. 3. The results given by the upper-bound solution in the framework of limit analysis presented by Soubra and Regenass (2000) seem to greatly overestimate the three dimensional passive earth pressure coefficients due to soil weight and surcharge

loading. Tables also proves that for the case of $b/h = 0$, 3D passive earth pressure coefficients are almost equal to the 2D ones from Caquot and Kérisel (1948), with a difference not exceeding 15%, which makes the three dimensional effect neglected starting from this width of the retaining wall.

Table 2. 2. Comparison of $K_{pq(3D)}$ from Benmebarek et al. (2006) and Soubra and Regenass (2000)

b/h	φ(°)	Soil-wall interface friction angle (δ/φ)							
		0		1/3		2/3		1	
		Soubra	FLAC3D	Soubra	FLAC3D	Soubra	FLAC3D	Soubra	FLAC3D
0.1	20	–	7.618	–	8.433	–	9.355	–	9.998
	25	–	12.443	–	14.343	–	16.327	–	18.388
	30	–	20.124	–	24.710	–	29.989	–	34.697
	35	–	32.526	–	42.960	–	55.149	–	67.880
	40	–	53.209	–	76.927	–	113.205	–	144.561
0.25	20	7.068	5.406	8.704	6.094	10.960	6.741	13.015	7.454
	25	10.736	8.080	14.202	9.647	19.770	11.278	24.817	12.851
	30	16.329	12.038	23.415	15.390	37.382	19.100	49.352	22.521
	35	28.104	17.858	40.698	24.897	77.039	33.391	104.684	42.628
	40	72.265	27.545	103.502	42.529	170.861	63.243	243.616	82.450
0.5	20	4.563	3.915	5.583	4.503	6.967	5.044	8.057	5.552
	25	6.606	5.534	8.690	6.706	11.984	7.869	14.599	9.019
	30	9.664	7.845	13.810	10.175	21.829	12.717	27.909	15.483
	35	16.014	11.190	23.190	15.797	43.615	21.305	57.371	27.996
	40	39.512	16.315	56.591	25.781	91.492	38.783	130.190	55.271
1	20	3.307	3.041	4.014	3.520	4.956	3.946	5.543	4.328
	25	4.540	4.098	5.926	4.977	8.073	5.857	9.445	6.756
	30	6.332	5.566	8.999	7.229	13.951	9.052	17.124	11.023
	35	9.969	7.634	14.436	10.765	25.670	14.608	33.627	18.823
	40	23.136	10.865	33.136	16.930	51.724	25.674	73.351	35.803
2	20	2.677	2.578	3.223	2.971	3.848	3.324	4.256	3.622
	25	3.505	3.329	4.536	4.046	5.902	4.754	6.819	5.398
	30	4.666	4.335	6.585	5.634	9.562	7.061	11.656	8.435
	35	6.946	5.769	10.059	8.090	16.622	10.971	21.638	14.056
	40	14.947	7.869	21.408	12.294	31.723	18.396	44.748	25.165
5	20	2.296	2.302	2.741	2.635	3.148	2.926	3.453	3.155
	25	2.882	2.872	3.694	3.461	4.533	4.029	5.189	4.510
	30	3.666	3.619	5.127	4.643	6.865	5.729	8.277	6.734
	35	5.133	4.609	7.433	6.358	11.077	8.556	14.269	10.690
	40	10.034	6.081	13.923	9.280	19.515	13.652	27.268	17.726
10	20	2.168	2.208	2.577	2.519	2.906	2.794	3.173	3.008
	25	2.673	2.717	3.410	3.266	4.060	3.796	4.620	4.228
	30	3.333	3.377	4.637	4.305	5.924	5.330	7.100	6.201
	35	4.528	4.132	6.558	5.833	9.155	7.821	11.708	9.565
	40	8.263	5.146	10.838	8.322	15.303	12.253	21.219	15.231

Table 2. 3. Comparison of $K_{p\gamma(3D)}$ from Benmebarek et al. (2006) and theorem of corresponding states solutions (Equation 2.41)

b/h	φ(°)	Soil-wall interface friction angle (δ/φ)							
		0		1/3		2/3		1	
		TCS	FLAC3D	TCS	FLAC3D	TCS	FLAC3D	TCS	FLAC3D
0.1	20	18.183	18.014	20.403	19.874	22.879	22.791	24.546	24.183
	25	24.54	24.129	28.591	28.076	32.775	32.455	37.067	36.574
	30	33.124	33.068	41.041	40.405	50.101	49.797	58.099	57.306
	35	45.024	44.913	59.893	59.210	77.203	76.136	95.196	94.084
	40	62.220	62.138	90.457	90.163	133.584	129.063	170.732	170.014
0.25	20	12.105	11.997	13.977	13.594	15.697	15.055	17.556	16.878
	25	15.183	15.101	18.521	18.053	21.947	21.315	25.193	24.523
	30	19.118	19.115	24.898	24.358	31.240	30.360	37.009	36.655
	35	24.076	24.056	34.097	33.506	46.130	45.043	59.134	58.544
	40	31.635	31.665	49.461	48.855	74.039	72.986	96.708	96.605
0.5	20	8.009	8.003	9.606	9.188	11.035	10.587	12.330	11.909
	25	9.723	9.701	12.214	11.756	14.636	13.994	16.975	16.316
	30	11.856	11.858	15.865	15.305	20.184	19.426	24.818	23.976
	35	14.552	14.582	21.101	20.380	28.870	27.760	38.238	37.433
	40	18.252	18.023	29.501	28.978	44.888	44.010	64.316	63.607
1	20	5.608	5.584	6.905	6.655	8.018	7.754	8.967	8.626
	25	6.644	6.591	8.506	8.030	10.322	9.903	12.122	11.710
	30	7.909	7.824	10.763	10.245	13.836	13.261	17.093	16.410
	35	9.474	9.467	13.915	13.330	19.306	18.464	25.138	24.766
	40	11.757	11.720	18.952	18.395	29.265	28.292	41.114	41.045
2	20	4.336	4.312	5.397	5.157	6.309	5.710	7.028	6.710
	25	4.995	4.963	6.509	6.259	7.956	7.294	9.210	8.776
	30	5.777	5.772	8.000	7.738	10.387	9.896	12.610	12.130
	35	6.811	6.798	10.095	9.678	14.112	13.461	18.330	17.823
	40	8.186	8.166	13.427	12.987	20.591	19.780	28.436	28.692
5	20	3.577	3.55	4.473	4.283	5.216	5.018	5.744	5.513
	25	4.015	3.990	5.255	5.023	6.402	6.116	7.306	6.986
	30	4.536	4.524	6.283	5.991	8.080	7.699	9.664	9.364
	35	5.154	5.174	7.622	7.315	10.663	10.167	13.523	13.234
	40	6.056	6.031	9.835	9.438	14.937	14.467	19.570	20.204
10	20	3.319	3.305	4.155	3.985	4.853	4.654	5.341	5.091
	25	3.682	3.674	4.836	4.757	5.902	5.666	6.701	6.396
	30	4.117	4.109	5.698	5.425	7.389	7.084	8.741	8.531
	35	4.473	4.266	6.872	6.575	9.614	9.223	11.916	11.831
	40	4.941	4.721	8.693	8.324	13.270	12.806	16.597	16.478

2.7. CONCLUSION

This chapter described the different types of lateral earth pressure; earth pressure at rest, which represent the lateral earth pressure under a stable ground where zero strain conditions are assumed. Earth pressure at rest can be estimated through many known methods; Terzaghi's (1923) equations (2.3), Jaky (1944) from equation (2.4) for normally consolidated soils, Meyerholf (1976) and Mayne & Kulhawy (1982) from equations (2.5) and (2.6), respectively for over-consolidated soil. Other categories of lateral earth pressure are active and passive earth pressure, which describe the load

behind a backfill when the retaining structure is push away (active) or toward (passive) the backfill. Coulomb's (1776) and Rankine's (1857) methods are the most commonly used for the evaluation of active and passive earth pressures. However, there exist many other analytical methods based on limit equilibrium method, slip line method or limit analysis theory. Effect of surcharge loading on lateral earth pressure was also described through this chapter, as well as its different types, which can be summarized in uniform surcharge loads, concentrated load, line load and strip load. Finally, the chapter explained the three-dimensional effect of lateral earth pressure and the different existing theories for evaluating passive earth pressure of limited width structures.

Chapter III

NUMERICAL MODELING

3.1. INTRODUCTION

Chapter II presented the various analytical methods for the determination of active and passive earth pressures. Most of them are approximated methods. Numerical modeling provides exact solutions for many geotechnical issues at the cost of much more complex and time-consuming procedures. This chapter presents an overview on numerical modeling. It should be noted, that only general concepts for numerical analysis are described. Deep mathematical, physical and computational background of the methods are not explained. A multitude of textbooks and technical literature on numerical modeling is available for this purpose, but even an abridgment would go beyond the scope of this thesis. Next, the different available numerical concepts for solving various geotechnical problems will be presented, although the background will be kept simple. A description of the two geotechnical numerical modeling software in two and three dimensions –FLAC and FLAC3D- used in the analysis will be added, in addition to the existing types of elements and interface basics in numerical modeling. Following, the two constitutive models implemented to describe the soil behavior in chapter IV and V will be detailed.

3.2. OVERVIEW ON NUMERICAL MODELING

In contrast to analytical methods, numerical modeling not only accounts for the potential for deformation but also captures the actual process of deformation. Given the array of methods tailored to specific domains and the strides made in technical and computational capabilities in recent decades, numerical modeling theoretically provides a virtually limitless range of possibilities for performing deformation analyses.

Over the years, the progression of numerical modeling has been accompanied by significant breakthroughs in various scientific domains, including continuum mechanics, rheology, and computer science during the 1960s and 1970s. Presently, numerical modeling is integrated with disciplines like thermodynamics, hydraulics, seismology, and numerous other physical sub-fields. This integration renders it an exceptionally potent instrument for the planning, monitoring, and maintenance of both natural and man-made structures.

In comparison to analytical methods, which often involve numerous simplifications and assumptions, numerical methods handle a much broader range of specifications and physical conditions relevant to the structure being studied:

- Structural heterogeneity, including layering, discontinuities, and complex boundary conditions.
- Property heterogeneity, encompassing location- and/or time-dependent variations, as well as anisotropy.
- Varying slope geometries, whether regular or irregular, and progressive changes in geometry.
- Diverse material behaviors, such as linear-elastic, (visco)-elasto-plastic, strain-softening, and non-linear.
- Consideration of water saturation levels, involving ground water levels, pore water pressure distribution, and fluctuations.
- Evaluation of stress states before, during, and after deformation, encompassing both static and dynamic analyses.
- Accounting for external solicitations, including cyclic and impulsive loading.
- Tracking developments over time.
- Addressing data uncertainties.
- Evaluating site-specific effects.
- Accounting for coupled processes, such as pore water pressure increase following seismic loading.
- Incorporating effects of construction, excavation, and overloading.
- Accounting for soil-structure interaction.

However, a significant challenge in numerical modeling lies in the fact that the accuracy of the output is heavily reliant on the quality and quantity of the input data. This necessitates substantial efforts in acquiring high-quality data, conducting extensive laboratory testing and material characterization, carefully selecting input motions (particularly in ground response analysis), and interpreting results (JIBSON, 2011). Furthermore, the inclusion of the aforementioned properties, conditions, and physical principles results in highly complex calculations that can become computationally demanding and time-consuming, especially when dealing with dense datasets. These

computations may occasionally approach their limits in terms of time constraints or hardware memory (Domej, 2018).

3.3. INTRODUCTION TO FLAC & FLAC3D PROGRAMS

FLAC, a commercial software developed by the American consulting group ITASCA since 1986, stands out as one of the most potent numerical codes for geotechnical analysis. Thanks to its extensive capabilities in addressing intricate mechanical challenges related to geological materials, it finds extensive application in civil and geotechnical engineering to simulate complex ground responses. Therefore, the software is equally adept at both design and testing purposes. FLAC is an abbreviation for 'Fast Lagrangian Analysis of Continua' that embodies an explicit finite difference methodology (see §3.4.2) for the numerical modeling of geotechnical engineering problems. With the association of exact date, the code creates a numerical image of the location of interest allowing for surveillance, analysis, design of construction measures and the prediction of effects caused by the latter.

During this analysis, both FLAC 2D and 3D software are utilized. Specifically, FLAC (2019) 2D version 8.1 is employed for the two-dimensional analyses outlined in Chapter IV, while FLAC3D (2019) version 6.0 is employed for the three-dimensional studies detailed in Chapter V. FLAC3D builds upon the analysis capabilities of FLAC2D and employs the numerical framework of the two-dimensional program. For simplicity, both will be referred to as FLAC henceforth.

3.4. AVAILABLE NUMERICAL METHODS (CONTINUUM MODELS)

Numerical models, also termed "continuum models," streamline the soil-structure interaction problem by segmenting the soil and any structural components (like a retaining wall) into discrete zones or elements. In each zone or element, the characteristics of the soil or structure are assumed to remain consistent. This simplification of geometry and property fluctuations enables computations to be carried out for each individual zone. With the substantial advancement in computing capabilities, these approaches are gaining popularity in the realm of retaining wall design (Figure 3. 1).

There are three available methods: the finite element method, finite difference methods, and the boundary element method. However, it is worth noting that only the first two are widely employed for retaining wall analyses (Clayont, 2013).

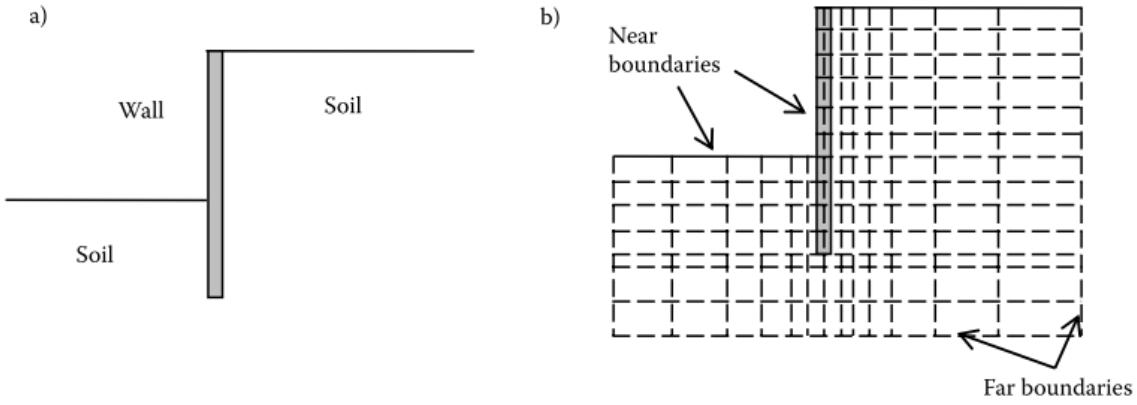

Figure 3. 1. Representation of a retaining wall a) Physical problem b) continuum model

3.4.1. Finite element method

The finite element method (FEM) is a numerical approach utilized to solve the differential equations governing a boundary value problem (Zienkiewicz in 1977). In this method, the region of interest is partitioned into discrete areas or elements, often taking the shape of triangles or rectangles. These elements are defined by node points situated at their vertices, and sometimes along their edges (see Figure 3. 2). Within each element, the behavior is simplified, focusing on a primary parameter of interest (such as displacement) which is assumed to vary in a prescribed manner (e.g., linear). The value of this parameter at any point within the element is determined based on its values at the nodes, using interpolation or shape functions denoted by N, which depend on the element's geometry:

$$\theta = \sum_{i=1}^{i=n} N_i \theta_i \qquad (3.1)$$

where θ represents the specific quantity, and n denotes the total number of nodes. In the analysis of retaining walls, the primary parameter of interest is displacement. By differentiating the shape functions, we obtain expressions for the strain vector ε in relation to the vector of nodal displacements, denoted *a*:

$$\varepsilon = Ba \qquad (3.2)$$

The value of B is contingent on the geometry of the element. Following this, an applicable constitutive relationship can be utilized to establish the correlation between stresses (σ) and strains (ε) within the element:

$$\sigma = D\varepsilon = DBa \qquad (3.3)$$

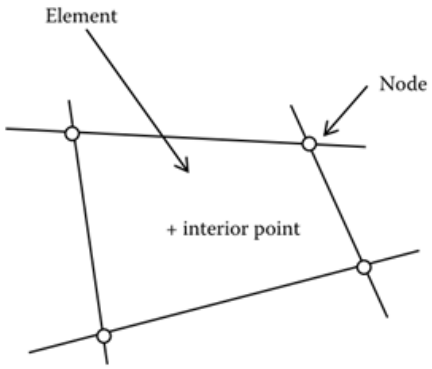

Figure 3. 2Finite element (Clayton, 1993)

where D is contingent on the material's properties. By employing virtual work principles, we can derive relationships for the stiffness of the element, connecting applied loads (F) to the resultant displacements at the nodes:

$$F = Ka = \int \left(B^T DBd(vol)\right) a \qquad (3.4)$$

At the end, the global stiffness matrix is constructed by combining the contributions from each individual element. Upon applying boundary conditions, which may include known forces and prescribed displacements, the global system of equations is solved to determine the unknown nodal displacements. Subsequently, internal strains within any given element can be computed from these displacements (as per equation 3.2), and then stresses can be determined using the constitutive relationships (as indicated in equation 3.3). For an in-depth exploration of the Finite Element Method (FEM) as it relates to geotechnical engineering as a whole, and specifically to earth retaining structures (Potts and Zdravkovic from 1999 and 2001).

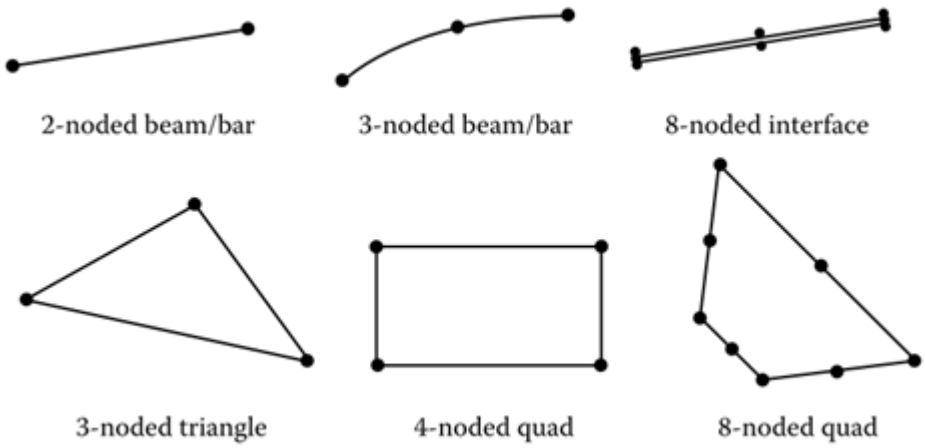

Figure 3. 3 Examples of two-dimensional finite elements

For problems in two dimensions, quadrilateral elements are the most commonly employed, followed by triangular elements. In some cases, a combination of both is used for specific geometries (see Figure 3. 3). Additionally, one-dimensional line elements may be added for relatively thin material zones that possess specific tensile, flexural, or interfacial properties. If a three-dimensional model is needed, the equivalent of 'bricks' and tetrahedral elements can be utilized, alongside two-dimensional elements for the thin zones. In situations where it's necessary to define the shear resistance between two parts of the mesh or to prevent the development of tensile stresses, special 'interface' elements may be required.

The element's order is determined by the interpolation functions it utilizes and is typically denoted by the number of nodes it possesses. Triangles with three nodes and quadrilaterals with four nodes can accurately represent a linear change in the primary quantity of interest. On the other hand, triangles with six nodes and quadrilaterals with eight nodes have the capacity to depict a quadratic variation. In the context of force-displacement, the strain variation that can be accommodated is one order lower than that in displacement. This is why the three-noded triangle is referred to as a constant strain triangle, and the eight-noded quadrilateral is known as a linear strain quadrilateral.

Another term employed in the realm of finite elements is "degrees of freedom" (d.o.f.), which signifies the count of independent values linked to the principal quantity of interest. A six-noded triangle possesses twelve degrees of freedom because each node encompasses two components of displacement (a vector quantity) in both the x and y directions. Some specialized elements may feature an extra degree of freedom at certain nodes. For instance, a one-dimensional beam element, in addition to x and y displacements, will have an extra rotational (θ) degree of freedom at each end. In another specialized element utilized in what's known as coupled-consolidation analysis, there exists an additional degree of freedom related to excess head (a scalar quantity) at the vertex nodes. This enables the superimposition of seepage onto a standard force-displacement analysis (Clayton, 2013).

3.4.2. Finite difference method

In the Finite Difference Method (FDM), materials are depicted as zones delimited by a grid of points. The user designs this grid to conform to the geometry of the physical problem being modeled. Each zone adheres to a predetermined pattern of stress-strain behavior (such as elastic or plastic). When yielding occurs, the grid undergoes distortion to update the positions of its points. The explicit FDM, as outlined by Cundall in 1976, employs the fundamental equations of motion and a time-stepping procedure to incrementally compute the accelerations (and subsequently, through integration, the velocities and displacements) of the zone mass, which is concentrated at the grid points. The resulting strains are then utilized in a constitutive law to ascertain the corresponding increment in stress for the zone. These stress increments are then aggregated to derive a new unbalanced force, and

this calculation cycle repeats. The dynamic response of the system is numerically damped, allowing the problem to reach equilibrium and achieve the desired solution with the progression of time steps. It's important to note that in this application of the finite difference method, time steps are employed to attain a solution rather than to model time-dependent material behavior.

Often it is necessary in a model to represent planes on which sliding or separation can occur. FLAC provides interfaces that are characterized by Coulomb sliding and/or tensile and shear bonding. A schematic of the FLAC interface element and the inclusive parameters is presented in Figure 3. 4. The element allows permanent separation and slip between the two separated materials, as controlled by the parameters tensile strength T and slider S, respectively. An interface is represented as a normal stiffness and a shear stiffness between two planes in contact. The interface constitutive model is defined by a linear Coulomb shear-strength criterion that limits the shear force acting at an interface node, normal and shear stiffnesses, tensile and shear bond strengths, and a dilation angle that causes an increase in effective normal force on the target face after the shear-strength limit is reached. The spring in the tangential direction, the slider and the limit strength represent the Coulomb shear-strength criterion. The spring in the normal direction, the limit strength and dilation represent the normal contact.

When determining the attributes of the interface, such as cohesion, dilatancy, limit traction, and friction, it's customary to assign values equivalent to those of the least resistant material. Estimating the stiffnesses *kn* and *ks* can be a more challenging task. FLAC suggests setting *kn* and *ks* to approximately ten times the equivalent stiffness of the stiffest adjacent zone, which serves as a practical guideline. The perceived stiffness (measured in stress-per-distance units) of a zone in the normal direction is then calculated as follows:

$$max\left[\frac{(K+\frac{4}{3}G)}{\Delta Z_{min}}\right] \qquad (3.5)$$

K and G represent the bulk modulus and shear modulus, respectively, while ΔZ_{min} denotes the smallest dimension in the normal direction (Figure 3. 5). This suggestion ensures that the calculation times are not unduly prolonged when assessing an interface. The Coulomb shear-strength criterion constrains the shear force according to the subsequent relationship:

$$F_{s\,max} = cA + tan\,\varphi(F_n - pA) \qquad (3.6)$$

here, A denotes the representative area linked with the interface node; p represents the pore pressure (interpolated from the target face); φ stands for the friction angle of the interface surfaces; and c denotes the cohesion along the interface. If the criterion is met (i.e., if $|F_s| \geq F_{s\,max}$), it indicates that sliding is taking place. The normal and shear forces describing the elastic response of the interface are computed at the time of calculation ($t + \Delta t$) using the following relationships:

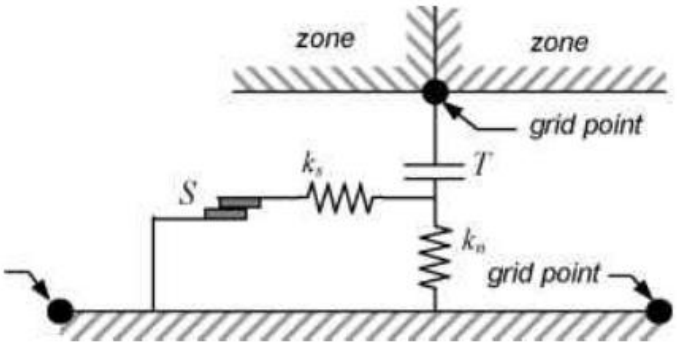

Figure 3. 4. Components of FLAC interface element

$$F_n^{(t+\Delta t)} = k_n u_n A + \sigma_N A \qquad (3.7)$$

$$F_{si}^{(t+\Delta t)} = k_{si}^{(t)} + k_s \Delta u_{si}^{(t+\frac{1}{2}\Delta t)} A + \sigma_{si} A \qquad (3.8)$$

$F_n^{(t+\Delta t)}$is the normal force at time $(t + \Delta t)$, $F_{si}^{(t+\Delta t)}$ is the shear force vector at time $(t + \Delta t)$, u_n is the absolute normal penetration of the interface node into the target face; $\Delta u_{si}^{(t+\frac{1}{2}\Delta t)}$ is the incremental relative shear displacement vector; σ_N σ n is the additional normal stress added due to interface stress initialization; σ_{si} is the additional shear stress vector due to interface stress initialization ; and A is the representative area associated with the interface node.

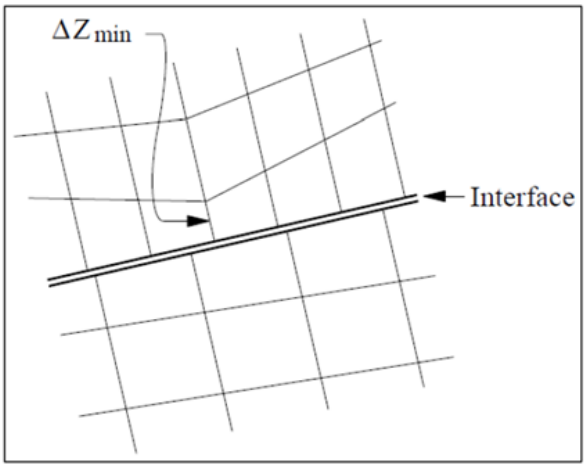

Figure 3. 5. Zone dimensions used in stiffness calculation (Itasca, 2013)

3.4.3. Discrete element method

The discrete element method (DEM) falls within the general classification of discontinuous analysis techniques. The method was developed by Cundall in the early 1960s for numerical research into the sliding of earth and rock masses. It is now presented in the commercial codes UDEC (Universal Distinct Element Code). Discrete element method models the materials with separate particles. This method is suitable not only to simulate the behavior of geomaterials but also the

behavior of any particulate matter like powders or grains. Soil and rock behave in a rather complicated manner due to their distinct properties. It is sometimes necessary to model the discontinuum behavior of these materials as in the case of soil liquefaction or in simulating the post-failure mechanism of slopes. Separation may take place on the slip surface or elsewhere with the sliding mass following failure and it can affect the reliability of analyses. Such a model can be properly handled by DEM simulations.

DEM methods can be divided into two categories: explicit ones and implicit ones. There exist two kinds of approaches for the explicit DEM methods, namely the dynamic relaxation method and the static relaxation method. The static relaxation method uses equations of equilibrium to obtain the displacement of particles at the next time step. However, for dynamic problems, the static relaxation method cannot be used. Dynamic relaxation based DEM use Newton's second law to get the displacement of particles at the next time step, and it is generally called the distinct element method. The distinct element method can simulate the complex mechanical interactions of a discontinuous system.

The Discrete Element Method allows for the explicit representation of individual particles, enabling a detailed understanding of particle-level interactions and phenomena such as particle rearrangement, rotation, and breakage. DEM simulations can be validated and calibrated using experimental data, enhancing confidence in the predictive capabilities of the method for specific geotechnical applications. On the other hand, DEM simulations can be computationally intensive, especially for large-scale problems with a large number of particles or complex geometries, requiring significant computational resources and time. Furthermore, modeling particle-scale interactions accurately may require detailed knowledge of particle properties such as size, shape, and material properties, which can be challenging to obtain experimentally and computationally.

3.4.4. Boundary element method

The Boundary Element Method (BEM) constitutes another numerical approach for tackling boundary value problems governed by differential equations (Banerjee and Butterfield, 1981). The key distinction between this method and FEM/FDM lies in the conversion of the differential equations into equivalent integral equations before solving. Typically, these integral equations establish a connection between boundary stresses and boundary displacements. Consequently, this method is especially well-suited for problems where the ratio of surface area to volume is low, as often seen in many three-dimensional foundation problems. BEM necessitates the discretization of only the boundary of the domain into segments or elements, without the need for interior discretization (i.e., focusing on surface rather than volume discretization). This effectively reduces the number of physical dimensions to be

considered by one, resulting in a smaller system of equations and significant computational time savings (typically about 10 times faster than FEM for the same problem).

This simplification is facilitated by leveraging a fundamental or singular solution, which provides the stresses and displacements at point B as a result of a load or displacement applied at point A. In geotechnical applications, Mindlin's (1936) solution for a point load within a semi-infinite solid, or Boussinesq's (1885) solution for a point load acting on the surface of a half-space, are commonly applied. By spreading the fundamental solution across the domain's surface, a comprehensive solution is derived in terms of a boundary density function. To establish boundary conditions, the density function must adhere to an integral equation on the boundary. The approach involves first determining the solution at the boundary and then extending it to points within the region using this boundary-derived solution.

While the computational efficiency of BEM in numerous problems is undeniable, it doesn't possess the robust physical and intuitive appeal of FEM or FDM. It is often overshadowed by complex mathematical formulations and notation. The advantage of BEM is significantly diminished in cases where there is substantial material non-homogeneity, as each distinct zone delimited by boundary elements must be homogeneous. This is one reason why BEM has found greater popularity in rock mechanics applications compared to soil mechanics. There are very few documented applications in retaining wall and excavation analysis. Therefore, further discussion will be focused exclusively on the FEM and FDM.

3.5. CONSTITUTIVE MODELS

Finite Element (FE) and Finite Difference (FD) software packages typically provide users with a variety of constitutive models. These models can span from basic elastic representations to advanced elasto-plastic models with strain-hardening/softening behavior. The decision on which model to choose is intimately tied to the selection of relevant soil parameters. The challenge for the designer boils down to determining how much of this complexity is necessary to attain a result that is both realistic and suitable for the intended purpose. Additionally, if such complexity is indeed needed, can the required parameters be measured during site investigation, or can they be reasonably estimated afterwards with sufficient accuracy?. Many constitutive models are implemented in FLAC software. Two among them will be used to simulate the soil behavior in the present analysis. Mohr-coulomb model which describes an elastic perfectly plastic behavior, and Plastic-Hardening which describes a hyperbolic behavior.

3.5.1. Mohr-Coulomb Model (linear elastic perfectly plastic model)

The Mohr-Coulomb constitutive model is widely embraced for assessing yielding in soils and rocks due to its straightforwardness and reasonably accurate predictions. It posits a linear correlation between the normal stress and shear stress at the point of failure, as expressed in Equation 3.9:

$$|\tau| = c + \sigma_n \tan\varphi \qquad (3.9)$$

σ_n and τ correspond respectively to the normal and shear stresses on a given surface. c is the cohesion and φ is the internal friction angle, as illustrated in Figure 3. 6.

Taking tensile stresses as positive, equation (3.9) can be written as (3.10) under plane strain condition:

$$\sqrt{\frac{(\sigma_x-\sigma_y)^2}{4} + \tau_{xy}^2} \leq c\cos\varphi \qquad (3.10)$$

Under three-dimensional condition, (3.9) can be written in terms of the principal stresses:

$$\sigma_1 - a\sigma_3 \leq k \qquad (3.11)$$

where

$$a = \frac{1-\sin\varphi}{1+\sin\varphi} \qquad (3.12)$$

And

$$k = \frac{2c\cos\varphi}{1+\sin\varphi} \qquad (3.13)$$

In the principal stress space, equation (3.11) is shaped like an irregular hexagonal pyramid as shown in Figure 3. 7.

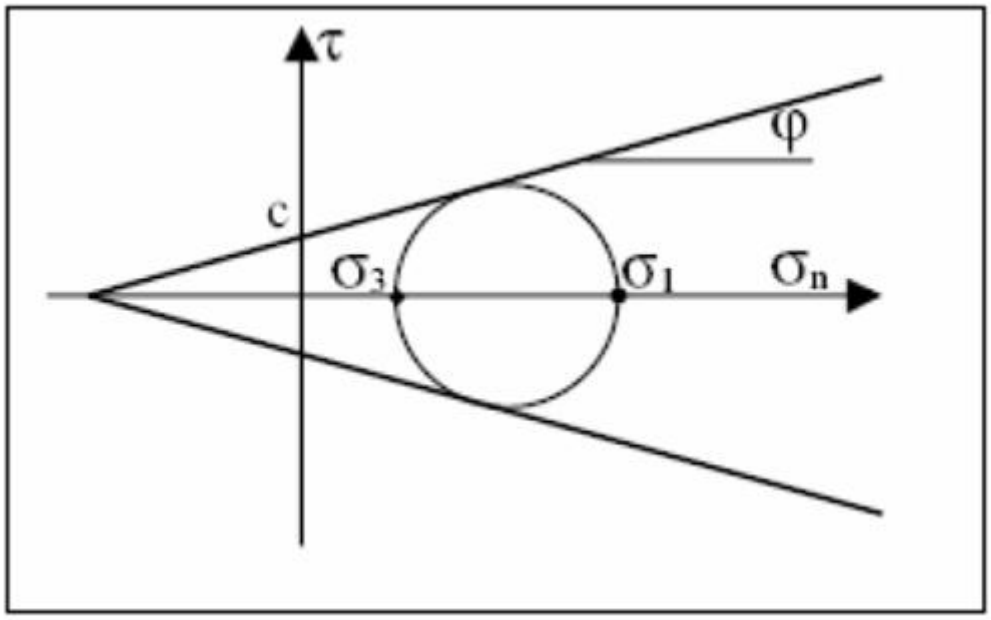

Figure 3. 6. Representation of the Mohr-Coulomb criterion in the Mohr plane

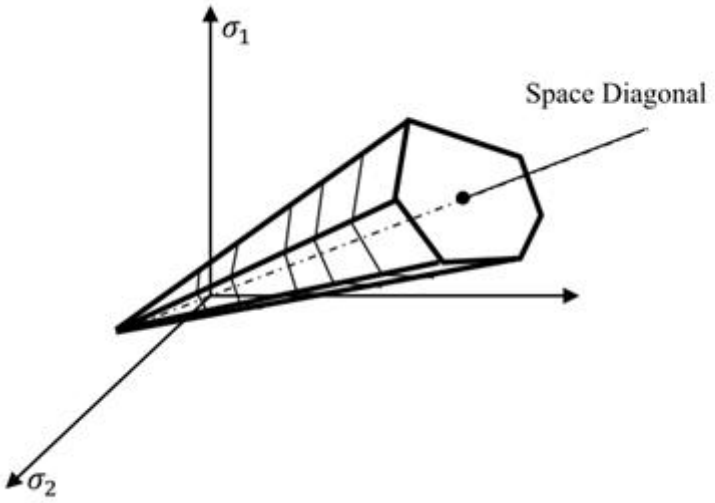

Figure 3. 7. Mohr Coulomb yield criterion in the principal stress space

This constitutive law is characterized by five (5) parameters; two elastic (E, v), and three failure ones (c, φ, ψ) as following:

E: Young's modulus: Also called "Elastic modulus", is defined as the ratio of tensile stress to tensile strain (σ/ε), as defined in Figure 3. 8. The latter is well detailed in §3.5.2.

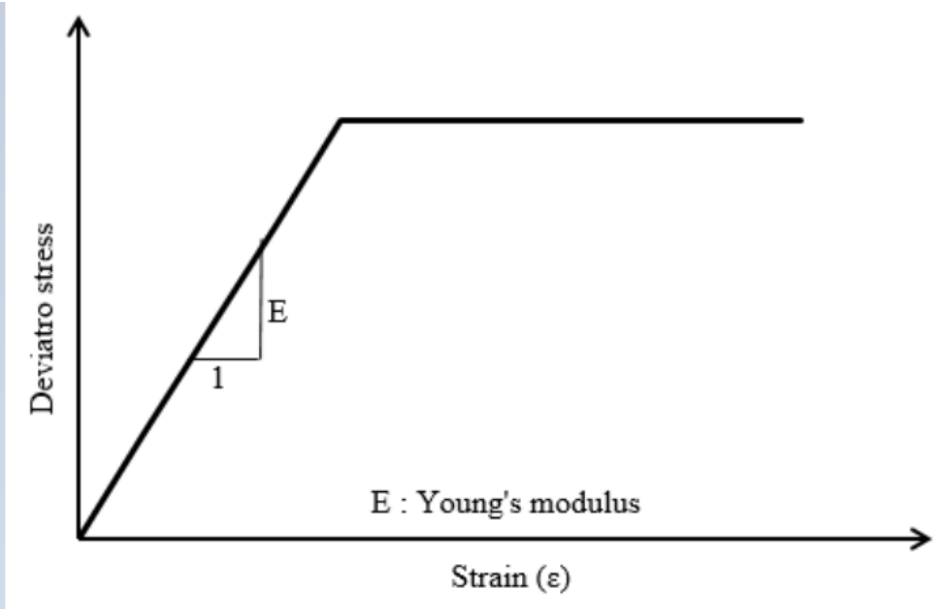

Figure 3. 8. Figure Stress-strain relationship for the Mohr-Coulomb model

v: Poisson coefficient: is the ratio of transversal contraction strain to longitudinal extension strain in the direction of stretching force, defined as:

$$v = -\varepsilon_{trans}/\varepsilon_{long} \qquad (3.14)$$

Elastic parameters (E, v) are fundamental for the determination of the simulated soil behavior. On the other hand, these two can be replaced with bulk (K) and shear (G) modulus. Note that Poisson's ratio is related to Young's modulus (E), bulk modulus (K) and shear modulus G for isotropic solids by the following equations:

$$E = 3K(1 - 2v) \qquad (3.15)$$

$$E = 2G(1 + v) \qquad (3.16)$$

Cohesion (c) and internal friction angle ($\boldsymbol{\varphi}$):

The shear strength of a soil mass is the internal resistance per unit area that the soil mass can offer to resist failure and sliding along any plane inside it. Soil derives its shear strength from two sources:

- Cohesion between particles, which is defined as the shear strength when the compressive stresses are equal to zero.
- Frictional resistance between particles, which is the measure of the shear strength of soils due to friction (Yokoi, 1968).

Mohr rupture theory assumes that failure of materials is due to the critical combination of normal and shear stresses , which describes a curved failure line as illustrated in Figure 3. 9. Nevertheless, most soil mechanics problems assume shear stress on the failure plane as a linear function of the normal stress (Coulomb, 1776). The functional relationship between normal and shear stresses on a failure plane can be expressed by means of the Mohr-Coulomb failure criterion:

$$\tau_f = c + \sigma \tan\varphi \qquad (3.17)$$

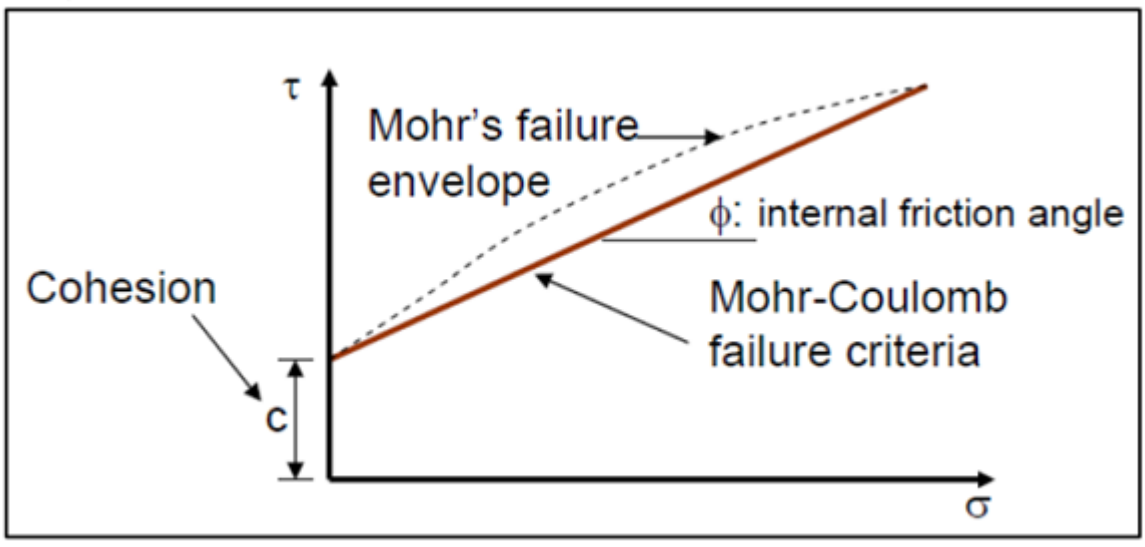

Figure 3. 9. Mohr-Coulomb failure

According to the Mohr-Coulomb failure criterion, shear failure happens when the shear stress on a plane equals the shear strength (τ_f). The orientation of this failure plane (φ) is determined by the major and minor principal planes, illustrated in Figure 3. 10, where σ_1 and σ_3 represent the major and minor effective principal stresses. To ascertain the angle θ and the relationship between σ_1 and σ_3, referred in Figure 3. 10b, which displays Mohr's circle for the stress-state depicted in Figure 3. 10a. If the Mohr circle remains within the envelope, the soil element does not experience failure. As loading progresses, the Mohr circle expands, ultimately leading to failure when it intersects with the envelope (Soekhoe, 2015).

Dilation angle (ψ):

The dilation angle, also known as the dilatancy angle denoted by ψ, governs the increase in volume that occurs during shearing of a material. This expansion arises from the interlocking nature of compacted granular materials, which restricts the freedom of individual grains to move. In cohesive soils with fine grains, the dilatancy angle tends to be minimal, often approximated as $\psi = 0$. Except for heavily overconsolidated layers, clayey soils exhibit little dilatancy ($\psi \approx 0$). The dilatancy of sandy soils is influenced by both density and the internal friction angle. For quartz sands, the magnitude is roughly $\psi \approx \varphi - 30$. However, for φ values below 30 degrees, the dilatancy angle is mostly negligible.

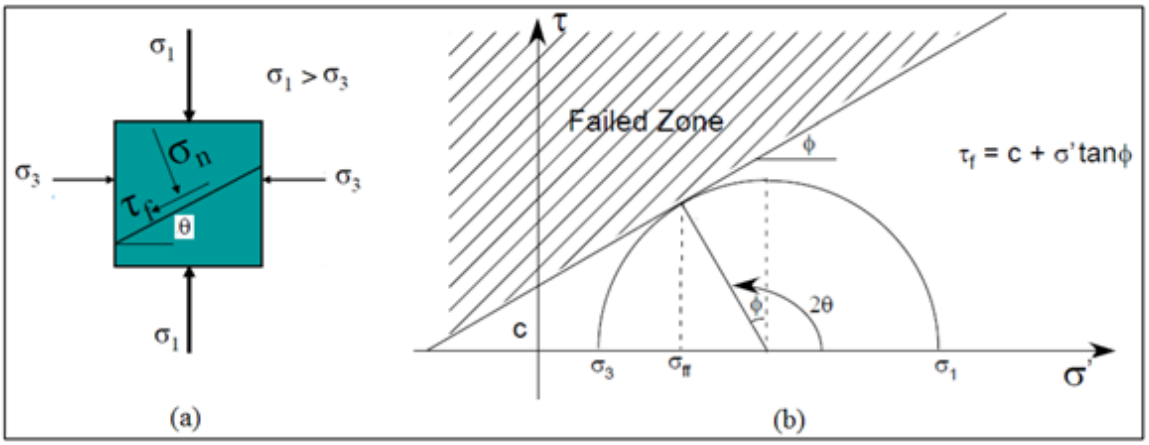

Figure 3. 10. a) Inclination of failure plan in soil with major principal plane b) Mohr's circle and failure envelope

When the friction angle φ and the dilation angle ψ are equal, the flow rule is said to be associated. The dilation angle is usually derived from triaxial tests or shear-box tests. For instance, the theoretical relationship describing dilatancy, derived from the Mohr-Coulomb failure surface, is illustrated in Figure 3. 11 for a triaxial test. The dilation angle is determined by examining the plot of volumetric strain against axial strain. It's important to observe that the initial slope in this plot represents the elastic phase, whereas the slope used to calculate the dilation angle pertains to the plastic phase.

3.5.2. Plastic-Hardening model (hyperbolic model)

The Plastic-Hardening (PH) model is a constitutive model that incorporates mechanisms for both shear and volumetric hardening to accurately simulate soil behavior. When soils are subjected to deviatoric loading, as seen in a conventional drained triaxial test, they typically experience a reduction in stiffness along with irreversible deformation. In many instances, the relationship between deviatoric stress and axial strain, observed in a drained triaxial test, can be approximated by a hyperbolic curve. This characteristic was extensively discussed by Duncan and Chang in their well-known "hyperbolic-soil" model from 1970, which is structured as a non-linear elastic model. The PH model is developed within the framework of hardening plasticity, as presented by Schanz et al. in 1999, which effectively addresses the primary limitations of the original non-linear elastic model formulation, such as the detection of loading/unloading patterns and the absence of a physically meaningful bulk modulus. The main attributes of the PH model encompass:

- Hyperbolic stress-strain relationship during axial drained compression.
- Plastic strain contributing to the mobilization of friction (shear hardening).
- Plastic strain associated with primary compression (volumetric hardening).
- Elastic stiffness that varies with stress following a power law.
- Elastic unloading/reloading behavior relative to the initial loading phase.
- Retention of pre-consolidation stress history.
- Adherence to the Mohr-Coulomb failure criterion.

Necessary parameters for defining a material behavior in FLAC software are secant stiffness (E_{50}^{ref}), initial stiffness (E_{0}^{ref}), unloading-reloading stiffness (E_{ur}^{ref}), tangent stiffness (E_{oed}^{ref}), reference pressure (p^{ref}), failure ration (R_f), exponent for elastic modulus (m), Poisson's ration (v), cohesion (c), internal fraction angle (φ) and dilation angle (ψ).

Since many soil materials exhibit non-linear behavior in the stress-strain diagram from the very beginning of loading, the soil stiffness is described much more accurately by using three different parameters:

- The triaxial loading stiffness or secant modulus E_{50}.
- The triaxial unloading stiffness, E_{ur}.
- The oedometer loading stiffness E_{oed} .
- In soil mechanics, the initial slope is commonly referred to as E_0, while the secant modulus at 50% strength is represented as E_{50}. While materials with a broad linear elastic range may

realistically use E_0, for soil loading scenarios, E_{50} is typically employed. When addressing unloading situations, such as in tunneling or excavations, it becomes necessary to consider E_{ur} instead of E_{50}. In the case of soils, both the unloading modulus (E_{ur}) and the first loading modulus (E_{50}) tend to escalate with increasing confining pressure. Consequently, deeper layers of soil generally exhibit greater stiffness compared to shallower layers. Additionally, the observed stiffness is contingent on the specific stress path followed. Stiffness is notably higher for unloading and reloading compared to primary loading. The stiffness moduli E_0, E_{50}, and E_{ur} are illustrated in the stress-strain diagram presented in Figure 3. 12. The oedometer modulus (E_{oed}) characterizes soil stiffness in scenarios of one-dimensional compression. It is related to Young's modulus in accordance with Hooke's law of isotropic elasticity, taking into account the Poisson's ratio (v):

- $E_{oed} = \frac{(1-v)E}{(1-2v)(1+v)}$ *(3.18)*

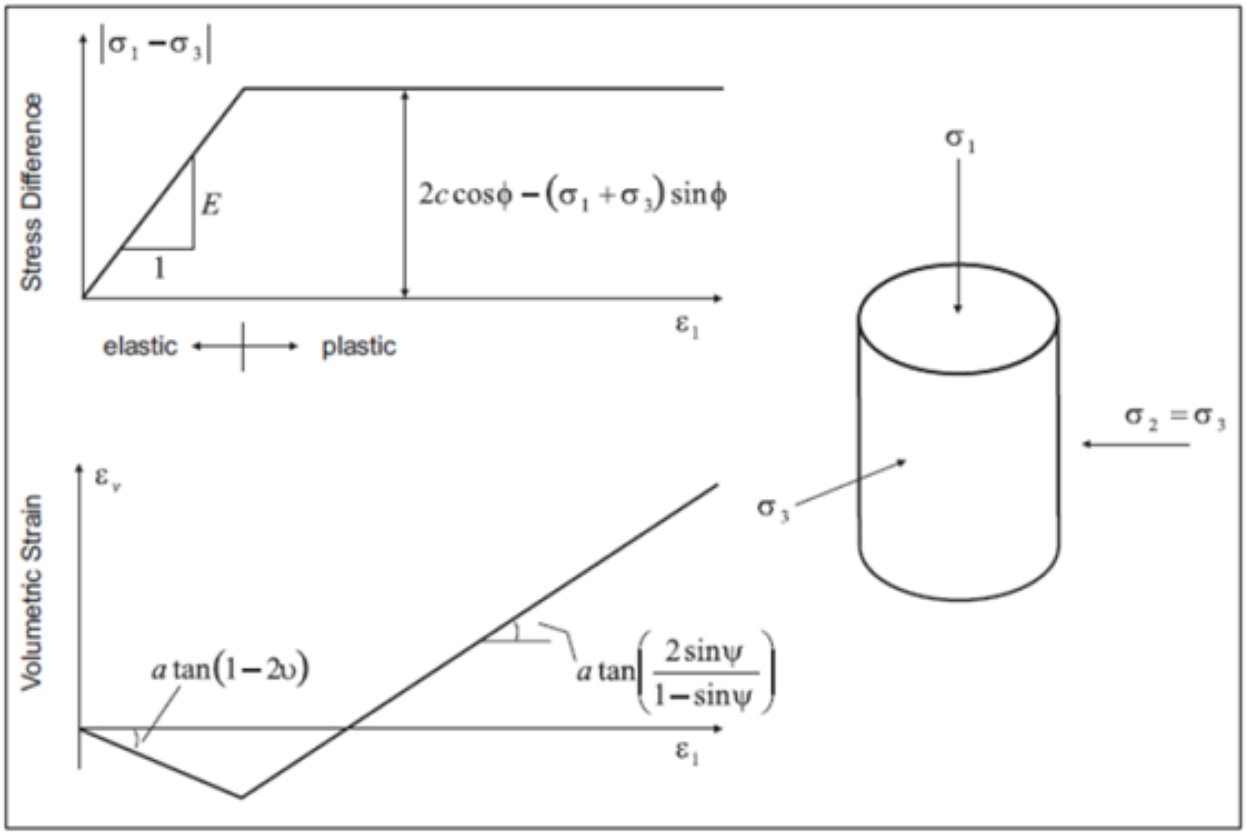

Figure 3. 11. Modeling of dilation angle from the triaxial test (Vermeer and de Borst, 1984)

A reference pressure (p^{ref}) should be defined in FLAC Plastic-Hardening model, based on the unit of stress/pressure adopted in the model. The most highly recommended and commonly used reference pressure is the atmospheric pressure (100 kPa), or any other value compatible to the adopted unit of stress/pressure. The reference unloading-reloading stiffness modulus E_{ur}^{ref} depends at the

reference pressure p^{ref}, by default in FLAC, it is equal to fours times the secant sriffness ($E_{ur}^{ref} = 4E_{50}^{ref}$). E_{50}^{ref} is determined at 50% of the ultimate deviatoric stress q_f. Reference initial stiffness E_0^{ref} must be above E_{ur}^{ref} ($E_0^{ref} > E_{ur}^{ref}$); FLAC default value is $E_0^{ref} = 3E_{ur}^{ref}$. Reference tangent stiffness (E_{ur}^{ref}) default values is $E_{ur}^{ref} = E_{50}^{ref}$. The amount of stress-dependency of the stiffness modulus is taken into account by means of a power parameter m, which is usually close to 1; $m = 0.5$ for gravel, $m = 0.55 - 0.75$ for sand, $m = 0.75$ for mud and $m = 1$ for clay (Józsa, 2011). The failure ratio R_f is defined by $R_f = q_f/q_a$ (see Figure 3. 12) has a value smaller than 1, typically $R_f = 0.9$ is used. Note that q_f is defined as:

$$q_f = \frac{2\sin\varphi(c\cot\varphi - \sigma_3)}{1-\sin\varphi} \qquad (3.19)$$

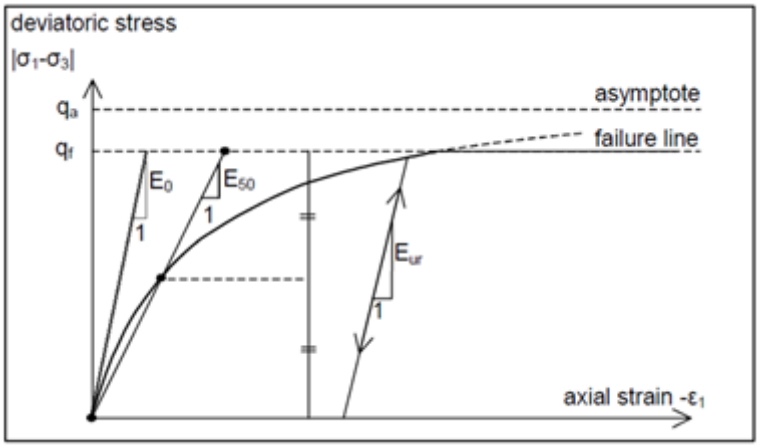

Figure 3. 12. Hyperbolic stress-strain relation in primary loading for a standard drained triaxial test

3.6. MODELING PROCEDURE

The evaluation of two-dimensional active and passive earth pressure distribution is conducted using the bi-dimensional FLAC code. The numerical model consists of a grid representing the soil and a structural beam corresponding to the retaining wall. The dimensions and geometry of the simulated model are depicted in Figure 3. 13. Initial numerical simulations demonstrated that extending the grid horizontally by six times and vertically by four times the wall height did not affect the development of failure surfaces. The grid size is finer near the simulated wall where deformations are concentrated. Horizontal constraints are applied to the left and right boundaries. Additionally, the bottom boundary is constrained both horizontally and vertically, while no constraints are imposed at the ground surface. The retaining wall is represented by structural beam elements connected to the soil grid through interface elements attached on both sides of the beam elements. The interface model, defined by

Coulomb's law and implemented in the FLAC code, is used to simulate the soil-wall contact. The interface model, implemented in the FLAC code, is used to simulate the soil-wall contact. The interface is characterized by a friction angle of interface (δ), shear stiffness (K_s= 10^9Pa/m), and normal stiffness (K_n= 10^9Pa/m).

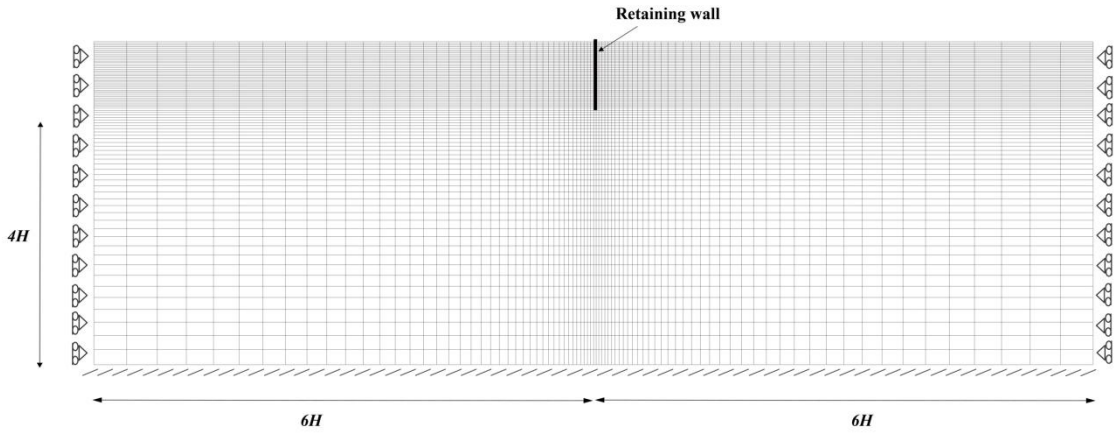

Figure 3. 13. FLAC Numerical model for the analysis of the three types of movement

Two constitutive models has been associated to the present numerical model for comparison purpose; Mohr-Coulomb model and Plastic Hardening model implemented in FLAC. Notably, the coefficients of passive earth pressure are unaffected by the parameters of the elastic soil and weight.

The estimation of active and passive earth pressure coefficient in this simulation first involves calculating the geostatic stresses, assuming the wall is fixed. These are computed using Jaky's formula (1944) for the earth pressure coefficient at rest (K_0) expressed as:

$$K_0 = 1 - \sin \varphi \qquad (3.20)$$

Next, a low adjusted horizontal velocity is applied to the model wall to generate an active zone in front of the wall and a passive one behind the wall through different modes of movement (T, RT, and RB). The simulation continues until the limit lateral earth pressure is reached, and the magnitude and point of application of the resulting forces are recorded for each stage of wall movement (expressed as S_{max}/H). *Here*, S_{max} represents the wall movement, and H denotes the height of the simulated wall, as illustrated in Figure 3. 14.

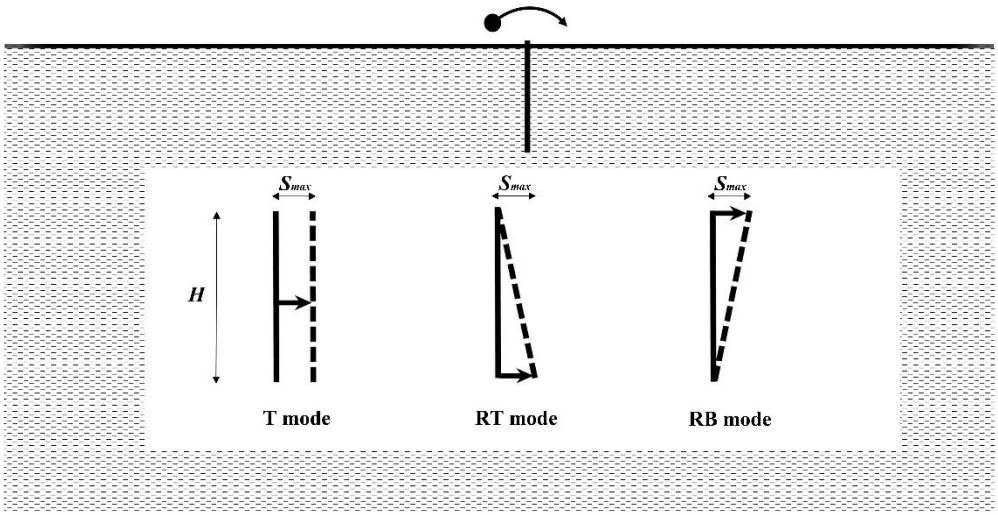

Figure 3. 14. Three types of wall movements: T, RT and RB.

The simplification of using the triangular diagram of earth pressure is retained to deduce earth pressure coefficients, allowing for the assessment of the influence of movement mode on earth pressure forces. Therefore, based on Figure 3. 15 and the subsequent equations, the active and passive earth pressure coefficients (K_a and K_p) can be determined through equations 3.21 and 3.22 respectively:

$$P_{ax} = P_a \cos\delta = K_a \frac{\gamma H^2}{2} \cos\delta \qquad (3.21)$$

$$P_{px} = P_p \cos\delta = K_p \frac{\gamma H^2}{2} \cos\delta \qquad (3.22)$$

where P_a and P_p represents the active and passive earth forces, and P_{ax} and P_{px} signifies the horizontal active and passive earth forces, respectively.

The three dimensional study of lateral earth pressure behind retaining wall was carried out using the three-dimensional FLAC3D (2019). The Geometry and dimensions of the simulation model are presented in Figure 3. 16. A half-symmetry condition is assumed for this problem. The model wall is 0.6m height, with varied width '*b*'. The vertical boundaries are located at *5h* and *2b* in the direction of x and y respectively. The boundary in x-direction situated behind the retaining wall is located at *2h*. The symmetry plane corresponding to y = 0 is restricted in y-direction. The displacements of the far x- and y- lateral boundaries are restricted in the horizontal x and y directions, respectively. The bottom boundary is located at *2h* under the base of the wall, where it is fixed in all directions. The size of the grid is fine near the model wall where deformations are concentrated. The stiffness of the simulated wall is much higher than the surrounding soil. The interface model implemented in FLAC3D code has

been used to simulate the soil-wall interface similar to that in FLAC for two-dimensional study, with a friction angle δ, a normal stiffness Kn = 10^9 Pa/m, and a shear stiffness Ks = 10^9 Pa/m and a cohesion c = 0.

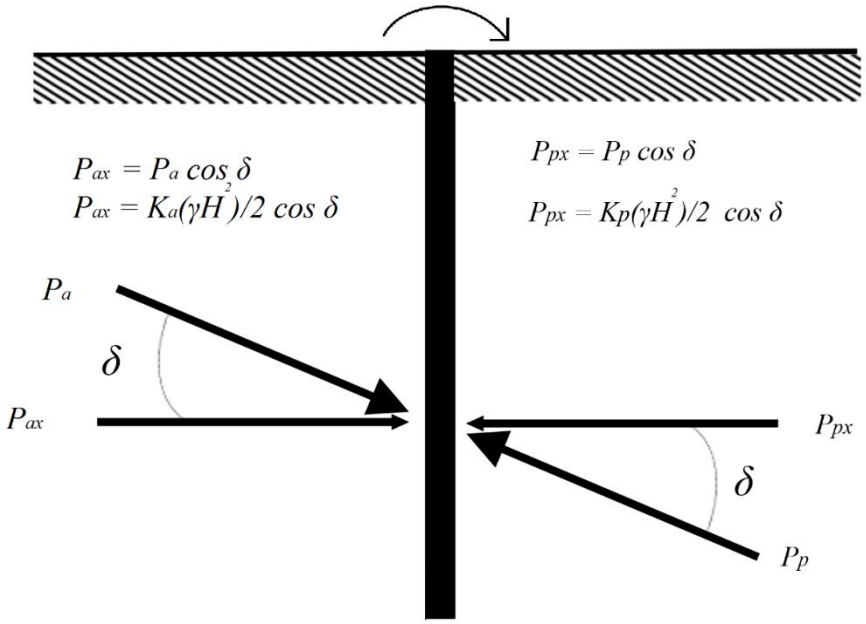

Figure 3. 15. Active (P_a) and passive (P_p) earth pressures acting on the retaining wall

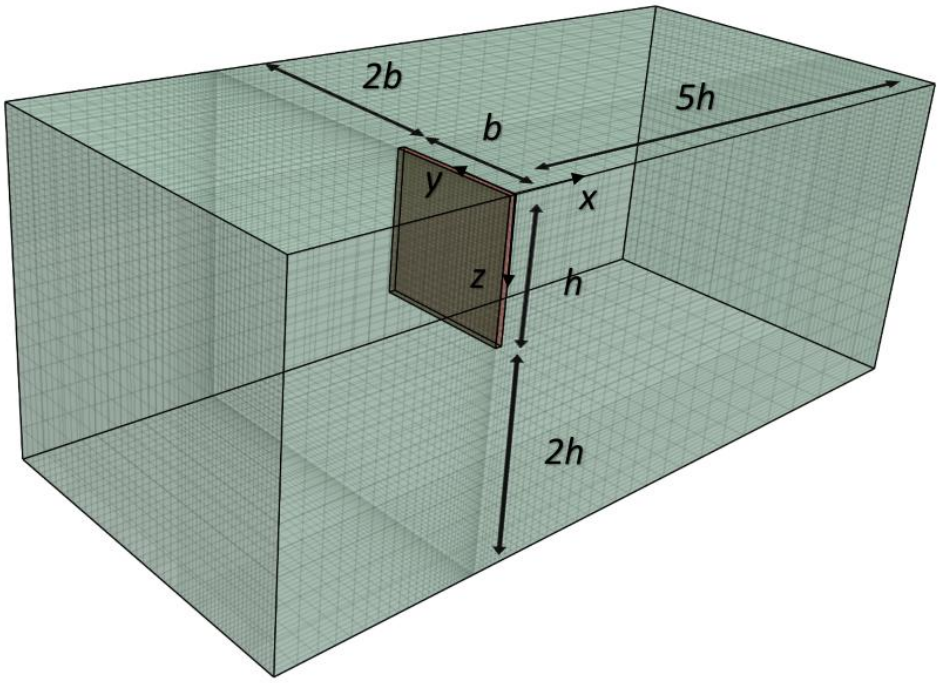

Figure 3. 16. FLAC3D numerical model

3.7. CONCLUSION

An overview on numerical modeling was presented in this chapter, in addition to a brief presentation of the two software used in the following chapters; FLAC and FLAC3D. The two dimensional FLAC is used to analysis the effect of wall movement on passive earth pressure due to soil weight in chapter IV. The three-dimensional version of the software (FLAC3D) will be used to analysis passive earth pressure due to surcharge loading in chapter V.

There exist many numerical methods of the analysis of geotechnical engineering issues. Three among them were detailed in this chapter. Note that FLAC use the difference finite method. Moreover, soil behavior can be simulated using many constitutive models depending on the available parameters and the results to obtain. Mohr-Coulomb and Plastic-Hardening models – which will be used in the analysis of lateral earth pressure in what follows – were briefly presented in this chapter, in addition to the mesh dimensions, boundary conditions and analysis concepts in both two and three dimensions.

Chapter IV

LATERAL EARTH PRESSURE DUE TO SOIL UNIT WEIGHT UNDER VARIOUS MODES OF WALL MOVEMENT

4.1. INTRODUCTION

Many researchers have approached theoretically both passive and active earth pressure problems using methods such as the limit equilibrium method (Coulomb, 1776; Rahardjo and Fredlun, 1984; Zhu et al., 2001; Shiyi et al., 2018), the slip line method (Caquot and Kerisel, 1948; Rankine, 1857; Graham, 1971; Kerisel and Absi, 1990), and the limit analysis theory to derive lower and upper bound solutions (Chen, 1975; Chen and Liu 1990; Soubra and Regenass, 2000; Soubra and Macuh, 2002). The findings of these studies indicated that lateral earth pressure is distributed in a triangular form along the backfill of the wall, and the resultant earth pressure is located at one-third of the wall height from the base. However, various experimental tests have shown that this assumption is not entirely accurate, and the distribution of active and passive earth pressure against a retaining wall does not follow a linear pattern with depth (Tsagareli, 1965; James and Bransby, 1970; Roscoe, 1970; Matsuo et al., 1978; Fang and Ishibashi, 1986; Fang et al., 1994; Ozgur and Aurelian, 2014; Vo et al., 2016; Dou et al., 2017; Patel and Deb, 2020). The primary reason for this nonlinearity is the soil arching effect, which arises from factors like the wall-soil friction angle or the type of wall movement affecting the failure surface, as reported by (Handy, 1985; Khosravi et al., 2016; Cai et al., 2016; Xie and Leshchinsky, 2016; Cao et al., 2019).

In recent decades, with advancements in computational techniques, several numerical simulations have been conducted to study earth pressure under various wall movements. The active case has garnered significant attention (Hazarika and Matsuzawa, 1996; Benmebarek et al., 2006; Fan and Fang, 2010; Wörden and Achmus, 2013; Benmebarek et al., 2016a, 2016b; Qian et al., 2020), whereas passive earth pressure has received less focus. Dayand Potts (1998) explored the effects of interface properties on the behavior of a retaining wall, demonstrating that the limiting pressure depends on the maximum wall friction angle. Benmebarek et al. (2008) investigated earth pressure in 3D translation mode, showing an increase in passive earth pressures due to a decrease in wall extension. Schmüdderich et al. (2019) studied three-dimensional passive earth pressure and improved lower and upper bounds for large friction angles, large wall friction ratios, and narrow geometries.

Active and Passive earth pressure depends not only on the wall movement, but also on how it moves. A backfill with a retaining wall rotating about its top or bottom reacts differently, leading to varied results that cannot be ignored. Potts and Fourie (1986) conducted a numerical study on the effect of the type of wall movement, demonstrating its influence on passive earth pressure. Subsequently, Fang et al. (1994) experimentally confirmed this impact using soil-pressure transducers mounted on a model wall, employing a steel soil bin that moved toward the soil in various modes: translation, rotation about the top, and rotation about the bottom. The model soil used in this experiment had weak bulk and shear modulus, and the maximum wall displacement tested was insufficient to reach the maximum value of passive earth pressure when the wall underwent rotational movement. Peng et al. (2012) and Tang et al. (2018) developed analytical equations to calculate passive earth pressure considering a rigid retaining wall undergoing various modes of movement, demonstrating that the earth pressure distribution and the position of the resultant force depend on the wall's mode of movement. The distribution of passive earth pressure obtained by these two methods in the case of rotation about the top is linear, which differs significantly from experimental observations. Soil arching effect, which involves the rotation of the principal stresses adjacent to the wall, leading to a curvilinear distribution of lateral earth pressure (Handy, 1985), is overlooked in these analytical methods, explaining the disparity. Additionally, both Tang et al. (2018) and Peng et al. (2012) base their methods on Fang et al.'s (1994) assumption that limit passive earth pressure is reached after a maximum wall rotation of 20% of the wall height. The accuracy of this assumption will be addressed in the following section. Vo et al. (2016) experimentally studied the interaction of a rigid retaining wall rotating about the bottom with unsaturated soil samples to demonstrate that the denser sample is stiffer and exhibits a more rapid increase in passive earth pressure as rotation progresses. Dou et al. (2017) also conducted experimental tests to assess the distribution of passive earth pressure when the retaining wall undergoes rotation about the top, revealing that the resultant passive earth pressure acting on the wall is lower than one-third of the wall height. Patel and Deb (2020) investigated, through an experimental test, the non-linearity of the distribution of passive earth pressure when the wall is subjected to rotation about the toe. The results of this test indicate that the maximum top displacement to reach limit passive earth pressure is 10% of the wall height (0.1H), which will be addressed in this paper.

This chapter presents an examination of the influence of the type of movement of a rigid retaining wall with different stages of wall movement on the distribution and coefficient of active and passive earth pressure, as well as the location of the load distribution centroid. This will be achieved using the explicit finite difference code FLAC, as existing laboratory tests and experimental studies have not fully addressed this impact. The numerical results will be discussed and compared with the existing experimental and theoretical findings available in the published literature.

4.2. VALIDATION OF NUMERICAL MODELING IN TRANSLATING MODE

4.2.1. Active and passive earth pressure coefficients

To assess the accuracy of the proposed method, the results obtained for the translation mode are compared with those from Kerisel and Absi (1990). The comparison, conducted for five practical values of internal friction angle (φ = 20°, 25°, 30°, 35°, and 40°) and each of the four interface friction values (expressed as δ / φ = 0, 1/3, 2/3, and 1), is presented in Table 4. 1. It is evident that both active and passive earth pressure coefficients are significantly affected by changes in the friction angle as well as the soil-wall interface friction angle. Active earth pressure values decrease with higher values of φ and δ while passive ones increase. The table demonstrates that the coefficients obtained in this study closely align with those from Kerisel and Absi (1990), with a difference of less than 3.6%. This agreement affirms the validity of the proposed method.

4.2.2. Active and passive earth pressure distributions

This section investigates the normalized active and passive earth pressures acting on the retaining wall (horizontal earth pressure divided by the vertical pressure at the base of the wall, γH) along the normalized height *h/H* (where *h* is the distance above the wall base and *H* is the wall height) in the translating wall mode. This is then compared with the findings from the experimental study conducted by Fang et al. (1997) for the active case and those by Fang et al. (1994) for the . In their experiments, Ottawa air-dry sand was used, possessing an internal friction angle of 30.9°, a sand-wall friction angle of 19.2°, and a unit weight of 15.5 KN/m³. The dilation angle for practical sands is less than the friction angle, however, the effect of dilation angle seems to be negligible with soils having friction angles less than 30° (Khelifa & Benmebarek, 2014; Schmüdderich et al., 2022). For this reason, the dilation angle has been taken equal to the friction angle in this model $\psi = \varphi$. The height of the wall was 0.55 m. The sand model employed in the FLAC simulation shares these same parameters. The constitutive model used for this comparison is Mohr-Coulomb, which necessitates the specification of a Young's modulus (E) and a Poisson's ratio (μ). Therefore, initial simulations were carried out to match the soil behavior observed in the experimental tests. The calibrated values for Young's modulus and Poisson's ratio are set at 2.7 MPa and 0.35 respectively. These parameters are detailed in

Table 4. 2. The comparison results are depicted in Figure 4. 1 for active case and Figure 4. 2 for passive case, where the analytical outcomes from Coulomb (1773) and Peng et al. (2012) for active and passive cases, respectively, are also included for comparison purpose. Across all three methods, the distribution of passive earth pressure closely approximates hydrostatic conditions. Notably, the

results from our numerical study demonstrate strong concordance with both the experimental findings and the analytical results. Furthermore, the centroid of the passive load distribution obtained in our study aligns with the established value of *1/3H* above the bottom of the wall, as reported in existing literature.

Table 4. 1. Active and passive earth pressure coefficients with various internal friction angles and soil-wall friction angles in translation mode

Friction angle φ(°)	δ/φ	Active Earth Pressure Coefficients (K_a)		Passive Earth Pressure Coefficients (K_p)	
		This study	Kerisel and Absi (1990)	This study	Kerisel and Absi (1990)
20	0	0.48	0.49	2.11	2.05
	1/3	0.45	0.46	2.45	2.40
	2/3	0.43	0.44	2.82	2.75
	1	0.43	0.44	3.13	3.10
25	0	0.40	0.41	2.54	2.45
	1/3	0.37	0.38	3.10	3.10
	2/3	0.36	0.36	3.74	3.70
	1	0.36	0.37	4.33	4.40
30	0	0.32	0.33	3.11	3.00
	1/3	0.30	0.30	4.08	4.00
	2/3	0.29	0.30	5.27	5.30
	1	0.30	0.30	6.51	6.50
35	0	0.26	0.27	3.69	3.70
	1/3	0.24	0.25	5.35	5.40
	2/3	0.24	0.25	7.75	8.00
	1	0.25	0.26	10.52	10.50
40	0	0.21	0.22	4.65	4.50
	1/3	0.20	0.20	7.70	7.60
	2/3	0.20	0.20	12.36	12.00
	1	0.20	0.20	18.30	18.00

Table 4. 2. Mohr-Coulomb soil parameters representing the Ottawa air-dry sand used in the experiment.

Parameter	***Value***
Unit weight (γ)	15.5 KN/m^3
Soil friction angle (φ)	30.9°
Dilation angle (ψ)	30.9°
Soil-wall friction angle (δ)	19.2°
Young's modulus	2.7 MPa
Poisson's ratio	0.35
Cohesion (c)	0

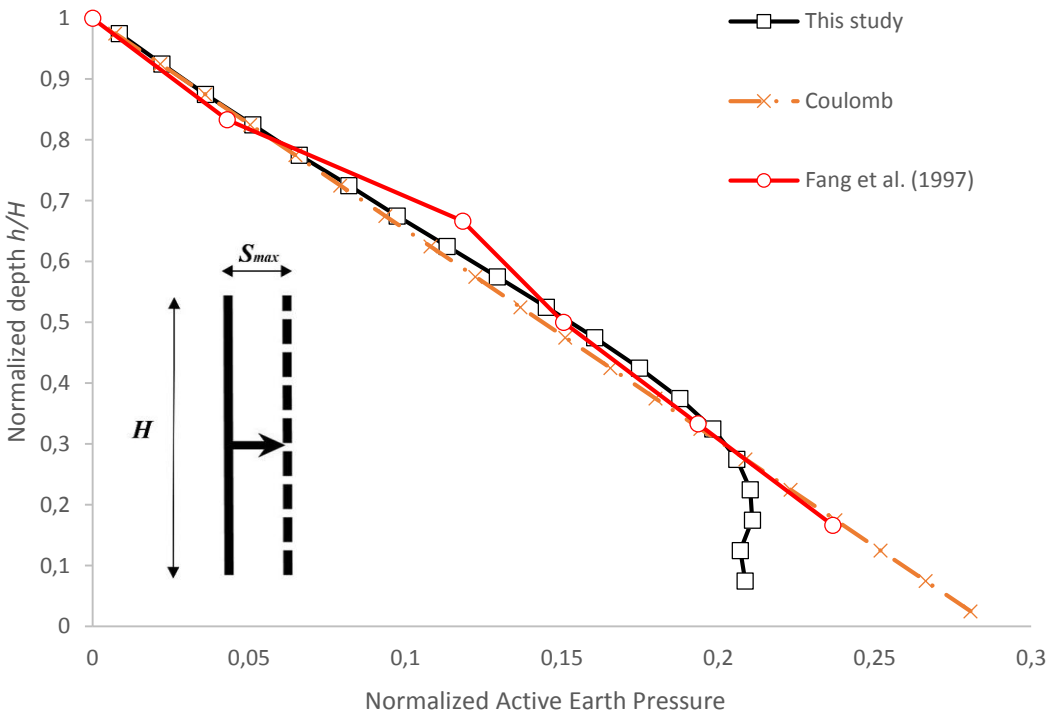

Figure 4. 1. Distribution of active earth pressure in T mode.

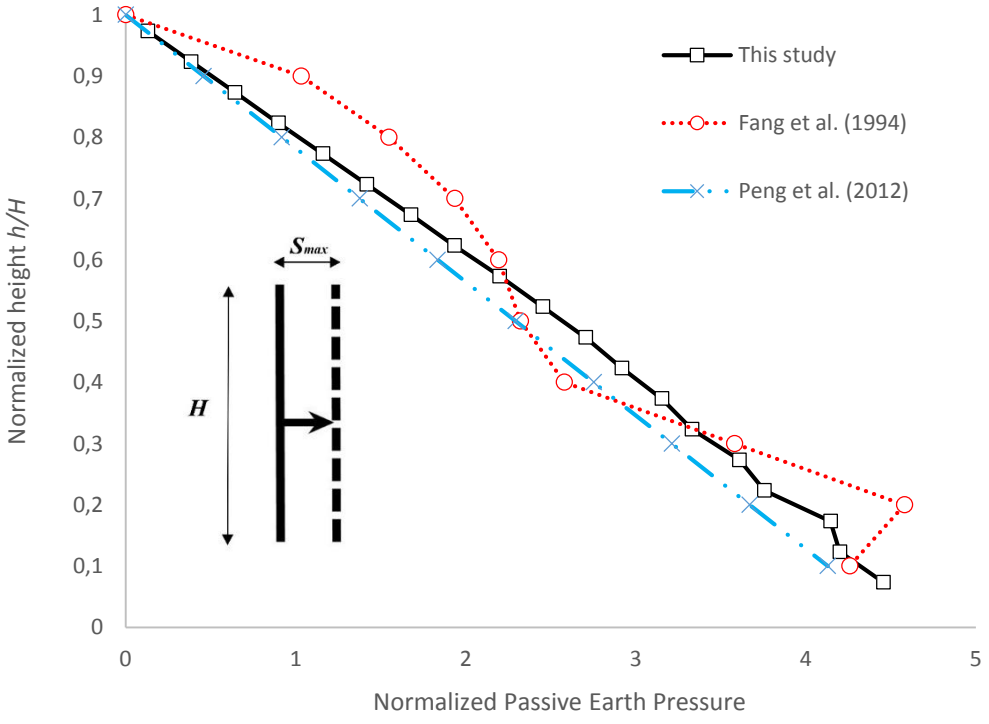

Figure 4. 2. Distribution of passive earth pressure in T mode.

4.3. ACTIVE AND PASSIVE EARTH PRESSURES IN VARIOUS MODES OF MOVEMENT

4.3.1. Maximum Shear strain rate Distribution

To obtain failure mechanisms and validate the capability of the numerical approach using FLAC code to replicate soil behavior, initial simulations were carried out to examine the prediction of the distribution of maximum shear strain rates. These predictions were then compared with experimental results available in the literature. Experimental investigations on earth pressure in sand were conducted at Cambridge University using the radiographic technique to study the evolution of shear localization in sand under three conditions: translation (Lucia, 1966), rotation about the top (Arthur, 1962), and rotation about the base (Bransby, 1968). Figure 4. 3 and Figure 4. 4 present a comparison between the distribution of maximum shear strain rates obtained through our numerical method and the experimental radiographs of shear zones reported by Widuliński et al. (2011) for the active case, while Figure 4. 4 present same comparison for the passive case. These experiments were conducted in dense sand with an estimated friction angle of $\varphi = 49°$ and a dilation angle of $\psi = 35°$, approximately 2⁄3 of φ (Bransby, 1968). The soil-wall friction angles were determined using load cells implemented in the wall, with higher values of δ occurring at the top of the wall and lower values (approximately $= 18°$) near the base of the wall. Thus, to replicate the same behavior in FLAC simulation, the model soil parameters used in this comparison are consistent with those of the experiment conducted in dense sand, as outlined in Table 4. 3. The chosen wall friction angle is $^1/_2\,\varphi$. Figure 4. 3a shows a linear distribution in the case of active earth pressure for a translation wall. However, RT mode represented in Figure 4. 3b resolve a clear curved distribution of maximal shear strain rates, while the distribution of shear curves in RB mode are localized at the upper part of the wall as depicted in Figure 4. 3c. What can be derived from the figure is that shear zone localizations occurred from the experiment match well with those from the present numerical results. In Figure 4. 4a, which pertains to the translation mode case, it is evident that the radiograph displays a curved shear zone propagating from the wall base, accompanied by a secondary, weaker shear zone originating from the top of the wall. The FLAC simulation predicts the same distribution of maximum shear strain rate localization. In the case of rotation about the top (Figure 4. 4b), only one curved shear zone starting from the wall base is observed in the experimental test, which aligns with the maximum shear strain rate distribution indicated by the numerical simulation. Finally, in the rotation about the bottom case (Figure 4. 4c), multiple parallel curved zones with matching shapes are observed in both the experimental and numerical studies. This similarity between the present computational approach and the radiographs obtained from experimental studies affirms the effectiveness of our numerical simulation.

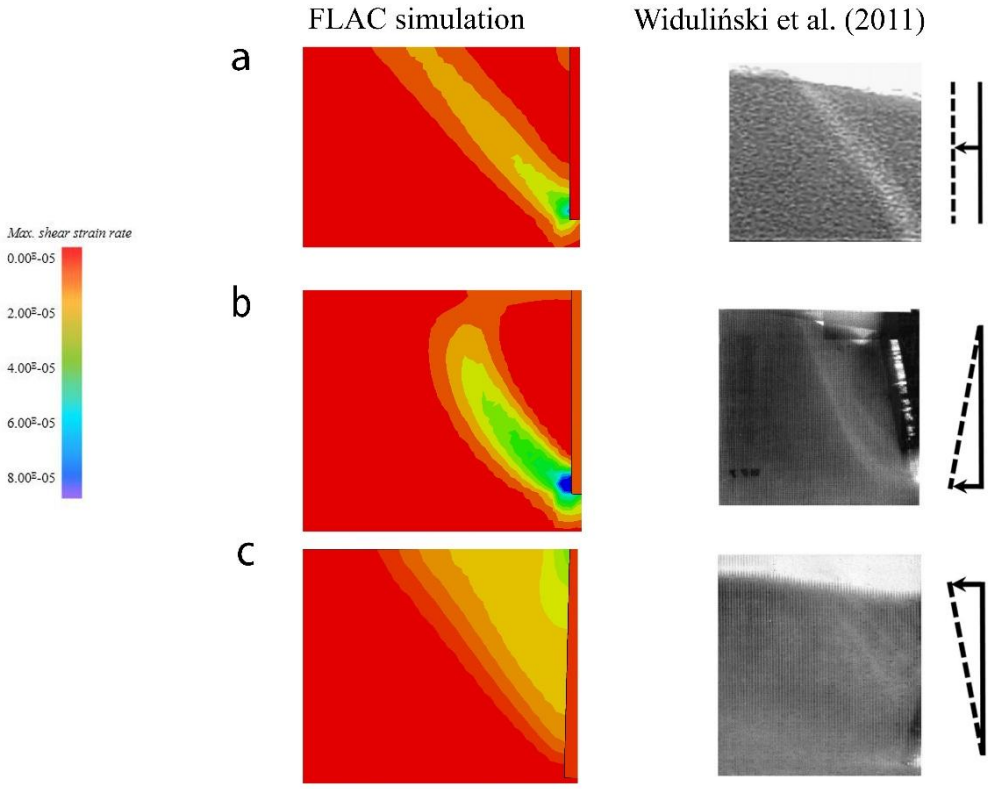

Figure 4. 3. FLAC distribution of maximum shear strain rates and shear zone radiographs (Widulinski et al. 2011) in active case a) Translation mode b) Rotation around top c) Rotation around base.

Table 4. 3. Soil parameters used in the prediction of the distribution of maximum shear strain rates and the comparison with Cambridge experimental results

Parameter	Value
Unit weight (γ)	18 KN/m^3
Soil friction angle (φ)	49°
Dilation angle (ψ)	35°
Soil-wall friction angle (δ)	24.5°
Young's modulus	2.7 MPa
Poisson's ratio	0.35
Cohesion (c)	0

4.3.2. Evolution of K_p with wall movement

It is well known that passive earth pressure requires further movements of the retaining wall than active earth pressure. In this section, the impact of different types of wall movement on the magnitude of passive earth pressure coefficient (K_p) has been investigated. Figure 4. 5 provides a comparison

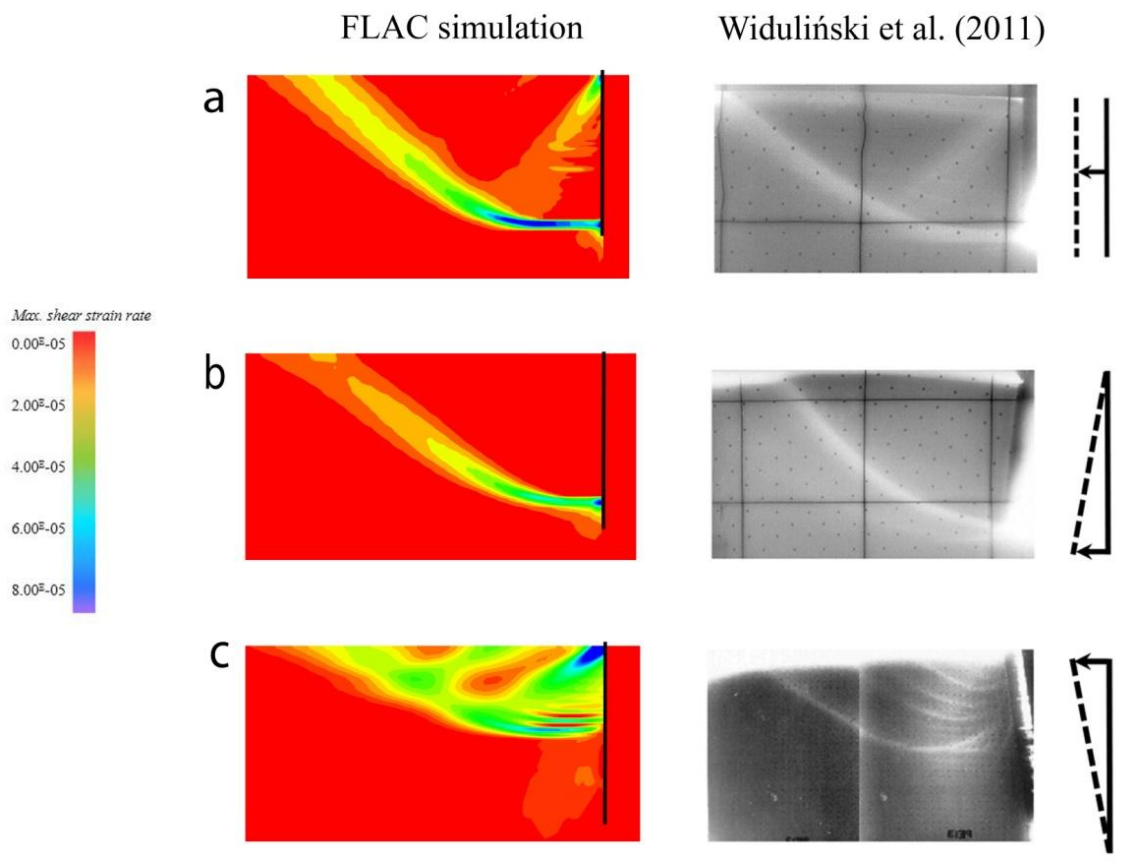

Figure 4. 4. FLAC distribution of maximum shear strain rates and shear zone radiographs (Widulinski et al. 2011) in passive case a) Translation mode b) Rotation around top c) Rotation around base.

between the current FLAC results and the experimental study conducted by Fang et al. (1994) illustrating the variation of K_p values with various wall movements. The same model soil, representing Ottawa air-dry sand with parameters outlined in

Table 4. 2, is employed for this comparison.

The curves reveals well that the evolution in K_p values with wall movement obtained in the current study for both Translation (T) and Rotation about Bottom (RB) modes closely align with those from Fang et al. (1994). The coefficient of passive earth pressure increases as wall displacement increases, eventually reaching a stable value in the case of translation mode when the wall displacement is approximately S_{max}/H =0.18. However, in RB mode, it is observed that the range of wall displacement (S_{max}/H =0.20) is insufficient to reach the limit passive earth pressure coefficient. This discrepancy can be attributed to the low stiffness of the model soil and indicates that RB mode requires more displacement than T mode to achieve the limit value of passive earth pressure.

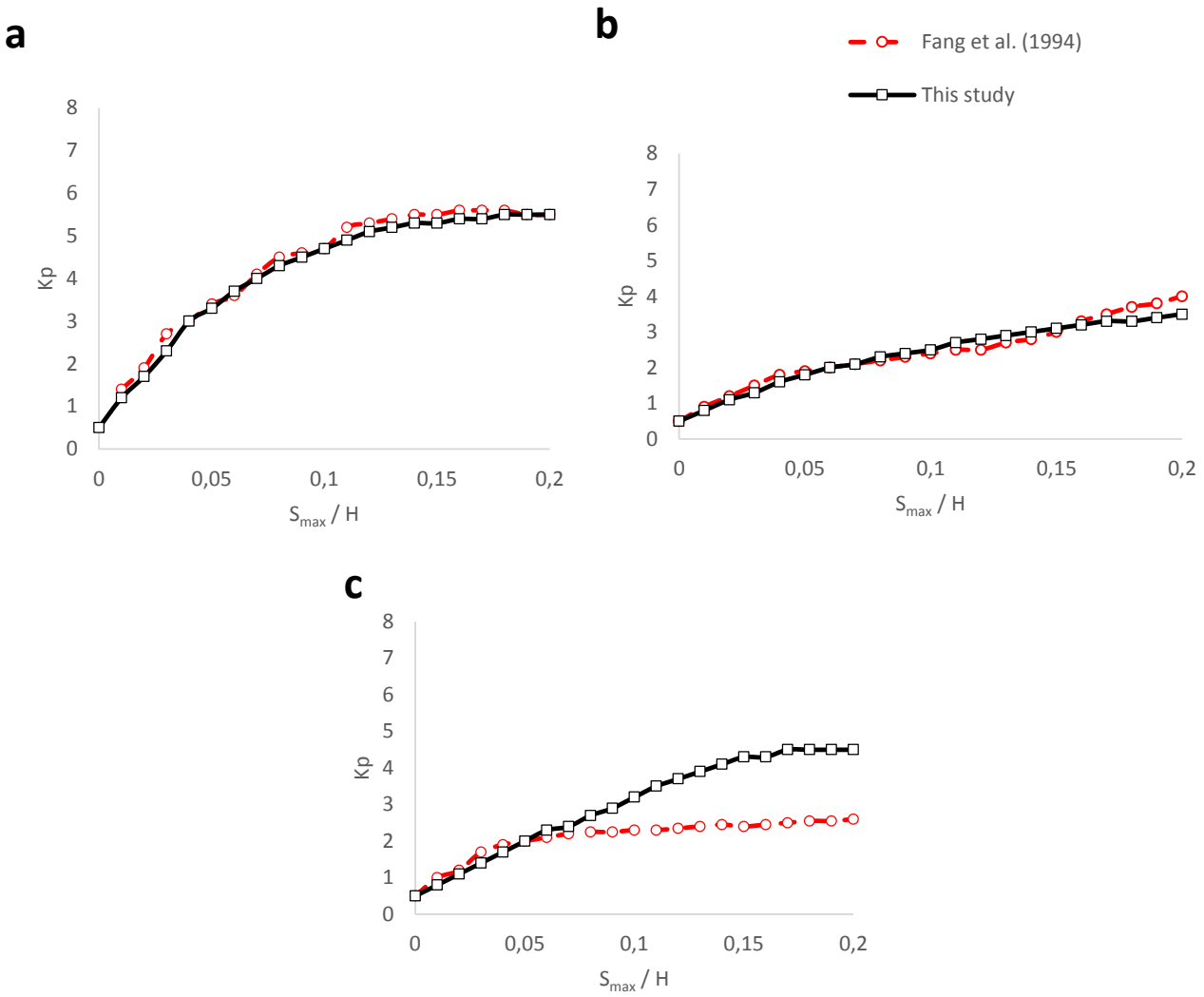

Figure 4. 5. Variation of K_p with different wall movement with $\varphi = 30.9°, \delta = 19.2°$ a) T mode b) RB mode c) RT mode.

In the case of Rotation about Top (RT) mode, both the numerical simulation and experimental study results closely match when S_{max}/H < 0.05. However, as rotation progresses, they begin to diverge. The evolution of passive earth pressure coefficients obtained through the current numerical study reaches a limit passive state at S_{max}/H = 0.17 with a value of K_p = 4.5. On the other hand, experimental results indicate a lower value of K_p = 2.7, approximately 51% of the value reported by Kerisel and Absi (1990) in practical applications. It is important to note the significant disparity in RT mode between the two methods.

4.3.3. Passive earth pressure distribution in RT mode

Previous studies, such as those by Fang et al. (1994) and Peng et al. (2012), have confirmed the nonlinear distribution of passive earth pressure with depth behind a wall subjected to rotation about the top. However, the observed disparity in Figure 4. 5 between the experimental results of Fang

et al. (1994) and the current study in RT mode warrants further investigation. To address this, two curves representing the passive earth pressure distribution along the wall height from FLAC simulation, corresponding to S_{max}/H = 0.05 (*5%H*) and S_{max}/H = 0.20 (*20%H*), are presented in Figure 4. 6. Additionally, the results from the experimental study of Fang et al. (1994) and those from the analytical methods of Peng et al. (2012) and Tang et al. (2018) are included for comparison.

The curves vividly illustrate that the passive earth pressure distribution in RT mode is nonlinear, except for the one obtained by Tang et al. (2018) which presents a linear distribution. Peng et al. (2012) method exhibits a slightly curved distribution of passive load, leading to a maximum normalized passive earth pressure of 4 at the base of the wall. In contrast, the experiment by Fang et al. (1994) and the present FLAC method yield significantly higher results at the wall base for both S_{max}/H = 0.05 and S_{max}/H = 0.20, with values of 5.1, 6.1, and 5.6 respectively. Both Tang et al. (2018) and Peng et al. (2012) explain that the observed nonlinear distribution of passive earth pressure in the experimental tests is a consequence of the arching effect, which is not accounted for in their methods. This clarification addresses the discrepancies found.

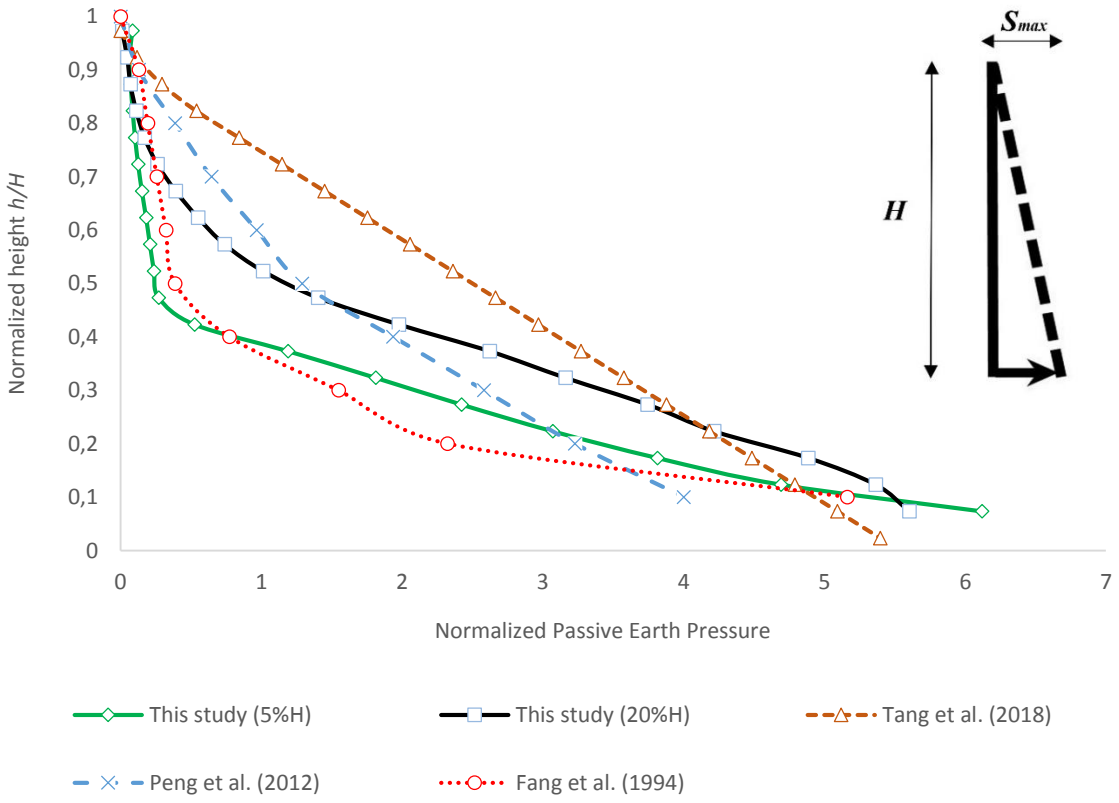

Figure 4. 6. Comparison of passive earth pressure distribution in RT mode corresponding to S_{max}/H = 0.05 (5%H) and S_{max}/H = 0.20 (20%H) with experimental data and analytical solutions.

Comparing the results obtained from Fang et al. (1994) experiment with those from the present numerical study, it is observed that the distribution in the case of S_{max}/H = 0.05 aligns well

with the experimental data. However, higher passive earth pressure values with the same distribution shape can be observed in cases of large wall movement (S_{max}/H = 0.20). This leads to the conclusion that the passive earth pressure distribution is no longer triangular, resulting in a centroid that differs from one-third of the wall height. Thus, it is affirmed that the distribution of passive earth pressure is influenced by the magnitude of wall movement (S_{max}/H). Additionally, it is worth noting that the arching effect emerges at the onset of rotational movement, diminishes with continued movement, and eventually disappears when reaching the limit state of passive earth pressure.

4.3.4. Passive earth pressure distribution in RB mode

Previous analytical and experimental investigations (Fang et al., 1994; Peng et al., 2012; Tang et al., 2018; Patel and Deb, 2020) have consistently demonstrated a curved distribution of passive earth pressure in cases involving a retaining wall subjected to rotation about the bottom (RB). To assess the influence of wall movement in the RB mode, the passive earth pressure distribution obtained through the present numerical study along the wall height is examined in Figure 4. 7. The soil parameters used are those detailed in

Table 4. 2, with a substantial wall movement corresponding to S_{max}/H = 0.20. These results are then compared to those from Fang et al. (1994) experiment, as well as the analytical approaches of Peng et al. (2012), Tang et al. (2018), and Patel and Deb (2020).

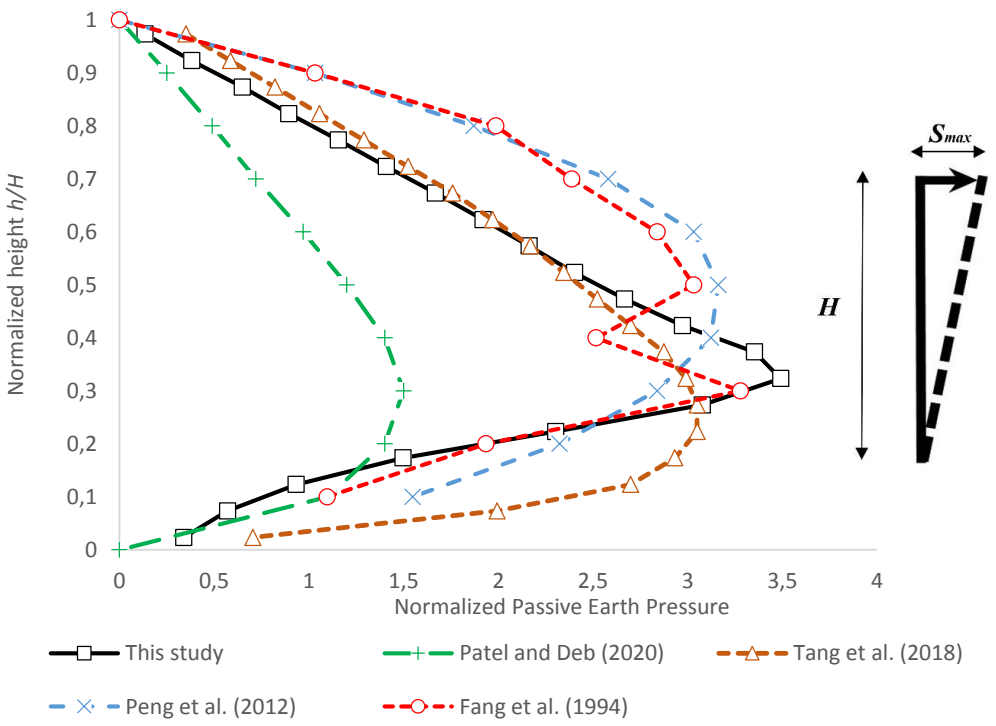

Figure 4. 7. Comparison of passive earth pressure distribution in RB mode (S_{max}/H = 0.20) with experimental data and analytical solutions

Patel and Deb (2020) report a maximum normalized passive earth pressure of 1.5. The authors offer an explanation, stating that passive earth pressure increases with wall movement, reaching its peak at a wall displacement of 0.1H. However, all other plotted results (Fang et al., 1994; Peng et al., 2012; Tang et al., 2018), including the present FLAC simulation, yield values for the maximum normalized passive earth pressure ranging from 3.0 to 3.5. These values are notably higher than the one obtained by Patel and Deb (2020), without a clear explanation for the discrepancy.

Furthermore, all curves in Figure 4. 7 (except for Patel and Deb, 2020) affirm that the centroid of the passive earth distribution in RB mode is approximately 0.50H, displaying a similar curved distribution shape. However, these methods (Fang et al., 1994; Peng et al., 2012; Tang et al., 2018) assume that this distribution, resulting from a wall displacement of 0.20H, represents the limit passive earth pressure.

4.3.5. Active and passive earth pressures with various magnitudes of wall movement

To explore the influence of the factor S_{max}/H, active and passive earth pressure distributions at various stages of wall rotation will be investigated in this section. Since the lateral earth pressure will be evaluated in the area before reaching the limit state, The Plastic-Hardening constitutive model will be used in addition to the Mohr-Coulomb. Higher stiffness is associated to the model soil to represents the behavior of real practical soils. For Mohr-Coulomb model, same parameters describing the Ottawa sand will be used, with a Young's modulus equal to 35MPa and a Poisson's ratio equal to 0.3. In the other hand, Plastic Hardening model requires a secant stiffness, which is chosen to be equal to young modulus (E) used in Mohr-Coulomb model; $E_{50}^{ref} = 35MPa$, a tangent stiffness $E_{oed}^{ref} = 35MPa$, an unloading-reloading stiffness $E_{ur}^{ref} = 140MPa$, an exponent $m = 0.63$, a reference pressure $p^{ref} = 100kPa$, and a Poisson's ratio $v = 0.3$. The adopted unit weight, internal friction angle and cohesion will be the same cited above, equal to 15.5 KN/ m^3, 30.9° and 0, respectively. The associated Mohr-Coulomb parameters are presented in Table 4. 4 and those of Plastic-Hardening model are presented in

Table 4. 5.

Table 4. 4. Mohr-Coulomb soil parameters used to study the impact of S_{max}/H

Parameter	Value
Unit weight (γ)	15.5 KN/m^3
Soil friction angle (φ)	30.9°
Dilation angle (ψ)	30.9°
Soil-wall friction angle (δ)	19.2°
Cohesion (c)	0
Poisson's ratio (v)	0.3
Young's modulus (E)	35 MPa

Table 4. 5. Plastic-Hardening soil parameters used to study the impact of S_{max}/H

Parameter	Value
Unit weight (γ)	15.5 KN/m^3
Soil friction angle (φ)	30.9°
Dilation angle (ψ)	30.9°
Soil-wall friction angle (δ)	19.2°
Cohesion (c)	0
Poisson's ratio (v)	0.3
Young's modulus (E)	35 MPa
Secant modulus (E_{50}^{ref})	35 MPa
oedometer modulus (E_{50}^{oed})	35 MPa
Unloading modulus (E_{ur}^{ref})	140 MPa
power parameter (m)	0.63

The behaviors of the two models were evaluated via triaxial test conducted with FLAC software, the confining pressure (σ_3) is taken equal to 100 kPa. The test stress-strain behavior is plotted in Figure 4. 8. It can be seen that both models demonstrate an ultimate value at 200 KPa which represents the limit plastic flow. However, the present study deals with the rotational movement of the retaining wall that exerts a partial mobilization on the backfill soil. In RT mode, the soil adjacent to the lower part of the wall would reach the limit state before the upper part and vice versa in RB mode. Using Plastic Hardening model in this case would be more accurate. A parametric study of the two models will be conducted in what follows.

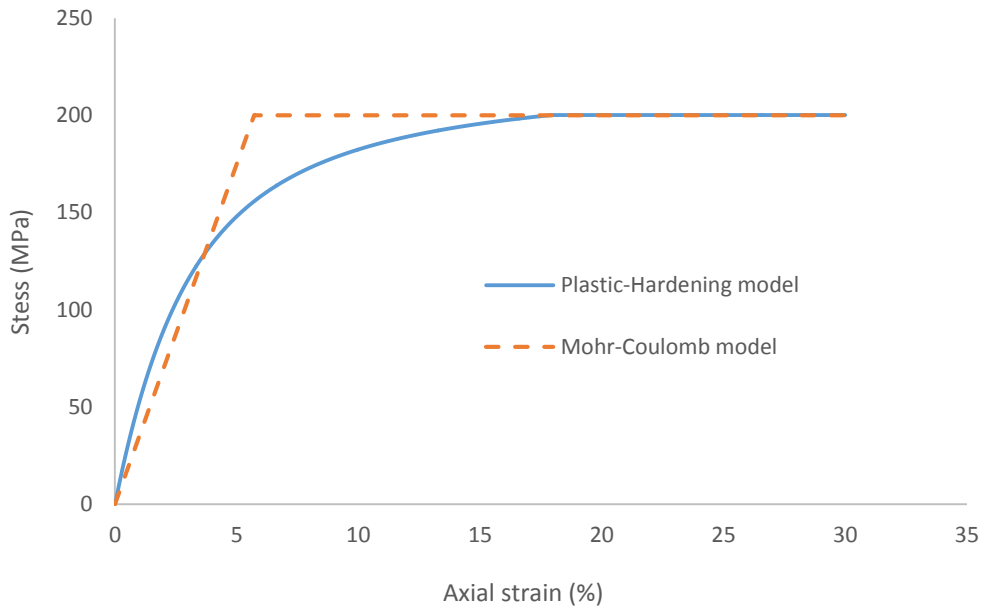

Figure 4. 8. Comparison of stress-strain behavior between Mohr-Coulomb and Plastic-Hardening model

Figure 4. 9 and Figure 4. 10 presents the changes in the distribution of active earth pressure with four values of wall rotation in RB mode; S_{max}/H = 3E-5, 5E-5, 10E-5 and 15E-5. Figure – represents the results in the case of Mohr-Coulomb model while figure – is the Plastic-Hardening case. It can be noticed that the distribution of active earth pressure with depth is quit linear, with a slight curvature at the bottom, The magnitude of lateral earth pressure decreases with more wall movement to reach the limit value at S_{max}/H=15E-5. Plastic-Hardening model shows a more curved shape at the middle of wall than that from Mohr-Coulomb. Table 4. 6 reveals values of active earth pressure coefficients (K_a) as well as the location of the point of application of the resultant force for the four wall movements (h/H), where H signifies the height of the wall and h indicates the distance above the wall base. K_a values are equal restricted between 0.31 and 0.34, with centroid that appears at the one third of the wall height, similar the one in translated mode reported in literature.

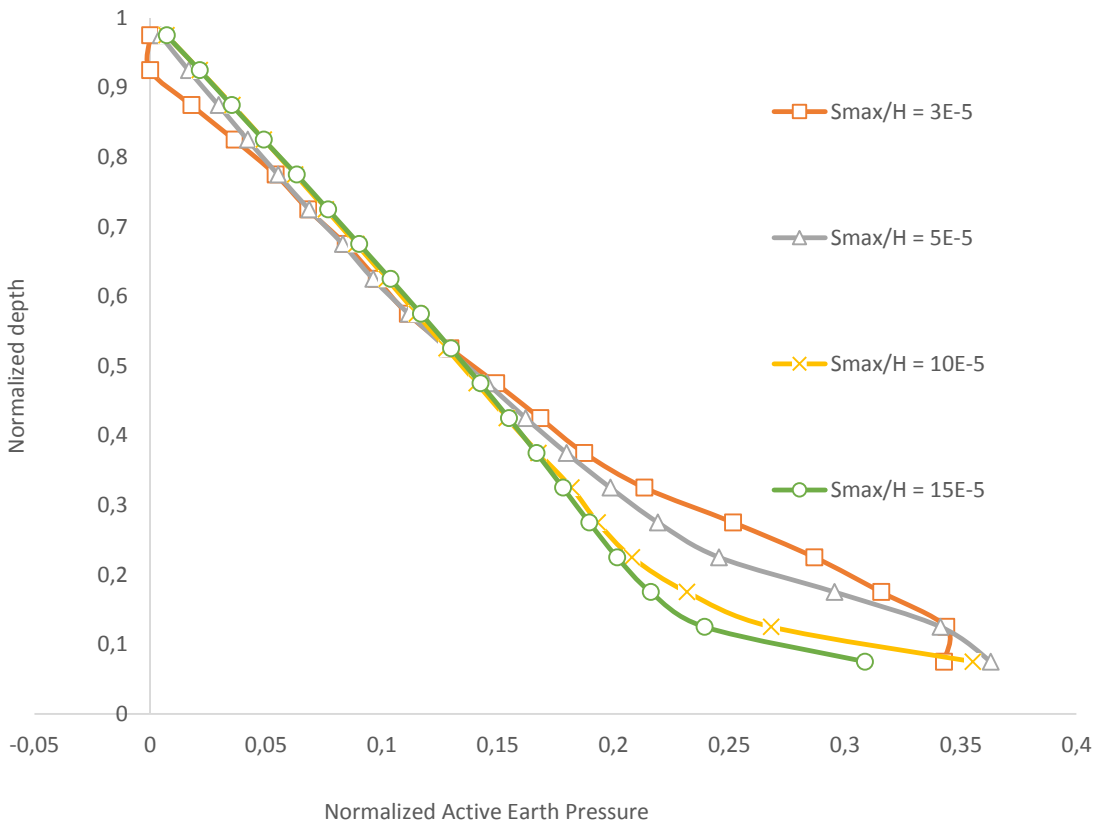

Figure 4. 9. Distribution of active earth pressure in RB mode for various distances – Mohr-Coulomb model

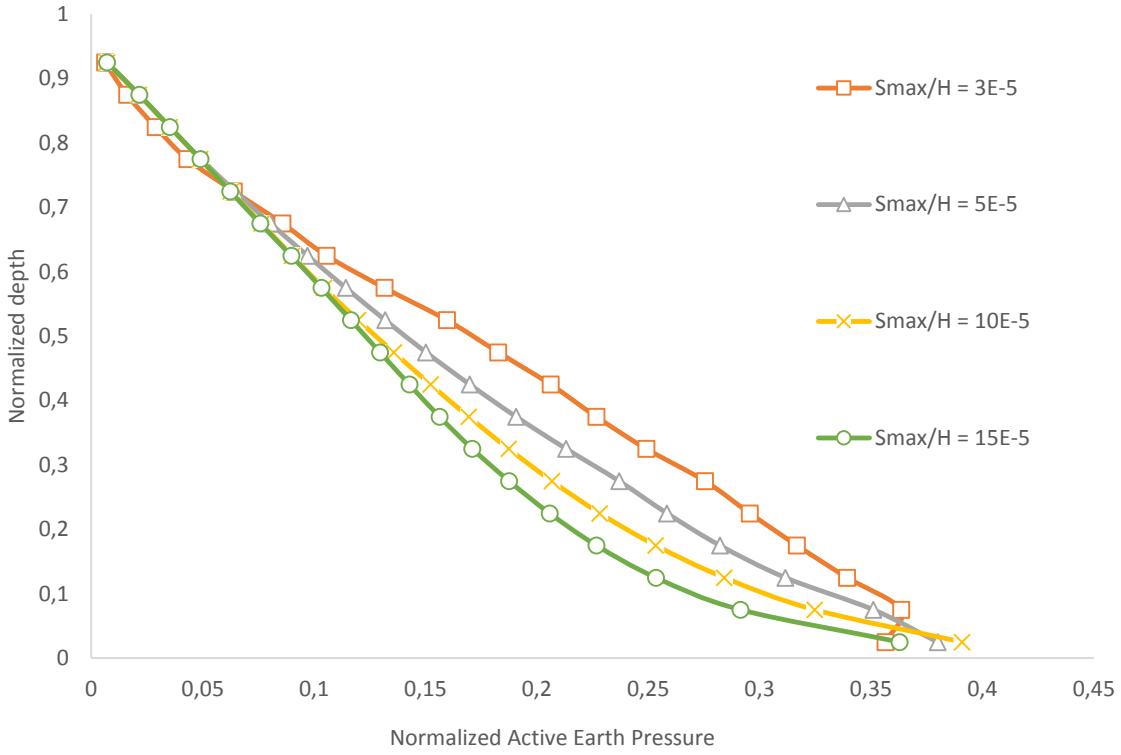

Figure 4. 10. Distribution of active earth pressure in RB mode for various distances – Plastic-Hardening model

Table 4. 6. Variation of K_a *and point of application with* S_{max}/H *for RB mode*

S_{max} / H	*Mohr-Coulomb*		*Plastic-Hardening*	
	h/H	K_a	*h/H*	K_a
3E-5	0.33	0.33	0.33	0.34
5E-5	0.33	0.33	0.33	0.33
10E-5	0.32	0.32	0.32	0.32
15E-5	0.32	0.31	0.32	0.31

The RT mode distributions for the active case are presented in Figure 4. 11 and Figure 4. 12 corresponding to Mohr-Coulomb and Plastic-Hardening models respectively. The wall movements registered in the two curves are S_{max}/H = 3E-4, 5E-4, 7E-4 and 10E-4, which explaines that RT mode requires more movement than RB mode to reach limit active earth pressure. The distribution in that case increases with more wall movement in the upper part of the wall, while decreases in lower part. The changes in the magnitude of active earth pressure between the upper part and lower part is well revealed in the Plastic-Hardening model contrary to that in Mohr-Coulomb. Values of active earth pressure coefficients appear to be between 0.31 and 0.39 as depicted in Table 4. 7, with a centroid varied from 0.38 to 0.49. As a result, limit active earth pressure is reached with low wall movements. Furthermore, the distribution shape, active earth pressure coefficient and the location of the resultant active force are slightly affected by the amount of wall movement.

Table 4. 7. Variation of K_a and point of application with S_{max}/H for RT mode

S_{max} / H	*Mohr-Coulomb*		*Plastic-Hardening*	
	h/H	K_a	*h/H*	K_a
3E-4	0.41	0.39	0.38	0.31
5E-4	0.46	0.36	0.45	0.30
7E-4	0.48	0.33	0.49	0.31
10E-4	0.48	0.33	0.48	0.33

The distribution of passive earth pressure with depth in RB mode for various stages of wall movement is illustrated in Figure 4. 13 for Mohr-Coulomb model and Figure 4. 14 for Plastic-Hardening model. It is evident that as rotation progresses, the distribution of passive earth pressure gradually transitions from nonlinear to linear at the limit state. Increasing the wall rotation leads to an augmentation of the upper part, causing the passive earth pressure diagram to progressively assume a linear profile throughout the depth of the wall. Limit passive earth pressure s reached at S_{max}/H = 0.008 in the case of Mohr-Coulomb model, while Plastic-Hardening requires more movement equal to S_{max}/H = 0.03 to reach the limit value. This discrepancy can be explained from the tiaxial test results from Figure 4. 8, clearly it can be noticed that Mohr-Coulomb case reaches 200 MPa with nearly 6% of axial strain, on the other hand, Plastic-Hardening case reaches the same limit value on 20% axial strain.

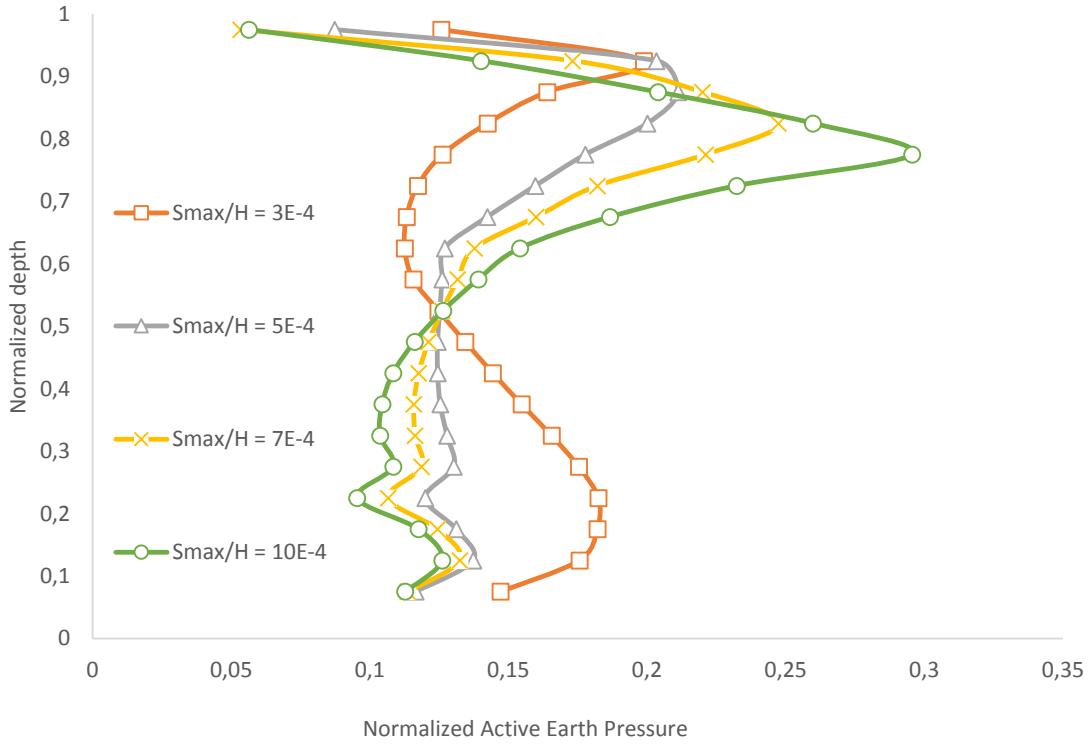

Figure 4. 11. Distribution of active earth pressure in RT mode for various distances – Mohr-Coulomb model

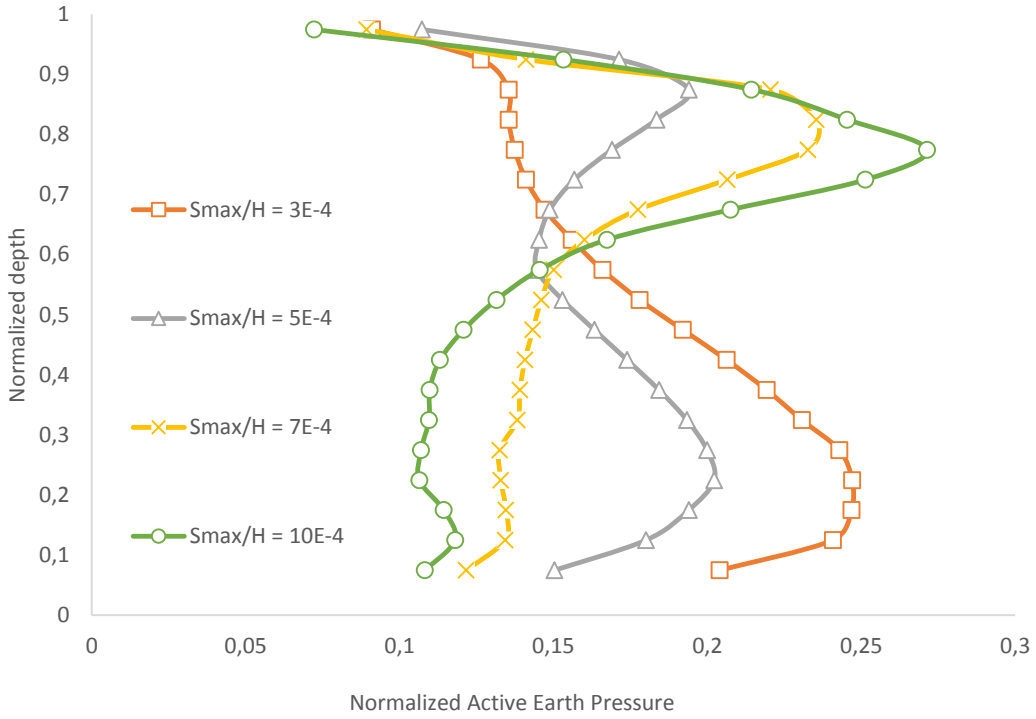

Figure 4. 12. Distribution of active earth pressure in RT mode for various distances – Plastic-Hardening model

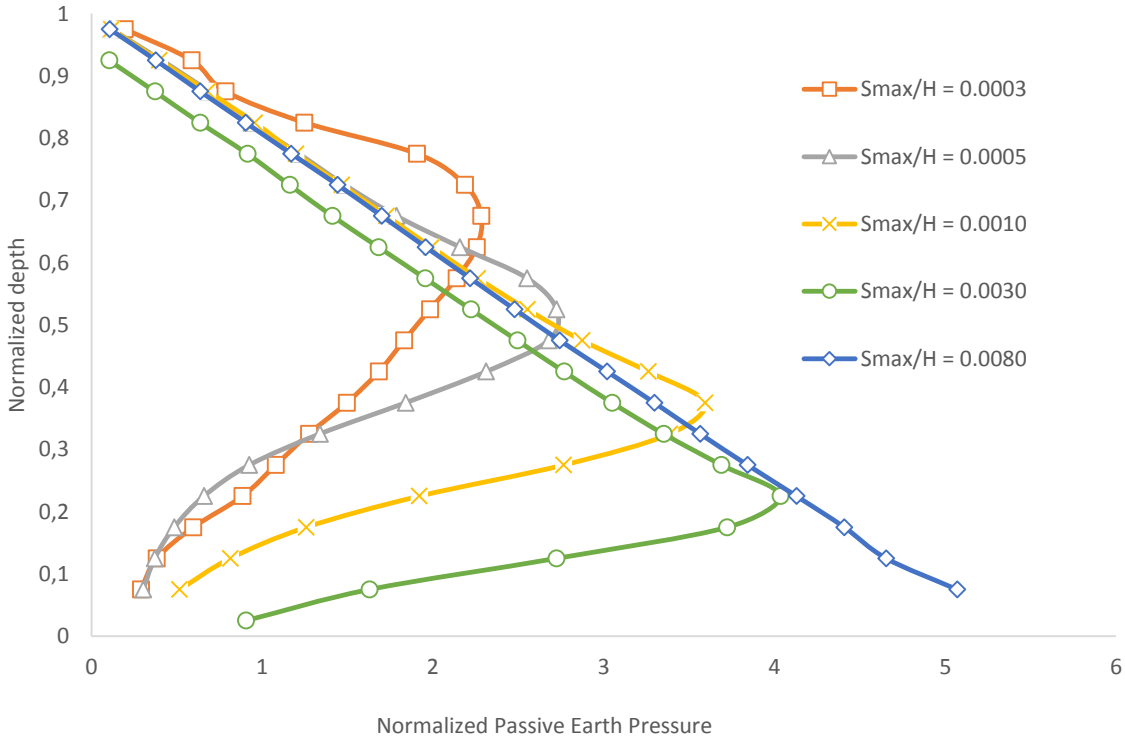

Figure 4. 13. Distribution of passive earth pressure in RB mode for various distances – Mohr-Coulomb model

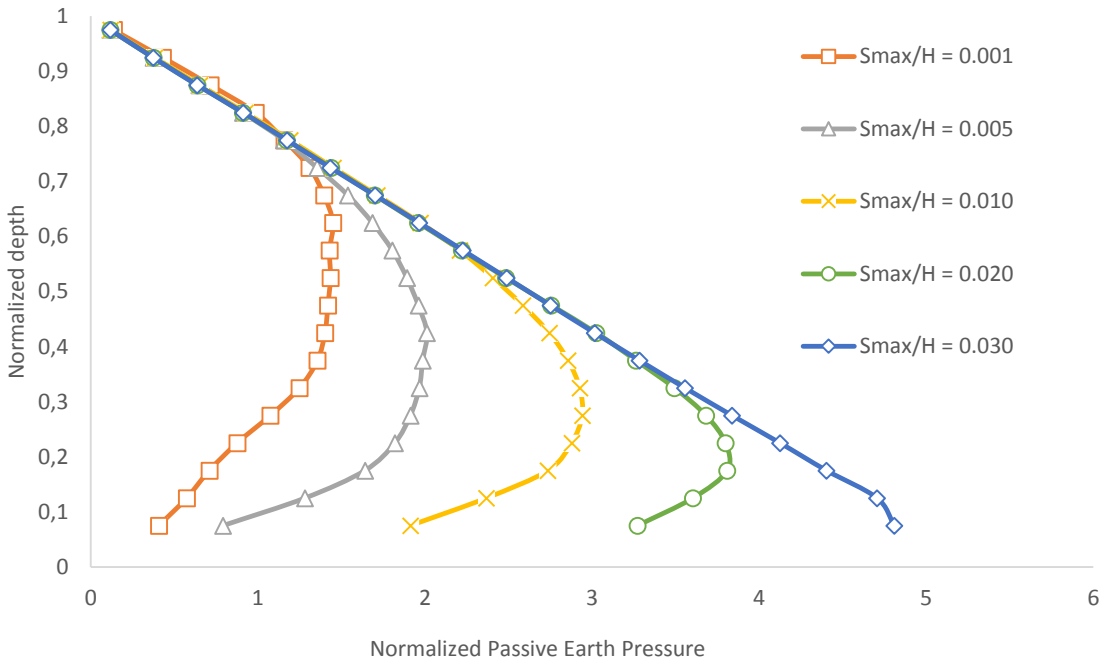

Figure 4. 14. Distribution of passive earth pressure in RB mode for various distances – Plastic-Hardening model

Moreover, the passive load distribution shape achieved with 0.20H of wall movement (S_{max}/H = 0.20) from Figure 4. 7 is attained with a wall movement of 0.001H (S_{max}/H = 0.001) in the case of the soil utilized in Figure 4. 13. This signifies that higher values of K and G result in more substantial soil stiffening and a swifter escalation of passive earth pressure as rotation intensifies. Additionally, soils with elevated stiffness reach the limit passive earth pressure with less wall movement.

The outcomes regarding the influence of wall displacement magnitude in RB mode on K_p, the location of the resultant force's point of application, and the percentage reduction rate are summarized in Table 4. 8. Here, the displacement required to achieve the limit passive earth pressure is labeled as D_{max}, with a corresponding value of K_{pmax}. The sensitivity of passive earth pressure coefficients to wall rotation is evident, with these values increasing as the magnitude of movement intensifies. However, the centroid of the earth pressure distribution decreases as the movement becomes more pronounced. Upon comparing the passive earth pressure coefficient at the limit displacement for achieving passive earth pressure (D_{max}) with the one corresponding to 10% of it in the case of Mohr-Coulomb (10% D_{max}), and 3% of it in the case of Plastic-Hardening (3% D_{max}), it is observed that the K_p value is 49% of K_{pmax} in Mohr-Coulomb and 39% of it in Plastic-Hardening. This is significantly lower than the value associated with D_{max}. Additionally, the point of application of the resulting force initially appears to be higher (positioned at *0.65H* from the wall toe in Mohr-Coulomb and .053 in Plastic-Hardening). However, this point gradually decreases with increasing wall movement until it reaches the one-third commonly utilized in classical solutions.

Table 4. 8. Variation of K_p and point of application with S_{max}/H for RB mode

Mohr-Coulomb					*Plastic-Hardening*				
S_{max}/H		*h/H*		K_p	S_{max}/H		*h/H*		K_p
0.001	10% D_{max}	0.65	2.54	49% K_{pmax}	0.001	*3% D_{max}*	0.53	1.99	*39% K_{pmax}*
0.002	20% D_{max}	0.54	2.52	49% K_{pmax}	0.005	*17% D_{max}*	0.48	2.73	*53% K_{pmax}*
0.003	30% D_{max}	0.42	3.40	66% K_{pmax}	0.010	*33% D_{max}*	0.41	3.76	*73% K_{pmax}*
0.005	50% D_{max}	0.38	3.92	76% K_{pmax}	0.020	*67% D_{max}*	0.37	4.54	*88% K_{pmax}*
0.010	D_{max}	0.33	5.16	K_{pmax}	0.030	D_{max}	*0.33*	*5.16*	K_{pmax}

The RT mode on passive earth pressure is illustrated in Figure 4. 15 and Figure 4. 16. The influence of the amount of wall movement is clear at the lower part of the wall, passive earth pressure increases with more rotation, while the lateral earth pressure at the upper part of the wall keeps null values at different stages of wall movement. Upon comparing Mohr-Hardening model in Figure 4. 15 with Plastic-Hardening model in Figure 4. 16, the later needs 0.01 of wall movement to reach limit passive earth pressure , which is much higher than that needed in Mohr-Coulomb (0.003). This increase in passive earth pressure leads to an increase on passive earth pressure coefficients with wall movement. Table 4. 9 presents those coefficients as well as the location of the centroids. K_p for $S_{max}/H = 0.0003$ in Mohr-Coulomb case starts with a value of 3, which is equal to 67% of $K_{pmax,}$ with a centroid located at *h/H=0.30*. This value increases to reach $K_{pmax} = 4.50$ *with* $S_{max}/H = 0.003$ *with a centroid equal to 0.24H*. On the other hand, K_p starts from a value of 2.11 which is equivalent to *47%* K_{pmax} at $S_{max}/H = 0.0002$ *(3%* D_{max}*)* to reach the same K_{pmax} at $S_{max}/H = 0.008$, with a resultant force situated *at* 0.30H with low wall movement to a position of 0.25H on $D_{max.}$

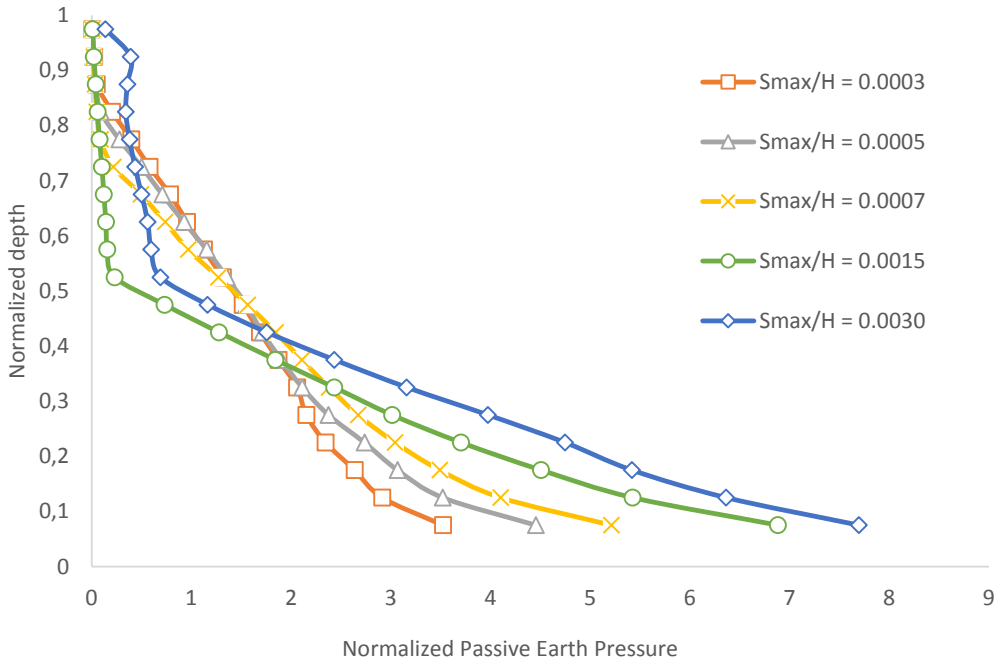

Figure 4. 15. Distribution of passive earth pressure in RT mode for various distances – Mohr-Coulomb model

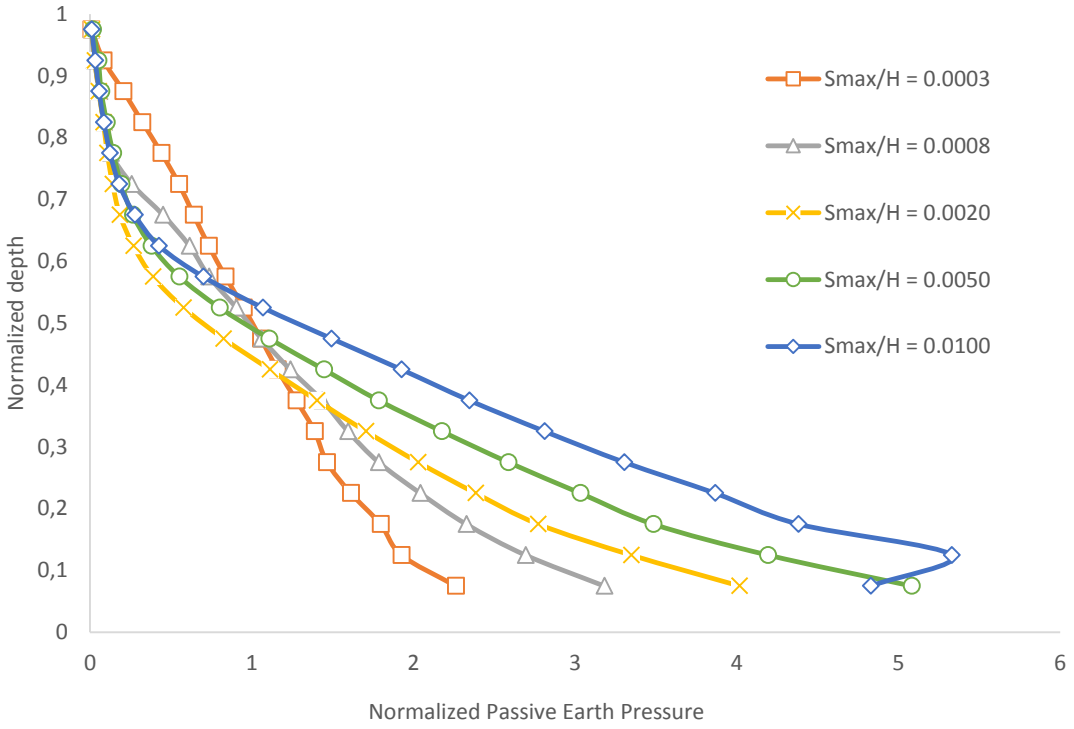

Figure 4. 16. Distribution of passive earth pressure in RT mode for various distances – Plastic-Hardening model

Table 4. 9. Variation of K_p *and point of application with* S_{max}/H *for RT mode*

Mohr-Coulomb					*Plastic-Hardening*				
S_{max}/H		*h/H*		K_p	S_{max}/H		*h/H*		K_p
0.0003	10% D_{max}	0.30	3.00	67% K_{pmax}	0.0002	*3% D_{max}*	0.30	2.11	*47% K_{pmax}*
0.0005	17% D_{max}	0.30	3.36	75% K_{pmax}	0.0007	*9% D_{max}*	0.26	2.50	*56% K_{pmax}*
0.0007	23% D_{max}	0.28	3.62	80% K_{pmax}	0.0015	*19% D_{max}*	0.24	2.78	*62% K_{pmax}*
0.0015	50% D_{max}	0.25	3.91	87% K_{pmax}	0.0030	*38% D_{max}*	0.24	3.57	*79% K_{pmax}*
0.0030	D_{max}	0.25	4.50	K_{pmax}	0.0080	D_{max}	0.25	*4.50*	K_{pmax}

4.3.6. Discussion of results for RB and RT modes

To examine the influence of wall rotation from bottom or top on the active and passive earth pressure coefficients (K_a and K_p), five values of internal friction angle φ (20°, 25°, 30°, 35°, and 40°) are considered for each of the four values of soil–wall interface friction angle δ (δ/φ = 0, 1/3, 2/3, and 1). Table 4. 10 and Table 4. 11 provides a comparative analysis between the results of Kérisel and Absi (1990) and the current numerical results of active and passive earth pressure coefficients, respectively, along with the positions of the resultant forces' points of application. The numerical study results are derived under two types of wall movement: rotation about the bottom and rotation about the top, with the wall movement being substantial enough to reach the limit passive earth pressure (D_{max}). Additionally, a case involving a wall rotating about its bottom with low wall movement (10% of D_{max})

is included in the passive case (Table 4. 11), as passive earth pressure distribution shape is notably affected by the extent of wall displacement in RB mode, as previously demonstrated. The model soil used for the analysis of the partially mobilized wall is Plastic-Hardening model, since it represent better the realistic behavior of the soil before reaching the limit stat. The results in Table 4. 10 considering the active case are provided from the study conducted by Benmebarek et al. (2016). As a results, active earth pressure magnitude is less sensitive to the type of wall movement. On the other hand, the stress distribution centroid is very far from the one-third used in the classical solutions in the case of rotation about top. The simulation results for passive earth pressure coefficients in the RB mode (seeTable 4. 11) match well with the values provided by Kérisel and Absi (1990) for sufficiently large wall movement to attain the limit passive earth pressure (D_{max}), with a discrepancy not exceeding 4.9% for K_p. The only exception occurs when φ=35° and δ/φ=2/3, resulting in a difference rate of 9.5%. This illustrates that a rigid retaining wall rotating about the base tends to exhibit similar behavior to a rigid translating wall in cases of substantial movement. However, when the wall experiences low displacement less than D_{max}, the passive earth pressure coefficients obtained from the present numerical simulation are lower. For instance, for φ =20° and δ/φ =0, K_p ranges from 1.40 to 11.15, which is approximately 60-65% of the values from Kérisel and Absi (1990). Moreover, the centroids of the passive load distribution determined by FLAC simulation in this scenario are positioned higher compared to the one-third ratio used by Kérisel and Absi (1990), ranging from 0.40H to 0.51H.

In the RT mode, the current numerical study reveals passive earth pressure coefficients that are lower than those obtained by Kérisel and Absi (1990). For example, the reduction rate reaches 22% when φ=40° and δ/φ=1. Additionally, the centroids in this mode range from 0.20H to 0.26H from the wall base, deviating significantly from the one-third ratio commonly used in literature.

These results underscore that classical solutions can adequately estimate passive earth pressure coefficients in cases of T and RB modes. However, in the RT mode, the difference rate is notably high, potentially affecting design moments and leading to non-conservative application of classical solutions. Furthermore, it is demonstrated that the conventional placement of the passive earth pressure centroid at 1/3H can be suitable for both T and RB modes, provided that the applied displacement allows passive earth pressure to stabilize. However, for RT mode, the values determined by the current numerical study offer more accurate results.

Table 4. 10. Active earth pressure coefficient (Ka) and point of application of the resultant force with various wall movement

Friction angle φ(°)	δ/φ	RT mode		RB mode		Kerisel and Absi (1990)	
		K_a	h/H	K_a	h/H	K_a	h/H
20	0	0.50	0.43	0.49	0.33	0.49	0.33
	1/3	0.48	0.43	0.46	0.33	0.46	
	2/3	0.47	0.43	0.45	0.33	0.44	
	1	0.47	0.43	0.44	0.33	0.44	
25	0	0.42	0.45	0.41	0.33	0.41	0.33
	1/3	0.40	0.45	0.38	0.33	0.38	
	2/3	0.39	0.46	0.37	0.33	0.36	
	1	0.40	0.46	0.37	0.33	0.37	
30	0	0.35	0.47	0.34	0.32	0.33	0.33
	1/3	0.33	0.47	0.32	0.32	0.30	
	2/3	0.33	0.48	0.31	0.32	0.30	
	1	0.34	0.49	0.31	0.32	0.30	
35	0	0.29	0.48	0.28	0.32	0.27	0.33
	1/3	0.27	0.48	0.26	0.32	0.25	
	2/3	0.28	0.51	0.26	0.32	0.25	
	1	0.29	0.52	0.27	0.32	0.26	
40	0	0.23	0.53	0.23	0.31	0.22	0.33
	1/3	0.22	0.54	0.21	0.31	0.20	
	2/3	0.22	0.55	0.21	0.31	0.20	
	1	0.22	0.55	0.23	0.31	0.20	

Table 4. 11. Passive earth pressure coefficient (Kp) and point of application of the resultant force with various wall movement

Friction angle φ(°)	δ/φ	RT $S_{max}/H=D_{max}$		RB $S_{max}/H=D_{max}$		RB $S_{max}/H=10\%D_{max}$		Kerisel and Absi (1990)	
		K_p	h/H	K_p	h/H	K_p	h/H	K_p	h/H
20	0	2.03	0.23	2.05	0.34	1.40	0.44	2.05	0.33
	1/3	2.31	0.24	2.42	0.34	1.47	0.48	2.40	
	2/3	2.59	0.25	2.78	0.34	1.66	0.49	2.75	
	1	2.81	0.26	3.01	0.33	2.17	0.45	3.10	
25	0	2.45	0.23	2.47	0.34	1.62	0.42	2.45	0.33
	1/3	2.95	0.25	3.12	0.33	1.74	0.45	3.10	
	2/3	3.30	0.25	3.78	0.33	1.98	0.48	3.70	
	1	3.72	0.26	4.32	0.33	2.15	0.51	4.40	
30	0	2.87	0.23	3.08	0.34	1.73	0.48	3.00	0.33
	1/3	3.42	0.24	4.05	0.33	2.63	0.42	4.00	
	2/3	4.50	0.25	5.16	0.33	2.44	0.51	5.30	
	1	5.18	0.26	6.26	0.34	3.64	0.47	6.50	
35	0	3.72	0.20	3.61	0.33	2.17	0.46	3.70	0.33
	1/3	4.95	0.22	5.29	0.33	3.17	0.48	5.40	
	2/3	6.11	0.24	7.24	0.33	5.07	0.41	8.00	
	1	7.62	0.23	10.11	0.34	6.37	0.45	10.50	
40	0	4.25	0.18	4.72	0.33	2.29	0.50	4.50	0.33
	1/3	6.30	0.20	7.65	0.34	5.02	0.42	7.60	
	2/3	9.54	0.23	12.14	0.34	7.04	0.46	12.00	
	1	14.03	0.26	17.24	0.34	11.15	0.42	18.00	

4.4. CONCLUSIONS

The numerical analysis of active and passive earth pressure coefficients, load distributions, and centroids for retaining walls undergoing translation (T), rotation about bottom (RB), and rotation about top (RT) modes has been conducted using FLAC code. Several key conclusions can be drawn from this study:

- The comparison of the current results of passive earth pressure distributions and coefficients with existing literature for the T mode demonstrates the effectiveness of the employed numerical model. Furthermore, the identified distributions of maximum shear strain rates for T, RB, and RT modes exhibit a close resemblance to the shear zones observed in experiments.

- In the RT mode, the obtained results reveal lower passive earth pressure coefficients compared to those in the T mode and those derived from the work of Kérisel and Absi (1990). The resulting earth pressure distribution centroids are situated below the commonly used one-third position as per standard literature. While conventional passive earth pressure methods are suitable for T and RB modes, they prove to be non-conservative for RT mode. Therefore, it is recommended to use the values proposed by the current numerical study for this mode.

- In the RB mode, wall rotation leads to full mobilization of the passive earth pressure at the upper part of the wall and partial mobilization, which diminishes rapidly, eventually approaching earth pressure at rest near the wall toe. As a result, the earth pressure centroid is positioned higher than one-third. This distribution shifts from nonlinear to linear with increased wall movement, ultimately reaching a steady state similar to that observed in the T mode.

- The distribution of active earth pressure behind the wall is nonlinear, and the earth pressure distribution differs depending on the mode of wall movement (T, RB, and RT). Based on the obtained results, it has been found that the active earth pressure resultant is less sensitive to the displacement modes, but the point of application of the resultant is very far from the value used by the classical solutions for rotation about the top (Benmebarek et al. 2016).

- The increase in passive earth pressure with wall movement is notably influenced by the stiffness of the soil. Soils with high stiffness exhibit a more rapid rise in passive earth pressure as the movement intensifies.

- RB and RT modes require more movement to attain the limit passive earth pressure compared to the T mode. For soils with low stiffness, a wall displacement of 0.1H, as commonly recommended in literature, may be insufficient for RB and RT modes.

- This study provides compelling evidence of the impact of the soil-wall friction angle on passive earth pressure in all three cases of wall movement. Furthermore, it furnishes passive earth pressure coefficients and passive load distribution centroids for practical values of soil internal friction angle and soil-wall friction angle when the wall is subjected to rotational movement.

Chapter V

LATERAL EARTH PRESSURE DUE TO SURCHARGE LOADING UNDER VARIOUS MODES OF WALL MOVEMENT

5.1. INTRODUCTION

The existing methods to evaluate the active and passive earth pressure until to date give less attention to the effect of surcharge loading. Reddy et al. (2014) coupled the limit equilibrium approach with method of slices to determinate passive earth pressure under surcharge loading. Patki et al. (2017) extended the analysis of Kame (2012) using the limit equilibrium analysis basing on Kötter's (1903) equation to investigate the passive earth pressure due to surcharge loading. Liu et al. (2018) developed a modified logarithmic spiral approach using the limit equilibrium method to numerically and analytically evaluate the effect of surcharge loading on passive earth pressure. Cai et al. (2017) investigated the existing arching effect theory (Handy, 1985; Paik & Salgado 2003; Ying et al. 2006; Shubhra & Patra 2008; Dalvi & Pise 2012) on passive earth pressure under a uniform surcharge loading. In addition to various studies in literature investigating strip surcharge (Georgiadis & Anagnostopoulos, 1998; Hou & Shu, 2019; Xiao & Xia ,2020), reinforced backfill (Xiao et al., 2016; Ertugrul & Aurelian, 2011; Li et al., 2020; Gade & Dasaka, 2022) and passive earth pressure due to surcharge loading under unsaturated conditions (Deng & Yang; 2019). However, those studies considered only the translation movement of the retaining wall.

The effect of type of wall movement on active and passive earth pressures has been evaluated in many previous studies (Potts and Fourie 1986; Fang et al., 1994 ; Peng et al., 2012 ; Vo et al., 2016; Dou et al., 2017; Tang et al., 2018; Patel & Deb, 2020; Lanabi et al., 2022). However, no one of those researchers investigated this effect under surcharge loading. Dave & Dasaka (2012) experimentally examined the variation of the distribution and the magnitude of lateral earth pressure on a small-scale rigid retaining wall with cohesionless backfill under uniform surcharge loading, subjected to rotating about base. The test investigated the variation of both active and passive earth pressures with the increment of wall rotation. The examined wall movement on the model wall in passive case was not enough to reach limit passive earth pressure, due to constraint from top surcharge plate as the authors explained. Based on this laboratory results, the effect of wall rotation on passive earth pressure due to surcharge loading will be investigated on this paper. Furthermore, various Previous researchers in last decades proved that three-dimensional studies can provide a more realistic solutions and more accurate

results (Soubra & Regenass, 2000; Škrabl & Macuh, 2005; Benmebarek et al., 2008; AbdelSalam et al., 2017; Yang & Li, 2017; Javankhoshdel et al.,2019; Schmüdderich et al., 2019; Schmüdderich et al., 2020; Tangjarusritaratorn et al., 2022; Wei et al, 2022). The aim of this chapter is to investigate the effect of a retaining wall subjected to three types of wall movement; translation (T), rotation about top (RT) and rotation about bottom (RB), on active and passive earth pressures due to uniform surcharge loading. The analysis evaluates the load distribution shape along depth, as well as the magnitude of earth pressure coefficients in both 2D and 3D cases using FLAC, as none of the existing experimental tests and laboratory studies coved this impact. The obtained numerical results were validated and compared with those available in literature.

5.2. VALIDATION OF THE NUMERICAL MODEL

Same mesh described previously (3.6) is used for the analysis of the lateral earth pressure. The soil parameters are set to be the same as the one used in the experimental study conducted by Dave and Dasaka (2012). The adopted unit weight is the same presented in the laboratory test $\gamma = 16\ kN/m^3$, the friction angle is $= 30°$ and the cohesion $c = 0$. Since limit passive earth pressure has not been reached in the experimental test, that is why the Plastic-Hardening constitutive model will be used for the comparison. The secant stiffness is taken equal to $E_{50}^{ref} = 35MPa$, with a tangent stiffness $E_{oed}^{ref} = 35MPa$, an unloading-reloading stiffness $E_{ur}^{ref} = 140MPa$, an exponent $m = 0.63$, a reference pressure $\mathrm{p}^{ref} = 100kPa$, and a Poisson's ratio $v = 0.3$. Parameters are summarized in Table 5. 1. The system is balanced under the gravity condition and extra stiffness from the interface element with some steps. Once the balance is reached, the model is returned to its initial state. Afterward, a vertical stress equal to 50kPa is applied on the ground surface in order to simulate the uniform surcharge loading, with a controlled velocity applied on the wall to simulate the three types of wall movement. The soil-wall interface friction angle has a zero value ($\boldsymbol{\delta = 0}$) in order to compare results with the ones from Rankine. During the displacement of the model wall, the plastic soil deformation behind the wall is increasing, and the horizontal passive earth pressure acting on the retaining wall side can be obtained using a FISH function until reaching a stable plastic flow state.

Figure 5. 1 and Figure 5. 2 present respectively the distributions along depth of active and passive earth pressure under 50 KPa of uniform surcharge loading with different rotation magnitudes about top, where they are compared with the experimental results of Dave and Dasaka (2012) in addition to Rankine's (1857) equation. Both results from experiment and numerical modeling in Figure 5. 1 represent a curved distribution of active earth pressure with depth, contraty to the one reported by Rankine's equation. Active earth pressure magnitude obtained by FLAC reaches with 2E-4 radians of wall rotation the same one obtained by the test with wall rotation equal to 4.21E-3. This is

due to the low stiffness of the reduced laboratory soil. However, an agreement can be noticed between the results of the two methods.

Table 5. 1. Plastic-Hardening soil parameters representing Dave and Dasaka (2012) experiment

Parameter	Value
Unit weight (γ)	16 KN/m^3
Soil friction angle (φ)	30°
Dilation angle (ψ)	30°
Cohesion (c)	0
E_{50}^{ref}	35 MPa
E_{50}^{oed}	35 MPa
E_{ur}^{ref}	140 MPa
m	0.63
Poisson's ratio (v)	0.30

Upon comparing the results of passive earth pressure from Figure 5. 2, it can be noticed that the magnitude of the obtained passive stress from laboratory test continue on increasing with more wall movement. The maximal wall rotation conducted in the test was 5.13e-3 Radians due to the limitation of the experimental set up used as described by the authors. Furthermore, a huge difference can be observed in the magnitude of passive earth pressure between the experiment and Rankine's formula. The reason is that the wall movement was not enough to reach limit passive earth pressure. In the other hand, the distribution of passive load from the experiment corresponding to 3.18e-4 radians of wall rotation seems to be reached with only 2.5e-4 radians from the present numerical study, and the other obtained with 5.13e-3 from the experimental test is reached with 2.00e-3 radians numerically. This is due to the difference in stiffness between the two models. Laboratory soil represents a reduced model, while the numerical one represents the behavior of rough compacted soils with higher stiffness parameters. Previous researches from literature proved that high stiffness soils exhibits a more rapid increase in passive earth pressure with the increase of wall movement (Vo et al., 2016; Lanabi et al., 2022). Moreover, it can be noticed from the figure that lateral earth pressure from the present study keeps on increasing with more wall movement until reaching Rankine's linear distribution at the upper half of the wall. This distribution changes from linear to non-linear starting from the middle of the wall, where lateral earth pressure decreases sharply to approach earth pressure at rest at the wall base. As a result, numerical simulation agrees with laboratory test at low wall rotations. Then later, more wall movement resolves higher passive earth pressure, which explains that the limit value has not reached yet. The distribution shape obtained with high wall movement converges to Rankine's result at the top of the wall with a curved distribution shape at the bottom.

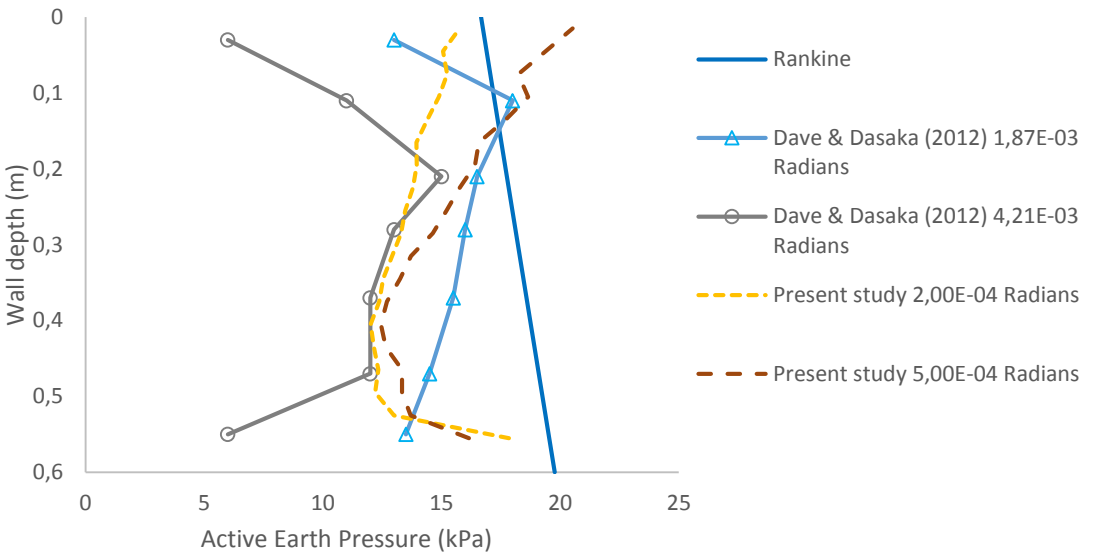

Figure 5. 1 Active earth pressure with 50kPa surcharge load

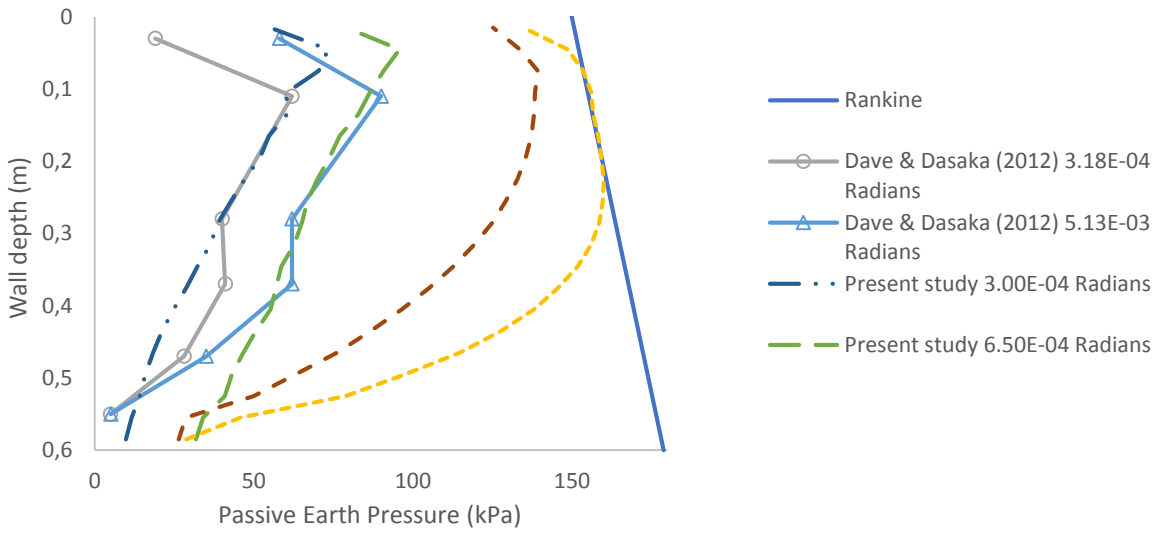

Figure 5. 2. Passive earth pressure with 50kPa surcharge load

5.3. EVOLUTION OF LATERAL EARTH PRESSURE WITH WALL MOVEMENT

Two constitutive models has been associated to the model soil for the present numerical model for comparison purpose in this section; Mohr-Coulomb and Plastic Hardening. The Plastic-Hardening possesses the same parameters described in Table 5. 1, while the associated Mohr-Coulomb constitutive model are summarized in Table 5. 2. Same surcharge loading of 50KPa is applied to the model soil, with various magnitudes of wall rotation in RT and RB modes.

Table 5. 2. Mohr-Coulomb soil parameters representing Dave and Dasaka (2012) experiment

Parameter	Value
Unit weight (γ)	16 KN/m^3
Soil friction angle (φ)	30°
Dilation angle (ψ)	30°
Cohesion (c)	0
E	35 MPa
Poisson's ratio (υ)	0.30

The active earth pressure is less sensitive to the magnitude of wall displacement as demonstrated in the previous chapter. The distributions of passive earth pressure with depth registered on various wall angles, either from bottom (in RT) or from top (in RB) are illustrated in Figure 5. 3 and Figure 5. 4 respectively. In RT mode, both Figure 5. 3a and Figure 5. 3b, representing Mohr-Coulomb and Plastic-Hardening models respectively, show an increase on the lateral earth pressure with wall movement until reaching the limit value at about 1.70E-02 Radians of wall rotation. Furthermore, it is clean that both constitutive models present curved distribution shapes, which are identical to each other in the case of a retaining wall rotating about top.

Figure 5. 4 representing the RB mode, shows that passive earth pressure increases with the increase of wall movement until reaching the limit stat on a wall rotation angle equal to 1.70E-04 Radians, with a curved distribution shape. What can be concluded here is that the distribution shape at the upper half of the wall is identical in the two models where the soil reaches a limit plastic state. However, the distributions obtained with Mohr-Coulomb model (Figure 5. 4a) decrease sharply with depth to reach a zero value at the wall base, where the ones from Plastic-Hardening model (Figure 5. 4b) show more curved distribution, which explains than using this last constitutive model gives more accurate results. Hence, Plastic-Hardening model will be used in evaluation of the effect of type of wall movement on passive earth pressure due to surcharge loading in the next sections

5.4. ACTIVE AND PASSIVE EARTH PRESSURE DISTRIBUTION

To investigate how the active and passive earth pressures due to surcharge loading is affected by the type of wall movement. The soil is considered weightless ($\gamma = 0$), and only applied forces to the mesh are the surcharge loading, in addition to the wall movement. In order to verify the accuracy of this weightless numerical model, the distribution of active and passive earth pressures along depth under a uniform surcharge loading equal to 50 KPa in two cases of wall roughness ($\delta/\varphi = 0 \; and \; \delta/\varphi = 2/3$) are compared with earth pressure coefficients due to surcharge loading from Caquot and Kérisel (1948). The comparison is presented in Figure 5. 5 for the active case and Figure 5. 6 for the passive one. It can be noticed that the distribution of both active and passive earth

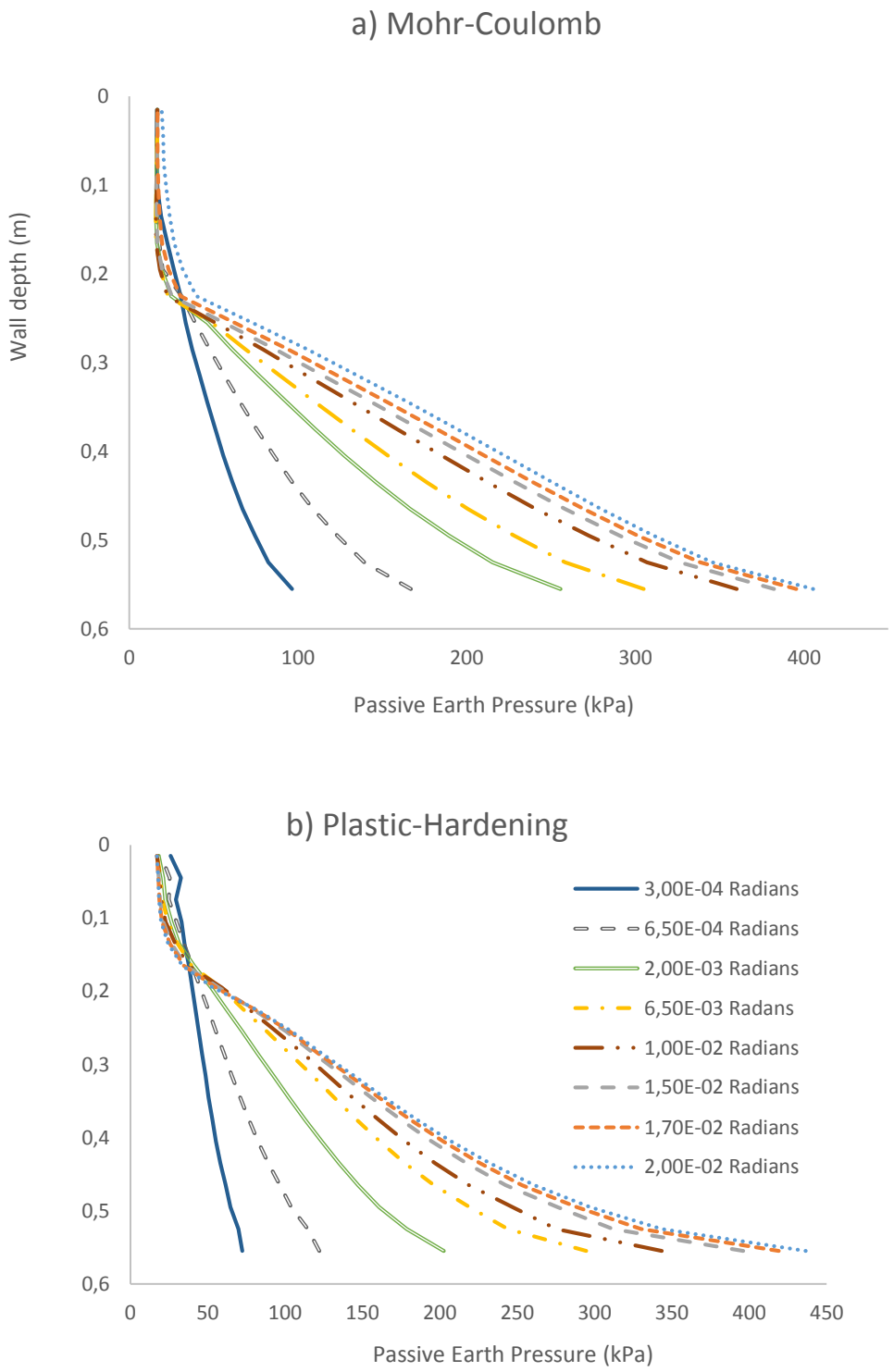

Figure 5. 3. Passive earth pressure distribution with various wall rotations in RT mode. A) Mohr-Couomb b) Plastic-Hardening

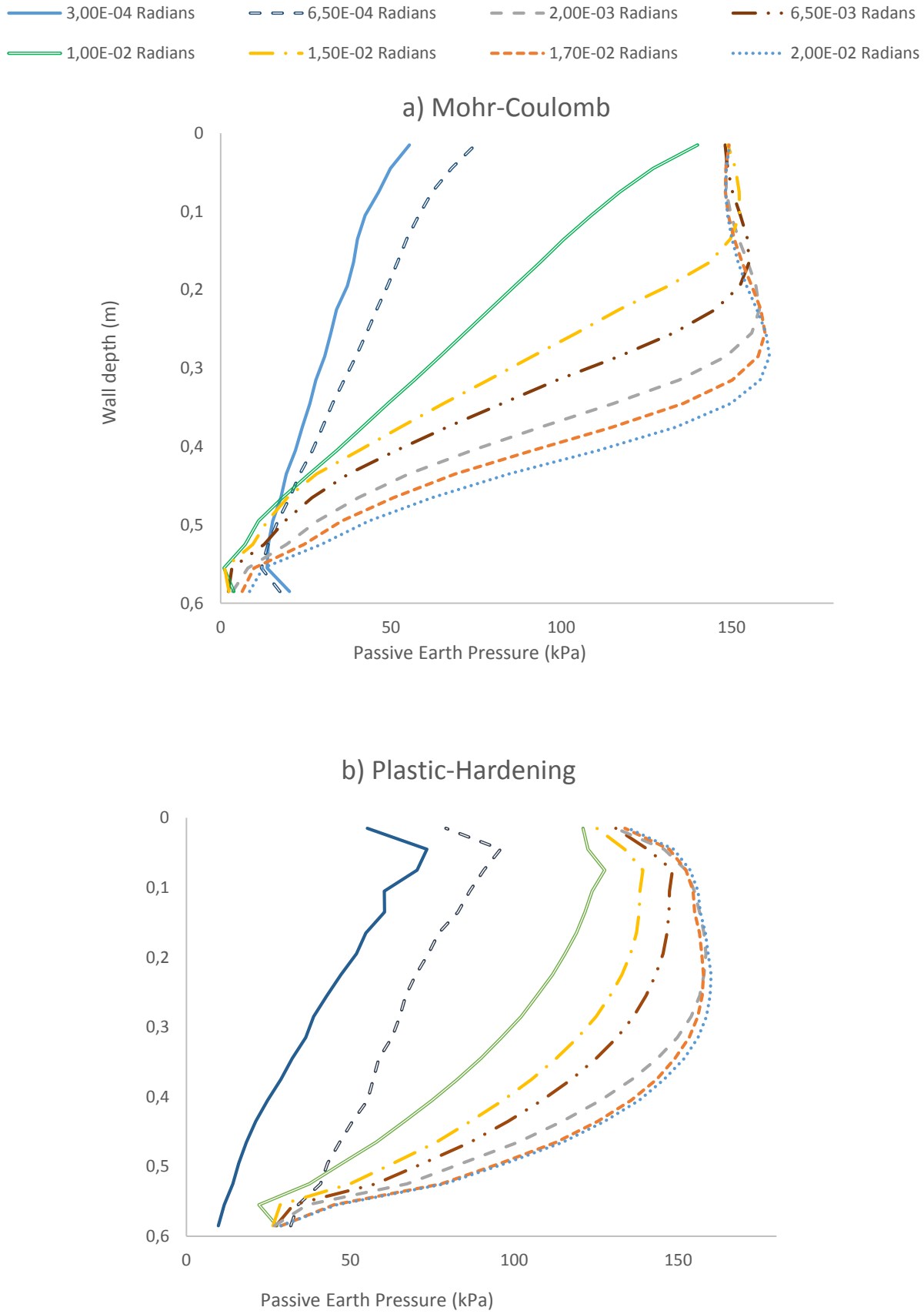

Figure 5. 4. Passive earth pressure distribution with various wall rotations in RB mode. A) Mohr-Coulomb b) Plastic-Hardening

pressures in translation mode case matches well with the one from Caquot and Kérisel (1948), representing a uniform distribution with a centroid situated at the middle of the wall. However, in the rotational mode case, either about top or about bottom, the distribution of lateral earth pressure heavily changes from linear to non-linear. This affects the earth pressure coefficients as well as the distribution centroid, which will be studied in the next session.

The distribution of active and passive earth pressures along the depth in both cases; rotation about top (RT) and rotation about bottom (RB) is investigated. Four different values of soil-wall interface friction angle ($\delta/\varphi = 0, 1/3, 2/3 \ and \ 1$) are taken into consideration for each of the three values of internal friction angle ($\varphi = 20°, 30° \ and \ 40°$). Results are presented in Figure 5. 7 and Figure 5. 8 for active and passive modes respectively. It can be noticed that Active earth pressure distribution is less not heavily affected by the type of wall movement (see Figure 5. 7). RT mode resolves an increase on earth pressure at the upper part with a decrease in the lower part, while RB mode shows a reverse situation; as the earth pressure increases at the lower half and decreases at the upper one. In the case passive earth pressure (Figure 5. 8), RT mode resolves almost null earth pressure at the wall top, then it increases with depth to reach a maximal value at the wall bottom with a curved distribution. Hence, the distribution centroid in this case is at about 0.25 of the wall height. RB mode shows a uniform distribution of passive earth pressure at the upper part. Afterwards, starting from the middle of the wall, passive earth pressure distribution sharply decreases with wall depth to reach a zero value at the bottom. Passive earth pressure centroid in this case is situated at a higher position of about 0.75H. As a results, curves presented in figures proves well that the rectangular distribution of active and passive earth pressure behind retaining walls with a centroid that appears at the middle of the wall is no longer valid in the case of a retaining wall subjected to rotation movement. The location of active and passive load centroid is situated either at 0.25H in RT mode, or 0.75H in RB mode.

5.5. FAILURE MECHANISM

Figure 5. 9 illustrates the failure mechanisms represented by the distribution of maximum shear strain increment at the end of the run for the weightless model soil subjected to 50 KPa of uniform surcharge loading. The three types of wall movement were considered when $\varphi = 30°$ and $\delta/\varphi = 2/3$. Passive shear zones are situated at the right of the wall, while the active zones are on the left. T mode shows a curved zone that starts from the wall bottom, accompanied by a second weaker shear zone propagating from the top of the retaining wall. However, RT mode shows only one shear zone with a curved shape appears at the wall bottom. RB mode results multiple curved shear zones

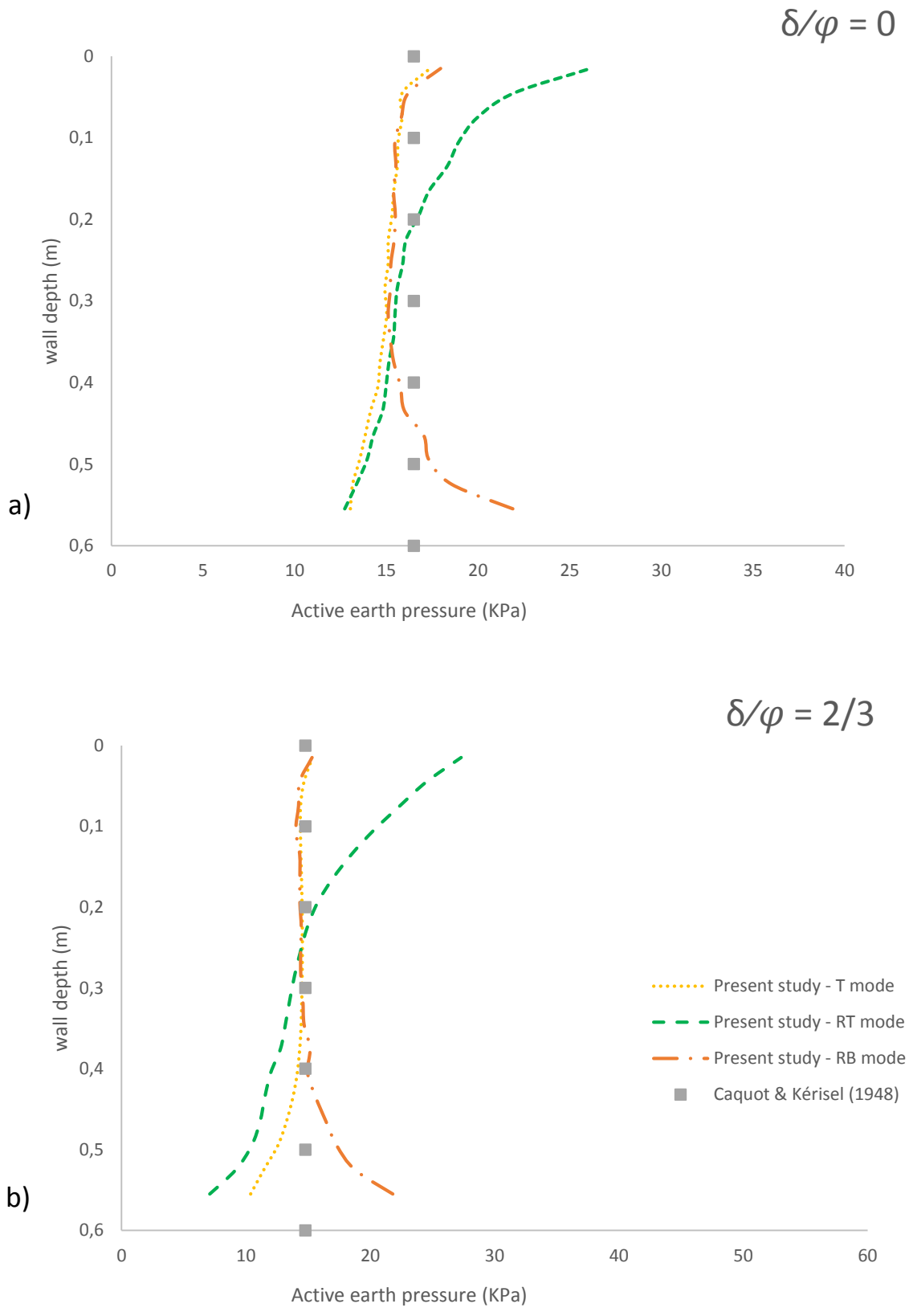

Figure 5. 5. Active earth pressure distribution with $\varphi = 30°$, (a) $\delta/\varphi = 0$ and (b) $\delta/\varphi = 2/3$

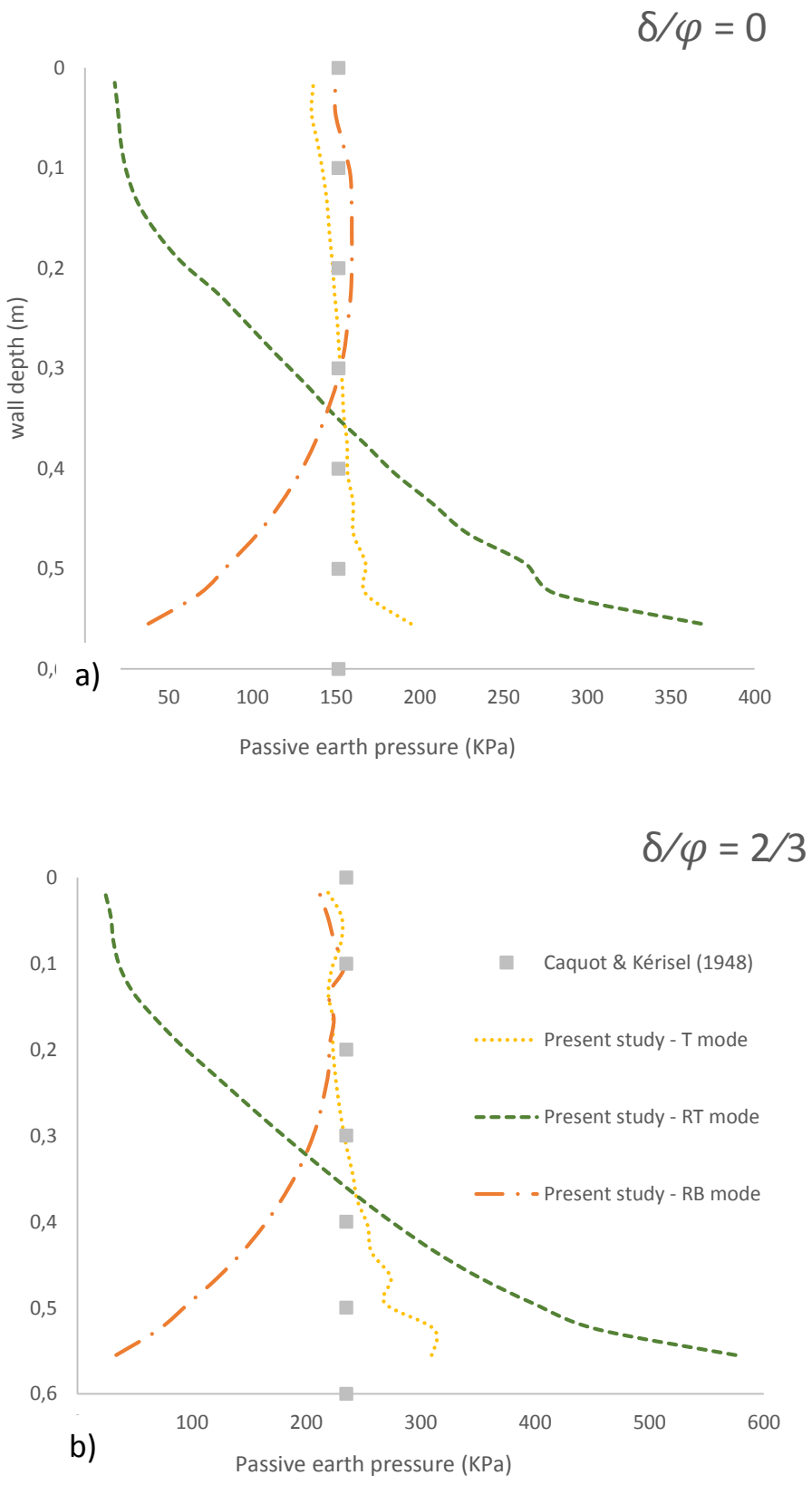

Figure 5. 6. Passive earth pressure distribution with $\varphi = 30°$, *(a)* $^{\delta}/_{\varphi} = 0$ *and (b)* $^{\delta}/_{\varphi} = {}^{2}/_{3}$

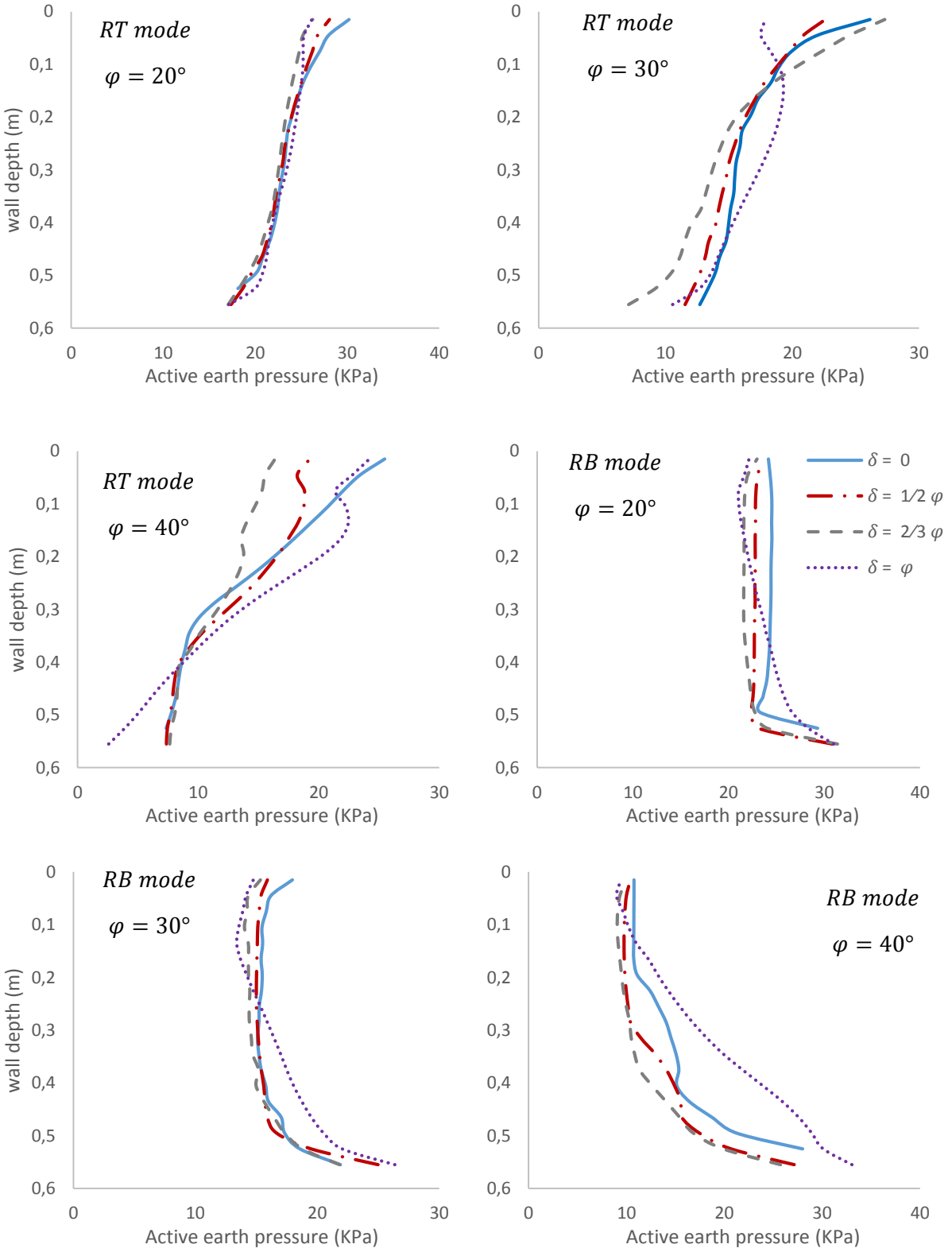

Figure 5. 7. Active earth pressure distribution in RT and RB modes with various φ and δ values

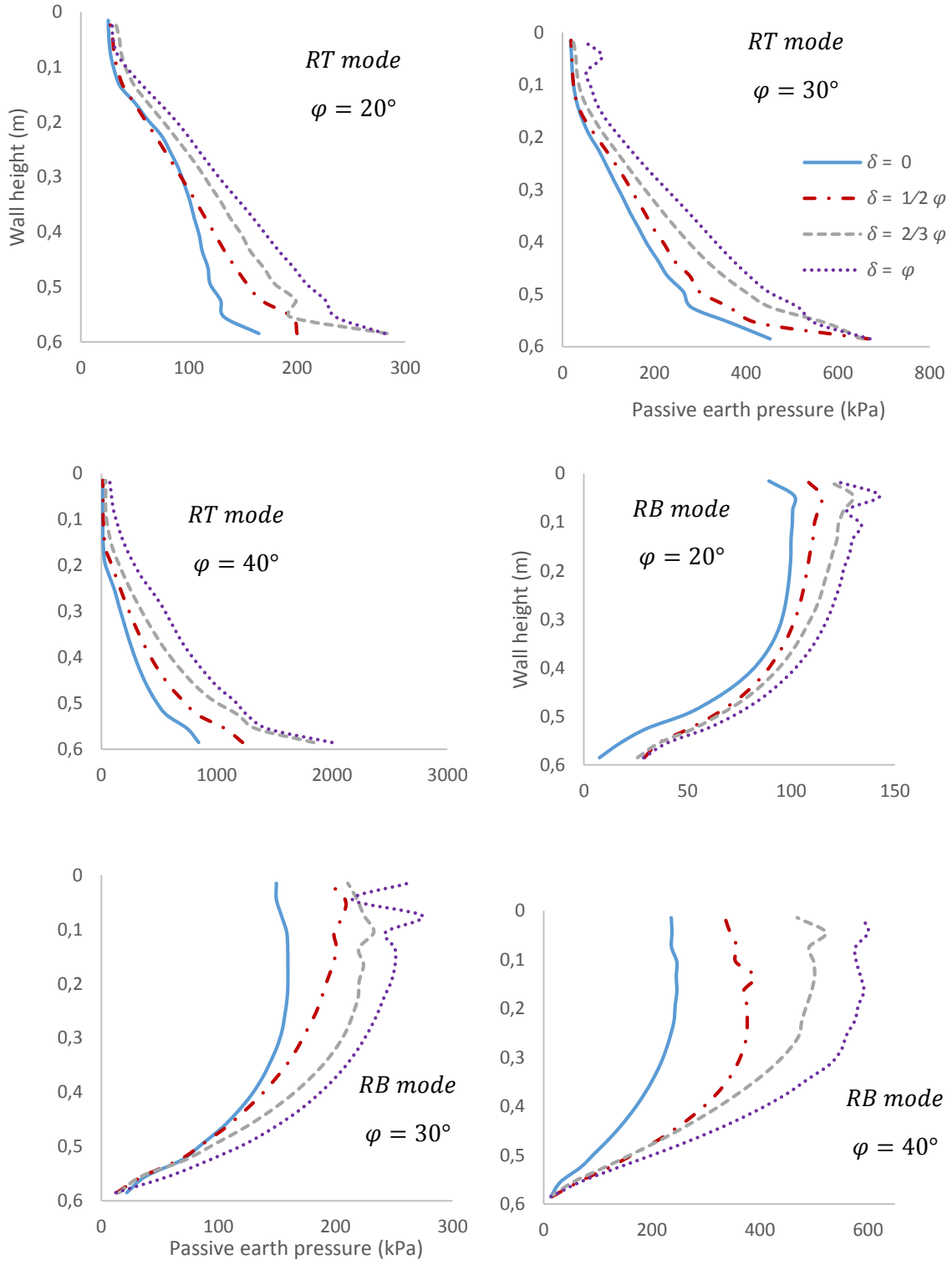

Figure 5. 8. Passive earth pressure distribution in RT and RB modes with various φ and δ values

parallel to each other concentrated at the upper part of the wall. The figure explains clearly the influence of the type of wall movement on the failure mechanism in both cases, active and passive earth pressures.

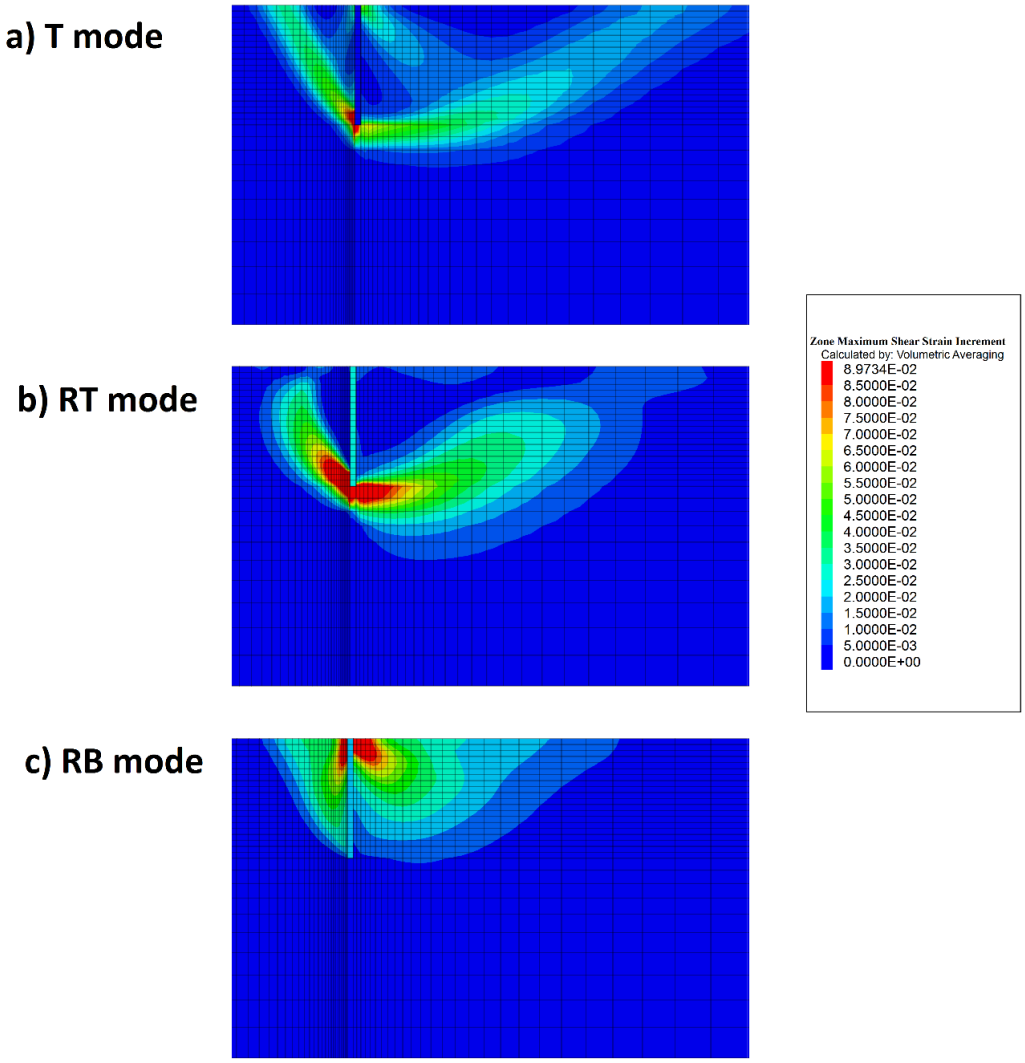

Figure 5. 9. Maximum shear strain increment under various modes of wall movements

5.6. THREE DIMENSIONAL PASSIVE EARTH PRESSURE

5.6.1. Calculation process

What follows describes how to obtain the three-dimensional active and passive earth pressure coefficients due to surcharge loading from the generalized formula described by (Caquot & Kérisel, 1948; Soubra & Regenass, 2000):

$$P_a = K_{a\gamma}.\gamma\frac{h^2}{2}.b + K_{aq}.q.h.b + K_{ac}.c.h.b \qquad (5.1)$$

$$P_p = K_{p\gamma}.\gamma\frac{h^2}{2}.b + K_{pq}.q.h.b + K_{pc}.c.h.b \qquad (5.2)$$

where γ is the soil unit weight; h is the wall depth; b is the width of the wall; c is the soil cohesion, q is the uniform surcharge loading on the ground surface. $K_{a\gamma}, K_{aq}$ and K_{ac} are active earth pressure coefficients while $K_{p\gamma}, K_{pq}$ and K_{pc} are passive earth pressure coefficients due to soil weight, cohesion and surcharge loading, respectively. P_a and P_p are the total active and passive earth pressures which can be extracted from the following relationship:

$$P_a = \frac{P_{ax}}{\cos\delta} \qquad (5.3)$$

$$P_p = \frac{P_{px}}{\cos\delta} \qquad (5.4)$$

P_{ax} and P_{px} are the horizontal active and passive earth pressures respectively obtained from FLAC fish functions, and δ is the soil–wall friction angle.

Since the current study investigates cohesionless soils, the third part of equations *(5.1)* and *(5.2)* considering the earth pressure coefficients due to cohesion will be null. Hence, it can be written as follow:

$$P_a = K_{a\gamma}.\gamma\frac{h^2}{2}.b + K_{aq}.q.h.b \qquad (5.5)$$

$$P_p = K_{p\gamma}.\gamma\frac{h^2}{2}.b + K_{pq}.q.h.b \qquad (5.6)$$

In the weightless model, γ is equal to zero, and the first part of the equations will be also null, and K_{aq} and K_{pq} can b then deduced from the following:

$$K_{aq} = \frac{P_{ax}}{q.h.b.\cos\delta} \qquad (5.7)$$

$$K_{pq} = \frac{P_{px}}{q.h.b.\cos\delta} \qquad (5.8)$$

Only equation 5.8 for determining the three-dimensional passive earth pressure coefficients will be used in the next section, due to the huge sensitivity of passive earth pressure to the type of wall movement proved previously. Active earth pressure can be investigated using equation 5.7 through further studies.

5.6.2. Passive earth pressure coefficient

In order to evaluate the three dimensional effect of wall rotational movement, passive earth pressure coefficients due to surcharge loading are evaluated for various wall geometries ($^{b}/_{h}$). Five

internal friction angles φ (20°, 25°, 30°, 35° and 40°) are taken into account for each of the four values of interface friction angle (δ/φ = 0, 1/3, 2/3 and 1). Results are listed in Table 5. 3. Three dimensional passive earth pressure coefficients obtained in translation mode case (T mode) for various values of b/h are extracted from Benmebarek et al. (2008). The ones in RT and RB modes, as well as those in 2D, are derived from the present numerical simulation, using equation (4). What is observed is that the displacement mode has a significant influence on the obtained passive earth pressure coefficients. RT mode resolves values ranging from 74 to 98% of the ones obtained in T mode. However, RB modes shows less values ranging from 63% to 93%. Those values are limit passive earth pressure coefficients behind retaining wall subjected to rotational movement, which are used for the stability of many retaining structures. The over estimation of passive earth pressure coefficients leads to the unsecure and instability on the design of such retaining structures.

5.6.3. Comparison with results from literature

Figure 5. 10 presents a comparison between the obtained passive earth pressure coefficients due to surcharge loading in RT and RB modes from the present numerical simulation and those from literature (Soubra & Regenass, 2000; Škrabl & Macuh, 2005; Benmebarek et al., 2008) when $\varphi = 30°$, $\delta/\varphi = 2/3$ and different values of b/h ratio. It can be seen that K_{pq} increases with the decrease of the width b/h. Soubra & Regenass (2000) as well as Škrabl & Macuh (2005) show higher values, which is due to the unrealistic estimation of failure mechanism of those analytical methods as explained by Benmebarek et al. (2008). However, passive earth pressure coefficient obtained in RT mode seem to be lower than the ones from previous studies. RB mode results much lower values, which explains passive earth pressure coefficients due to surcharge loading are heavily influenced by the rotational movement of the retaining wall.

5.1.1. Shape factors

In many previous studies (Soubra & Regenass, 2000; Schmüdderich et al., 2020), a shape factor has been proposed to facilitate the practical application of passive earth pressure coefficients. In this study, two values μ_{RT} and μ_{RB} were defined to represent the shape factors matching K_P^{RT} and K_P^{RB} values with K_P^T ones respectively, described as:

$$\mu_{RT} = \frac{K_P^{RT}}{K_P^T} \quad (5.5)$$

$$\mu_{RB} = \frac{K_P^{RB}}{K_P^T} \quad (5.6)$$

Table 5. 3. Three dimensional Passive earth pressure coefficients due to surcharge loading

b/h	φ(°)	Soil-wall interface friction angle (δ/φ)											
		0			1/3			2/3			1		
		T	RT	RB	T	RT	RB	T	RT	RB	T	RT	RB
0.25	20	5.41	5.30	4.79	6.09	5.80	5.30	6.74	6.46	5.83	7.45	6.80	6.13
	25	8.08	7.75	7.36	9.65	9.02	8.79	11.28	10.94	9.81	12.85	11.98	10.30
	30	12.04	11.60	11.03	15.39	15.00	14.23	19.10	18.06	16.72	22.52	21.00	17.99
	35	17.86	17.50	16.38	24.90	23.76	23.25	33.39	30.63	28.44	42.63	38.38	32.07
	40	27.55	27.10	25.21	42.53	39.06	39.28	63.24	53.68	53.48	82.45	75.65	58.25
0.5	20	3.92	3.69	3.31	4.50	4.24	3.85	5.04	4.49	4.09	5.55	4.73	4.53
	25	5.53	5.34	4.78	6.70	6.20	5.84	7.87	7.20	6.48	9.02	8.34	7.03
	30	7.85	7.71	6.87	10.17	9.33	8.82	12.72	11.45	10.44	15.48	13.78	11.93
	35	11.19	11.01	10.08	15.80	14.35	13.84	21.30	18.21	17.81	28.00	24.04	19.92
	40	16.32	16.01	14.93	25.78	22.78	22.52	38.78	31.99	31.04	55.27	46.24	37.63
1	20	3.04	2.76	2.57	3.52	3.15	2.92	3.95	3.34	3.32	4.33	3.52	3.50
	25	4.10	3.74	3.60	4.98	4.38	4.38	5.86	5.30	4.87	6.76	5.89	5.37
	30	5.57	5.12	4.87	7.23	6.20	6.39	9.05	7.56	7.57	11.02	9.29	8.26
	35	7.63	7.12	6.75	10.76	9.04	9.79	14.61	11.95	11.88	18.82	15.60	13.65
	40	10.86	10.12	9.58	16.93	14.86	14.51	25.67	19.61	20.35	35.80	28.89	23.00
2	20	2.58	2.32	2.04	2.97	2.60	2.37	3.32	2.73	2.59	3.62	2.87	2.74
	25	3.33	2.98	2.79	4.05	3.44	3.36	4.75	3.95	3.69	5.39	4.52	3.93
	30	4.33	3.88	3.58	5.63	4.66	4.61	7.06	5.59	5.47	8.43	6.83	6.26
	35	5.77	5.14	4.86	8.09	6.52	6.82	10.97	8.23	8.67	14.06	11.05	10.00
	40	7.87	6.99	6.55	12.29	9.92	10.23	18.39	14.00	14.58	25.16	19.61	16.81
5	20	2.30	2.07	1.84	2.63	2.26	2.08	2.93	2.36	2.37	3.15	2.64	2.43
	25	2.87	2.55	2.32	3.46	2.87	2.79	4.03	3.28	3.25	4.51	3.65	3.29
	30	3.62	3.18	2.99	4.64	3.73	3.99	5.73	4.49	4.57	6.73	5.24	4.90
	35	4.61	4.06	3.96	6.36	5.11	5.41	8.56	6.32	6.83	10.69	8.01	7.32
	40	6.08	5.26	5.36	9.28	8.31	7.80	13.65	10.87	10.93	17.73	13.53	11.50
10	20	2.21	1.98	1.83	2.52	2.13	2.05	2.79	2.29	2.29	3.01	2.51	2.30
	25	2.72	2.41	2.21	3.26	2.67	2.66	3.80	2.94	2.95	4.23	3.38	3.24
	30	3.38	2.97	2.85	4.30	3.45	3.63	5.33	4.50	4.21	6.20	4.90	4.60
	35	4.13	3.61	3.52	5.83	4.46	5.06	7.82	6.13	6.30	9.57	7.44	6.68
	40	5.15	4.36	4.32	8.32	7.58	6.99	12.25	10.25	9.62	15.23	12.21	10.08
2D	20	2.04	1.81	1.65	2.35	1.99	1.87	2.65	2.17	2.02	2.83	2.47	2.17
	25	2.44	2.12	2.11	3.03	2.59	2.50	3.56	3.05	2.73	4.00	3.23	2.87
	30	3.03	2.61	2.67	3.69	3.11	3.13	5.00	3.99	3.58	5.88	4.78	4.05
	35	3.60	3.29	3.13	5.28	4.26	4.23	7.10	5.83	5.11	8.90	7.29	6.04
	40	4.68	4.14	3.82	7.79	7.06	6.10	10.72	8.70	7.58	14.60	11.46	9.17

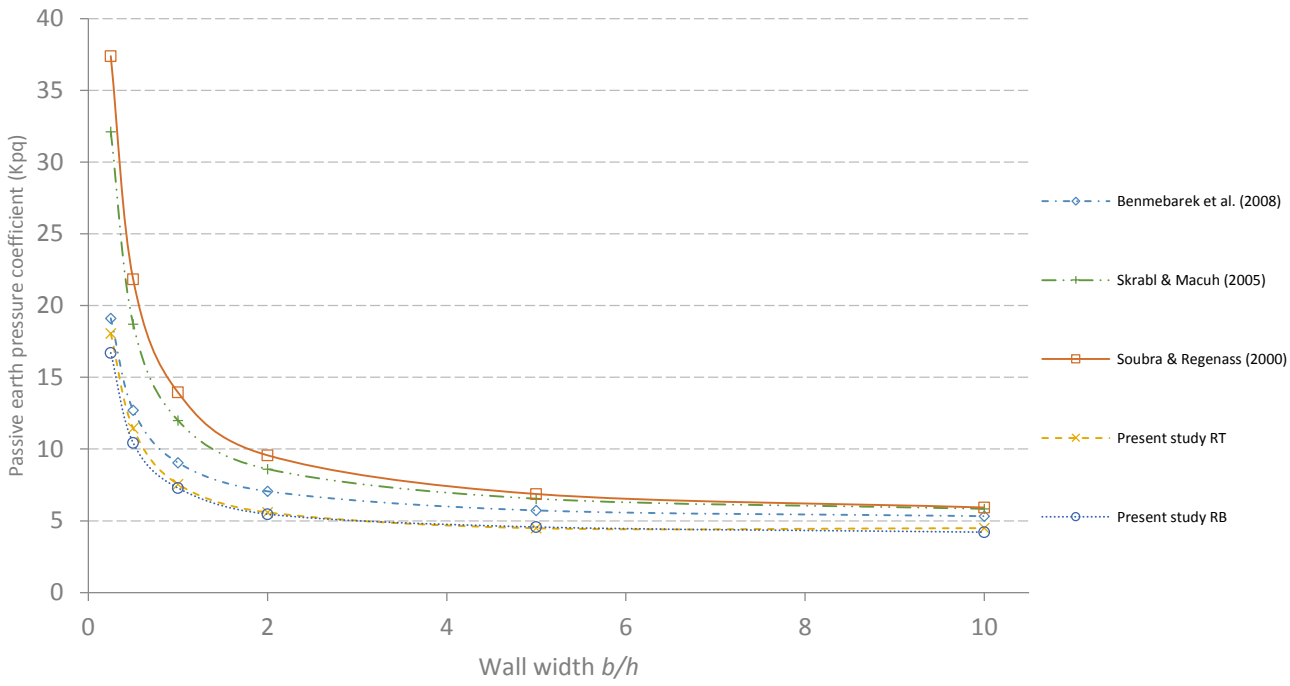

Figure 5. 10. Comparison of passive earth pressure coefficients for $\varphi = 30°$, $\delta/\varphi = 2/3$ and different values of the ration b/h

K_P^T is the passive earth pressure coefficient due to surcharge loading in T mode, K_P^{RT} *and* K_P^{RB} are the coefficients obtained in RT and RB modes respectively. Shape factors evaluation was based on values presented in Table 5. 3. Afterwards, interpolation functions have been extracted for both μ_{RT} and μ_{RB} for various soil friction angles and soil-wall interface friction angles. The proposed formulas were derived using Solver add-on implemented in Microsoft Excel, described as follow:

$$\mu_{RT} = \frac{\alpha_1 \varphi^{\alpha_2}}{e^{\alpha_3 (\delta)^2}} \quad (5.7)$$

$$\mu_{RB} = \frac{\beta_1 \varphi^{\beta_2}}{e^{\beta_3 (\delta)^2}} \quad (5.8)$$

where φ is the soil internal friction angle, δ is the soil-wall interface friction angle. $\alpha_1, \alpha_2, \alpha_3, \beta_1, \beta_2, \beta_3$ are fitting parameters presented as follow:

$$\alpha_1 = 0.790$$

$$\alpha_2 = 0.0197$$

$$\alpha_3 = 3.30\text{E} - 5$$

$$\beta_1 = 0.577$$

$$\beta_2 = 0.108$$

$$\beta_3 = 1.82E - 4$$

The two-dimensional K_P^{RT} and K_P^{RB} obtained from equations (7) and (8) are plotted in Figure 5. 11 for different values of internal friction angles and soil-wall interface friction angles. The results of the present numerical simulation as well as the ones from Caquot & Kérisel (1948) are also plotted for comparison purpose. The figure shows that passive earth pressure coefficients obtained analytically match with those from numerical simulation in both RT and RB modes, with a deviation not exceeding 6% and 7% respectively. In addition, Passive earth pressure coefficients obtained in rotational movement of the retaining wall are much lesser than the common ones from Caquot & Kérisel (1948) used in the literature. Equations (7) and (8) can also be used to match the three-dimensional passive earth pressure coefficients obtained in rotational mode with the ones obtained in translation mode. The difference between the analytical and numerical three-dimensional K_{pq} can reach 14% in RT mode and 13% in RB mode in some values. Even so, the proposed shape factors are acceptable for practical application.

5.2. CONCLUSIONS

Numerical computation of both 2D and 3D active and passive earth pressures due to surcharge loading behind a rigid retaining wall subjected to different types of wall movement; translation, rotation about top and rotation about bottom were evaluated using FLAC code. The below conclusions were drown from this analysis:

- Active and Passive earth pressure distribution along the wall depth in translation mode has a rectangular form with a centroid situated in the middle of the wall. However, both RT and RB modes resolve a nonlinear distribution different of the one reported in literature.

- In RT mode, passive earth pressure is almost null at the wall top, then it increases with depth to reach a maximal value at the wall bottom with a curved distribution. Hence, the distribution centroid in this case is at about 0.3 of the wall height. For the active case in RT mode, high earth pressures appears at the upper half of the wall, then it tends to decrease with depth.

- RB mode resolves a uniform distribution of passive earth pressure at the upper part of the wall, which is similar to the one obtained in T mode. Afterward, starting from the middle of the wall, passive earth pressure sharply decreases with wall depth to reach a zero value at the wall toe. Active earth pressure resolves a non-linear distribution with depth with high earth pressure at the top of the wall and a low one and its bottom. As a result, earth

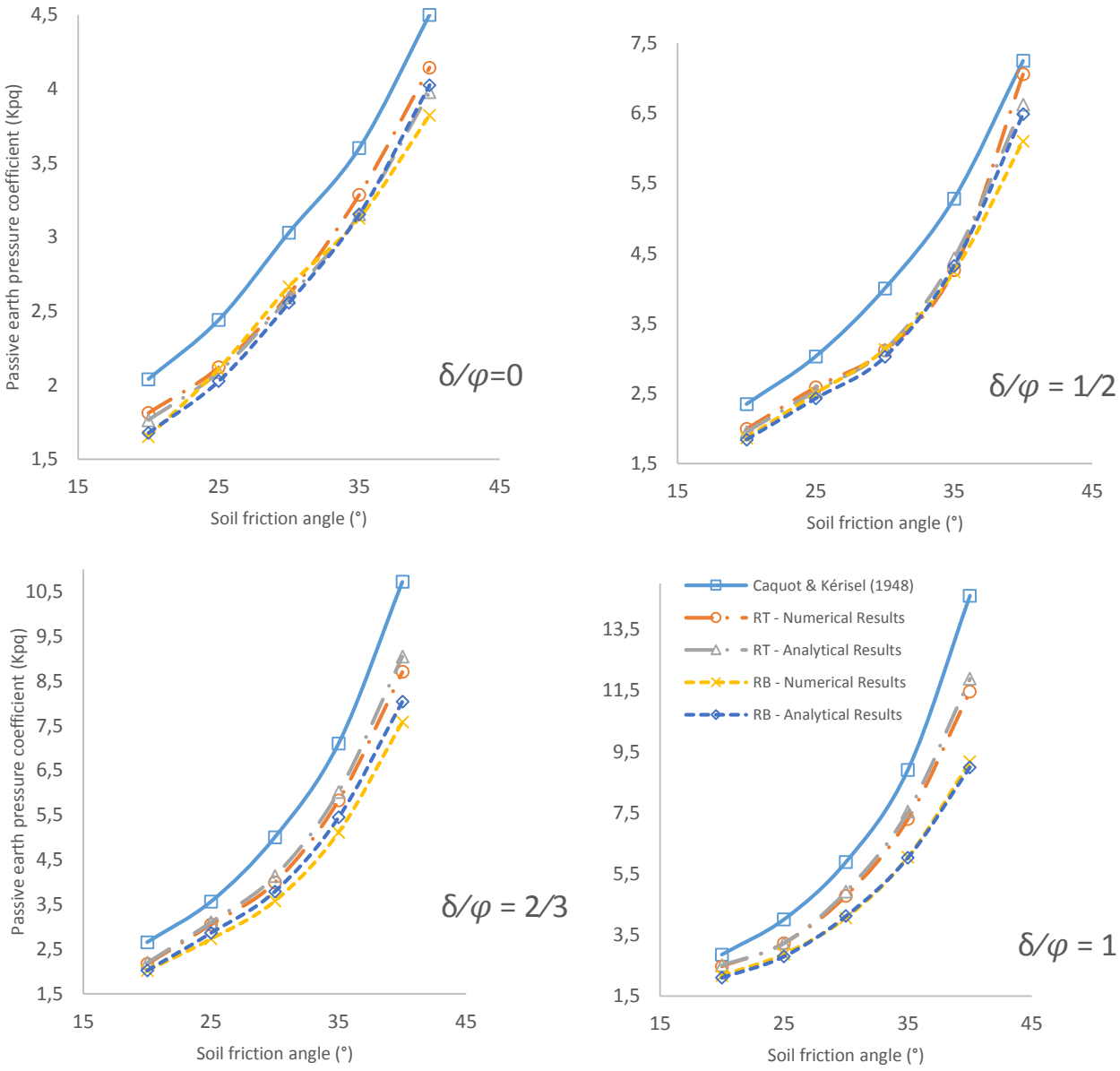

Figure 5. 11. Comparison of passive earth pressure coefficients between analytical and numerical results

pressure distribution centroid in RB mode is situated at a higher position of about 0.75 of the wall height.

- The magnitude of passive earth pressure coefficients is influenced by the type of movement of the retaining wall. RT mode resolves values ranging from 74 to 98% of the ones obtained in T mode. However, RB modes resolves less values ranging from 63% to 93%.

- Three-dimensional passive earth pressure coefficients increase with the decrease of wall width ratio $^{b}/_{h}$. The increase of the friction angle φ and soil-wall interface friction angle δ.

- Based on the obtained numerical results, shape factors were derived linking passive earth pressure coefficients in RT and RB modes to the one in T mode to ease the practice application of passive earth pressure due to uniform surcharge loading under rotational movement of the retaining wall.

GENERAL CONCLUSION

The study of earth pressure theories provides crucial insights into the behavior of soils and retaining structures under various loading conditions. The classical theories, including Rankine's and Coulomb's, have laid the foundation for understanding lateral earth pressure and have been instrumental in practical engineering applications. However, it is important to acknowledge the limitations of these classical theories, notably if the type and magnitude of wall movement can widely affects the predicted earth pressure, which may lead to the insecure in designing retaining structures.

Furthermore, continuum models has emerged as a powerful tool for numerically simulating the complex interactions between soil and retaining structures. It allows for a detailed and accurate assessment of earth pressure behavior under various conditions. In practice, a combination of classical theories, advanced analytical methods, and numerical modeling techniques is often employed to design safe and cost-effective retaining structures. This comprehensive approach ensures that the unique characteristics of each project are appropriately considered, leading to reliable and efficient engineering solutions. Overall, the study of earth pressure theories continues to be of paramount importance in geotechnical engineering, contributing significantly to the success and stability of various construction projects worldwide.

The present thesis aims to assess how different types of wall movements impact the magnitude and distribution shape of active and passive earth pressures. This evaluation will be conducted using both two-dimensional FLAC and three-dimensional FLAC3D codes. The numerical analysis is expected to yield a series of significant conclusions, which can be summarized as follows:

- The existing approaches for evaluating lateral earth pressure are primarily founded on the assumption of translational movement of the wall, assuming a linear distribution of earth pressure with depth. However, numerous field and laboratory tests have demonstrated that for certain types of walls subjected to rotational movement—such as bridge abutments, embedded and anchored retaining walls—this assumption does not hold perfectly true. In such cases, the lateral earth pressure distribution with depth seems to be non-linear. Furthermore, accounting for this rotational movement in the analysis of lateral earth pressure is crucial for accurately predicting the structural behavior and stability of such walls. A more comprehensive understanding of these dynamic forces will lead to more

precise design and construction practices, ultimately enhancing the safety and longevity of these structures.

- The rotational movement of the retaining wall induces partial mobilization within the backfill soil. Consequently, the soil proximate to the mobilized side of the wall tends to reach the limit state much faster than the rest of the soil mass. The obtained results demonstrate that the Mohr-Coulomb model yields lateral earth pressure values similar to those acquired with the Plastic-Hardening model in the upper section of the wall for the RB case, and in the lower section for the RT case. Nevertheless, it is noteworthy that the Plastic-Hardening model provides more realistic outcomes for the partially mobilized side of the soil compared to those derived from the Mohr-Coulomb constitutive model. This observation underscores the significance of accurately accounting for partial mobilization effects in the analysis of retaining walls subjected to rotational movements. Furthermore, the preference for the Plastic-Hardening model on the partially mobilized side suggests its potential as a more reliable tool for predicting the behavior of backfill soil in practical engineering applications. This insight holds implications for the refinement of design methodologies in geotechnical engineering, with the aim of creating safer and more resilient retaining wall systems.

- Active and passive earth pressures due to the soil weight exhibits a conventional linear rectangular distribution with depth, aligning closely with established findings in the literature. However, in the case of RT mode, our current results diverge, revealing higher values of active earth pressure coefficients and lower passive ones compared to those provided by Kérisel & Absi (1990) widely used in the design of retaining structures . Additionally, the resultant earth pressure centroid lies below the one-third of the wall height commonly reported in literature in the passive case and above it in active case. This deviation is attributed to the presence of an arching effect that manifests at the onset of rotational movement. This effect in the passive case, however, gradually diminishes as the limit state of passive earth pressure is approached. In contrast, in RB mode, the rotational movement of the wall leads to a comprehensive mobilization of lateral earth pressure in the upper half of the wall, followed by a partial mobilization that rapidly diminishes, ultimately approaching the earth pressure at rest near the wall's base. This type of movement resolves a passive earth pressure distribution centroid surpassing the one-third of the wall, and an active earth pressure distribution centroid situated at a lower position. Notably, this distribution undergoes a transition from nonlinearity to linearity with increased wall movement, eventually stabilizing into a triangular form similar to that observed in the translational mode.

- The distribution of active and passive earth pressures due to surcharge loading in translation mode exhibits a characteristic rectangular form, with its centroid positioned at the midpoint of the wall. However, in both RT and RB modes, we observe a distinctly non-linear distribution that deviates from the patterns reported in existing literature. Within the RT mode, passive earth pressure is minimal near the top of the wall, gradually increasing in magnitude with depth until it reaches its peak value at the bottom. This results in a curved distribution. Consequently, the centroid of this distribution is located at approximately 0.3 of the wall's height. In contrast, the RB mode reveals a uniform distribution of passive earth pressure in the upper segment of the wall, resembling that of the translational mode (T mode). Moving from the middle of the wall towards its base, passive earth pressure experiences a sharp decline until it reaches zero at the wall's toe. Consequently, the centroid of the passive earth pressure distribution in RB mode is positioned at a higher level, approximately 0.75 of the wall's height. On the other hand, active earth pressure tends to have a centroid which is situated at a lower position than the middle of well reported in literature in the case of rotation about bottom, while the location of the active load centroid is situated at higher position. These nuanced variations in active and passive earth pressure distributions under different modes of wall movement underscore the complexity of soil-structure interactions. The comprehensive understanding of these behaviors not only refines our theoretical models but also carries practical implications for the design and stability of retaining structures subjected to rotational movements.

The ultimate objective of this research is to make a contribution toward a better understanding of the effect of rotational movement on the generated active and passive earth pressures. It is hope that the outcomes of this research will contribute to a greater understanding of soil-foundation-interaction. The direct beneficiaries of this study would be ground engineering contractors, asset owners and software developers, who may be able to exploit the developments reported in this work to inform their projects.

REFERENCES

AASHTO. “Aashto Lrfd Bridge Design Specifications.” 6th ed. Washington, D.C.: American Association of State Highway and Transportation Officials (2012).

Absi, E. “Active and Passive Earth Pressure Tables.” Routledge, 2017.

Anderson William, F., H. Hanna Thomas, and N. Abdel-Malek Magued. "Overall Stability of Anchored Retaining Walls." Journal of Geotechnical Engineering 109, no. 11 (1983/11/01 1983): 1416-33. https://doi.org/10.1061/(ASCE)0733-9410(1983)109:11(1416).

Arsoy, S. "Mobilization of Passive Earth Pressures Behind Abutments of Jointless Bridges." Transportation Research Record 1868 (2004): 199-204.

Arthur, JRF & Cambridge, UK: Univ. of Cambridge. "Strains and Lateral Force in Sand." (1962).

Banerjee, Prasanta Kumar, and Roy & Butterfield. "Boundary Element Methods in Engineering Science." (1981).

Belabdelouhab, F. "Etude Expérimentale De La Butée Discontinue Sur Mode`Le Réduit." PhD thesis, Institut National des Sciences Appliquées de Lyon, France (1988).

Benmebarek, N, S Benmebarek, R Kastner, and A-H Soubra. "Passive and Active Earth Pressures in the Presence of Groundwater Flow." Géotechnique 56, no. 3 (2006): 149-58.

Benmebarek, N, H Labdi, S Benmebarek. "A Numerical Study of the Active Earth Pressure on a Rigid Retaining Wall for Various Modes of Movements." Soil Mechanics and Foundation Engineering. 53, no. 1 (2016): 39-45.

Benmebarek, S, T Khelifa, N Benmebarek and R Kastner. "Numerical Evaluation of 3d Passive Earth Pressure Coefficients for Retaining Wall Subjected to Translation." Computers and Geotechnics. 35, no. 1 (2008): 47-60.

Benmebarek, S, S Attallaoui and N Benmebarek. "Interaction Analysis of Back-to-Back Mechanically Stabilized Earth Walls." Journal of Rock Mechanics and Geotechnical Engineering. 8, no. 5 (2016): 697-702.

Bica, A.V.D., and C.R.I. Clayton. "An Experimental Study of the Behaviour of Embedded Lengths of Cantilever Walls." Géotechnique 48, no. 6 (1998): 731-45.

Blum, H. "Einspannungsverhältnisse Bei Bohlwerken." Diss. Tech. Hochschule Braunnschweig (1930).

Bolton, Mr D, and CK & Canadian Geotechnical Journal Lau. "Vertical Bearing Capacity Factors for Circular and Strip Footings on Mohr–Coulomb Soil." 30, no. 6 (1993): 1024-33.

Boussinesq, J. "Application Des Potentiels À L'étude De L'équilibre Et Du Mouvement Des Solides Élastiques: Principalement Au Calcul Des Deformations Et Des Pressions Que Produisent, Dans Ces Solides, Des Efforts Quelconques Exercés Sur Und Petite Partie De Leur Surface Ou De Leur Intérieur." memoire suivi de notes étendues sur divers points de physique mathématique et d'analyse. Gauthier-Villars. (1885).

Bransby, Peter Leigh. "Stress and Strain in Sand Caused by Rotation of a Model Wall." 1968.

Brinch-Hansen, J. "Resistance of a Rectangular Anchor Slab." Bulletin No. 21, Danish Geotechnical Institute, Copenhagen (1966): 12-13.

Cai, Yanyan, Qingsheng Chen, Yitao Zhou, Sanjay Nimbalkar, and Jin & International Journal of Geomechanics Yu. "Estimation of Passive Earth Pressure against Rigid Retaining Wall Considering Arching Effect in Cohesive-Frictional Backfill under Translation Mode." 17, no. 4 (2017): 04016093.

Caltrans. " California Amendments to the Aashto Lrfd Bridge Design Specifications." 4th ed.Department of Transportation, State of California (2011).

Cao, Wengui, Tao Liu, Zan & Computers Xu, and Geotechnics. "Calculation of Passive Earth Pressure Using the Simplified Principal Stress Trajectory Method on Rigid Retaining Walls." 109 (2019): 108-16.

Caquot, A, and J & Gauthier-Villars Kerisel, Paris. "Tables De Poussée Et De Butée." (1948).

Caquot, Albert Irénée, and Jean Lehuérou Kérisel. Tables for the Calculation of Passive Pressure, Active Pressure and Bearing Capacity of Foundations. Gautier-Villars, 1948.

Chen, Wai-Fah, and XL Liu. Limit Analysis in Soil Mechanics. Elsevier, 2012.

Cheng, Yung Ming & Computers, and Geotechnics. "Seismic Lateral Earth Pressure Coefficients for C–Φ Soils by Slip Line Method." 30, no. 8 (2003): 661-70.

Chowdhury, S.S., K. Deb, and A. Sengupta. "Behavior of Underground Strutted Retaining Structure under Seismic Condition." Earthquakes and Structures 8, no. 5 (2015): 1147-70.

Clayton, C. "Earth Pressure and Earth-Retaining Structures." 2nd edn. Taylor & Francis, New York (1993).

Clayton, C.R.., M. Xu, and A. Bloodworth. " A Laboratory Study of the Development of Earth Pressure Behind Integral Bridge Abutments." Géotechnique 56, no. 8 (2006): 561-71.

Clayont, C.R., Woods, R., Bond, A.J. & Milititsky j. "Earth Pressure and Earth-Retaining Structures – third edition. Taylor & Francis Group, LLC (2013).

Coulomb, Charles Augustin & Mem. Div. Sav. Acad. "Essai Sur Une Application Des Regles De Maximis Et Minimis a Quelques Problemes De Statique Relatifs a 1'architecture." (1773).

Cundall, P. " Explicit Finite-Difference Methods in Geomechanics." Proc. 2nd Int. Conf. Num. Meth. in Geomechanics, Blackshurg 1 (1976): 132-50.

Dalvi, Rupa Sunil, and Prabhakar Jagannath & Indian Geotechnical Journal Pise. "Analysis of Arching in Soil-Passive State." 42 (2012): 106-12.

Day, RA, DM & International Journal for Numerical Potts, and Analytical Methods in Geomechanics. "The Effect of Interface Properties on Retaining Wall Behaviour." 22, no. 12 (1998): 1021-33.

Dembicki, E., J. Dravtchenko, and E. Sibille. "Sur Les Solutions Analytiques Approchées Des Problèmes D'équilibre Limite Plan Pour Milieux Cohérents Et Pèsants.". Journal de Mécanique 3 (1964).

Domej, Gisela. ‘’Seismically induced effects and slope stability in urbanized areas via numerical modeling”. Phd thesis, Ecole doctorale, Paris-est, France (2018)

Dou, Guotao, Junwu Xia, Wenjie Yu, Fang Yuan, Weigang & International Journal of Mining Science Bai, and Technology. "Non-Limit Passive Soil Pressure on Rigid Retaining Walls." 27, no. 3 (2017): 581-87.

Drucker, D.C, H.J. Greenberg, and W. Prager. "Extended Limit Design Theorems for Continuous Media.". Quarterly of Applied Mathematics 9 (1952): 381-89.

Duncan, J. Michael, and L. Mokwa Robert. "Passive Earth Pressures: Theories and Tests." Journal of Geotechnical and Geoenvironmental Engineering 127, no. 3 (2001/03/01 2001): 248-57. https://doi.org/10.1061/(ASCE)1090-0241(2001)127:3(248).

Duncan, J.M., and C.Y. Chang. "Nonlinear Analysis of Stress and Strain in Soils." Journal of the Soil Mechanics and Foundations Division 96, no. 5 (1970): 1629-53.

England, G. L., and N.C.M. Tsang. "Design of Soil Loading for Integral Bridges." Indian Concrete Journal 79, no. 53-59 (2005).

Ertugrul, Ozgur L, Aurelian C & Journal of Rock Mechanics Trandafir, and Geotechnical Engineering. "Seismic Earth Pressures on Flexible Cantilever Retaining Walls with Deformable Inclusions." 6, no. 5 (2014): 417-27.

Fan C., and Fang Y.S. “Numerical solution of active earth pressures on rigid retaining walls built near rock faces”. Computers and Geotechnics 37, no. 7–8 (2010):1023–1029.

Fang, Y.S., and Ishibashi I. "Static Earth Pressures with Various Wall Movements". Journal of Geotechnical Engineering 112, no. 3 (1986): 317-33.

Fang Y.S., Chen T.J. and Wu B.F. “Passive Earth Pressures with Various Wall Movements”. Journal of Geotechnical Engineering 120, no. 8 (1994):1307–1023.

Fang Y.S., Chen J.M., Chen C.Y. “Earth Pressures With Sloping Backfill”. Journal Of Geotechnical And Geoenvironmental Engineering. 123 (1997): 250-259.

FLAC, Itasca Consulting Group, Inc. (2019) FLAC — Fast Lagrangian Analysis of Continua, Ver. 8.1. Minneapolis: Itasca.

FLAC3D, Itasca Consulting Group, Inc. (2019) FLAC3D — Fast Lagrangian Analysis of Continua in Three-Dimensions, Ver. 6.0. Minneapolis: Itasca.

French Code of Practice "Recommendation Concernant la Conception, le Calcul, l'execution et le Control des Tirants d'Ancrage," Recommendation T.A.72, Bureau Securitas, 1st ed., Paris, France, 1972.

Georgiadis, M., and C. Anagnostopoulos. "Displacement of Structures Adjacent to Cantilever Sheet Pile Walls." Soils and Foundations 39, no. 2 (1999/04/01/ 1999): 99-104. https://doi.org/https://doi.org/10.3208/sandf.39.2_99.

Georgiadis, Michael, Christos & Journal of geotechnical Anagnostopoulos, and geoenvironmental engineering. "Lateral Pressure on Sheet Pile Walls Due to Strip Load." 124, no. 1 (1998): 95-98.

Graham, J. "Calculation of Passive Pressure in Sand." Canadian Geotechnical Journal 8, no. 4 (1971): 566-79.

Handy, Richard L & Journal of Geotechnical Engineering. "The Arch in Soil Arching." 111, no. 3 (1985): 302-18.

Handy, Richard L. "The Arch in Soil Arching." 111, no. 3 (1985): 302-18. https://doi.org/doi:10.1061/(ASCE)0733-9410(1985)111:3(302).

Hanna, T. H., and G. A. Matallana. "The Behavior of Tied-Back Retaining Walls." Canadian Geotechnical Journal 7, no. 4 (1970/11/01 1970): 372-96. https://doi.org/10.1139/t70-050.

Hazarika, Hemanta, Hiroshi & Computers Matsuzawa, and Geotechnics. "Wall Displacement Modes Dependent Active Earth Pressure Analyses Using Smeared Shear Band Method with Two Bands." 19, no. 3 (1996): 193-219.

Hou, Guangxian, and Shanzhi Shu. "Trial Wedge Approach to Determine Lateral Earth Pressures." 19, no. 1 (2019): 06018035. https://doi.org/doi:10.1061/(ASCE)GM.1943-5622.0001326.

Hueckel, S. "Model Tests on Anchoring Capacity of Vertical and Inclined Plates." In: Proceedings of 4th international conference on soil mechanics and foundation engineering, London 2 (1957): 203-06.

Huntley, Shelley A., and Arun J. Valsangkar. "Field Monitoring of Earth Pressures on Integral Bridge Abutments." Canadian Geotechnical Journal 50, no. 8 (2013/08/01 2013): 841-57. https://doi.org/10.1139/cgj-2012-0440.

Jaky, J. "The Coefficient of Earth Pressure at Rest." Journal for Society of Hungarian Architects and Engineers. Budapest, Hungary 1944 (1944): 355-58.

James, E.L., and B.J. Jack. "A Design Study of Diaphragm Walls," Proceedings." Conference of Diaphragm Walls and Anchorages, Institution of Civil Engineers, London (1974): 41-49.

James, R.G., and P.L. Bransby. "Experimental and Theoretical Investigations of a Passive Earth Pressure Problem." Géotechnique 20, no. 1 (1970): 17-37.

James, RG, and P_L & Geotechnique Bransby. "Experimental and Theoretical Investigations of a Passive Earth Pressure Problem." 20, no. 1 (1970): 17-37.

Janbu, N. "Soil Compressibility as Determined by Oedometer and Triaxial Tests." In Proc., of the European Conf. on Soil Mechanics and Foundation Engineering. Wiesbaden, Germany: Deutsche Gesellschaft für Erd- und Grundbau. (1963): 19-25.

Javankhoshdel, S., Shokri, S., Rezvani, M., Cami, B., Yacoub, T. “2D and 3D Sensitivity Analysis of a Multitiered Retaining Wall”. Global Journal of Engineering Sciences 1, no 5 (2019).

Jibson, Randall W. "Methods for Assessing the Stability of Slopes During Earthquakes—a Retrospective." Engineering Geology 122, no. 1 (2011/09/12/ 2011): 43-50. https://doi.org/https://doi.org/10.1016/j.enggeo.2010.09.017.

Jong, D.J.G. De. " Graphical Method for the Determination of Slip-Line Fields in Soil Mechanics." Ingenieur 69, no. 29 (1957): 61-65.

Kame, G. S.. “Analysis of a continuous vertical plate anchor embedded in cohesionless soil.” Dissertation, Indian Institute of Technology, Bombay, India (2012).

Kerisel, J., and E. Absi. " Active and Passive Earth Pressure Tables." Balkema, Rotterdam (1990).

Khelifa, T., & Benmebarek, S. Dilation effect on 3D Passive Earth Pressure Coefficients for Retaining Wall. Academic Platform - Journal of Engineering and Science.2, no 2 (2014) :1-6.

Khosravi, Mohammad Hossein, Thirapong Pipatpongsa, Jiro & Soils Takemura, and Foundations. "Theoretical Analysis of Earth Pressure against Rigid Retaining Walls under Translation Mode." 56, no. 4 (2016): 664-75.

Kötter, F. "Die Bestimmung Des Drucks an Gekrümmten Gleitflächen, Eine Aufgabe Aus Der Lehre Vom Erddruck." Sitzungsberichteder Akademie der Wissenschaften, Berlin 229-233 (1903).

Kranz, E. " Uber Die Verankerung Von Spudwanden." W. Ernst & Sohn, Berlin (1953).

Krey, H. "Erddruck, Erdwiderstand Und Tragfahõègkeit Des Baugrundes." Berlin: Ernst (1932).

Kumar, J., & Subba Rao, K. S. "Passive pressure coefficients, critical failure surface and its kinematic admissibility". Géotechnique 47, no. 1(1997): 185–192.

LEE, CF & 钱七虎院士论文选集. "Active and Passive Critical Slip Fields for Cohesionless Soils and Calculation of Lateral Earth Pressures." (2007).

Littlejohn, G.S. "Anchored Diaphragm Walls in Sand—Anchor Design." Ground Engineering 5, no. 1 (1972): 12-17.

Liu, F. Q., & Wang, J. H. "A generalized slip line solution to the active earth pressure on circular retaining walls". Computers and Geotechnics 35 no. 2(2008): 155–164.

Liu, Shiyi, Yang Xia, Li & Journal of Rock Mechanics Liang, and Geotechnical Engineering. "A Modified Logarithmic Spiral Method for Determining Passive Earth Pressure." 10, no. 6 (2018): 1171-82.

Lucia, JBA & Research project report, Mechanical Sciences Tripos, Part IIA, University of Cambridge. "Passive Earth Pressure and Failure in Sand." (1966).

Lyndon, A., and R. A. Pearson. "Pressure Distribution on a Rigid Retaining Wall in Cohesionless Material." Proceedings of a symposium on the application of centrifuge modelling to geotechnical design, Manchester (1984): 271-80.

Matsuo, Minoru, Satoru Kenmochi, Hideki & Soils Yagi, and Foundations. "Experimental Study on Earth Pressure of Retaining Wall by Field Tests." 18, no. 3 (1978): 27-41.

Mayne Paul, W., and H. Kulhawy Fred. "Closure to "Ko-Ocr Relationships in Soils" by Paul W. Mayne and Fred H. Kulhawy (June, 1982)." Journal of Geotechnical Engineering 109, no. 6 (1983/06/01 1983): 867-69. https://doi.org/10.1061/(ASCE)0733-9410(1983)109:6(867).

Mei, Guo-xiong, Rui Chen, and Jian Liu. "New Insight into Developing Mathematical Models for Predicting Deformation-Dependent Lateral Earth Pressure." International Journal of Geomechanics 17, no. 8 (2017/08/01 2017): 06017003. https://doi.org/10.1061/(ASCE)GM.1943-5622.0000902.

Meksaouine, M. "Etude Expe´Rimentale Et the´Orique De La Poussée Passive Sur Pieux Rigides." PhD thesis, Institut National des Sciences Appliquées de Lyon, France (1993).

Meyerhof, G.G. "Bearing Capacity and Settlement of Pile Foundations." Journal of the Geotechnical Engineering Division 102, no. 3 (1976): 197-228.

Mindlin, RD. "Discussion: Pressure Distribution on Retaining Walls." Paper presented at the Proc., Int. Conf. Soil Mechanic and Foundation Engineering, Graduate School of Engineering, Harvard University., Cambridge, Mass, 1936.

Motta, E. "Generalized Coulomb active earth pressure for distanced surcharge". Journal of Geotechnical and Geoenvironmental Engineering 120 no. 6(1994): 1072–1079.

Nakai, T., H. Kawano, K. Murata, M. Banno, and T. Hashimoto. "Model Test and Numerical Simulation of Braced Excavation in Sandy Ground: Influences of Construction History, Wall Friction, Wall Stiffness, Strut Position and Strut Stiffness." Soils and Foundations 39, no. 3 (1999): 1-12.

Novotortsev, V.I. " Application of the Theory of Plasticity to Problems of Determining the Bearing Capacity of Building Foundations." Izv., VNIG 22 (1938).

Ostermayer, H. "Practice in the Detail Design Application of Anchorages." A Review of Diaphragm Walls, Institution of Civil Engineers, London (1977): 55-61.

Ovesen, N.K. "Anchor Slabs, Calculation Methods, and Model Tests." Bull. No. 16, Danish Geotechnical Institute, Copenhagen (1964): 5-39.

Ovesen, N.K., and H. Stromann. "Design Method for Vertical Anchor Slabs in Sand." ASCE Proceedings, Specialty Conference on Performance of Earth and Earth-Supported Structures 1, no. 2 (1972): 1481-500.

Paik, K. H., & Salgado, R. "Estimation of active earth pressure against rigid retaining walls considering arching effects". Géotechnique 53 no. 7(2003): 643–653.

Patel, Smita, Kousik & European Journal of Environmental Deb, and Civil Engineering. "Experimental and Analytical Study of Passive Earth Pressure Behind a Vertical Rigid Retaining Wall Rotating About Base." 26, no. 6 (2022): 2371-99.

Peng, Shu-quan, Xi-bing Li, FAN Ling, and Ai-hua & Transactions of Nonferrous Metals Society of China Liu. "A General Method to Calculate Passive Earth Pressure on Rigid Retaining Wall for All Displacement Modes." 22, no. 6 (2012): 1526-32.

Potts, D.M., and L. Zdravkovic. "Finite Element Analysis in Geotechnical Engineering: Application." London, Thomas Telford (2001).

Potts, D.M., and L. Zdravkovic. " Finite Element Analysis in Geotechnical Engineering: Theory." London, Thomas Telford (1999).

Potts, DM, AB & International journal for numerical Fourie, and analytical methods in geomechanics. "A Numerical Study of the Effects of Wall Deformation on Earth Pressures." 10, no. 4 (1986): 383-405.

Prandtl, L. "Uber Die Harte Plastischer Korper." Nachr. Ges. Wiss. Goettingen Math. Phys. Kl (1920): 74-85.

Qian, Ze-hang, Jin-feng Zou, Jie Tian, Qiu-jing & Computers Pan, and Geotechnics. "Estimations of Active and Passive Earth Thrusts of Non-Homogeneous Frictional Soils Using a Discretisation Technique." 119 (2020): 103366.

Rahardjo, Harianto, and Delwyn G & Canadian Geotechnical Journal Fredlund. "General Limit Equilibrium Method for Lateral Earth Force." 21, no. 1 (1984): 166-75.

Rankine, William John Macquorn & Philosophical transactions of the Royal Society of London. "Ii. On the Stability of Loose Earth." no. 147 (1857): 9-27.

Reissner, H. " Zum Erddruckproblem." In: C.B. Biezend and J.M. Burgers (Editors), Proc. 1st Int. Congr. Appl. Mech., Del (1924): 295-311.

Roscoe, K_ H_ & Geotechnique. "The Influence of Strains in Soil Mechanics." 20, no. 2 (1970): 129-70.

Schanz, T, PA Vermeer, and P Gc & Beyond in computational geotechnics Bonnier. "The Hardening Soil Model: Formulation and Verification." 1 (1999): 281-96.

Schmüdderich, Christoph, Franz Tschuchnigg, and Torsten & Géotechnique Letters Wichtmann. "Rigorous Lower and Upper Bounds for the 3d Passive Earth Pressure Problem." 10, no. 2 (2020): 100-05.

Shubhra, G., & Patra, N. R. « Effect of arching on active earth pressure for rigid retaining walls considering translation mode". International Journal of Geomechanics 8, no. 2 (2008): 123–133.

Shukla, S. K., Gupta, S. K., & Sivakugan, N. "Active earth pressure on retaining wall for c–ϕ soil backfill under seismic loading condition". Journal of Geotechnical and Geoenvironmental Engineering 135, no. 5 (2009): 690–696.

Škrabl, S., & Macuh, B. "Upper-bound solutions of three dimensional passive earth pressures". Canadian Geotechnical Journal 42, no. 5 (2005): 1449–1460.

Soekhoe R. "Realistic bending stiffness of diaphragm walls for structural analysis". A comparison with the uncracked and totally cracked stiffness for the case of The Waalbrug Nijmegen. Delft University of Technology, Mekelweg, Netherlands (2015)

Sokolovskii, V.V. "Statics of Soil Media." Butterworths Scientific Publications, London. (1960).

Sokolovskii "Statics of Granular Media." Pergamon Press, New York (1965).

Soubra, A. H., & Regenass, P. "Three-dimensional passive earth pressures by kinematical approach". Journal of Geotechnical and Geoenvironmental Engineering (2000): 969–978.

Soubra, A-H, and Borut Macuh "Active and Passive Earth Pressure Coefficients by a Kinematical Approach" Proceedings of the Institution of Civil Engineers-Geotechnical Engineering 155, no. 2 (2002): 119-31.

Soubra, Abdul-Hamid, Pierre "Three-Dimensional Passive Earth Pressures by Kinematical Approach." Journal of Geotechnical Regenass, and Geoenvironmental Engineering 126, no. 11 (2000): 969-78.

Spangler, M. G. "The distribution of normal presssure on retaining wall due to a concentrated surface load," Proc., of Int. Conf. Soil Mechs and Found. Engg., Graduate School of Engineering, Harvard University (1936): 200-207.

Spencer, A.J.M. " Perturbation Methods in Plasticity. Ill, Plane Strain of Ideal Soils and Plastic Solids with Body Forces." Journal of the Mechanics and Physics of Solids 10 (1962): 165-77.

Steinberg, E., S. M. Sargand, and C. Bettinger. "Forces in Wingwalls of Skewed Semiintegral Bridges." Journal of Bridge Engineering 9, no. 6 (2004): 563-71.

Subba Rao, K.-S., & Choudhury, D. “Seismic passive earth pressures in soils”. Journal of Geotechnical and Geoenvironmental Engineering 131, no. 1 (2005): 131–135.

Takemura, J., M. Kondoh, T. Esaki, M. Kouda, and O. Kusakabe. "Centrifuge Model Tests on Double Propped Wall Excavation in Soft Clay." Soils and Foundations 39, no. 3 (1999): 75-87.

Tang, Yao, Jing Pei Li, and Yuan & International Journal of Geomechanics Ma. "Lateral Earth Pressure Considering the Displacement of a Rigid Retaining Wall." 18, no. 11 (2018): 06018031.

Taylor, D.W. " Fundamentals of Soil Mechanics." Wiley, New York (1948).

Tefera, T.H., S. Nordal, L. Grande, R. Sandven, and A. Emdal. "Ground Settlement and Wall Deformation from a Large Scale Model Test on as Single Strutted Sheet Pile Wall in Sand." International Journal of Physical Modelling in Geotechnics 6, no. 2 (2006): 1-13.

Tejchman, J, J Kozicki, D & International Journal of Solids Leśniewska, and Structures. "Discrete Simulations of Shear Zone Patterning in Sand in Earth Pressure Problems of a Retaining Wall." 48, no. 7-8 (2011): 1191-209.

Teng, W.C. "Prentice-Hall of India, New Delhi." (Foundation Design).

Terzaghi, C. "Discussion of Lateral Earth Pressure: The Accurate Experimental Determination of the Lateral Earth Pressure, Together with a Resume of Previous Experiments." Transactions of the American Society of Civil Engineers 86 (1923): 1525-43.

Terzaghi, K. " Anchored Bulk Heads." Transactions ASCE 119 (1954).

Terzaghi, K. " Theoretical Soil Mechanics." Wiley (1943).

Terzaghi, K., and R.B. Peck. " Soil Mechanics on Engineering Practice." John Wiley & Sons, New York (1948).

Terzaghi, K., R.B. Peck, and G. Mesri. "Mechanics in Engineering Practice." 3rd Edition, John Wiley and Sons, Inc., New York (1996).

Tom Wörden, Florian, Martin & Computers Achmus, and Geotechnics. "Numerical Modeling of Three-Dimensional Active Earth Pressure Acting on Rigid Walls." 51 (2013): 83-90.

Tsagareli, ZV & Soil Mechanics, and Foundation Engineering. "Experimental Investigation of the Pressure of a Loose Medium on Retaining Walls with a Vertical Back Face and Horizontal Backfill Surface." 2, no. 4 (1965): 197-200.

Vermeer, Pieter A, and R & HERON De Borst, 29 ,. "Non-Associated Plasticity for Soils, Concrete and Rock." (1984).

Vo, T, H Taiebat, and AR & Géotechnique Russell. "Interaction of a Rotating Rigid Retaining Wall with an Unsaturated Soil in Experiments." 66, no. 5 (2016): 366-77.

Wai, FAH. "Limit Analysis and Soil Plasticity." (1975).

Weissenbach, A. "Der Erdwiderstand Vor Schmalen Druckflechen." PhD thesis, Franzius Institut fur Grund und Wasserbau der Technischen Hochschule, Hannover (1961): 338.

Widuliński L., Tejchman J., Kozicki J. and Leśniewska D. “Discrete Simulations of Shear Zone Patterning in Sand in Earth Pressure Problems of a Retaining Wall”. International Journal of Solids and Structures 48, no. 7–8 (2011): 1191–1209.

Wilun, Z., and K. Starzewski. "Soil Mechanics in Foundation Engineering." Vol. II, Surrey University Press, London (1975).

Wörden F.T., and Achmus M. “Numerical modeling of three-dimensional active earth pressure acting on rigid walls”. Computers and Geotechnics 51 (2013) 83–90.

Xie, Y, and B & Géotechnique Letters Leshchinsky. "Active Earth Pressures from a Log-Spiral Slip Surface with Arching Effects." 6, no. 2 (2016): 149-55.

Yang, Y., Chen, L., Sun, R., Chen, Y., & Wang, W. “A depth-consistent SPT-based empirical equation for evaluating sand liquefaction”. Engineering Geology 221 (2017): 41-49.

Ying, H. W., Jiang, B., & Xie, K. H. “Analysis of the minor principal stress arch behind retaining wall”. Advances in Earth Structure, (2006): 340–347.

Yokoi, Hajime. "Relationship between Soil Cohesion and Shear Strength." Soil Science and Plant Nutrition 14, no. 3 (1968/05/01 1968): 89-93.

Zhu, D. Y., Qian, Q. H., & Lee, C.-F. “Active and passive critical slip fields for cohesionless soils and calculation of lateral pressures”. Géotechnique 51, no. 5 (2001): 407–423.

Zienkiewicz, O.C. "The Finite Element Method." 3rd edn. McGraw-Hill, London (1977).